



# Far-from-Equilibrium Quasiparticle Dynamics in Graphene

**Dissertation**

for the award of the degree

”Doctor rerum naturalium” (Dr.rer.nat.)

of the Georg-August-Universität Göttingen

within the doctoral program ProPhys  
of the Georg-August-University School of Science (GAUSS)

submitted by

**Marten Düvel**

from Celle

Göttingen, 2022

**Thesis Committee**

Prof. Dr. Stefan Mathias,  
AG Mathias, I. Physikalisches Institut

Prof. Dr. Martin Wenderoth,  
AG Wenderoth, IV. Physikalisches Institut

Prof. Dr. Vasily Moshnyaga,  
AG Moshnyaga, I. Physikalisches Institut

**Members of the Examination Board**

**Reviewer:**

Prof. Dr. Stefan Mathias,  
AG Mathias, I. Physikalisches Institut

**Second Reviewer:**

Prof. Dr. Martin Wenderoth,  
AG Wenderoth, IV. Physikalisches Institut

**Further Members of the Examination Board**

Prof. Dr. Thomas Weitz,  
AG Weitz, I. Physikalisches Institut

Prof. Dr. Christian Jooss  
AG Jooß, Institut für Materialphysik

PD Dr. Salvatore R. Manmana  
Kondensierte Materie, Institut für Theoretische Physik

Junior Professorin Jasnamol Palakkal  
Gruppe Komplexe dünne Schichten / Laserdeposition, Institut für Materialphysik

**Date of oral examination: 25.11.2022 11:45**

## Abstract

Comprehending far-from-equilibrium many-body interactions is one of the major goals of current ultrafast condensed matter physics research. Here, a particularly interesting but barely understood situation occurs during a strong optical excitation, where the electron and phonon systems can be significantly perturbed and the quasiparticle distributions cannot be described with equilibrium functions. In this thesis, we use time- and angle-resolved photoelectron spectroscopy (trARPES) to study such far-from-equilibrium many-body interactions for the prototypical material graphene by evaluating the low-energy non-equilibrium quasiparticle self-energy at the femtosecond timescale. The low-energy quasiparticle response, however, is at first inaccessible due to resolution artifacts caused by the spectrally our broad XUV probe pulses, which are unavoidable due to the time-bandwidth-product. Therefore, we apply a Lucy-Richardson deconvolution algorithm (LRD) to the ARPES spectra. Furthermore, we introduce rigorous benchmarking of the LRD to assure physical-meaningful results. To deliver angle-resolved photoemission spectroscopy (ARPES) data in the necessary quality for this LRD approach, we built a trARPES setup with an extreme ultraviolet (XUV) probe source in this thesis. This XUV probe source can be switched between an energy-resolution optimized beamline and time-resolution optimized beamline. With this experiment, we find remarkable transient renormalizations of the quasiparticle self-energy caused by the photo-induced non-equilibrium conditions, which are in accordance with first-principles theoretical modeling. These observations can be understood by ultrafast scatterings between far-from-equilibrium electrons and strongly-coupled optical phonons, which signifies the crucial role of ultrafast non-equilibrium dynamics on many-body interactions. Our results advance the understanding of many-body physics in extreme conditions, which is important for any endeavor to optically manipulate or create emergent states of matter.

## Acknowledgements

Hier würde ich gerne einigen Personen danken. Ich danke meiner ganzen Familie und allen Freunden für die Unterstützung während der Arbeit. Ich danke Prof. Dr. Stefan Mathias für die Ermöglichung und Betreuung bei dieser Arbeit. Ich danke Dr. Marcel Reutzel, Dr. Sabine Steil, Dr. Matthijs Jansen und Dr. Daniel Steil für die Unterstützung und Betreuung während der Arbeit. Ich danke meiner Prüfungskommission, Gutachtern und dem Betreuungsausschusses Prof. Dr. Martin Wenderoth, Prof. Dr. Vasily Moshnyaga, Prof. Dr. Thomas Weitz, Prof. Dr. Christian Jooss, PD Dr. Salvatore R. Manmana und Junior Professorin Jasnamol Palakkal. Ich danke besonders Marco Merboldt für die Übernahme von Kammer 4 und Durchführung vieler wichtiger Messungen. Ich hoffe, die Kammer funktioniert für den Rest deiner Arbeit jetzt einfach. Weiterhin danke ich allen Bachelor und Master Studenten/Studentinnen, die mir beim Aufbau von Kammer 4 und der Durchführung von Messungen zur Seite standen. Dies waren Hannah Strauch, Michael Stellbrink, Jan-Hendrik Müller, Christopher Wendeln, Tim Titze, Sarina Vogt, Jasmin Kappert, Daniel Marx, Germaine Arend, Jonas Pöhls, David Schmitt und Jan Philipp Bange. Ich danke Dr. Sabine Steil für die Mitbetreuung dieser vielen Bachelor- und Master-Studenten/Studentinnen. Ich danke Marcel Reutzel, Marco Merboldt, Dino Novko und Stefan Mathias, die Zusammenarbeit an der Publication<sup>1</sup>. Ich danke Marcel Reutzel, Marco Merboldt, Henrike Probst, Stefan Mathias für die Anregungen beim Verfassen dieser Arbeit. Ich danke den Technikern des I. Physikalischen Instituts Uta Filippich, Carsten Mahn, Kai Dörner, Hartmut Eichenberg, Bastian Beyland, Simon Stoldt, Katrin Gehrke, Dennis Kohl und Michael Tetzlaff für jede Hilfe. Ich danke ebenso den Mitgliedern der Zentral- und Elektrowerkstatt. Ich danke Michaela Mecke und Finn Krummacker für die Hilfe bei bürokratischen Hürden. Ich danke Henrike Probst und Christina Möller für die gute Atmosphäre im Büro. Ich danke allen anderen Mitgliedern der Arbeitsgruppe Mathias für jede Hilfe. Ebenso danke ich auch allen anderen Mitgliedern des I. Physikalischen Institutes für jede Hilfe.

## Contents

<b>Abstract</b>	<b>iii</b>
<b>Acknowledgements</b>	<b>iv</b>
<b>Contents</b>	<b>v</b>
<b>Acronyms</b>	<b>x</b>
<b>Publications</b>	<b>xii</b>
Parts of the thesis are based on the following publication.....	xii
Further Publications .....	xii
<b>Chapter 1 Introduction</b>	<b>1</b>
<b>Chapter 2 Background</b>	<b>7</b>
2.1 Photoemission Spectroscopy .....	8
2.1.1 Angle-Resolved Photoemission Spectroscopy .....	8
2.1.1.1 One-Step-Model .....	12
2.1.2 Many-Body Interactions in the Quasiparticle Picture measured with ARPES	15
2.1.3 Two-Photon-Photoemission.....	17
2.1.4 Time- and Angle-Resolved Photoemission Spectroscopy .....	20
2.1.4.1 Population Dynamics.....	20
Far-from-Equilibrium Dynamics .....	20
Non-Equilibrium Dynamics .....	22
2.1.4.2 Quasiparticle Dynamics in trARPES .....	24
2.1.5 Photoemission Horizon .....	25
2.2 Dirac Materials .....	26
2.2.1 Electron-Hole Excitations .....	30

<b>Chapter 3</b>	<b>Establishment of an Ultrafast Time-Resolved XUV ARPES Setup</b>	<b>34</b>
3.1	Vacuum Chamber.....	35
3.2	Phoibos 150 2D CCD ARPES Detector.....	35
3.3	Light Sources and Beamline Setups.....	37
3.3.1	Vacuum-Ultraviolet Plasma Discharge Lamp.....	37
3.3.2	Fiber Laser by Active Fiber Systems.....	38
3.3.3	2PPE Beamline.....	39
3.3.4	High-Harmonic Generation.....	41
3.3.5	Time- and Angle-Resolved Photoemission Spectroscopy Beamline.....	45
<b>Chapter 4</b>	<b>Establishment of the Lucy-Richardson Deconvolution for Short Pulse trARPES</b>	<b>48</b>
4.1	Resolution Artifact.....	50
4.2	Lucy-Richardson Deconvolution Algorithm.....	54
4.3	Estimation of the Point-Spread-Function.....	55
4.4	Benchmarking of the Lucy-Richardson Deconvolution Algorithm.....	57
4.5	Effects of the LRD on the trARPES Spectra.....	62
4.6	Discussion of our Approach to the LRD.....	65
<b>Chapter 5</b>	<b>Far-from-Equilibrium Electron-Phonon Interactions in Optically-Excited Graphene</b>	<b>68</b>
5.1	Introduction.....	69
5.2	Review on Quasiparticle Dynamics in Doped Graphene/SiC with Static ARPES	72
5.2.1	Electron-Phonon Coupling.....	76
5.2.2	Electron-Hole and Electron-Plasmon Coupling.....	80
5.2.3	Plasmaron.....	84
5.3	Review on Ultrafast Population Dynamics in Graphene.....	85
	Far-from-Equilibrium Electron-Electron Scattering.....	86
	Far-from-Equilibrium Electron-Phonon Scattering.....	88
	Interplay between Electron-Electron and Electron-Phonon Processes.....	89
5.4	Quasiparticle Dynamics under Far-from-Equilibrium Conditions.....	90

5.5	Experimental Results from ARPES and trARPES on Graphene	92
5.5.1	Quasiparticle Dynamics Analysed with Static ARPES	92
5.5.2	Far-from-Equilibrium Quasiparticle Dynamics with trARPES	97
5.5.2.1	Electron-Phonon Interaction under Far-from-Equilibrium Conditions	100
5.5.2.2	Overall Increase of $\text{Im}\Sigma$ under Far-from-Equilibrium Conditions	104
	Electron-Electron Scattering Channels	107
	Comparison of the Electron-Hole Generation Model to Literature	110
	Electron-Plasmon and Electron-Hole Interaction around the Dirac Point	111
	Conclusion on Electron-Electron Scattering	112
	Electron-Phonon Scattering	112
	Interaction Strengths	113
	Conclusion on the Overall Increase in the $\text{Im}\Sigma$	113
5.6	Outlook	114
5.6.1	Interaction Strength Enhancement	114
	Additional Studies in Graphene/SiC	115
5.6.2	Phonon Absorption Signatures	115
5.6.3	LRD in other Sample Systems	116
5.6.3.1	Gated Samples and Plasmons in Photoinverted Graphene	117
5.6.3.2	Plasmarons in Freestanding Graphene	118
5.7	Conclusion	118
	<b>Bibliography</b>	<b>119</b>
	<b>List of Figures</b>	<b>135</b>
	<b>Chapter A Appendix</b>	<b>146</b>
A.1	Energy Resolution in ARPES with the XUV Beamlines	146
A.2	Time Resolution of the trARPES Experiment	148
A.3	Self-Consistent Calculation of the Self-Energy	149
A.4	Additional data from the trARPES measurements from Graphene	152
A.5	Far-from-Equilibrium Resolution Artifact	153
A.6	Momentum Broadening Dependence of the LRD	155

A.7 Pump-Fluence-Dependent Analysis of the Self-Energy .....	155
--	-----



## Acronyms

1PPE	One-Photon-Photoemission
2DEG	Two-Dimensional-Electron-Gas
2PPE	Two-Photon-Photoemission
AFS	Active-Fiber-Systems
ARPES	Angle-Resolved Photoemission Spectroscopy
BBO	Non-Linear- $\beta$ -Barium-Borate Crystal
CDW	Charge-Density-Wave
DFT	Density-Functional-Theory
EDC	Energy-Distribution-Curve
e-e	Electron-Electron
e-h	Electron-Hole
ELDOS	Electron-Density of States
e-ph	Electron-Phonon
e-pl	Electron-Plasmon
EQ	Equilibrium
FHG	Fourth-Harmonic-Generation
FWHM	Full-Width-Half-Maximum
HFC	Hollow-Core Fiber Compression
HHG	High-Harmonic Generation
HOPG	Highly-Ordered-Pyrolytic-Graphite
HSA	Hemispherical-Analyzer
IR	Infrared
KK	Kramers-Kronig Relations
LEED	Low-Energy-Electron-Diffraction

LN2	Liquid-Nitrogen
LRD	Lucy-Richardson Deconvolution Algorithm
MDC	Momentum-Distribution-Curve
NEQ	Non-Equilibrium
NTC	Non-Thermal-Charge-Carriers
OPA	Optical-Parametric-Amplifier
PBN	Pyrolytic Boron Nitride
PES	Photoemission Spectroscopy
PSF	Point-Spread-Function
PTCDA	Perylenetetracarboxylic Dianhydride
RA	Resolution Artifact
RT	Room Temperature
SHG	Second-Harmonic Generation
SS	Shockley-Surface-State
THG	Third-Harmonic Generation
tr2PPE	Time-Resolved Two-Photon-Photoemission
trARPES	Time- and Angle-Resolved Photoemission Spectroscopy
UHV	Ultra-High-Vacuum
UPS	Ultraviolet Photoemission Spectroscopy
UV	Ultraviolet
XPS	X-Ray Photoemission Spectroscopy
XUV	Extreme-Ultraviolet

## Publications

Parts of the thesis are based on the following publication.

- Düvel, M. *et al.* Far-from-Equilibrium Electron–Phonon Interactions in Optically Excited Graphene. *Nano Letters*. ISSN: 1530-6984. <https://pubs.acs.org/doi/full/10.1021/acs.nanolett.2c01325> (June 2022)

### Further Publications.

- Maniraj, M. *et al.* A case study for the formation of stanene on a metal surface. *Communications Physics* **2**, 12. ISSN: 2399-3650. <https://www.nature.com/articles/s42005-019-0111-2> (Dec. 2019)
- Jansen, G. S. M. *et al.* Efficient orbital imaging based on ultrafast momentum microscopy and sparsity-driven phase retrieval. *New Journal of Physics* **22**, 063012. ISSN: 1367-2630. arXiv: 2001.10918. <https://doi.org/10.1088/1367-2630/ab8aae> (June 2020)

## CHAPTER 1

### Introduction

---

In condensed matter physics, strong many-body-interactions can create exotic quantum phases such as Mott insulating states<sup>4,5</sup>, CDW phases<sup>6</sup> and superconductivity<sup>7</sup>. A common ansatz to understand these many-body effects is to separate the material system into subsystems, for example, the charge, the lattice, the orbital, and the spin, and then to study the interactions between these subsystems. With its massless fermionic quasiparticle, graphene is an excellent prototypical system for studying such interactions. Furthermore, in such 2D systems, confinement of the charge carriers further facilitates strong interactions between the subsystems<sup>8</sup>.

The quasiparticle picture is a common way to describe the interactions of the charge carrier subsystem with the other subsystems. In this approach, the self-energy describes the corrections to the single-particle electron band structure. These corrections become visible in the dispersion and the MDC line width in the ARPES spectra. The MDC line width is inverse proportional to the quasiparticle lifetime. Therefore, the quasiparticle dynamics can be studied using this approach.<sup>9-11</sup> In this thesis, we will use angle-resolved-photoemission spectroscopy (ARPES) to extract these corrections, i.e., the self-energy, and thereby study the many-body interactions in graphene. An advanced goal in modern solid-state physics is to control such many-body interactions. One control strategy is to use strong femtosecond laser pulses to excite the subsystems to non-equilibrium (NEQ)<sup>12-14</sup> conditions to create and to subsequently investigate, for instance new "hidden"<sup>15-17</sup> and/or dynamically evolving<sup>18,24-31,19-23</sup> states in experiments. This thesis explores the situation that occurs during a strong optical excitation, where the electron and phonon systems can be significantly perturbed, and the quasiparticle distributions cannot be described with equilibrium functions. In a pump-probe scheme, we will

use time- and angle-resolved photoelectron spectroscopy (trARPES) to study the many-body interactions in such a far-from-equilibrium situation in graphene. Fig. 1.1 gives an overview of the main results of this thesis. ARPES spectra (see Fig. 1.1 right panel) of the Dirac-Cone (see Fig. 1.1 middle panel) of graphene contain the quasiparticle-dynamics. We will use IR femtosecond pulses (see Fig. 1.1 red laser pulse arrow) to create an far-from-equilibrium charge carrier distribution (see Fig. 1.1 left panel). In this far-from-equilibrium distribution, the phase-space for electron-phonon coupling is strongly modified. In our publication<sup>1</sup>, we can measure this modification in the quasiparticle dynamics with trARPES for the first time.

For this experiment, we built a trARPES setup with an femtosecond ultraviolet (XUV) source. Fig. 1.2 depicts an overview of our pump-probe trARPES setup. A femtosecond fiber laser system provides IR and green femtosecond pulses. The green laser beam is focused into a

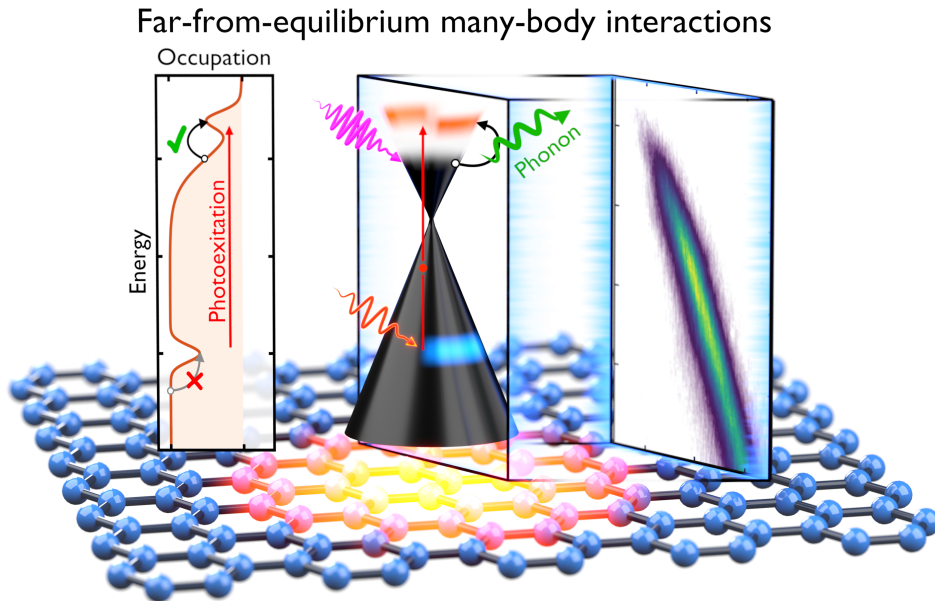


FIGURE 1.1. Far-from-equilibrium electron-phonon interactions in optically-excited graphene. Femtosecond infrared pulses (red arrow) optically excite charge carriers above the Fermi energy (middle panel) in n-doped graphene. These charge carriers form an far-from-equilibrium non-equilibrium charge carrier distribution (left panel). These charge carriers can interact with strongly coupled phonon modes (green arrow middle panel). Femtosecond extreme ultraviolet pulses are used to measure angle-resolved photoemission spectroscopy spectra (right panel) and to track the electron-phonon interaction with the quasiparticle dynamics. Figure created by Lukas Kroll.

noble gas jet, where the non-linear high-harmonic-generation (HHG) process creates XUV pulses. The spectrum of these pulses consists of multiple odd harmonics HHG lines. An array of optics selects the ninth harmonic. These femtosecond XUV pulses serve as probe pulses for our ARPES setup. The delayed IR pulses serve as a pump. APRES spectra are then measured pump-probe delay-dependent with a hemispherical 2D-CCD ARPES detector. A series of trARPES spectra of the Dirac-cone of graphene is also shown in the bottom right of Fig. 1.2. In these spectra, an optical excitation in graphene creates an far-from-equilibrium charge

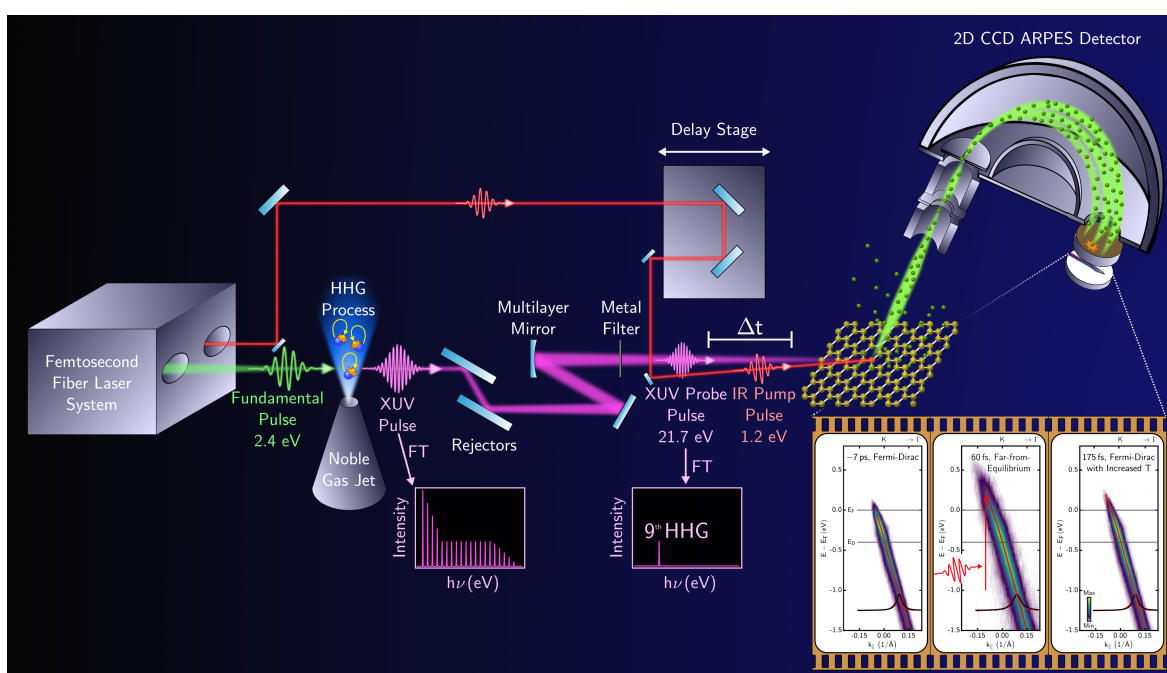


FIGURE 1.2. Schematic of the time-resolved angle-resolved photoemission spectroscopy setup of this thesis. The schematic of the setup has been reduced to the most important parts. A femtosecond fiber laser system provides IR and green pulses with a pulse length of  $\approx 40$  fs. The green laser beam is focused into a noble gas jet, where the non-linear HHG process creates XUV pulses. The spectrum of these pulses consists of multiple odd harmonics HHG lines. For angle-resolved photoemission spectroscopy, we require a single HHG line with a photon energy of  $\approx 20$  eV. Therefore an array of grazing-incidence plate rejector, multilayer mirrors, and metal filters select the ninth harmonic. The femtosecond XUV pulses serve as probe pulses for our ARPES setup. On the other beam path, the IR pump pulses can be delayed with a delay stage. APRES spectra are then measured pump-probe delay-dependent with a hemispherical 2D-CCD ARPES detector. An exemplary series of trARPES spectra of the Dirac-cone of graphene after strong excitation is shown in the bottom right.

carrier population above the Fermi energy, which subsequently decays into a equilibrium distribution with increased temperature. With this setup, we can track graphene's population decay dynamics on a femtosecond timescale.

The low-energy quasiparticle response, i.e., the self-energy  $\approx 500$  meV around the Fermi energy, however, is at first inaccessible due to resolution artifacts (see Fig. 1.3 (b)) caused by the spectrally broad XUV (FWHM = 200 – 300 meV) probe pulses, which are unavoidable

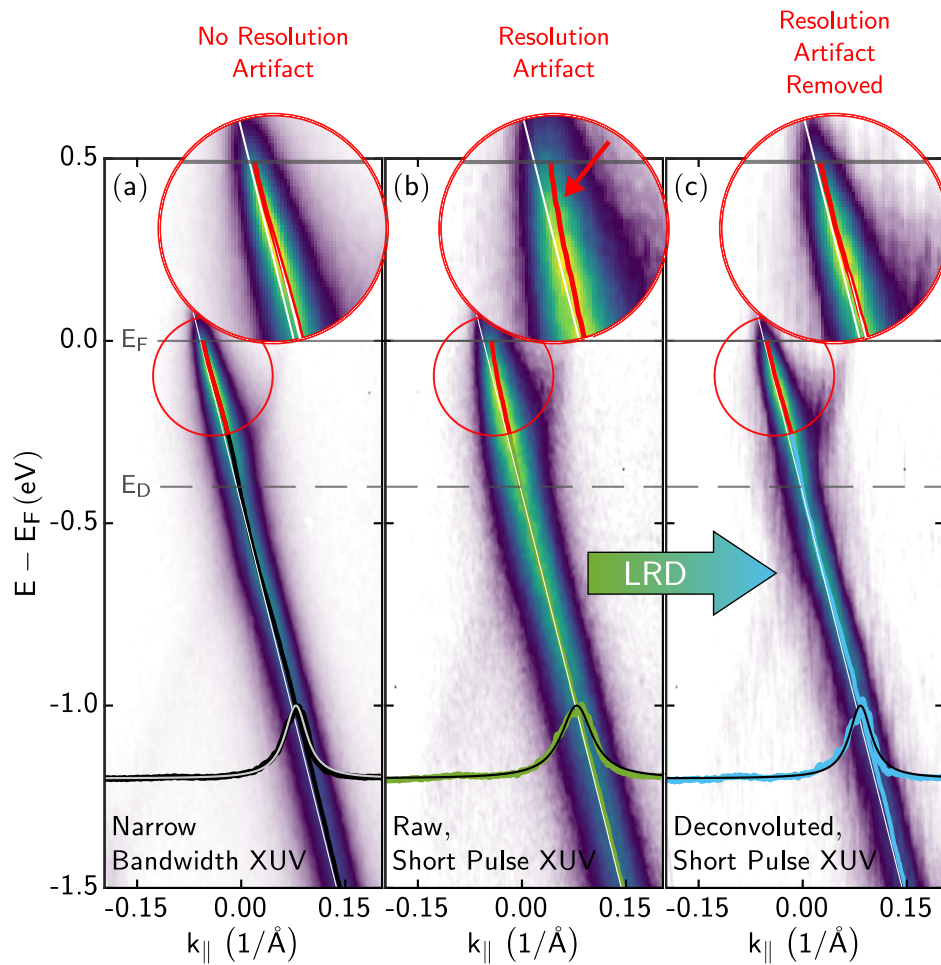


FIGURE 1.3. Application of the Lucy-Richardson deconvolution algorithm (LRD) to trARPES data. (a) An APRES spectrum measured with the narrow-bandwidth XUV line (70 meV energy-resolution) has no notable resolution artifact. (b) An APRES spectrum measured with the spectrally broad short pulse XUV (200 – 300 meV energy-resolution) line has a resolution artifact, i.e., the dispersion bends towards the Fermi energy. (c) The LRD has been applied to the ARPES spectrum from (b). The resolution artifact has been removed in the resulting ARPES spectrum.

due to the time-bandwidth product. Therefore, we apply a Lucy-Richardson-deconvolution algorithm (LRD) to the 2D ARPES spectra (see Fig. 1.3 (c)). With rigorous benchmarking of the LRD results, we produce spectra comparable to spectra with higher energy-resolution measured with a narrow-bandwidth XUV line (see Fig. 1.3 (a)).

The narrow-bandwidth XUV is another key feature of our setup. Here we use temporally long fundamental pulses ( $\tau \approx 220$  fs) to create spectrally narrow pulses with a FWHM of  $\approx 70$  meV. Only the availability of the narrow-bandwidth and short-pulse XUV line in practically the same measurement geometry makes the benchmarking of the LRD and, thereby, the entire experiment viable.

The thesis is structured as follows. First, I will explain the necessary background in photoemission spectroscopy and Dirac materials in chapter 2. Then I will describe the trARPES setup and its components in detail in chapter 3. Third, the use of the LRD on ARPES spectra measured with spectrally broad short XUV pulses is established in chapter 4. Finally, the main results of the thesis are discussed in chapter 5, which are the far-from-equilibrium quasi-particle dynamics in doped graphene after IR femtosecond pulse excitation. We published these results in Ref. <sup>1</sup>.



## CHAPTER 2

### **Background**

---

This chapter reviews the necessary background in photoemission spectroscopy and Dirac materials. First, in the photoemission spectroscopy section, I will explain why angle-resolved photoemission spectroscopy (ARPES) is a powerful tool to investigate the electronic structure of materials. In particular, quasiparticle dynamics measured from ARPES spectra give insights into many-body interactions in materials. Then I will introduce the femtosecond-laser-pulse-based time- and angle-resolved photoemission spectroscopy techniques. These techniques enable us to create and investigate new and dynamically evolving states of matter. In the Dirac-material section, I will explore how the emergence of Dirac cones creates a new class of materials different from more traditional Schrödinger materials.

## 2.1 Photoemission Spectroscopy

In the following sections photoemission spectroscopy (PES) will be introduced briefly. First, I will explain traditional ultraviolet photoemission spectroscopy (UPS), which measures the occupied electronic structure. In UPS, an UV-XUV photon photoemits an electron directly in to the vacuum in a one-photon-photoemission (1PPE) process. The electron carries information about the electronic structure of the material.

In ARPES, many-body interactions of the investigated material are contained in the electronic structure. These effects can be theoretically described with the self-energy in the quasiparticle picture. Thus I will discuss how the self-energy can be extracted from ARPES spectra.

Next, I explain how femtosecond two-photon-photoemission (2PPE) based on femtosecond laser pulses measures the unoccupied electronic structure. In 2PPE, the first photon of an ultrafast laser pulse excites an electron into the unoccupied region. Then, a second photon from the same pulse photoemits this electron. The electron carries information about the unoccupied region. Subsequently to that, I will expand this to time-resolved 2PPE (tr2PPE). In tr2PPE, a time-delay between two ultrafast laser pulses gives access to the lifetimes of charge carriers in the unoccupied region.

Finally, I will introduce trARPES. In trARPES, a pump-probe scheme is used to change the state of a system with a strong ultrafast laser pump pulse and then tracks these changes with a time-delayed UV to XUV probe pulse. I will also review how these changes can be analyzed in different aspects of the trARPES spectra.

### 2.1.1 Angle-Resolved Photoemission Spectroscopy

Photoemission spectroscopy (PES) is a powerful tool for investigating the electronic structure of solid-state matter based on the photoelectric effect<sup>10</sup>. The photoelectric effect was discovered by Heinrich Hertz in 1886<sup>32</sup>, and in 1921 the Nobel Prize in Physics was awarded to Albert Einstein for his theoretical work from 1905 on the effect<sup>33</sup>. In the photoelectric effect, a photon photoemits an electron from a material into the vacuum in a 1PPE process.

The kinetic energy  $E_k$  of the electron is related to binding energy  $E_B$  of the electron, and the work function  $\Phi$  of the material as follows

$$E_k = h\nu - E_B - \Phi. \quad (2.1)$$

Thus, the photoemitted electron contains information about the material's electronic structure (see Fig 2.1 (a)). The process is also called one-photon-photoemission (1PPE) since one photon with an  $h\nu > \Phi$  excites an electron from below the Fermi energy above the vacuum energy. Consequently, we can only probe the occupied electronic structure with 1PPE<sup>10</sup>.

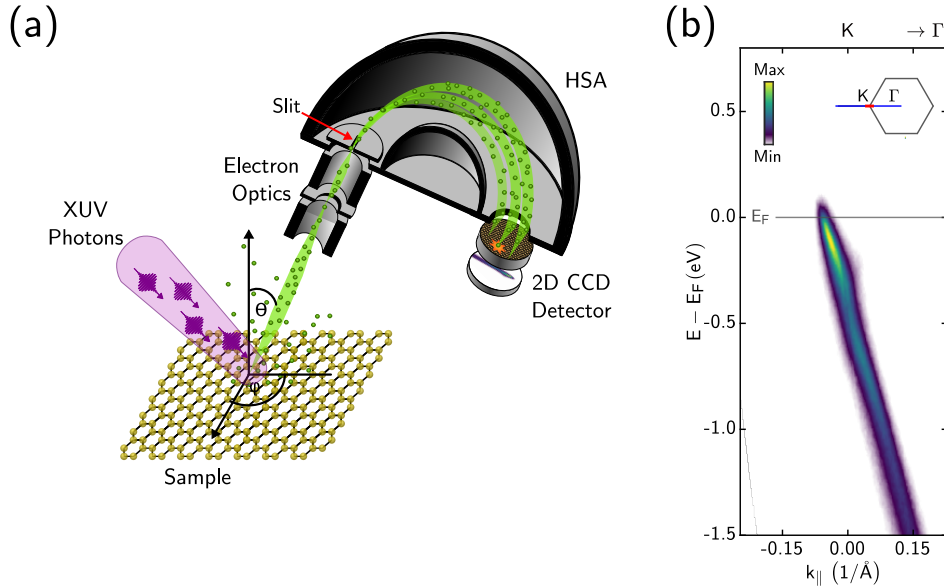


FIGURE 2.1. ARPES with hemispherical 2D CDD detectors. (a) In ARPES, XUV photons photo emit electrons (green sphere) from a sample. These electrons carry information in their kinetic energy, their emission angle  $\theta$ , and the azimuth angle  $\phi$ , which are measured by the analyzer. First, the photoelectrons pass through an electrostatic lens system, where the emission angle is mapped onto the radial distance. Then, a slit selects electrons from only one azimuth. Third, the hemispherical analyzer maps the kinetic energy into the direction perpendicular to the emission angle mapping direction. In the 2D CCD detector, the electrons are amplified in a multichannel plate (MCP) and then detected with a phosphor screen and CCD camera. (b) The picture collected with the CCD camera is the ARPES spectrum. In the ARPES spectrum, the photoemission intensity is color-coded against  $k_{\parallel}$  and energy. The picture in (a) is adapted Ref. <sup>34</sup>.

An intuitive model to describe this process is the three-step model<sup>10</sup> (see Fig 2.2 (c)), where the photoemission process is divided into three steps.

- (1) An incoming photon excites an electron from its initial state to a final state above the vacuum energy.
- (2) The excited electron travels towards the surface. On that trajectory, the electron may scatter within the material. These scattered electrons will add a signal of secondary electrons.
- (3) The electron moves through the surface into the vacuum. In this process the momentum parallel to the surface  $k_{\parallel}$  is conserved (see Fig 2.2 (b)).

In angle-resolved photoemission spectroscopy (ARPES), the emission angle  $\theta$  and the kinetic energy  $E_k$  of the emitted electrons are measured. The momentum parallel to the surface can be calculated by geometry considerations (see Fig. 2.2 (b)) as follows<sup>10</sup>

$$k_{\parallel} = \sin(\theta) \cdot \sqrt{\frac{2m_e \cdot E_k}{\hbar^2}}. \quad (2.2)$$

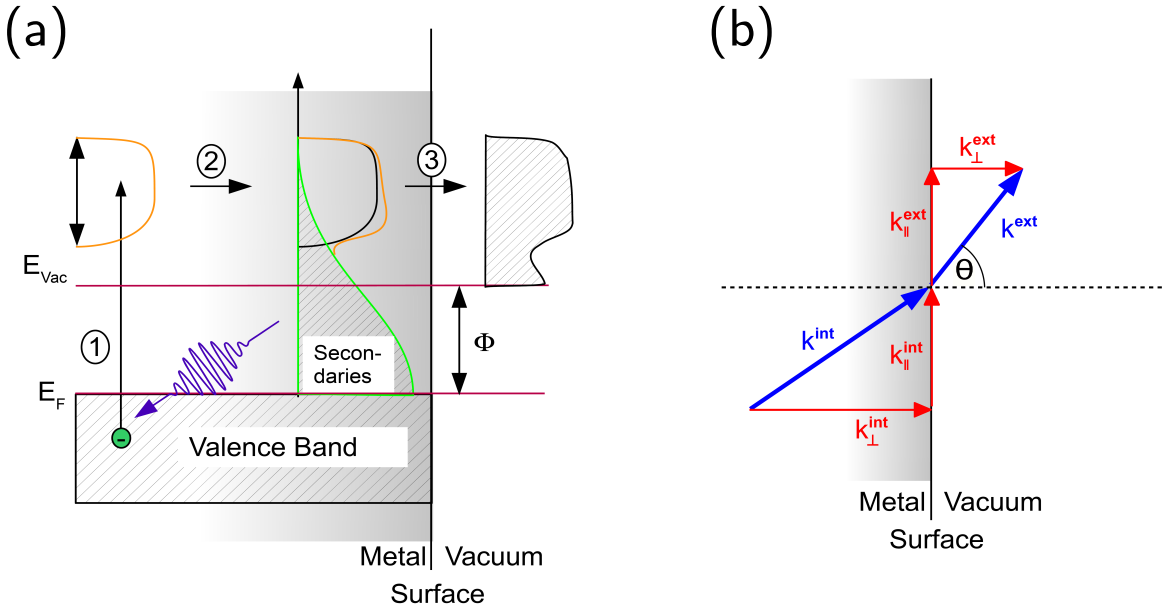


FIGURE 2.2. (a) Three-step-model of photoemission. (b) Momentum conservation at the surface. The photoelectron's  $k_{\parallel}$  is conserved in the transmission process. Figures are reprinted from Ref. <sup>35</sup>.

In this thesis, a *Phoibos 150 Hemispherical 2D CCD Detector* (see Fig 2.1 (a)) is used to measure the ARPES spectra. The photoemitted electrons are imaged onto a 2D image sensor. This image is the so-called APRES spectrum (see Fig 2.1 (b)). In the ARPES spectrum, one axis corresponds to the emission angle ( $k_{\parallel}$  after transformation as above), and the other perpendicular axis corresponds to the kinetic energy ( $E - E_F$  when the initial state is referenced to the Fermi energy  $E_F$ ). Fig. 2.1 (b) is an exemplary ARPES spectrum of a Dirac Cone in graphene.

PES can be classified depending on the used photon energy. In X-Ray photoemission spectroscopy (XPS), X-ray photons with energies greater than 100 eV are used to most dominantly investigate core levels. With ultraviolet photoemission spectroscopy (UPS), photons with energies below 100 eV are used to probe the valence band structure<sup>10</sup>. In this thesis we will either use photon energies of 20 – 40 eV or energies between 1 – 7 eV.

In UPS, the excited electrons have kinetic energies of  $\approx 20$  eV. The universal curve from Ref. <sup>37</sup> (see Fig 2.3) shows the mean free path of the electron as a function of the electron's

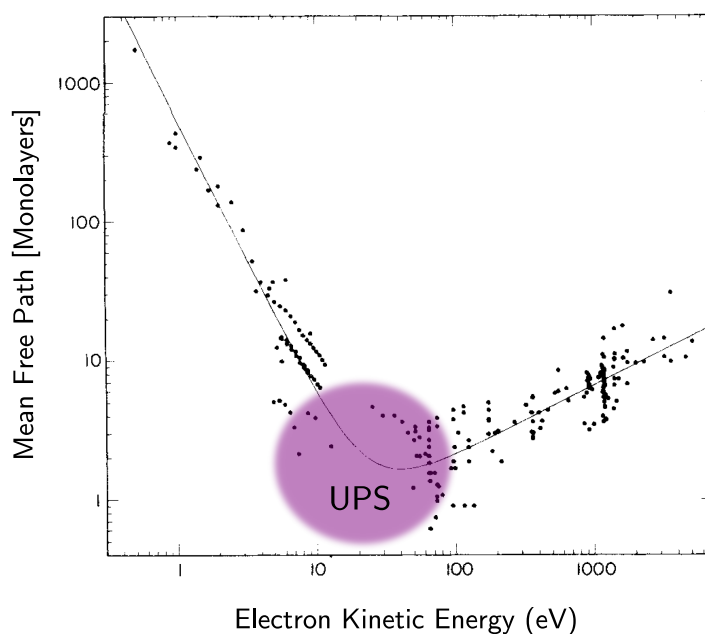


FIGURE 2.3. The universal curve for different materials. The mean free path of electrons in different materials is plotted vs. electron's kinetic energy. The magenta area marks the energy range for UPS ARPES. The graph is adapted from Ref. <sup>36</sup>. © 2022 John Wiley & Son, Inc..

kinetic energy. In UPS (see Fig 2.3 magenta area), the mean free path is on the order of a few monolayers. Consequently, electrons emanating from deeper in the sample will not be emitted or lose their information before detection due to scattering. Thus UPS is a surface-sensitive technique<sup>10</sup>.

### 2.1.1.1 One-Step-Model

The three step model is a approximate description of the photoemission process. So-called one-step models are more exact<sup>10</sup>. The photoemission process is described in one step where the electron is excited from an initial to a final state (see Fig 2.4). However, the final state differs from that in the three-step-model. The final state is constructed of an excited state in the material and an inverse-low-energy-electron-wave state outside the material. Furthermore, these states must be matched to describe the passage at the surface. In a one-step model, the photoemission process is characterized depending on the involved initial and final states. The initial state can be a bulk Bloch wave (see Fig. 2.5 (d)) or surface state (see Fig. 2.5 (e)). For final states, there can be damped and undamped Bloch waves (see Fig. 2.5 (a)) or surface states (see Fig. 2.5 (b)). Furthermore, the final state might be described as an inverse-LEED state outside the sample that extends into the material. Inside the material, the inverse-LEED

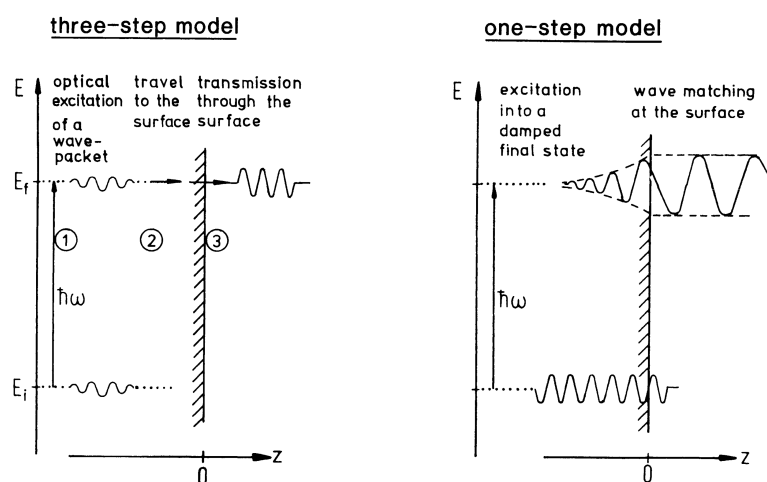


FIGURE 2.4. One-step-model versus three-step-model of photoemission. Figure adapted and reprinted from Ref. <sup>10</sup>. © 2022 Springer Nature.

state will drop exponentially. With such a final state the process is referred to as surface emission.<sup>10</sup>

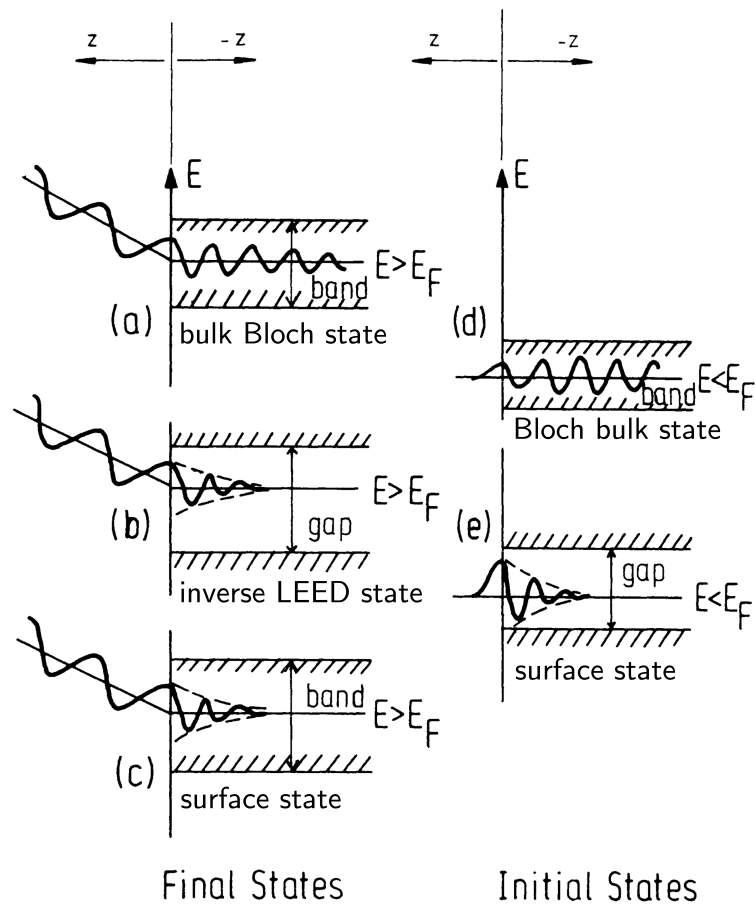


FIGURE 2.5. Possible initial (d-e) and final states (a-c) in the one-step-model of PES. Figure adapted and reprinted from Ref. <sup>10</sup>. © 2022 Springer Nature.



### 2.1.2 Many-Body Interactions in the Quasiparticle Picture measured with ARPES

Many-body interactions are described in the the spectral function  $A(k, \omega)$  in Refs. [9,10,38](#). In ARPES, we can write the photoemitted intensity for two dimensional single band systems as<sup>9</sup>

$$I(k, \omega) = I_0(k, \nu, \mathbf{A})A(k, \omega)f(\omega). \quad (2.3)$$

$I_0(k, \nu, \mathbf{A})$  describes one electron matrix element effects and thus depends on the electron momentum  $k$ , the photon energy  $h\nu$ , and the light polarization, which is described by the vector potential  $\mathbf{A}$ .  $f(\omega)$  is the Fermi-Dirac distribution. In the following we neglect the matrix element effects in equation [2.3](#). Thereby the photoemission spectrum is determined by spectral function.

The quasiparticle picture is a common approach to describe many-body interactions. In this approach, the composition of the charge carrier and the cloud of interactions with the surrounding 'particles' (e.g., phonons, plasmons) form a quasiparticle. The quasiparticle is then a free particle with renormalized energy. In ARPES, the photoemitted electron leaves behind a photohole that interacts with the surrounding particles. Thus we can measure the quasiparticle interactions in ARPES<sup>39</sup>.

An established approach to model many-body interactions is the use of the Green's function formalism<sup>9,38</sup>. The time-ordered one-electron Green's-function  $G(t - t')$  describes the probability that an electron (hole) added (removed) in a many-body system in a Bloch state is still there after a time  $t - t'$ . The Fourier transform then calculates the Green's function momentum representation. In this picture, the complex self-energy  $\Sigma$  introduces the many-body effects to the Greens-function  $G(k, \omega)$  as

$$G(k, \omega) = \frac{1}{\omega - \epsilon_b(k) - \Sigma(k, \omega)}, \quad (2.4)$$

where  $\epsilon_b(k)$  is the bare band band structure (i.e. single particle electron band structure without many-body interactions). The spectral function is then derived as

$$A(k, \omega) = -\frac{1}{\pi} \text{Im}G(k, \omega) = -\frac{1}{\pi} \frac{\text{Im}\Sigma(k, \omega)}{[\omega - \epsilon_b(k) - \text{Re}\Sigma(k, \omega)]^2 + [\text{Im}\Sigma(k, \omega)]^2} \quad (2.5)$$

The bands are located at the poles of the Green's function, the real part of the self-energy  $\text{Re}\Sigma$  encodes the band renormalization, and the imaginary part encodes the coherent quasiparticle

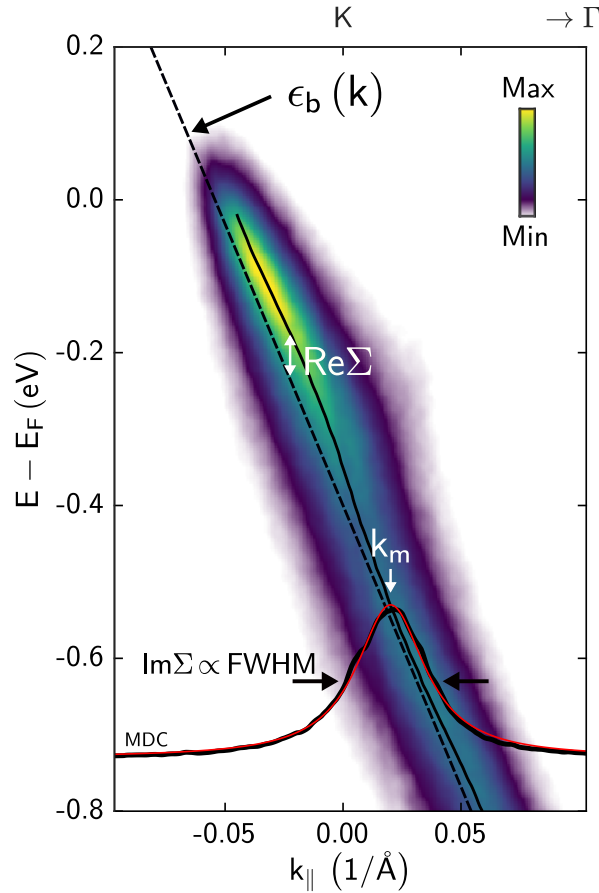


FIGURE 2.6. Estimation of the self-energy from ARPES spectra. The many-body interactions induce band renormalizations on the electronic structure, which are measured by ARPES. The bare band structure (dashed black line) is renormalized by the  $\text{Re}\Sigma$  (white double arrow) to the measured dispersion (black line). An MDC profile (black MDC profile) is a Lorentzian profile where the  $\text{FWHM} \propto \text{Im}\Sigma$  and  $k_m$  can be extracted with a Lorentzian fit (red line). In this spectrum, the experimental resolution broadens this profile. However, the broadening effect is small, and thus a Lorentzian fit suffices. Still, this broadening introduces an offset to  $\text{Im}\Sigma$ . See section 5.5.1 for a more detailed discussion of the resolution effects.

lifetime. Fig. 2.6 exemplifies the effect of many-body interactions on a 2D ARPES spectrum of one arm of a Dirac cone of n-doped graphene. The extracted dispersion (Fig. 2.6 solid black line) is not linear as one might expect for graphene (see chapter 2.2). Instead, the bare linear band (Fig. 2.6 dashed black line) is renormalized, and the  $\text{Re}\Sigma$  (Fig. 2.6 white double arrow) describes these deviations. This renormalization can be understood when we assume a weak  $k$ -dependence of the self-energy in eq. 2.5. Then a momentum-distribution-curve (MDC) of the spectral function has the form of a Lorentzian peak. The maximum of the MDC  $k_m$ , i.e, the measured band position, is determined by  $\omega - \epsilon_b(k_m) - \text{Re}\Sigma = 0$ . Therefore,  $\text{Re}\Sigma$  can be calculated by<sup>40</sup>

$$\text{Re}\Sigma(\omega) = \omega - \epsilon_b(k_m) \stackrel{\text{linear } \epsilon_b}{=} \omega - v_F \cdot (k_m(\omega) - k_f). \quad (2.6)$$

The FWHM of the MDC is proportional to  $\text{Im}\Sigma$ , where we get

$$\text{Im}\Sigma = -\frac{1}{2}v_F \cdot \text{FWHM}, \quad (2.7)$$

for a linear bare band<sup>40</sup> with the Fermi velocity  $v_F$ . The self-energy satisfies the Kramers-Kronig relation, and thus real and imaginary parts can be transformed into each other by the Hilbert transformation<sup>9,38</sup>. These relations will be necessary for the self-consistent extraction of the self-energy (see appendix A.3). The discussion of self-energies extracted from ARPES data is also referred to as discussing the quasiparticle dynamics.

### 2.1.3 Two-Photon-Photoemission

1PPE is limited to the measurement of occupied electronic structure. Two-photon-photoemission (2PPE), on the other side, is a tool to also measure the unoccupied electronic structure<sup>41-43</sup>. In 2PPE, a first photon (see Fig. 2.7 (a)) excites an electron from an occupied state into an unoccupied state. The photon energy has to be smaller than the material's work function  $\Phi$ . Then, the second photon excites this electron into the vacuum. The photoemitted electron carries energy and momentum-dependent information about the unoccupied electronic structure. The same detector as in 1PPE is then used to measure ARPES spectra. The main difference to 1PPE is the photon source. The 2PPE process is less likely than a

1PPE process since it is a second-order nonlinear process, so high intensities are needed. Therefore we use ultrashort high peak intensity laser pulses for the process. 2PPE can be expanded to a time-resolved pump-probe technique (tr-2PPE). Here, the two femtosecond pulses are temporally delayed with respect to each other by an interferometer (see Fig. 2.7 (a)). The first pulse is used to excite (pump) an electron into an unoccupied intermediate state. Then we use the second pulse to probe the population after a certain time delay. Since the excited population will decay during the time-delay, we can use this technique to probe the lifetimes of excited electrons in the unoccupied region. This technique can be performed with different photon energies (two-color experiment) or with the same photon energies (one-color experiment)<sup>41-47</sup>. When we plot the integrated 2PPE intensity in a given energy and momentum area vs. the pump-probe delay, we call such a curve a time trace (see Fig. 2.7 (b)). In a one-color-experiment, the time trace can be modelled as the convolution of the pump laser-pulse, the probe laser-pulse, and an exponential decay<sup>48</sup>. In this model the FWHM is proportional to the lifetime of the unoccupied state. Furthermore, the lifetime can be extracted from the FWHM if pump and probe pulse parameters are known. Accordingly, the lifetime can be determined for the entire 2D-ARPES spectrum. Then the lifetime can be color-coded against energy and momentum to create a lifetime map<sup>48</sup> (see Fig. 2.7 (c)). In a rigorous approach, Liouville-von Neumann equations can be used to calculate the lifetimes<sup>48</sup> from the data.

If the interferometer is stable enough, interference fringes can be measured<sup>44-47</sup>.

Finally, in 2PPE, laser pulse intensities are chosen so that one electron is excited per pulse. Therefore the single electron lifetime is measured. This one-photon excitation regime is one of the main differences from the trARPES technique in the following chapter.

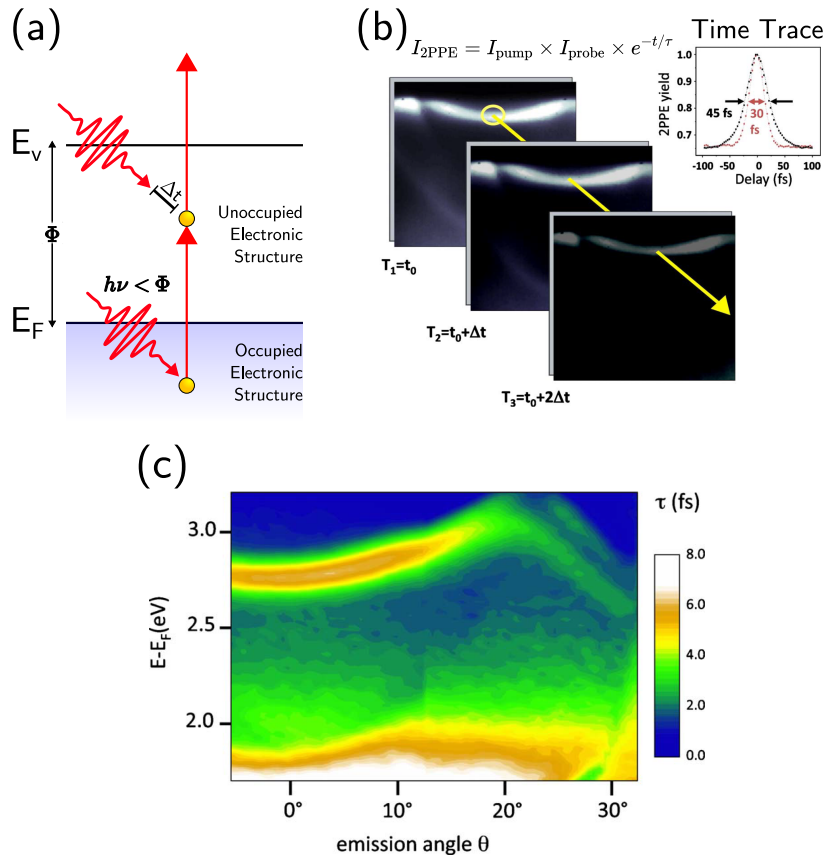


FIGURE 2.7. Two-photon-photoemission. (a) An electron (yellow sphere) is excited in the unoccupied band structure and then photoemitted with a second photon after a time-delay  $\Delta t$ . The electron carries information about the unoccupied band structure. (b) In tr2PPE, several ARPES spectra are collected  $\Delta t$ -dependent. In a time trace, the 2PPE yield is plotted vs. delay for an area of the ARPES spectrum (yellow arrow). The FWHM of the time trace is proportional to the lifetime  $\tau$  of the unoccupied state. (c) Lifetime Map. The lifetime can then be calculated from time traces for every point of the underlying ARPES spectrum and then plotted in a lifetime map for the energy and momentum range of the underlying ARPES spectrum. Figure adapted and reprinted from Ref. <sup>48</sup>. © 2022 American Physical Society.

## 2.1.4 Time- and Angle-Resolved Photoemission Spectroscopy

In principle, time- and angle-resolved photoemission Spectroscopy (trARPES) is based on the same scheme as tr2PPE. First, a pump photon excites the system, and then a probe photon is used to track the time-delay-dependent changes in the electronic structure with ARPES. In contrast to 2PPE (see section 2.1.3), the pump pulse induces strong changes in the material properties and, thereby, the electronic structure. To that end, the intensity of the probe pulse is usually higher than in tr2PPE, and the number of excited electrons is not limited to one per pulse. The changes in electronic structure might appear in the occupied and the unoccupied electronic structure. Therefore, probe photons usually have photon energies above the work function to access both regions. Many of these studies aim at active optical control of material states and parameters (more details chapter in 5).

The trARPES spectra contain a wealth of information about the electronic structure and, thereby, the material's properties. In the following I will give an overview of some of the information that can be gained.

### 2.1.4.1 Population Dynamics

A common way to evaluate trARPES experiments is to track the population dynamics via the photoemission intensities. In that case, a strong pulse excites a population of many electrons (holes) above (below) the Fermi energy. Then the time-delay dependent evolution of these charge carriers is investigated from the corresponding intensities in the ARPES spectra. This technique is well established and used to monitor ultrafast energy dissipation pathways<sup>49,52–55,45,56–58,50,51</sup>. We can classify these experiments further depending on the timescales.

#### **Far-from-Equilibrium Dynamics.**

In far-from-equilibrium dynamics, the electron distribution during and shortly after the pump is investigated. On these timescales (tens of fs), the electron distribution cannot be described by a Fermi-Dirac distribution. The dynamics arise mainly from electron-electron (e-e)

interactions due to these far-from-equilibrium charge carrier distributions and the electrons' interactions with other subsystems, e.g., phonon and spin.

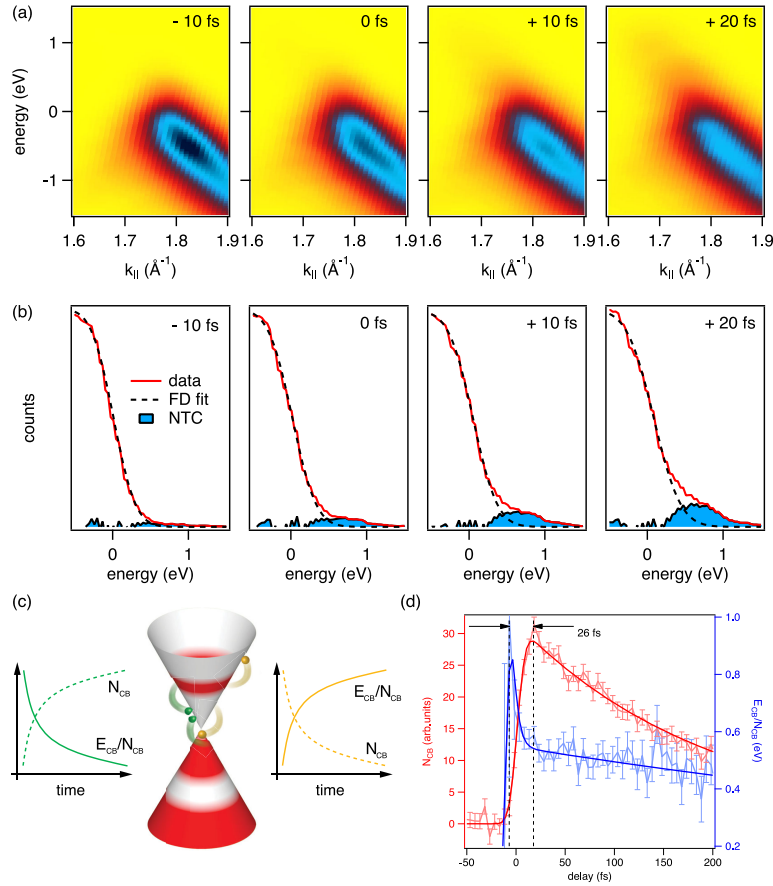


FIGURE 2.8. Tracking primary thermalization events in graphene with photoemission at extreme time scales. (a) trARPES spectra of photo excited graphene at different pump-probe delays. (b) Energy-distribution-curve (EDC) (black line) from the Spectra in (a). A Fermi-Dirac (FD) fit (red line) has been performed to extract the non-thermal charge carriers (NTC) contribution (blue area) to EDC. (c) Sketch of impact ionization (green) and Auger heating (yellow) processes on a Dirac NTC. Occupied states are marked in red and Unoccupied states are marked in white on the Dirac cone. In the population dynamics, the two processes show different signatures when the number of electrons inside the conduction band ( $N_{CB}$ ) and their average kinetic energy ( $E_{CB}/N_{CB}$ ) are plotted vs. the pump-probe delay. (d) Experimental ( $N_{CB}$ ) and ( $E_{CB}/N_{CB}$ ) vs. time-delay. The signature shows directly that impact ionization governs the ultrafast thermalization of the charge carriers. These experiments have been conducted with sub 10 fs pump and probe pulses. Figure adapted and reprinted from<sup>59</sup>. © 2022 American Physical Society.

A good example for far-from-equilibrium dynamics is studied in Ref. <sup>59</sup> by Gierz et al.. They investigated e-e scattering events after the excitation of charge carriers on time scales below 30 fs (see in Fig. 2.8 (d)) in the Dirac Cone of a graphene sample. A number of non-thermal charge carriers (NTC) is excited in the conduction band (see blue area in Fig. 2.8 (c)) at 0 fs. Then with increasing time-delay, this number of NTC increases although the pump pulse has passed. Furthermore, the average kinetic energy of the NTC decreases (see Fig. 2.8 (d)). This signature shows that impact ionization scattering events (see Fig. 2.8 (c) green curves and processes) dominate the population dynamics on these time scales.

### **Non-Equilibrium Dynamics.**

In non-equilibrium dynamics dynamics, the focus is on timescales where electron distribution is thermalized and thus described by a Fermi-Dirac distribution. The dynamics are governed by the difference in temperature between subsystems, e.g., phonon and spin. For example, Perfetti et al.<sup>60</sup> investigated the population dynamics in the superconductor  $\text{Bi}_2\text{Sr}_2\text{CaCu}_2\text{O}_{8+\delta}$  (see Fig. 2.9). The excited far-from-equilibrium charge carriers thermalize after 50 fs (see Fig. 2.9 (c) and (e)). Beyond these timescales, the population dynamics can be described by the temperature of the Fermi-Dirac distribution with increased temperature (see Fig. 2.9 (f)). These thermally excited electrons dissipate their energy on two different time scales: the generation and subsequent decay of NEQ phonons. The electron-phonon (e-ph) coupling can be estimated from these timescales. The insight into the e-ph coupling ultimately helps to understand the origin of the superconductivity in this material.

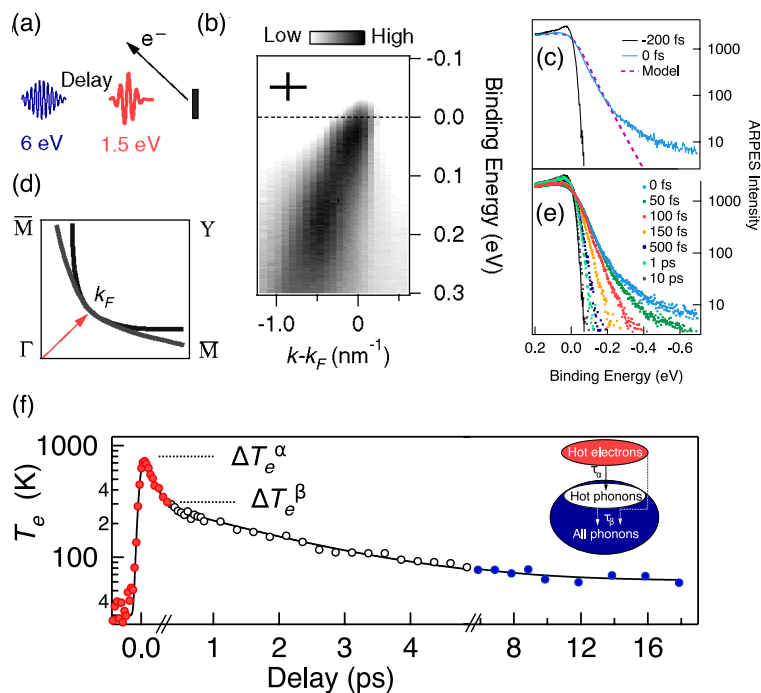


FIGURE 2.9. Ultrafast electron relaxation in superconducting  $\text{Bi}_2\text{Sr}_2\text{CaCu}_2\text{O}_{8+\delta}$  by time-resolved photoemission spectroscopy. (a) Schematic of the excitation scheme. 50 fs pulses were used. (b) ARPES spectrum at 30 K of along the nodal momentum cut indicated in the momentum map band structure in (d). (c) trARPES intensity for 0 fs (blue line) and  $-200$  fs (black line). The dashed pink line indicates a fully thermalized Fermi-Dirac Distribution. Hence at 0 fs, there are NEQ contributions in the ARPES intensity (compare blue and pink dashed line). (e) trARPES intensity for several pump-probe delays. At 100 fs (green line), the NEQ contributions have vanished. Thus the photo-excited population has thermalized. (f) Temperatures have been extracted from the ARPES intensity distributions and plotted logarithmically vs. time-delay. The temperature decay on three different timescales. First the charge carrier distribution thermalizes in Fermi-Dirac distribution with increased temperature (red points). Second energy is transferred from the electron system into hot phonons (white points). Third, the energy is transferred into the entire phonon system (blue points). Figure adapted and reprinted from Ref. <sup>60</sup>. © 2022 American Physical Society.

### 2.1.4.2 Quasiparticle Dynamics in trARPES

Section 2.1.2 discussed how the many-body self-energy could be extracted from ARPES spectra. The next step is extract the self-energy from trARPES data. A number of trARPES studies tackle band renormalizations (in Refs. [61,63–65,46,66–69,62](#)). However, the direct exper-

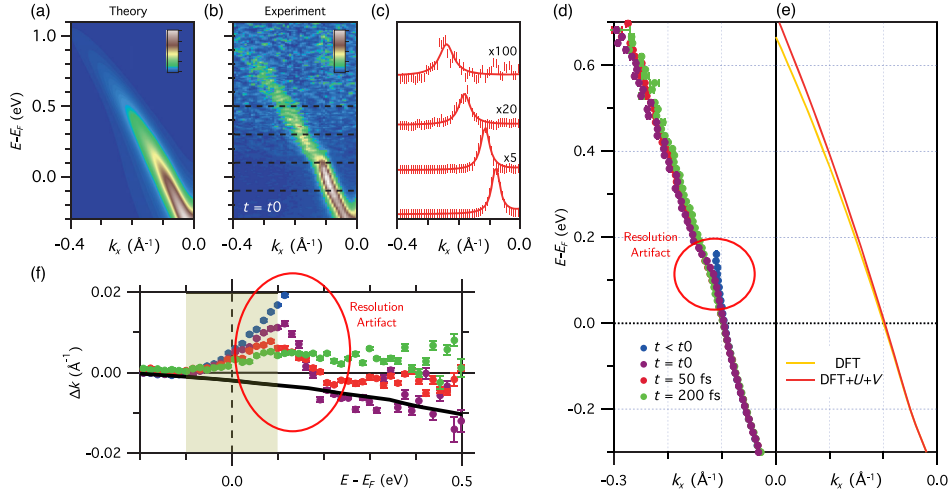


FIGURE 2.10. Light-induced renormalization of the Dirac quasiparticles in the nodal-line semimetal ZrSiSe. (a) Simulated ARPES spectrum from ab-initio DFT+U+V broadened by experimental resolution. (b) Experimental trARPES spectrum at  $t_0$ . (c) MDC curve (red bars) and Lorentzian fits (red lines). The energies of the MDC have been indicated in (b) with dashed lines. (d) Energy vs. peak positions from the Lorentzian fits in (c) for different time-delays. (e) Energy vs. peak positions from the DFT+U+V (red) and DFT (yellow). (f) Change in band position  $\Delta k$  with respect to DFT+U+V calculations. The black line is the change in band position between the DFT and DFT+U+V calculations. The DFT+U+V calculations include electron correlations, whereas the DFT calculations do not include them. Thus electron correlations are suppressed by the excited high-energy electron-hole pairs since, in temporal overlap, the data resemble the DFT calculations. Figure adapted and reprinted from<sup>61</sup>. © 2022 American Physical Society.

imental quantification of the low-energy far-from-equilibrium quasiparticle self-energy at the femtosecond timescale is still a formidable task<sup>51,61,69</sup>. Gatti et al.<sup>61</sup> investigated band-renormalization after ultrafast pump excitation in the nodal-line semimetal ZrSiSe (see Fig. 2.10). The band-renormalization can be explained by transient high-energy electron-hole pairs which screen the Coulomb interaction (see caption 2.10 for more details). Although the physics in this example are unrelated to this thesis, some challenging experimental aspects

can be explained with this example. First, the observed effects are small (compare red and yellow curves in Fig. 2.10 (e)) thus, good signal-to-noise ratios are required to extract these quasiparticle dynamics. Second, we notice the appearance of resolution artifacts (see chapter 4.1) near the Fermi energy (see Fig. 2.10 (d,f)), which obscure the quasiparticle dynamics in that region for delay when the electron distribution is not thermalized yet. We will remove such resolution artifacts from our data in this thesis with the Lucy-Richardson deconvolution algorithm.

### 2.1.5 Photoemission Horizon

Another essential concept when choosing the probe photon energy is the photoemission horizon (as depicted Fig. 2.11). The photoemission horizon is the border of the area in electronic structure from which photoelectrons can be emitted with a given photon energy [70]. The extent of the horizon decreases quadratically with  $k_{\parallel}$  since an energy amount proportional to  $k_{\parallel}^2$  is not available for  $k_{\perp}$ . The photoemission horizon is plotted in the band structure of graphene for different photon energies (see Fig. 2.11). For example, a photon

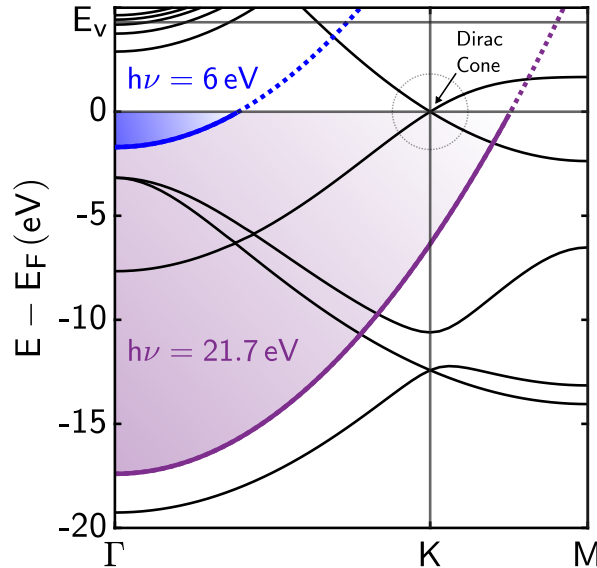


FIGURE 2.11. The extent of the photoemission horizon is plotted in the band structure of graphene for photon energies of 6 eV (Fifth-harmonic with BBOs, blue) and 21.7 eV (Ninth-harmonic of the HHG, purple). A work function of 4.3 eV was assumed for this plot. The band structure is from DFT calculations from the Jarvis DFT repository<sup>71,72</sup>.

energy of 6 eV is insufficient to access the Dirac cone of graphene at the edge of the Brillouin zone, whereas 21 eV suffice. In 1PPE, plasma-discharge lamps (see section 3.3.1) can readily generate photons with energies of 21.21 eV or higher. Thus these lamps are a standard tool for 1PPE. However, these lamps do not provide femtosecond photon pulses and thus are not suitable for trARPES. Furthermore, femtosecond laser pulses combined with non-linear crystals are limited to photon energies of about 7 eV due to absorption in the air and the crystals themselves. For our experiment, we therefore generate femtosecond photon pulses with energies of 21.7 eV via a high-harmonic generation (HHG) (see section 3.3.4).

## 2.2 Dirac Materials

In 2004 Novoselov et al. reported the creation of freestanding graphene for the first time<sup>73</sup>. Although graphene had been theoretically studied for over sixty years<sup>74–79</sup> by that time, it was thought that 2D crystals were thermodynamically unstable<sup>80,81</sup>. One of the most intriguing properties of graphene is that its charge carriers behave as massless fermionic particles<sup>82,83</sup>. This behavior sparked a so-called "gold rush" into graphene research<sup>84</sup>.

The emergence of the Dirac fermions has been discovered in many different materials in recent years<sup>85</sup>. Discoveries reach from high-temperature *d*-wave superconductors<sup>86</sup>, topological insulators<sup>87,88</sup>, superfluid phases of <sup>3</sup>He<sup>89,90</sup>, 3D Dirac semimetals<sup>91</sup>, and to a number of group IV graphene analogues<sup>92</sup>.

In these vastly different materials, Dirac fermions can emerge through different principles. These principles can be connected to be sublattice symmetries in graphene or a time-reversal symmetry in topological insulators. Nevertheless, Dirac fermions lead to universal response functions and susceptibilities across these different materials.<sup>85</sup> Therefore, they form a class of materials distinct from semiconductors or metals, which are called Dirac materials<sup>85</sup>.

A good start for further reading into Dirac materials are the review articles<sup>85,84,93</sup>, which serve as a template and reference for this section.

In metals and doped semiconductors, nearly free quasiparticles that obey Schrödinger's equation with a Hamiltonian of the form  $H_S = \mathbf{p}/2m^*$  describe the system with much success. These particles are called "Schrödinger fermions". Dirac fermions, on the other side,

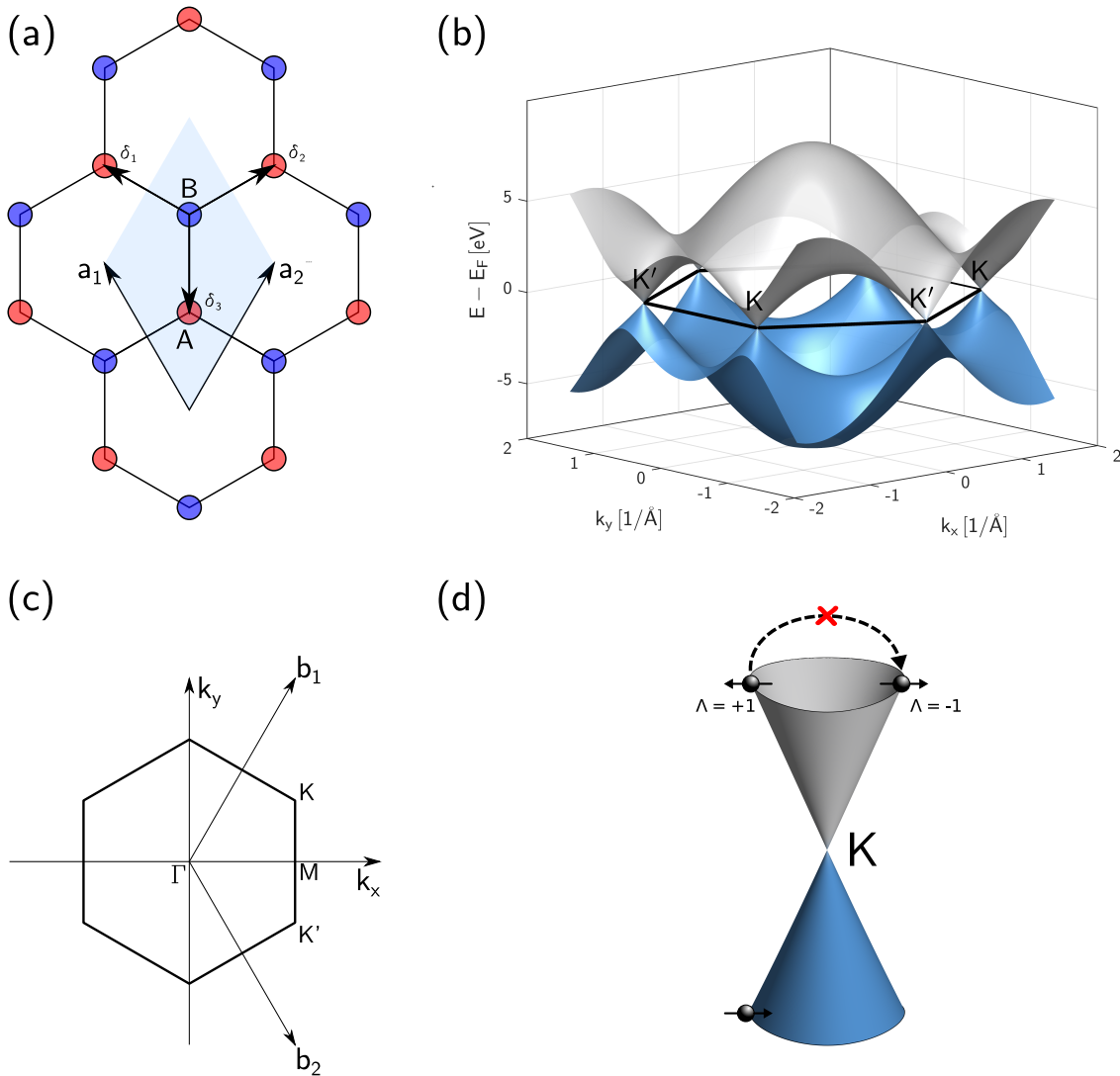


FIGURE 2.12. Spatial and electronic structure of graphene. (a) Crystal structure of graphene made from two sublattices A (red) and B (blue). The vectors  $\delta_i$  connect each atom to its nearest-neighbors. The lattice vectors  $a_1$  and  $a_2$  span the unit cell (blue shaded area). (b) Tight-binding band structure of graphene  $\pi$ -bands. (c) Brillouin zone of graphene.  $b_1$  and  $b_2$  are the reciprocal lattice vectors. (d) Dirac cone in graphene. Around the  $K$  point, graphene has a linear quasi-relativistic Dirac dispersion. The chirality (helicity)  $\Lambda = \sigma \cdot k/|k| = \pm 1$  is the quantum number of the Pseudospin (black spheres). The chirality conservation suppresses backscattering on impurities in graphene (dashed arrow).

obey the following Hamiltonian:

$$H_D = v_F \boldsymbol{\sigma} \cdot \mathbf{p} + mv_F^2 \sigma_z, \quad (2.8)$$

with the Pauli matrices  $\boldsymbol{\sigma} = (\sigma_x, \sigma_y)$  and  $\sigma_z$ . In Dirac materials,  $v_F$  is the Fermi velocity. When the Dirac mass  $m \rightarrow 0$  vanishes, the spectrum of  $H_D$  is gapless, and it follows a linear dispersion, in contrast to the quadratic dispersion of Schrödinger fermions. In the case of a non-vanishing Dirac mass, the gapped eigenstates above and below the gap are still derived from the same spinor wave functions and have the same effective mass. Furthermore, the effective mass is related to the gap by  $\Delta = 2mc^2$ . In contrast, the effective mass in ordinary metals and semiconductors is unrelated to the spectral gap. In that case, holes and charge carriers are described by different Schrödinger equations with different effective masses<sup>85,84</sup>.

We will now explore how the Dirac fermions emerge in the most famous Dirac material, graphene. Furthermore, we discuss some universal phenomena that emerge from the Dirac fermions. Graphene is a 2D single-layer sheet of carbon. A hexagonal Bravais lattice describes graphene with two carbon atoms per unit cell. Therefore, there are two sublattices  $A, B$ , where all the nearest neighbors for any atom are atoms of the other sublattice (see Fig. 2.12 (a) and (c)). To describe the states near the Fermi level, we look at the out-of-plane  $p_z$  carbon orbitals, which form  $\pi$ -bonds. The system is described by the tight-binding Hamiltonian  $\hat{H}$  in the nearest-neighbor approximation as

$$\hat{H} = -t \sum_{\langle i,j \rangle} \left( a_{\sigma,i}^\dagger b_{\sigma,j} + H.c. \right). \quad (2.9)$$

$t \approx 2.7eV$  is the hopping parameter,  $a_i$  and  $b_i$  are the annihilation/creation operators of electrons in the  $p_z$  orbital of the respective sublattice  $A, B$  in the unit cell  $i$ . The real electron spin is not considered since graphene has only negligible spin-orbit coupling. In the momentum space, the Hamiltonian can be written as a  $2 \times 2$  matrix

$$H(\mathbf{k}) = \hbar v_F \begin{pmatrix} 0 & \xi(\mathbf{k}) \\ \xi(\mathbf{k}) & 0 \end{pmatrix} \quad \text{with} \quad \xi(\mathbf{k}) = -t \sum_{i=1,2,3} e^{i\delta_i}. \quad (2.10)$$

Three partial hopping amplitudes are contained in  $\xi(\mathbf{k})$ . These amplitudes describe the hopping processes between each atom with its three nearest neighbors with the vectors  $\delta_i$  (see Fig. 2.12 (a)). The energy bands  $E(\mathbf{k})$  can be written as

$$E(\mathbf{k}) = \pm t \sqrt{3 + f(\mathbf{k})}, \quad (2.11)$$

with

$$f(\mathbf{k}) = 2 \cos(\sqrt{3}k_y a) + 4 \cos\left(\frac{3}{2}k_x a\right) + 4 \cos\left(\frac{\sqrt{3}}{2}k_y a\right). \quad (2.12)$$

The bands are plotted in Fig. 2.12 (b). All three hopping amplitudes interfere destructively at the  $K$ -Points and  $K'$ -Points so that the dispersive term becomes zero  $\xi(\mathbf{k}) = 0$ . This means the two bands are degenerate there. There are two atoms per unit cell with one  $p_z$  electron each; thus, the lower band is filled so that the Fermi level  $E_F$  lies at the degenerate  $K$ -Points and  $K'$ -Points in intrinsic graphene. For that reason, the low energy excitation spectrum is governed by the band dispersion near the  $K$ -Points. It follows that the Hamiltonian is expanded around the  $K$ -Points. The expansion near  $K$  up to a constant phase factor yields:

$$H(\pm K + q) = \hbar v_F \begin{pmatrix} 0 & q_x \pm iq_y \\ q_x \mp iq_y & 0 \end{pmatrix} = \hbar v_F \boldsymbol{\sigma} \cdot \mathbf{q}, \quad (2.13)$$

with the vector  $\mathbf{q} = (q_x, \pm q_y)^T$ . Thus a Dirac Hamiltonian as in equation 2.8 emerges in graphene around the  $K$ -Points.

The Pseudospin is a concept that arises in graphene. One can define the helicity operator  $\Lambda$  as

$$\Lambda = \frac{\boldsymbol{\sigma} \cdot \mathbf{q}}{|\mathbf{q}|} \quad (2.14)$$

with eigenvalues  $\pm 1$ . This conserved quantity behaves mathematically similar to the elemental spin. However, in graphene, it corresponds to sublattice degree freedom. Thus it is often called pseudospin. The conservation of the pseudospin suppresses backscattering, as depicted (see Fig. 2.12 (d)). Furthermore, in optical excitations, only electrons perpendicular to the light polarization are excited due to pseudospin conservation<sup>94</sup>.

## 2.2.1 Electron-Hole Excitations

The low-energy excitation response is one unifying and unique property across Dirac materials. The electron-hole (e-h) excitation continuum can explain the low energy excitation response of Dirac materials<sup>85,84</sup>.

First, we discuss the e-h continuum of a 2D free electron gas (2DEG) (see Fig. 2.13 (a)) as a prototypical 2D Schrödinger material. In an e-h excitation an electron is excited across the Fermi energy into a hole state (see inset Fig. 2.13 (a)). The e-h excitation is characterized by the energy the electron  $E_{e-h}$  gains and by the momentum vector of the excitation  $k_{e-h}$ . We plot  $E_{e-h}$  vs.  $k_{e-h}$  and mark the area of allowed e-h excitations (see shaded areas Fig. 2.13). These areas mark the e-h excitation continuum. In a 2DEG all allowed low-energy excitations are intraband excitations (see inset Fig. 2.13 (a)). The dispersion near the Fermi energy is approximated by  $E(k) = v_F|k|$  for low energies. Hence the maximal energy gained in a e-h excitation with a given  $k_{e-h}$  is  $E_{e-h} = v_F k_{e-h}$ . Furthermore, the maximal  $k_{e-h}$  gained in an e-h excitation with a given energy is  $k_{e-h} = 2k_F + E_{e-h}/v_F$ . Third, any e-h excitation with a vanishing energy can still appear with a  $k_{e-h}$  up to  $2k_F$ . These three limits correspond to the left, right, and bottom borders of the 2DEG's e-h excitation continuum respectively (see borders of the blue shaded area in Fig. 2.13 (a)).

In intrinsic graphene, on the other hand, all the allowed low-energy excitations are interband excitations (see inset Fig. 2.13 (b)). In intrinsic graphene optical e-h excitations with zero  $k_{e-h}$  and arbitrary  $E_{e-h}$  mark the left border of the e-h continuum. Furthermore, for a given  $E_{e-h}$  an e-h excitation can have a maximal  $k_{e-h} < E_{e-h}/v_F$ . This limit marks the right border.

In doped graphene (see Fig. 2.13 (c)), intra- and interband e-h excitations are both allowed. However, a part of the interband transitions are forbidden now due to the additional electrons(holes) above(below) the Fermi energy in n-doped(p-doped) graphene.

These differences in the electron-hole continuum have consequences for collective excitations of electrons (plasmons). Plasmons follow a dispersion of  $E \propto \sqrt{k}$ <sup>95</sup> (see Fig. 2.13) and overlap with the e-h continuum for intrinsic graphene. Therefore, plasmons are suppressed

due to Landau damping, i.e., they decay into e-h pairs. In contrast, in a 2DEG, plasmons

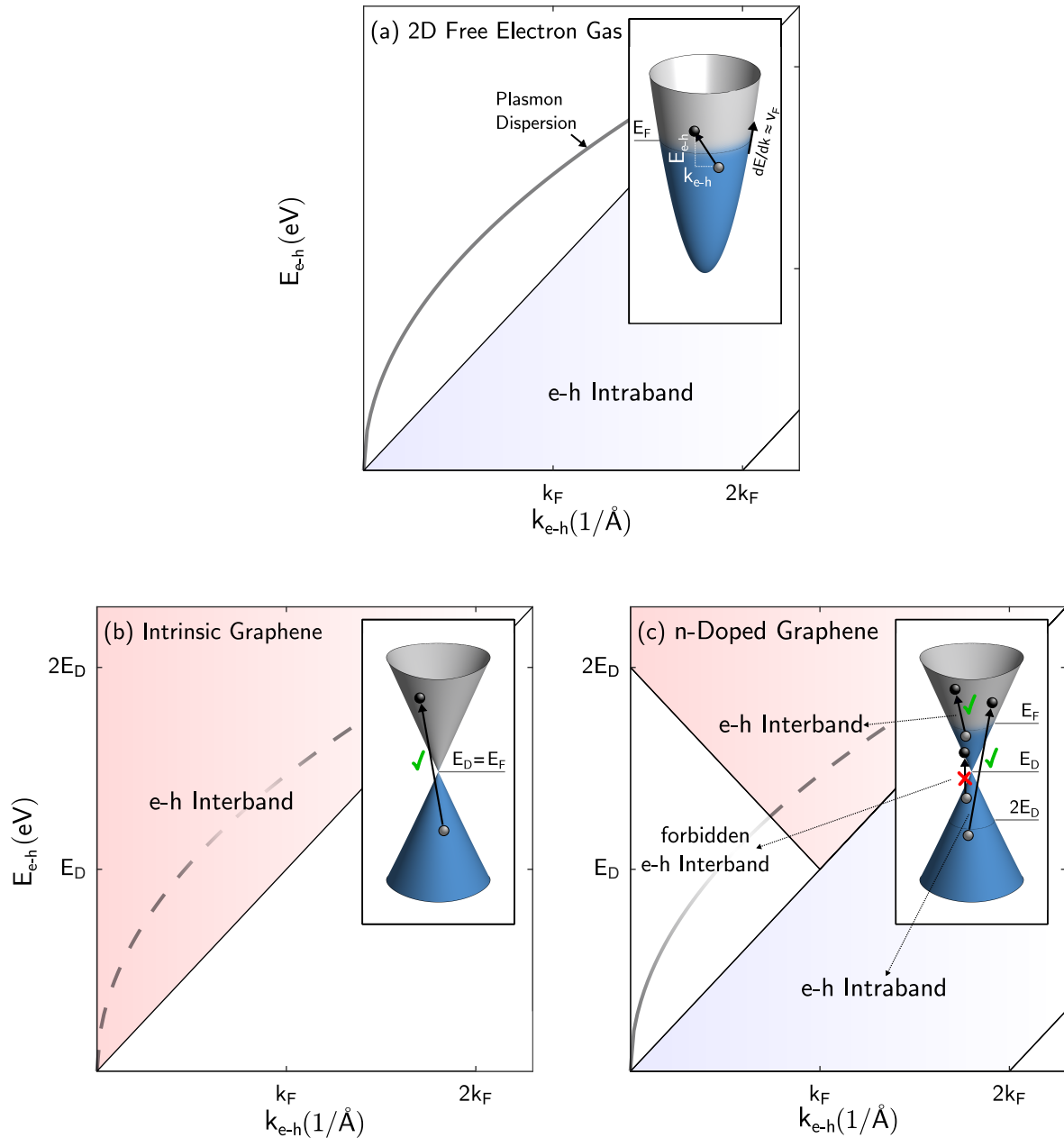


FIGURE 2.13. Electron-hole continuum (blue and red shaded areas) in: (a) Two-dimensional-free-electron-gas, (b) Intrinsic graphene and (c) Doped graphene. The insets show exemplary e-h excitations for the e-h continua, i.e., areas of allowed e-h excitations, in the respective materials. The collective plasmon dispersions are marked as grey lines. Dashed grey lines mark Landau damped parts of the plasmon dispersion, whereas solid lines mark persistent parts.

are not suppressed. Furthermore, in doped graphene, the window of forbidden interband transitions in the e-h continuum allows the presence of plasmons excitations again.



## CHAPTER 3

### **Establishment of an Ultrafast Time-Resolved XUV ARPES Setup**

---

This chapter will explain the experimental setups I built for this thesis. The main purpose of the setup is to perform ultrafast time- and angle-resolved photoemission spectroscopy experiments. First, I will describe the vacuum chamber for the ARPES experiments. Then I will describe the photoelectron detector. Finally, the photon sources and beamlines which provide ultrashort laser and XUV pulses for tr2PPE and trARPES measurement schemes will be explained. I built up much of the setup during my master's and this thesis. Furthermore I supervised the bachelor's or master's theses of Jan-Hendrik Müller, Christopher Wendeln, Hannah Strauch, Tim Titze, Sarina Vogt, Jasmin Kappert, Daniel Marx, Germaine Arend, Jonas Pöhls and Jan Philipp Bange, where parts of the system were built up. Furthermore, Marco Merboldt, Hannah Strauch, and Michael Stellbrink expanded the setup further during the second half of my doctoral studies.

### 3.1 Vacuum Chamber

In ARPES experiments, UHV conditions  $p \approx 10^{-10}$  mbar are necessary to prepare and maintain sufficiently clean sample surfaces. Figure 3.1 shows a schematic of the main UHV chamber used for the ARPES experiments in this thesis. A sputter gun and a Pyrolytic Boron Nitride (PBN) heater allow sputter-annealing cleaning procedures (an example for this method can be found, Ref. <sup>96</sup>). In a connected chamber (evaporation chamber), atomically thin layer systems can be prepared with metal and organic evaporators. These evaporators have been utilized to prepare Stanene/Au(111) in our Publication<sup>2</sup> and PTCDA/Ag(110) in our Publication<sup>3</sup>. The LEED/Auger instrument serves for structural and chemical characterizations of the surface systems<sup>97,98</sup>. ARPES measurements are carried out with the Phoibos 150 2D CCD ARPES detector. With a manipulator, the sample rotation and azimuth angle can be adjusted. In addition, the sample can be cooled down to Liquid-Nitrogen (LN2) temperature with LN2 on the main manipulator. The He-Kryostat allows ARPES measurements down to  $\approx 20$  K with a fixed preset sample rotation and azimuth angle. The HHG and 2PPE laser lines are coupled into the chamber in a  $\pm 45^\circ$  angle with respect to the ARPES detector. The ARPES light sources will be explained in the following chapters. More detailed descriptions of the chamber and its components can be found in my master's thesis<sup>99</sup>.

### 3.2 Phoibos 150 2D CCD ARPES Detector

The *Specs* Phoibos 150 2D CCD ARPES Detector is used for ARPES experiments in this thesis. A schematic of the detector is shown in Fig. 2.1 (a) in section 2.1.1. The detector can be divided into three main parts: the electron optics, the hemispherical sector analyzer (HSA), and the 2D CCD detector. Photoemitted electrons enter the electron optics where the emission angle  $\Theta$  is mapped to the radial distance. Then a slit (in horizontal direction) selects all electrons with one azimuth angle and transmits them into the HSA. In the HSA, an electrostatic potential forces the electrons onto circular trajectories where their radius depends on their kinetic energy. Thus, the HSA maps the kinetic energy to the direction perpendicular to the slit. Therefore, the electrons are mapped so that one direction corresponds to kinetic

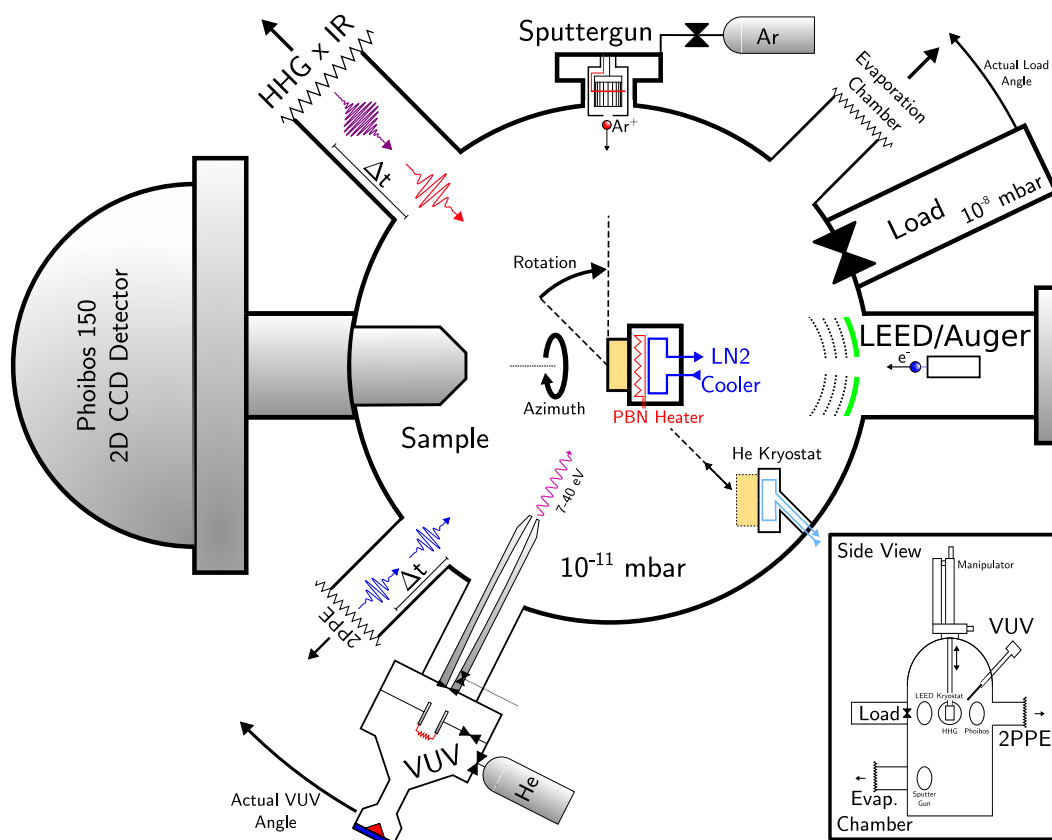


FIGURE 3.1. Schematic configuration of the main UHV chamber for ARPES experiments. The main chamber is under UHV ( $p \approx 10^{-11}$  mbar). Samples can be inserted from a separate Load chamber. The manipulator allows for sample movement and rotation. An LN2 cooler and resistive PBN heater element are integrated into the manipulator. For sample preparation, a sputter gun is attached to the main chamber, and an organic and a metal evaporator in the evaporation chamber. Sample surfaces can be investigated with the LEED/Auger device. The *Specs* Phoibos 150 2D CCD detector is the ARPES detector. The 2PPE beamlines are coupled into the chamber with a UV transparent window. In contrast, part of the trARPES beamline and the entire VUV lamp are connected with the main chamber's vacuum during measurements. A helium cryostat can be used for ARPES measurements down to 20 K. For clarity, some components are sketched at different angles. The actual angle indicates where those components are actually mounted.

energy and the perpendicular direction to the emission angle. These electrons are amplified with a multichannel plate. Then the electron signal is converted into a photon signal with a phosphor screen. Finally, the phosphor screen is imaged with a CCD camera, where the ARPES spectrum is collected over an integration time of seconds to minutes. To create an ARPES spectrum as in Fig. 2.1 (b) in section 2.1.1, the axes of the CDD image are first transformed into kinetic energy and emission angle (see Ref. <sup>100</sup>) and then transformed into kinetic energy and parallel momentum according to equation 2.2. The resulting spectrum ( Fig. 2.1 (b)) shows the electronic structure from a slice of the Brillouin zone (red line in the inset in Fig. 2.1 (b)). Changing the sample rotation (see Fig. 2.1) will shift the slice along the blue line in the inset in Fig. 2.1 (b).

One advantage of the detector is the robustness against space charge in contrast to a momentum microscope<sup>70,101,102</sup>. Therefore, higher pump and probe-beam intensities can be used, leading to higher signal-to-noise ratios in the ARPES spectra and shorter integration times. A detailed comparison between momentum microscope and 2D hemispherical analyzer is in Ref. <sup>70</sup>.

### 3.3 Light Sources and Beamline Setups

This chapter describes the different photon sources and beamline setups available in this thesis. First, I will shortly explain the He plasma discharge lamp and its use in static ARPES. All time-resolved techniques and static 2PPE are based on the AFS fiber laser system, which will be explained briefly. Then I will describe the 2PPE beamlines. The HHG process enables us to create short XUV pulses, which are the basis for the trARPES technique. Thus, I review the HHG process theoretically and then introduce our trARPES beamline.

#### 3.3.1 Vacuum-Ultraviolet Plasma Discharge Lamp

The He plasma emission lamp produces ultraviolet photons at the HeI line ( $h\nu = 21.21 \text{ eV}$ ) and at the HeII line ( $h\nu = 40.82 \text{ eV}$ ). Photons with these energies give access to the entire first Brillouin zone (see section 2.1.5). The lamp is connected to the main chamber's vacuum to avoid air absorption. Thus, the lamp is sometimes called a vacuum-ultraviolet (VUV) lamp.

Other noble gases can be used for different photon energies. The energetic linewidth is below  $1\text{ meV}$ <sup>103,104</sup>. Therefore, the experimental resolution is limited by the resolution of the HSA.

### 3.3.2 Fiber Laser by Active Fiber Systems

All pulsed photon sources in this thesis are based on fiber laser systems. Two different fiber laser systems were used during this thesis. The first was used until March 2020, and after that, it was replaced by a newer system with a greater average power.

Both systems provide ultrafast laser pulses with  $\approx 40$  fs pulse lengths with a central wavelength of 1030 nm after compression. The repetition rate can be adjusted between 50 and 1900 kHz. In this thesis, we use either 500 kHz or 1000 kHz repetition rates. The main difference between the two systems is the available average output power. The second laser allows us to perform HHG-based trARPES measurements simultaneously at the 2D ARPES detector and the momentum microscope (see Ref. <sup>105,106</sup>). In contrast, the first laser only could provide enough power for one experiment.

Both laser systems were produced by the company *Active Fiber Systems* (AFS). In both systems, a (Yb)-doped fiber amplifier provides long pulses (pulse length  $\approx 300$  fs). The older system has only one main amplifier, whereas the newer system has four main amplifiers with a coherent combination to combine the four amplifier outputs. As a result, the newer system has a power of 300 W, and the older one has a maximum power of 100 W. After the amplifier, the beams are coupled into a hollow-core fiber compression (HFC) module. In the HFC, the pulses are spectrally broadened by self-phase-modulation in Ar (new system), or Kr (old system) filled fiber and then temporally compressed with chirped mirrors. The HFC output can then be used for the ultrafast HHG or in the FHG and THG lines. Furthermore, the uncompressed output of the amplifier can also be fed into the optical parametric amplifier (see Ref. <sup>105</sup>) or the narrow-bandwidth-HHG.

One main advantage of these two laser systems is the high repetition rate, which allows for high signal-to-noise ratios trARPES measurements with this setup.

### 3.3.3 2PPE Beamline

I describe the two 2PPE beamlines in this chapter. Figure 3.2 schematically depicts the beamlines. Both beamlines use the HFC output of the laser ( $h\nu = 1.2$  eV,  $\lambda = 1030$  nm,  $\tau = 40$  fs) as the fundamental pulse (red lines Fig. 3.2). Series of non-linear- $\beta$ -Barium-Borate crystals (BBO)<sup>107</sup> either triple the photon energy to 3.6 eV in the third-harmonic generation (THG) beamline (green area Fig. 3.2) or quadruple the energy to 4.8 eV in the fourth-harmonic generation (FHG) beamline (magenta area Fig. 3.2). In both beamlines, interferometers (yellow areas Fig. 3.2) enable tr-2PPE experiments. In the THG beamline (green area Fig. 3.2), pulses with a photon energy of 2.4 eV (blue lines Fig. 3.2) are created via second-harmonic generation (SHG) in a BBO. Then, a  $\lambda/2$  plate aligns the polarisation of the fundamental to the SHG pulse. After that, a calcite plate between the BBOs compensates for the time-delay between the fundamental and SHG pulse. Then, a second BBO generates pulses with 3.6 eV (green line Fig. 3.2) via third-harmonic generation (THG) by sum-frequency generation from the fundamental and SHG pulse. After that, the fundamental and SHG pulses are filtered out with dielectric mirrors, which are tuned to the THG wavelength of 343 nm.

In the FHG beamline, SHG pulses are created with a BBO (magenta area Fig. 3.2). Afterward, the SHG pulses are energy doubled again with a second differently cut BBO. Thus FHG pulses with a photon energy of 4.8 eV are created (magenta lines Fig. 3.2). In both lines, the beam is focused into the BBOs with lenses in order to achieve higher conversion efficiency. After that, the THG and FHG pulses are temporally compressed by prism-compressors (yellow areas Fig. 3.2)<sup>109</sup>. The compressor is also used to sort out the fundamental and SHG beams in the FHG beamline. In the interferometers (grey area Fig. 3.2), beamsplitters split the pulses into two pulses. One of the pulse is delayed in time with a delay stage. To reliably measure the phase-averaged time trace, one of the mirrors on one of the interferometer's arms has a so-called wobbler. The wobbler is a small vibration motor that destroys the interferometer's phase stability. Behind the interferometers, the polarisation is controlled with  $\lambda/2$ -plates. After that, the beamlines are focussed onto the sample into the vacuum through a UV-transparent window (see Fig. 3.1). A more detailed description of the 2PPE setup can be found in the master's thesis of Germaine Arend<sup>108</sup> and the bachelor's theses of Daniel

Marx<sup>110</sup> and Sarina Vogt<sup>111</sup>. A phase-resolved setup based on Refs. <sup>45,46,43</sup> is currently built up in the master's thesis of Hannah Strauch.

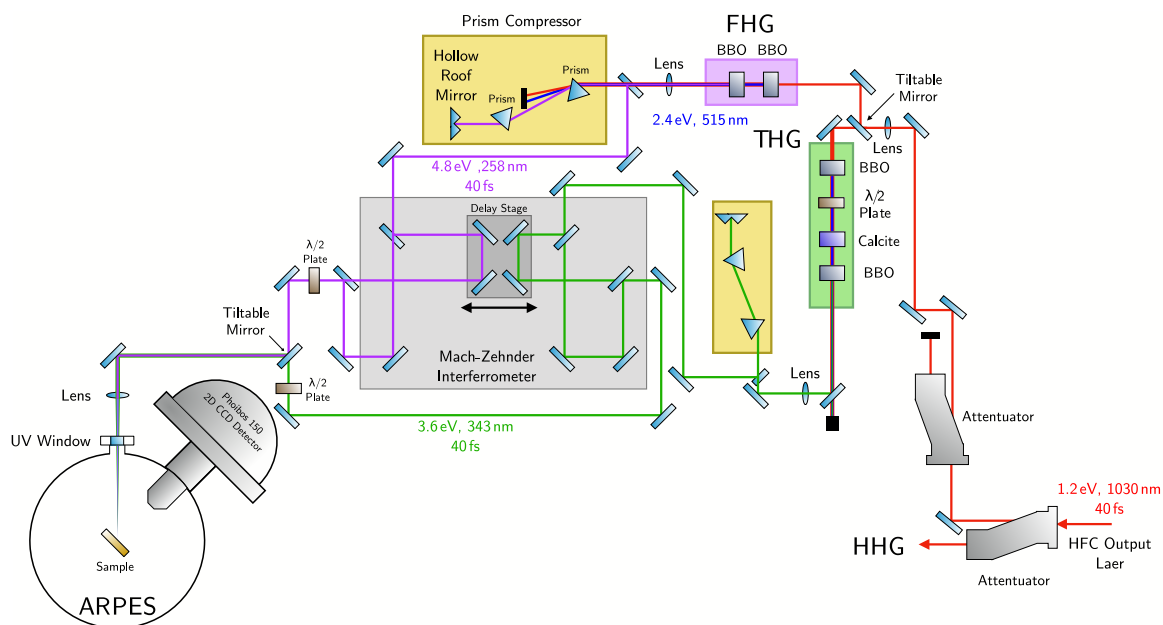


FIGURE 3.2. FHG and THG beamlines for 2PPE. Both beamlines start with the laser pulses ( $\lambda = 1030 \text{ nm}$ ,  $h\nu = 1.2 \text{ eV}$ ,  $\tau = 40 \text{ fs}$ ) from the HFC laser output (red line). Attenuators regulate the input power  $P_{in} = 0 - 5 \text{ W}$ . A tiltable mirror can switch the beam path between the THG or FHG line. Series of nonlinear crystals triple or quadruple the photon energy in the THG (green rectangle) or FHG (magenta rectangle) lines. Both beams are temporally compressed with a prism compressor (yellow rectangles). The time-delays for tr2PPE are introduced with interferometers (grey rectangle). Both beams are focused down on the sample through a UV transparent window. The beams' polarisations are controlled with  $\lambda/2$ -plates. The picture is adapted from <sup>108</sup>.

### 3.3.4 High-Harmonic Generation

For trARPES experiments, we require an XUV ( $h\nu \approx 20$  eV) photon pulse with femtosecond pulse lengths (see section 2.1.5) in a tabletop setup. We use high-harmonic Generation (HHG) to generate the XUV pulses. In HHG, atoms that are subjected to high-intensity ( $p > 10^{14}$  W/cm<sup>2</sup>) short-pulse laser fields emit XUV pulses<sup>112,113</sup>. In our case we focus high-intensity laser pulses into an argon gas jet. This process can be understood in the intuitive three-step model<sup>114,115</sup> (see Fig. 3.3).

- (1) **Tunnel Ionization:** The atom's Coulomb potential is bent by the electric field of an intense laser pulse. This bending increases the probability of tunnel ionization processes for electrons and thus creates free electrons.
- (2) **Propagation in the Electric Field:** The laser pulse's oscillatory electric field and electron's emission time govern the free electron's movement. There are trajectories where the emitted electron returns to its former atom and has a chance to recombine with it. These electrons have collected kinetic energy from their trajectory's oscillating laser fields.
- (3) **Recombination:** When the electron recombines with its former atom, it emits the excess kinetic energy as a high-energy photon.

A quantum mechanical description of this process can be found in<sup>116,117</sup>. Fig. 3.4 illustrates

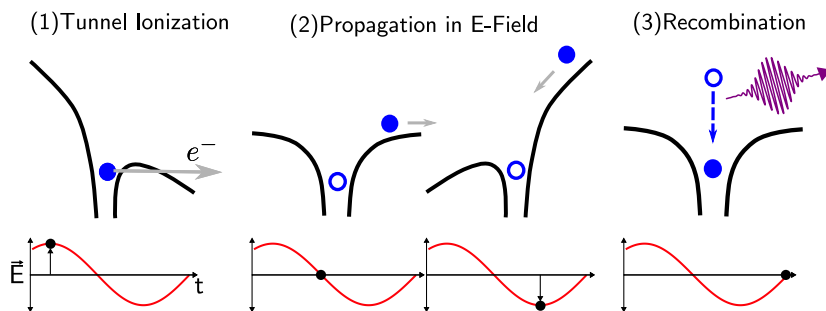


FIGURE 3.3. Three-step model of high-harmonic generation. (1) The Coulomb potential of the atom is bent by a high-intensity laser pulse leading to tunnel ionization processes. (2) The free electron propagates in the electric field and collects excess kinetic energy. (3) The electron recombines with the atom and emits its excess energy as a high-energy photon. Reprinted and adapted from<sup>118</sup>. © 2022 Springer Nature.

the free-electron trajectory depending on the ionization time relative to the laser oscillation. These trajectories are calculated classically where the initial velocity is zero in the inertial system of the ion. The excess kinetic energy is color-coded onto the electron trajectories. The maximal excess energy is given by  $E_{k,max} = 3.17 \cdot U_P$  with the pondermotive force  $U_P = \frac{e^2 E_0^2}{4m\omega^2}$ . When the electron is emitted at  $\omega t_0 = 18^\circ$ , it collects the maximal excess energy<sup>120</sup>. If it is emitted later, it cannot collect all the energy before the laser field changes direction (dotted lines Fig. 3.4). If the electron is emitted earlier, it collects the maximal energy. However, before the electron reaches the atom, the electric field changes direction a second time and thus decelerates the electron (dashed lines Fig. 3.4). If the electron is emitted too early, it will leave the vicinity of the atom and will not recombine (grey lines). These emitted electrons will generate a plasma in the generation medium. The emitted photons now have a maximal cut-off energy of  $E_{cut-off} = 3.17U_P + I_P$  with the atom's ionization potential

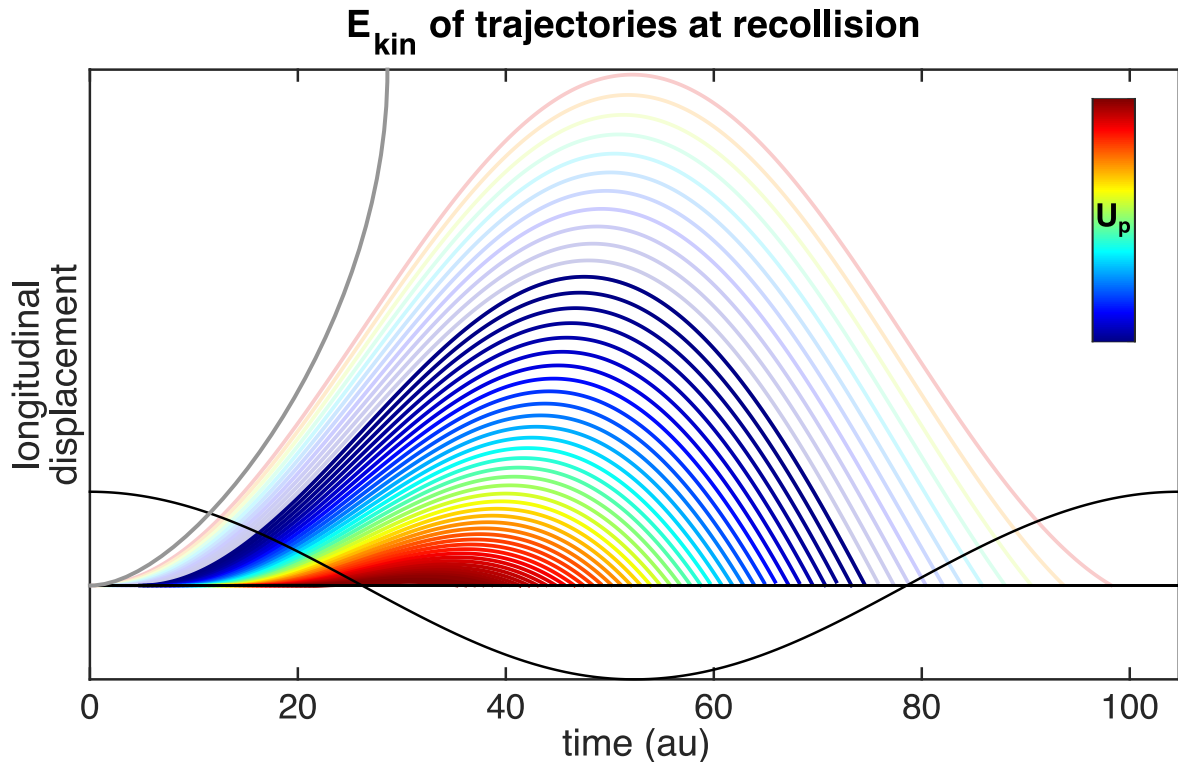


FIGURE 3.4. Electron trajectories in the HHG Process. The electron trajectories for different transmission times during the fundamental laser period. The excess energy of electron recombining with the core is color-coded onto the trajectories.  $U_p$  is the pondermotive force. Reprinted and adapted from<sup>119</sup> under Creative Commons Attribution License 4.0.

$I_p$ . Therefore, the cut-off energy will rise with increasing intensity or decreasing wavelength. Furthermore, the choice of atoms will influence  $E_{\text{cut-off}}$ .

This process repeats every half laser pulse cycle at every atom in the medium. As a result, all the emitted photons will interfere with each other leading to a macroscopic spectrum consisting of a comb of peaks (see Fig. 3.5). This spectrum is calculated by Fourier transformation from the time to the spectral domain. The distance of peaks is two times the fundamental pulse frequency  $2\omega$ , and the peaks appear at every odd multiple of  $\omega$ . This form is caused by destructive interference between pulses emitted at different half cycles of the laser field. The resulting comb of HHG lines can be divided into different regimes. In the perturbative regime, low order harmonic generation processes (For example SHG, THG and FHG) contribute to the spectrum. The probability for such processes decreases at higher order. In the plateau regime only the HHG processes contributes. Close to the cut-off energy, the HHG intensity decreases quickly. Furthermore, photons emitted throughout the medium from different atoms must be phase-matched to facilitate constructive interference. Therefore the phase velocity of

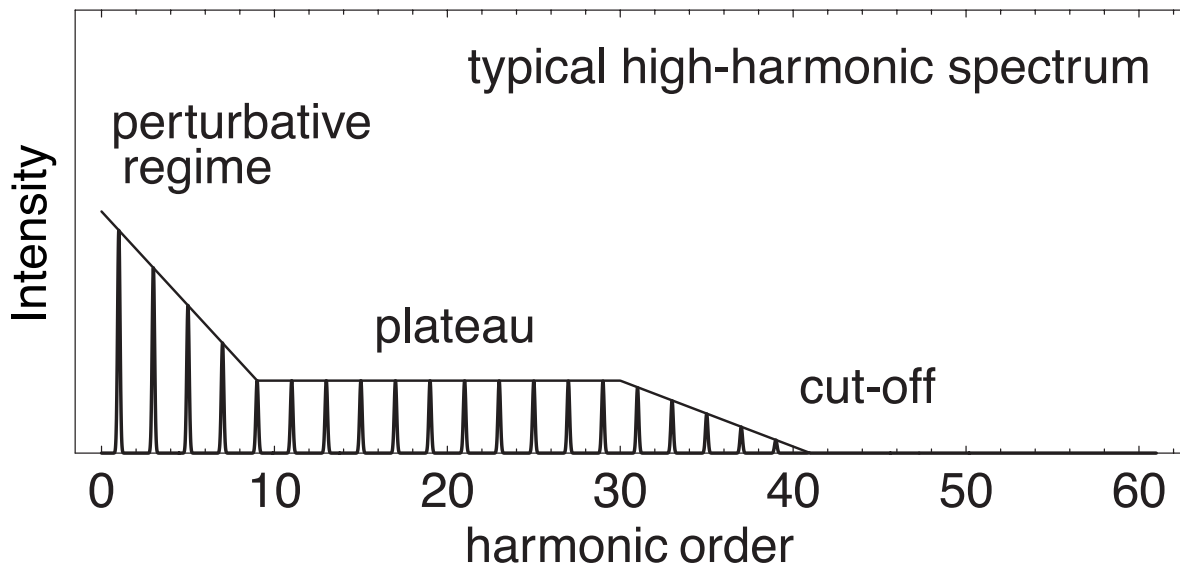


FIGURE 3.5. A typical HHG spectrum. The HHG spectrum consists of a comb of harmonics. In the perturbative regime, low-order harmonic processes contribute but decrease with harmonic order. HHG peaks dominate the spectrum with constant intensity in the plateau region. Near the cut-off, the HHG intensity drops off rapidly. The picture is reprinted and adapted from<sup>121</sup>. © 2022 American Physical Society.

the fundamental laser and that of the desired HHG line must be matched, i.e., the wave vector mismatch must be zero ( $\Delta k = 0$ ). The wave vector mismatch can be divided into a number of contributions<sup>122</sup>

$$\Delta k = \Delta k_n + \Delta k_G + \Delta k_p + \Delta k_d. \quad (3.1)$$

The plasma  $\Delta k_p$  and the neutral gas  $\Delta k_n$  contribute via their respective dispersions. Both contributions have opposite signs. The Gouy phase shifts  $\Delta k_G$  stems from the beam geometry near the focus and therefore is highly dependent on the focussing condition. Furthermore, on its trajectory, the electron collects the dipole phase  $\Delta k_d$ . All these contributions have to be balanced to maximize the HHG output. To achieve this, one can either vary the gas pressure, the focussing conditions, the focus point with respect to the gas jet, or the beam intensity. The reabsorption of the XUV in the gas also has to be considered. This optimization is generally known as phase matching.

### 3.3.5 Time- and Angle-Resolved Photoemission Spectroscopy Beamline

A time- and angle-resolved photoemission spectroscopy (trARPES) beamline with XUV ( $h\nu = 21.7$  eV, ninth harmonic) pump pulses and IR probe pulses has been set up during this thesis. Fig. 3.6 shows a schematic of the trARPES beamline. A critical feature of the beamline is the availability of short XUV pulses and narrow-bandwidth XUV pulses for different purposes but at the same beamline with the use of different fundamental pulses.

- (1) The **short pulse XUV** line allows for ultrafast trARPES experiments with an IR-pump-XUV-probe cross-correlation of  $\approx 45$  fs (estimated in appendix section A.2). This time-resolution is sufficient to observe graphene's electronic structure under far-from-equilibrium conditions (see chapter 5). However, the energy-resolution in our experiments is 200-300 meV (see appendix section A.1) due to the spectrally broad pulses of the XUV.
- (2) **Narrow-Bandwidth XUV pulses** are advantageous for measurements where higher experimental energy-resolutions are needed. In chapter 5 we will present measurements with an overall experimental energy-resolution of about 70 meV (determined in appendix section A.1). However, due to the time-bandwidth product, the time-resolution is on the order of hundreds of femtoseconds.

Now I describe the HHG beam path in Fig. 3.6. Detailed descriptions and characterizations of the HHG beamline can be found in the master's thesis of Germaine Arendt<sup>108</sup>. The HFC output ( $\tau \approx 40$  fs) of the AFS fiber laser provides fundamental laser pulses for the short XUV pulses and the (temporally) uncompressed amplifier output ( $\tau \approx 300$  fs) for the narrow-bandwidth HHG pulses. A BBO creates the second harmonic ( $\lambda = 515$  nm). These SHG laser pulses are the fundamental pulses for the HHG process. Then the HHG fundamental pulses enter the HHG generation vacuum chamber through a window that serves as a focusing lens at the same time. In the generation chamber, the fundamental is focused into an argon gas jet where HHG pulses are generated. The argon gas jet is emitted from a nozzle (diameter=  $120 \mu\text{m}$ ) into the vacuum chamber. Under operation, the pressure inside the generation chamber is  $10^1$  to  $10^0$  mbar. After this, the beam path passes through a small hole in a metal cone into the mirror

chamber. This hole minimizes the flow of argon into the mirror chamber, i.e., it serves as a differential pumping unit. Hence the mirror chamber's pressure of about  $6 \cdot 10^{-4}$  mbar during operation minimizes the XUV pulses from being reabsorbed in the mirror chamber. For the same reason, the nozzle and thereby the HHG generation point are placed close to the cone to avoid reabsorption of HHG pulses in argon gas. In the mirror chamber, a number of optics separate out the ninth harmonic line. First,  $\text{SiO}_2$  coated rejector plates reflect the XUV light and transmit most of the fundamental beam. Then two specially designed multilayer mirrors filter<sup>108</sup> out the ninth harmonic from the HHG spectrum. Finally, the second multilayer mirror is curved to focus the HHG beam onto the sample. After the mirror chamber, thin metal filters mounted in UHV valves serve multiple purposes. First, they divide the mirror chamber's vacuum from the main chamber's vacuum. Secondly, they filter the remaining fundamental light from the probe beam path. There is an Sn filter and an Al filter. Both filters are  $200 \mu\text{m}$  thick. After the multilayer mirrors, the HHG spectrum is already dominated by the ninth harmonic. However, contributions from the seventh and eleventh harmonics remain in the

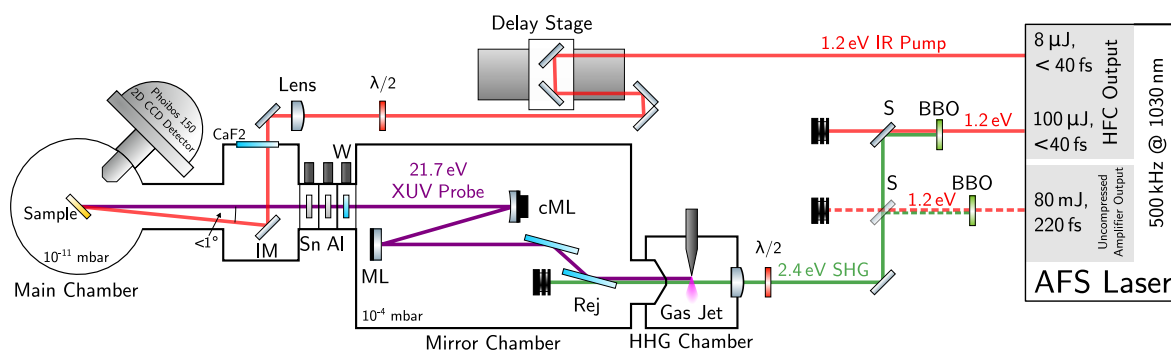


FIGURE 3.6. Schematic of the trARPES beamline. The femtosecond XUV probe pulse is created in the HHG chamber from the SHG of the HFC or uncompressed amplifier output. At first both laser outputs were frequency-doubled with BBOs and the 1.2 eV components were removed with separator mirrors (S). In the mirror chamber, the ninth harmonic line is filtered from the HHG spectrum with rejectors (Rej), multilayer mirrors (ML), and thin Al/Sn foil filters. The XUV beam is focused onto the sample with a curved multilayer mirror (cML). A window (W) can separate the mirror chamber's and the main chamber's vacuum. The pump beam is temporally delayed with the delay stage. Then it is focused onto the sample and coupled into the main chamber's vacuum through a  $\text{CaF}_2$  window.

beam path. The Al-filter transmits all three harmonics approximately equally. In contrast, the Sn filter maximizes the transmission of the ninth harmonic and suppresses the others.

In this thesis, a 1.2 eV IR pump beam was used. The pump beam is temporally delayed on a delay stage and then focused onto the sample. The pump beam enters the main chamber's vacuum through a CaF<sub>2</sub> window. The pump and probe beam hit the sample at nearly the same angle. Beyond the HFC output of the laser, the optical parametric amplifier<sup>106</sup> or nonlinear crystals can also provide photon energies in the near UV, optical, and infrared range. To that end, the CaF<sub>2</sub> window has high transmission in the IR range. A detailed description of the pump line can be found in the master's thesis of Jan Philipp Bange Ref. <sup>123</sup>.

## Establishment of the Lucy-Richardson Deconvolution for Short Pulse trARPES

---

It is known from Ref. <sup>124</sup> that a resolution artifact around Fermi energy in ARPES spectra (see Fig 4.1) is caused by the lower energy-resolution, i.e., the higher spectral width of the short pulse XUV light. This artifact prevents reliable conclusions about the extracted self energies, especially in the interesting region close to the Fermi energy. For that reason, we made use of the Lucy-Richardson deconvolution algorithm (LRD)<sup>125,126</sup> for ARPES based on the work by Rameau<sup>127</sup> and Yang et al.<sup>127</sup>. With this approach, we are able to remove the resolution artifact.

The following sections are structured as follows. First, the resolution artifact is discussed in detail by simulations similar to Ref. <sup>124</sup>, but for our sample system and setup parameters. Then I introduce the LRD and discuss the benchmarking. After that, I will discuss the effect of the LRD procedure on the trARPES measurements as introduced in chapter 5.5.2. At last, I will discuss the approach.

However, we make some general considerations first. The energy-resolution in our time-resolution optimized setup is  $\approx 200\text{-}300$  meV (see appendix section A.1). Considering our gaussian XUV pulse length of 17 fs (see appendix A.2) and the ideal time-bandwidth-product, the bandwidth of our pulse cannot be better than  $\approx 110$  meV\*. This value is also our setup's best achievable energy-resolution. Such an energy-resolution would still produce resolution artifacts (see the next section 4.1 Fig. 4.3). Thus, applying the LRD to our trAPRES spectra

---

\*The detector's energy-resolution is on the order of 10-30 meV. Thus it is negligibly small compared to the XUV band width

is necessary to remove the resolution artifact and gain access to the far-from-equilibrium quasiparticle dynamics.

Although the use of deconvolution algorithms is quite established in astronomical and medical imaging<sup>128–130</sup>, in ARPES, this method is rarely used. The reason for this in static ARPES is

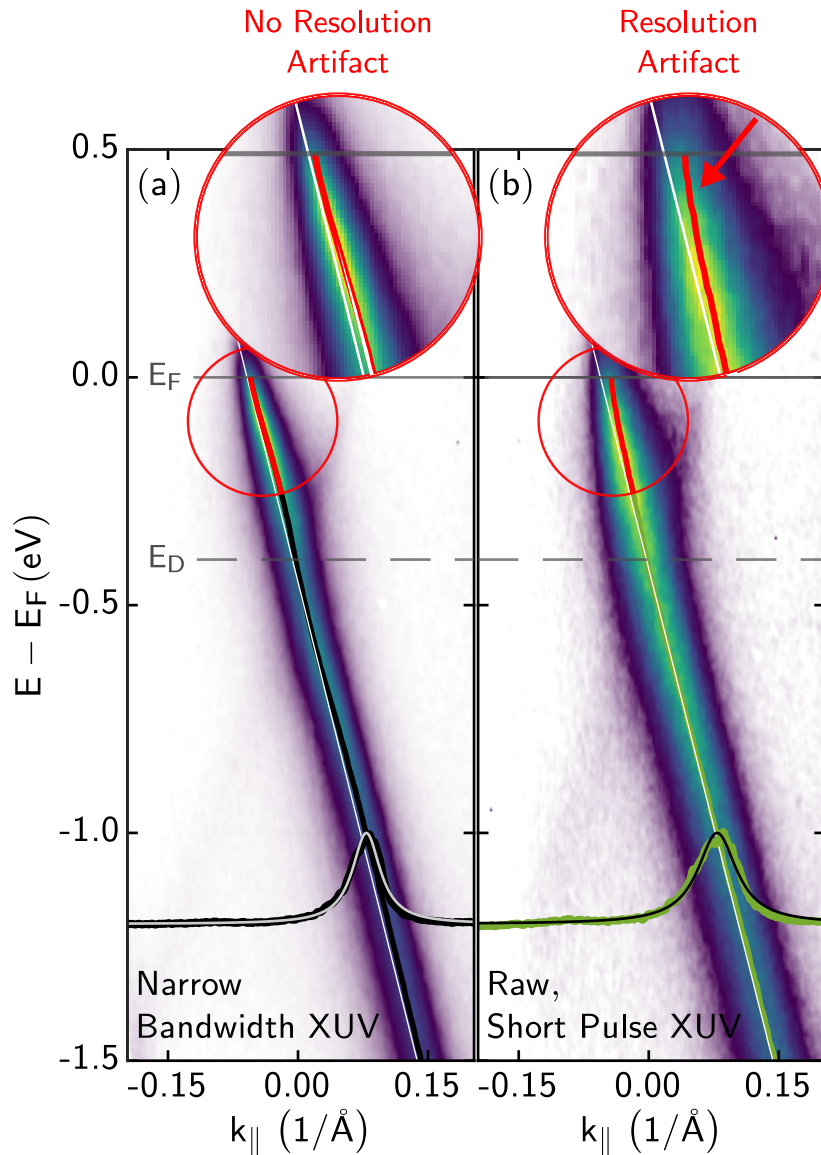


FIGURE 4.1. Application of the Lucy-Richardson deconvolution algorithm (LRD) to trARPES data. (a) A high-resolution APRES spectrum measured with the narrow-bandwidth XUV line has no notable resolution artifact. (b) An APRES spectrum measured with the spectrally broad short pulse XUV line has a resolution artifact, i.e., the dispersion bends towards the Fermi energy.

probably the availability of high experimental resolutions<sup>10,103</sup>, making such deconvolution methods mostly unnecessary. In this thesis, the LRD is benchmarked with by comparing the  $\text{Re}\Sigma$ , and  $\text{Im}\Sigma$  obtained from deconvolved static short pulse XUV spectrum and the  $\text{Re}\Sigma$ , and  $\text{Im}\Sigma$  obtained from a static 70 meV energy-resolution narrow-bandwidth-XUV measurement to assure physically correct results.

## 4.1 Resolution Artifact

First, we discuss how the resolution artifact (RA) will affect the ARPES spectra. To this end, we write the photoemission intensity  $I(k, \omega)$  as<sup>131,127,124</sup>

$$I(k, \omega) = [I_0(k, \nu, \mathbf{A})A(k, \omega')f(\omega')] \otimes \text{PSF}_{Ana}(\omega - \omega', k - k'), \quad (4.1)$$

with the Fermi-Dirac distribution  $f(\omega')$ . The convolution with the point spread function  $\text{PSF}_{Ana}(k, \omega)$  describes the broadening due to the experimental setup in momentum and energy. The bandwidth of our XUV pulses causes the main broadening in our spectra. How this broadening acts on the ARPES spectra depends on the nature of initial and final states in the photoemission process. For graphene, the initial states are 2D surface states. With our photon energy range, the final state is an inverse LEED state that decays exponentially into the material. In literature, this case is referred to as surface photoemission<sup>10</sup>. When the same state is measured with different photon energies, the measured spectrum will shift in kinetic energy but not in  $k_{\parallel}$ . Thus, a spectrally broad photon pulse will only broaden the ARPES spectra in energy, where the broadening  $\Delta_E$  is equal to the XUV pulse bandwidth (see Fig. 4.2 (a)). Hence the corresponding point spread function  $\text{PSF}_{Photon}(\omega)$  is one-dimensional in the energy direction of the ARPES spectrum. This line of argumentation does not necessarily hold for all types of materials. For example, in bulk PES, the initial and final states inside the sample are both states of the material. Accordingly, in bulk PES, spectrally broad photon pulse can lead to broadening in energy, perpendicular momentum, and parallel momentum  $\Delta_{k_{\parallel}}$  in the ARPES spectra (see Fig. 4.2 (a)). The broadening may even vary in different parts of the spectrum depending on the underlying band structure (see Fig. 4.2 (a)  $\Delta_{E'}$  and  $\Delta_{E''}$ ).

In graphene, however, we write  $I(k, \omega)$  with the bandwidth broadening  $\text{PSF}_{\text{Photon}}(\omega - \omega')$  as

$$I(k, \omega) = [I_0(k, \nu, \mathbf{A})A(k, \omega')f(\omega')] \otimes \text{PSF}_{\text{Ana.}}(\omega - \omega', k - k') \otimes \text{PSF}_{\text{Photon}}(\omega - \omega'). \quad (4.2)$$

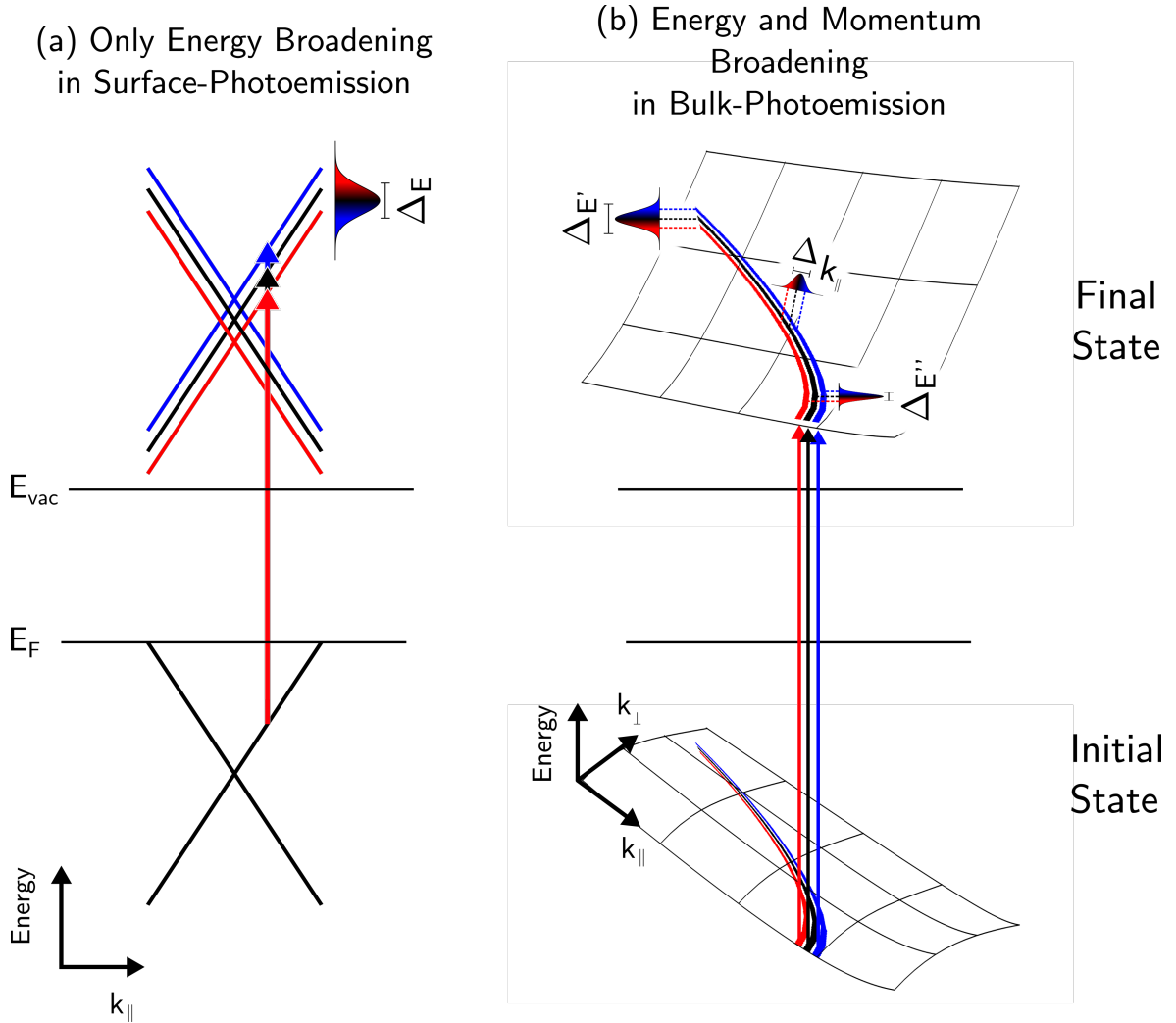


FIGURE 4.2. Energy and momentum broadening due to spectrally broad XUV pulses in different photoemission processes. (a) Since the final state is an inverse LEED state inside and outside the materials, the ARPES signal is only broadened in kinetic energy  $\Delta E$ . (b) In bulk photoemission, the ARPES signal can be broadened in  $\Delta k_{\parallel}$  and energy, where the extent of the broadening also depends on the underlying band structure. The photoemission processes are sketched for different spectral components of the XUV pulse, lower energy (red), center energy (black), and higher energy (blue).

Matrix elements effect have been neglected. The photoemission signal can thus be seen as the function  $S(k, \omega') = A(k, \omega')f(\omega')$  convolved with the PSFs.

$$I \propto S \otimes \text{PSF}_{\text{photon}} \otimes \text{PSF}_{\text{Ana.}} \quad (4.3)$$

For illustration of the impact of the RA, we simulate  $S(k, \omega)$  in Fig. 4.3 (a). A linear bare band structure with a constant momentum linewidth for all energies is assumed. The Fermi velocity ( $v_f = 1.1186 * 10^6 \text{m/s}$ ) is from DFT calculations from Dr. Dino Novko. The value is similar to that measured in the graphene sample (see chapter 5.5.1). Multiplication with a Fermi-Dirac distribution with temperature  $T$  simulates the occupation of this band. The experimental broadening is simulated by matrix convolution with a 2D Gaussian peak PSF (See inset in Fig. 4.3 (a-b)). The momentum resolution FWHM  $\Delta_k$  is chosen negligibly small compared to the energy-resolution FWHM  $\Delta_E$  as we are mainly interested in the broadening due to the photon bandwidth. In Fig. 4.3 (c) we have plotted such an exemplary simulated image of  $I(k, \omega)$ . Here, we employed an MDC Gauss Fit analysis\*(red line). The extracted peak maximum dispersion starts to bend to higher energies just below the Fermi energy, reproducing the resolution artifact we saw in chapter 5.5.1. For a systematic analysis, we extracted the dispersion and MDC FWHM for a constant temperature  $T = 300 \text{K}$  (see Fig. 4.3 (c)) and varied  $\Delta_E$  in Fig. 4.3 (d). Furthermore, we extracted the  $\text{Re}\Sigma$  and the  $\text{Im}\Sigma$  and plotted them in the insets that the RA has influenced. In the  $\text{Re}\Sigma$ , the RA shows an increase starting just below  $E_F$  which saturates for higher energies. The magnitude of the RA increases with  $\Delta_E$ . In the  $\text{Im}\Sigma$ , the resolution artifact is a dip where the center shifts to higher energies (black marker in the inset in Fig. 4.3 (c)) with increasing  $\Delta_E$ . Thereby the RA's amplitude increases with  $\Delta_E$ . Thus the overall magnitude of the artifact depends on  $\Delta_E$ , where the artifact starts to become negligible between  $40 \text{meV} < \Delta_E < 100 \text{meV}$ . In Fig. 4.3 (c) we extracted the temperature-dependence of the analyzed dispersion for constant  $\Delta_E = 120 \text{meV}$  together with the extracted  $\text{Re}\Sigma$  and  $\text{Im}\Sigma$ . The RA in  $\text{Re}\Sigma$  is smaller for higher temperatures and becomes negligible for  $1500 - 2000 \text{K}$ . In the  $\text{Im}\Sigma$ , the resolution artifact is a dip where

---

\*Instead of Lorentzian peaks, Gauss peaks are used in the simulation of the intrinsic linewidth as a first approximation. Simulations with different peak forms showed that this approximation does not change the major trends observed in the model.

the center (black marker in the inset in Fig. 4.3 (d)) shifts to higher energies with decreasing  $T$  and the amplitude increases.

To summarize, the measurement of sharp features with limited energy-resolution causes RAs in ARPES data.

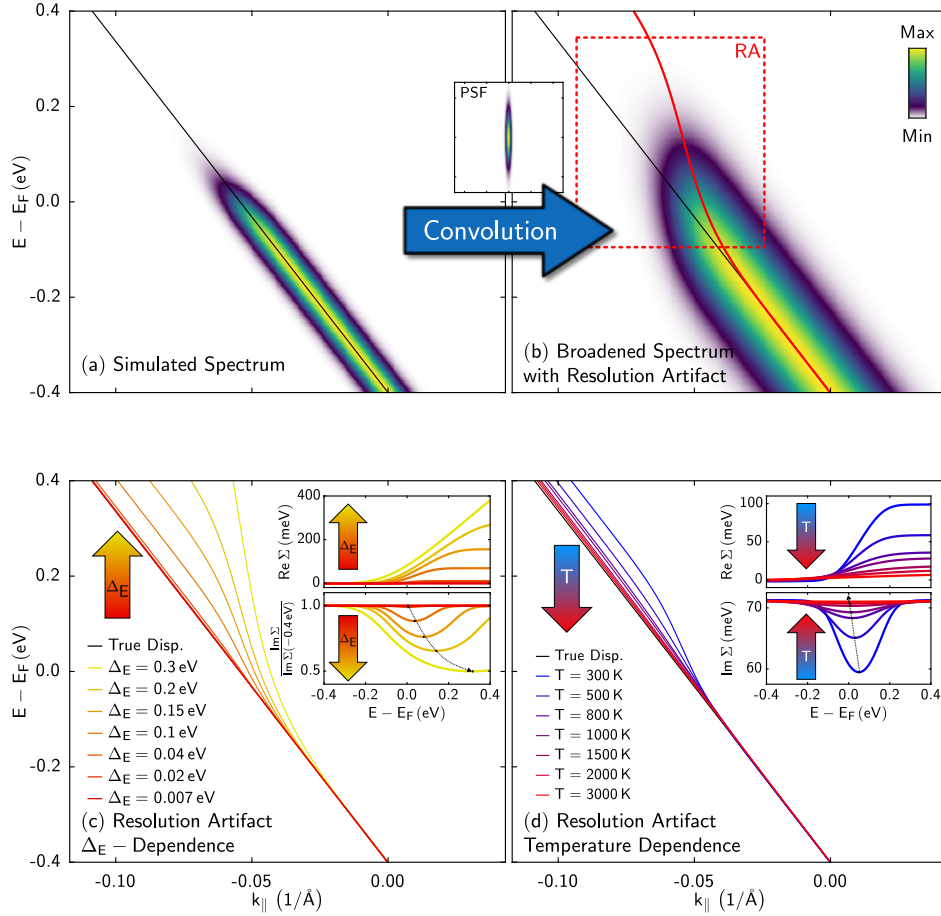


FIGURE 4.3. Simulation of the resolution artifact. (a) Simulated ARPES spectrum of a linear Dirac-arm. (b) The experimental resolution was introduced by a convolution with a two-dimensional Gaussian PSF (see inset), and the dispersion was extracted with an MDC Gauss-fit evaluation (red line). The RA (red box) is the deviation from the underlying linear dispersion (black line). (c) Dependence of the RA at 300 K of the resolution FWHM used in the PSF. (d) Temperature dependence of the RA for  $\Delta E = 120$  meV. The insets in the (c) and (d) show how the RA influences the extracted  $\text{Re } \Sigma$  and  $\text{Im } \Sigma$ . The  $\text{Im } \Sigma$  in the inset in (c) has been normalized for a better clarity. Note that the trend of an increasing RA amplitude in  $\text{Im } \Sigma$  is also visible in the unnormalized data in absolute values.

## 4.2 Lucy-Richardson Deconvolution Algorithm

To discuss the quasiparticle dynamics, we need a procedure where we can deconvolute the PSF in equation 4.2 from the ARPES spectra. Refs. <sup>127,131</sup> employed a Lucy-Richardson deconvolution algorithm (LRD)<sup>125,126</sup> to ARPES spectra. They deconvolve the PSF from  $I(k, \omega)$  to calculate the function  $S(k, \omega)$ . The LRD algorithm is iterative, and  $S^{N+1}$  can be written in 1D as,

$$S_i^{N+1} = S_i^N \sum_j \frac{I_j}{\bar{I}} \cdot \text{PSF}_{ij} \quad \text{with} \quad \bar{I} = \sum_i S_i^N \cdot \text{PSF}_{ij}, \quad (4.4)$$

with the number of iterations  $N$ . It can be expanded to 2D (see supplements of Refs. <sup>127,131</sup>). This procedure produces the statistical most likely form of  $S$  if it converges. It obeys the spectroscopic sum rule and the result is always positive so that it is suitable for ARPES data. The finally resulting spectrum from the LRD can be validated. For this validation, the final spectrum is convoluted with the point spread function. The convoluted spectrum should match the input spectrum. Thus the differences between the initial and the final spectrum are a measure for the validity of the deconvolution.

To conclude, the algorithm requires knowledge of the PSF. However, we note that the deconvolution yields better results for better initial signal-to-noise ratios. Our combination of a high repetition rate short pulse XUV source together with the Phoibos 150 2D CCD detector provides an excellent basis for achieving such high signal-to-noise ratio spectra in a reasonable measurement time.

### 4.3 Estimation of the Point-Spread-Function

Knowledge of the Point-Spread-Function (PSF) is not readily available, and we will now show how to obtain it from ARPES spectra.

First, we look at our available photon sources at our setup. The HeI line of the gas discharge lamp has bandwidths of  $< 1 \text{ meV}$ <sup>104</sup>. With the narrow-bandwidth-XUV the total resolution is estimated to be  $70 \text{ meV}$  and with the ultrashort XUV pulse the total resolution is  $\approx 200 - 300 \text{ meV}$  (see appendix section A.1)).

For the ARPES spectrum, we can write the complete PSF from equation 4.2 as a convolution between the different contributions to the broadening<sup>127,131</sup>. We measure the same spectrum with different photon sources, hence, the same  $S(k, \omega')$ . For spectra measured with the HeI line the influence of  $\text{PSF}_{\text{HeI}}$  is negligible compared to the influence of  $\text{PSF}_{\text{Ana.}}$ . So we write,

$$I_{\text{HeI}} = S \otimes \text{PSF}_{\text{Ana.}} \otimes \text{PSF}_{\text{HeI}} \approx S \otimes \text{PSF}_{\text{Ana.}}, \quad (4.5)$$

with equation 4.5 we can write  $I_{\text{XUV}}$  as

$$I_{\text{XUV}} = S \otimes \text{PSF}_{\text{Ana.}} \otimes \text{PSF}_{\text{XUV}} \approx I_{\text{HeI}} \otimes \text{PSF}_{\text{XUV}}. \quad (4.6)$$

Now we can use the LRD to deconvolve  $I_{\text{HeI}}$  from  $I_{\text{XUV}}$  and extract the  $\text{PSF}_{\text{XUV}}$

$$\text{PSF}_{\text{XUV}} = \text{LRD}(I_{\text{XUV}}, I_{\text{HeI}}). \quad (4.7)$$

In practice, we need to choose a suitable sample for this calibration measurement. Deconvolution on simple peak forms is well established in many spectroscopic fields such as XPS. For example, in astronomy, point-like stars are ideal for determining the whole PSF function in both dimensions at once<sup>128-130</sup>. The main advantage is that simple peak forms avoid unwanted artifacts appearing in the deconvolution of complex spectra. In ARPES spectra, to the best of our knowledge, there are no point-like signatures or circular-like peak features in energy-momentum maps. However, EDC or MDC cuts can have simple peak forms. To measure a simple peak form, we took spectra of the Au(111) Shockley-surface-state (SS)<sup>132-135</sup> (see Fig. 4.4 (a-b)) with the HeI line and with the short pulse XUV.

Broadening from photon bandwidth on the ARPES spectra depends on the nature of the initial and final states in the PES process (as discussed in chapter 4.1). In the case of the SS on Au(111) and in our photon energy range, the final state is not necessarily an exponentially decaying inverse LEED state in the material, but could be a bulk state. However, since the

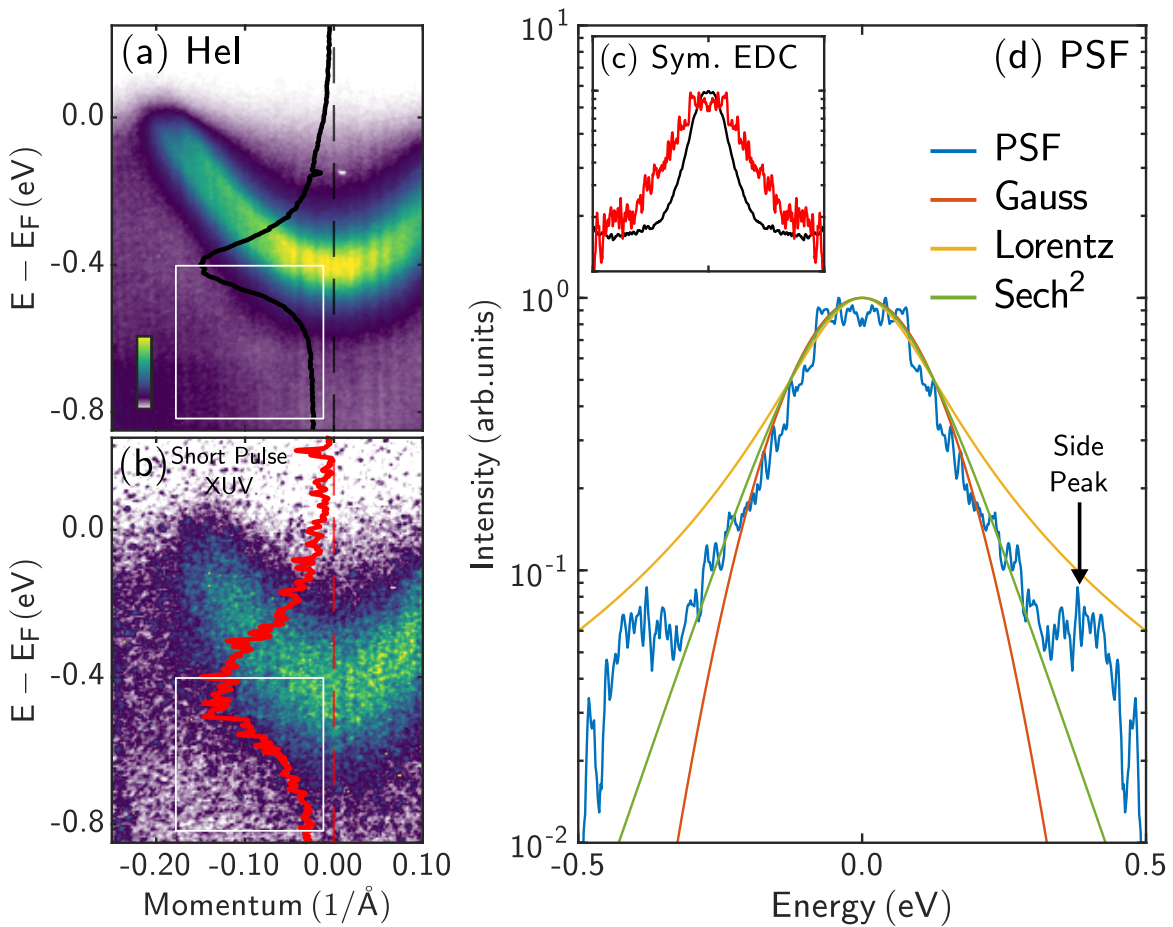


FIGURE 4.4. (a) ARPES spectrum of the SS with the HeI line. (b) ARPES spectrum of the SS with the short pulse XUV line. The EDCs (black and red profiles) were extracted in normal emission. The EDCs were symmetrized in (c), then the symmetric HeI EDC was deconvolved from the symmetric XUV EDC, leading to the PSF, e.g., the spectrum of the XUV line (d) (blue). Several simple peak forms with an FWHM of 250 meV were plotted for comparison.

initial state has no  $k_{\perp}$  dependence, a shift in photon energy will again only shift the measured kinetic energy, but not  $k_{\parallel}$ . Therefore, the photon bandwidth broadens the spectra only in kinetic energy, but not  $k_{\parallel}$ . Any EDC is only affected by the energy broadening equal to the photon bandwidth. In this way we can extract the bandwidth and spectrum of the XUV light from the SS.

Thus we extracted the EDC in normal emission (see Fig. 4.4 (a-b)) and mirrored the lower half (white box in Fig. 4.4) in energy, thereby producing simple symmetric peaks (see Fig. 4.4 (c)). The lower energetic half of the SS EDC is more suitable here than the half close to the Fermi energy since the Fermi edge does not influence it. These EDCs are used as  $I_{XUV}$  and  $I_{HeI}$  in equation 4.7 to deconvolute  $I_{HeI}$  from  $I_{XUV}$  and to gain the PSF. Fig. 4.4 (d) is a semi-logarithmic plot of the resulting  $PSF_{XUV}$  (blue line). The PSF should, in fact, be the energetic spectrum of the short pulse XUV source. We see one main peak and side peaks. A  $\text{sech}^2$  form describes the main peak well. To visualize this, we have plotted multiple simple peak forms with an FWHM of 250 meV, which was extracted from the main peak of the PSF (blue line). The side peaks might stem from the side peaks of the fundamental laser pulse, or they might be artifacts from the SS spectrum or the LRD process itself<sup>†</sup>.

## 4.4 Benchmarking of the Lucy-Richardson Deconvolution Algorithm

In this section, we benchmark the LRD process in ARPES spectra. We use narrow-bandwidth ARPES spectra with 70 meV energy-resolution to benchmark the LRD. Thus the energy-resolution broadening in the APRES measured with the short pulse XUV is removed by deconvolution until the resulting ARPES spectra are comparable to the ARPES spectra measured with narrow-bandwidth XUV. This approach assures that the results are physically accurate and correct, i.e., that artifacts from the LRD procedure do not falsify the results. Furthermore, this approach is justified since the ARPES spectra from narrow-bandwidth XUV

---

<sup>†</sup>These side peaks are not related to the Rashba spin-orbit splitting as this splitting vanishes in the  $\Gamma$ -point of the Brillouin zone<sup>136</sup>.

suffice to discuss quasiparticle dynamics (see chapter 5.5.1). Thus, deconvolved ARPES spectra should also suffice to discuss the quasiparticle dynamics.

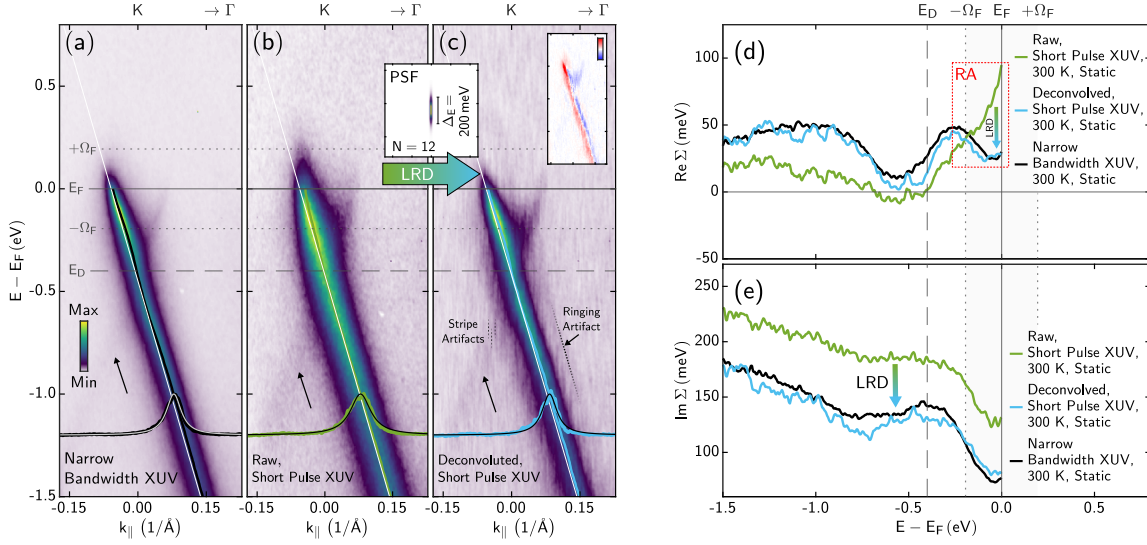


FIGURE 4.5. Benchmarking of the LRD. A short pulse XUV ARPES spectrum (b) was deconvolved with a 2D  $\text{sech}^2$  PSF (see inset), producing a deconvolved ARPES spectrum (c). A high-resolution ARPES spectrum (a), taken with the narrow-bandwidth XUV line, is shown for benchmarking. (d-e) show that the LRD successfully removed the RA from the  $\text{Re}\Sigma$  and  $\text{Im}\Sigma$ . The inset (c) is the difference map between (a) and (c). The dashed lines in (c) indicate some exemplary LRD artifacts.

In Fig. 4.5 (a, c) we deconvolved the static spectrum taken with the short pulse XUV and extracted the  $\text{Re}\Sigma$  and the  $\text{Im}\Sigma$  in Fig. 4.5 (d, e). We anticipate the final LRD parameters, which we will determine in this chapter. For the PSF, we used a 2D  $\text{sech}^2$  peak where the energy-resolution FWHM  $\Delta_E$  was 200 meV in energy and negligible  $0.003 \text{ \AA}^{-1}$  in momentum. The LRD algorithm was stopped after 12 iterations ( $N$ ).  $\text{Re}\Sigma$  and  $\text{Im}\Sigma$  (light blue vs black line) reproduce the static narrow-bandwidth-XUV results with good agreement. The resolution artifact in  $\text{Re}\Sigma$  (red box in Fig. 4.5 (e)) has been successfully removed.

We will now discuss how we chose these parameters for the PSF. For the benchmark, we calculated  $\text{Re}\Sigma$  and  $\text{Im}\Sigma$  for the whole energy range and compared them to the narrow-bandwidth measurements. Unfortunately, this is a computationally demanding process that makes the use of a fit algorithm unviable. For this reason, we resorted to manual benchmarking

by comparing curves and adjusting the PSF parameters accordingly. Here I only show that finally extracted parameters do remove the resolution artifact and produce results that are comparable to narrow-bandwidth XUV measurements.

The form of the PSF is known from Fig. 4.4 (d) to be a  $\text{sech}^2$  peak. Furthermore, at first it seems reasonable to choose the extracted XUV bandwidth as the resolution FWHM in energy ( $\Delta_E$ ). However, we do not aim to deconvolve the full XUV bandwidth from our spectra. Instead, we deconvolve only part of the total short-pulse bandwidth broadening so

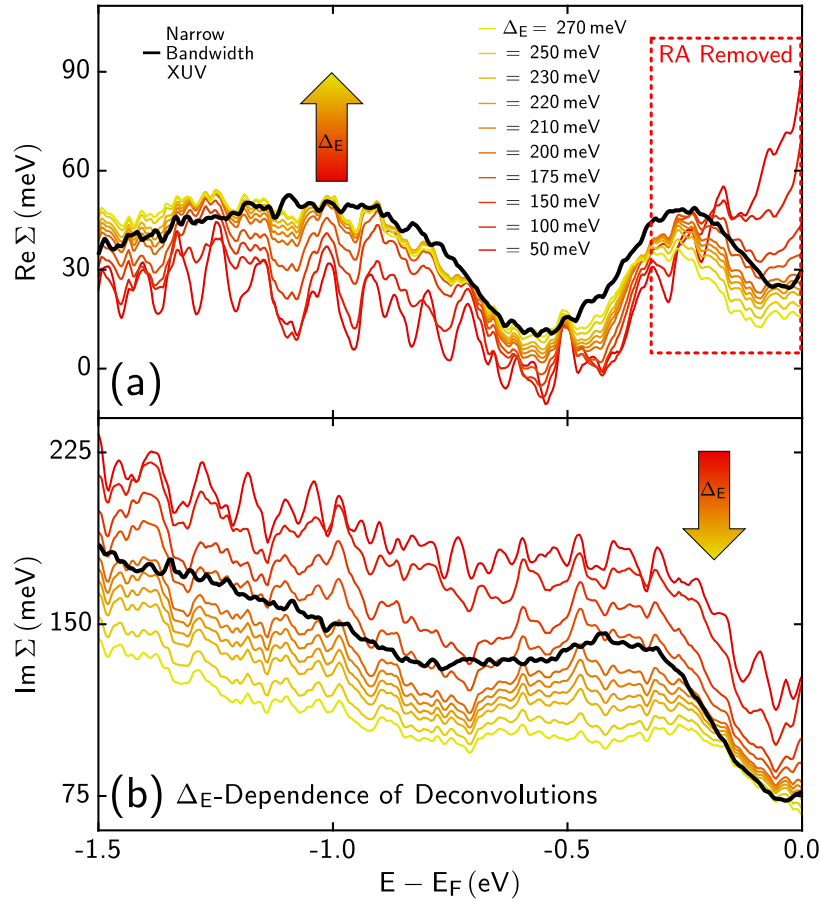


FIGURE 4.6.  $\Delta_E$  dependence of the LRD. The extracted  $\text{Re} \Sigma$  (a) and  $\text{Im} \Sigma$  (b) depend on the variation of  $\Delta_E$  in the PSF for the LRD. The  $\text{Re} \Sigma$  converges onto the  $\text{Re} \Sigma$  from the narrow-bandwidth ARPES spectrum (black line). In contrast the  $\text{Im} \Sigma$  decreases with increasing  $\Delta_E$ .  $\text{Re} \Sigma$  and  $\text{Im} \Sigma$  from the narrow-bandwidth ARPES spectrum have been plotted as black lines. The number of iterations is  $N = 12$ .

that the resulting ARPES spectrum reproduces the narrow-bandwidth XUV ARPES spectrum to achieve physical correct results (as explained above). Moreover, we measured the SS on different days than the graphene spectra. As a result, we should not assume constant XUV generation conditions and constant bandwidths outright. Ref. <sup>137,138</sup>, for example, show that the XUV spectrum depends sensitively on the HHG generation conditions. For these reasons, we vary the energy-resolution FWHM ( $\Delta_E$ ) and compare the resulting  $\text{Re}\Sigma$  and  $\text{Im}\Sigma$  in Fig. 4.6 with the narrow-bandwidth-XUV results (black line).

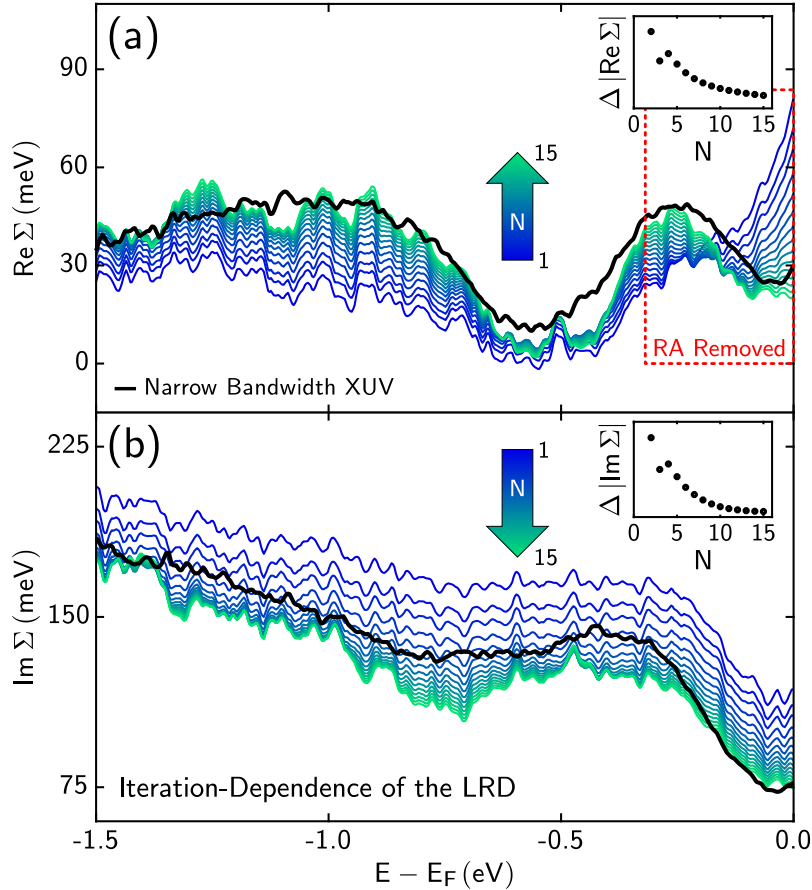


FIGURE 4.7. Iteration ( $N$ ) dependence of the LRD. The  $\text{Re}\Sigma$  (a) and  $\text{Im}\Sigma$  (b) converge with  $N$  unto the  $\text{Re}\Sigma$  and  $\text{Im}\Sigma$  from the narrow-bandwidth measurement (black lines).  $\Delta|\text{Im}\Sigma|$  and  $\Delta|\text{Re}\Sigma|$  are a measure for the convergence of the LRD (see insets) and show that 12 iterations suffice while avoiding artifacts.  $\Delta_E$  is 200meV.

We notice that  $\text{Re}\Sigma$  (Fig. 4.6 (a)) starts to converge around  $\Delta_E \approx 200$  meV and that it resembles qualitatively the narrow-bandwidth-XUV results. Note that the absolute difference between  $\text{Re}\Sigma$  from the narrow-bandwidth-XUV data and  $\text{Re}\Sigma$  from the short pulse XUV data cannot be used as a benchmark. The reason is a possible unknown systematic shift in  $\text{Re}\Sigma$  between the two data sets. The self-consistent calculation of the  $\text{Re}\Sigma$  leaves an undetermined offset open (see appendix A.3). This offset might vary between the narrow-bandwidth ARPES data and the short pulse XUV ARPES data, leading to the undetermined shift. In the  $\text{Im}\Sigma$  (Fig. 4.6 (a)), a energy-resolution FWHM  $\Delta_E = 200$  meV reproduces the narrow-bandwidth data the closest. As a result from this observations we choose  $\Delta_E = 200$  meV.

The momentum resolution FWHM  $\Delta_{k_{\parallel}}$  should not be broadened by the photon bandwidth as discussed in chapter 4. Still, we verified this by varying  $\Delta_{k_{\parallel}}$  in the PSF in a similar way as for the energy-resolution (see appendix Fig. A.6). When we increased the momentum resolution in the PSF, a deconvolution artifact appears in  $\text{Re}\Sigma$ . Furthermore, we could reproduce the narrow-bandwidth results only when the momentum resolution FWHM was negligible. We conclude that the assumption of no broadening in  $k_{\parallel}$  due to the XUV line is consistent with our results.

Fig. 4.7 (h) shows the iteration dependent results for  $\Delta_E = 200$  meV. In the insets we plotted the absolute integral difference between following iterations  $\Delta|\text{Im}\Sigma|$  and  $\Delta|\text{Re}\Sigma|$  \*. The results converge around  $N = 12$  iterations in both quantities. A larger number of iterations, e.g.,  $N \approx 50$ , introduced strong artifacts in the spectra, and thus we used as few iterations as possible. The LRD becomes more sensitive to higher spatial frequencies, i.e., smaller features like noise and artifacts, when the number of iterations is increased and thus causes the artifacts<sup>127,131,130,139</sup>. However, in Fig. 4.5 (c), there is still a ring artifact around the bright Dirac arm, and there are vertical stripes along the energy direction. These well-known stripe and ringing artifacts are created by the LRD procedure<sup>139</sup>. The artifacts do not influence the extracted self-energies and are thus negligible †.

---

\*These are defined as  $\Delta|\text{Im}\Sigma| = \int dE |\text{Im}\Sigma(E)^N - \text{Im}\Sigma(E)^{N-1}|$  and  $\Delta|\text{Re}\Sigma| = \int dE |\text{Re}\Sigma(E)^N - \text{Re}\Sigma(E)^{N-1}|$ .

†Furthermore, in Fig. 4.5 the color code was chosen to make the background noise and, consequently, these artifacts visible. In other ARPES spectra throughout the thesis, these features are not visible in the color code.

Although our LRD procedure reproduces the narrow-bandwidth-XUV results with good agreement, we still notice some deviations. The phonon kink, for example (see Fig. 4.5 (e) between  $\pm\Omega_F$ ) is less pronounced in the deconvolved data. This deviation could not be addressed by varying the energy-resolution FWHM nor by the number of iterations in the LRD. These deviations probably stem from slight deviations in measurement geometry between measurements, namely the sample azimuth and polarisation of the XUV pulse. The difference in polarization is also evident in the slightly more pronounced second Dirac arm (pointed out by black arrows in Fig. 4.5 (a-c)) in the short pulse XUV spectra.

## 4.5 Effects of the LRD on the trARPES Spectra

With the established LRD procedure, we can apply it to the trARPES data. This section compares the MDC analysis before and after applying the LRD to the trARPES data. Therefore, in Fig. 4.8, we show ARPES spectra for the three exemplary time-delays ( $-7$  ps,  $60$  fs and  $175$  fs). As expected, we observe an overall sharpening of the MDC FWHM after applying the LRD. In the following, we will describe the impact of the LRD on the  $\text{Re}\Sigma$  and  $\text{Im}\Sigma$  in detail, first for (i) a Fermi-Dirac charge-carrier distribution under RT ( $-7$  ps, blue lines), subsequently for (ii) a far-from-equilibrium charge-carrier distribution ( $60$  fs, red line), and then for (iii) a Fermi-Dirac charge-carrier distribution with increased temperature ( $175$  fs, yellow line).

- (i) With a Fermi-Dirac charge-carrier distribution with RT (see Fig. 4.9 blue lines), the phonon kink has been restored in the  $\text{Re}\Sigma$  after application of the LRD and the RA has been removed (see Fig. 4.9 (a) red box (black dashed line) and compare with Fig. 4.9 (b) red box). In  $\text{Im}\Sigma$ , the resolution artifact has also been removed. This is evident in the decrease in  $\text{Im}\Sigma$  in the phonon window ( $\pm\Omega_F$  around  $E_F$ , see Fig. 4.9 (c) red bars on blue lines). After the application of the LRD, the amplitude of this phonon feature decreases slightly. This decrease is expected after the removal of the  $\text{Im}\Sigma$  resolution artifact, which introduces a decrease in MDC linewidth close to the Fermi energy (see section 4.1 Fig. 4.3).

- (ii) With a far-from-equilibrium charge-carrier distribution, in  $\text{Im}\Sigma$ , many features are sharper and more distinct after the LRD, e.g., around  $E_i$  (see Fig. 4.9 (c) red box). In addition, the extracted  $\text{Re}\Sigma$  decreases stronger with energy above  $E_F$  after application of the LRD (compare red lines in Fig. 4.9 (a) and (b)). This change is important since the RA in the far-from-equilibrium conditions at 60 fs is not as

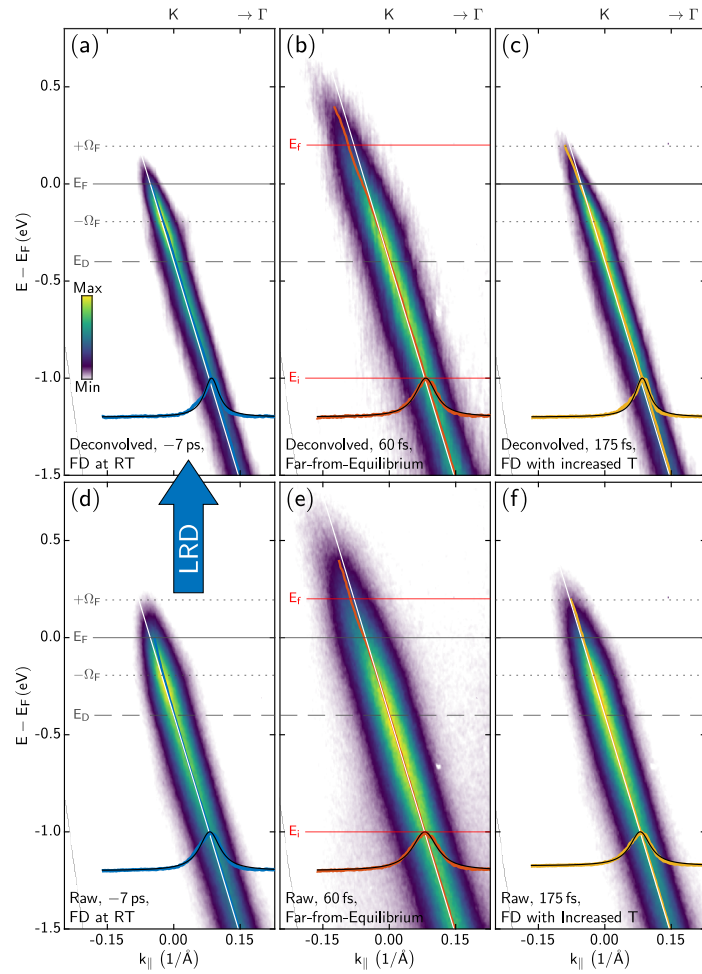


FIGURE 4.8. Comparison of raw and deconvolved trARPES spectra. In (a-f), we compare the ARPES spectra before and after the deconvolution. White lines mark the bare band structure. Colored lines mark the dispersion extracted from the Lorentz fit evaluation. One exemplary MDC profile (colored profile) together with the fitted Lorentzian peak (black curve) is shown for each ARPES spectrum. The bare band structure has been plotted in white.

obvious as the RA with a Fermi-Dirac distribution at RT at  $-7$  ps. Before and after the LRD, the extracted  $\text{Re}\Sigma$  at 60 fs decreases overall with energy above  $E_F$ . The resolution artifact only weakens this decrease.

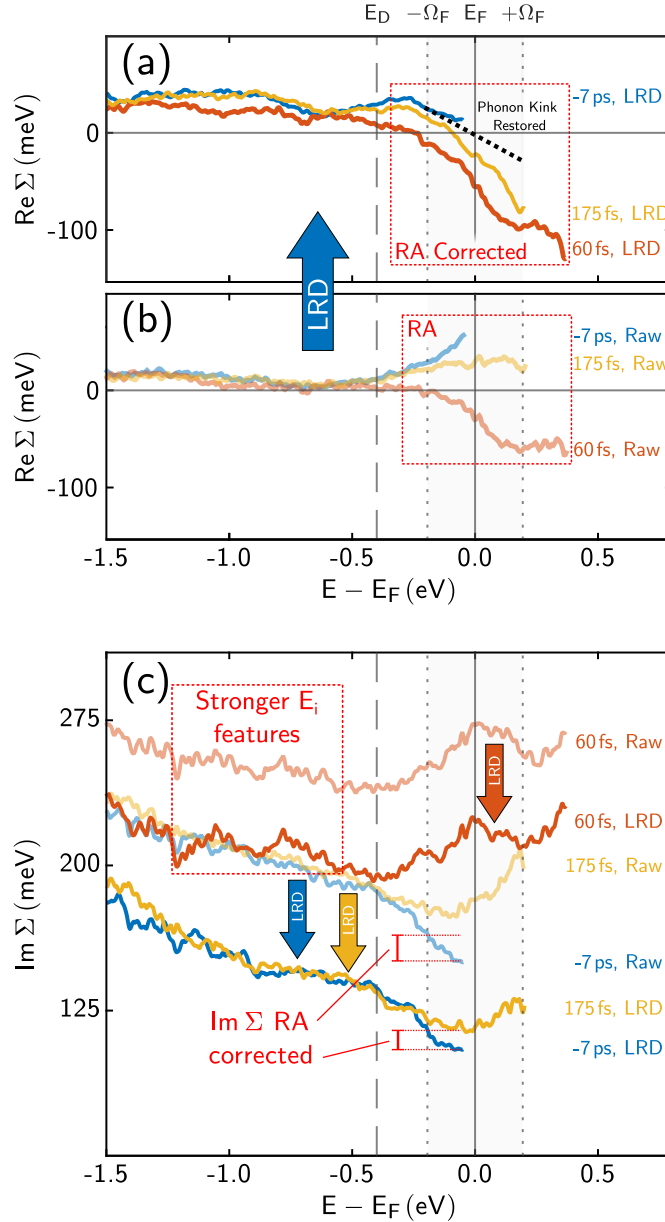


FIGURE 4.9. Influence of the LRD on the extracted self energies in trARPES. (a-c) compares the extracted  $\text{Re}\Sigma$  and  $\text{Im}\Sigma$  before (semi-transparent lines) and after (opaque lines) application of the LRD to a ARPES spectrum with a Fermi-Dirac distribution at RT ( $-7$  ps, blue lines), to a ARPES spectrum with a far-from-equilibrium distribution (60 fs, red lines) and to a ARPES spectrum with a Fermi-Dirac distribution at increased temperature (175 fs, yellow lines).

- (iii) With a Fermi-Dirac charge-carrier distribution with increased temperature (see Fig. 4.9 yellow lines), the RAs are also corrected in a similar way as at RT in case (i).

Furthermore the features at  $E_i$  and  $E_f$  at  $-60$  fs don't decrease in amplitude, i.e. they are more discernible and stronger (see Fig. 4.9 (c) red lines). This is important, since it means that these features are unlikely to be caused by far-from-equilibrium RAs (for details see appendix Chapter A.5).

In conclusion, the application of the LRD corrected the RAs as we expected from our simulations. Furthermore, many features are now more pronounced and discernible.

## 4.6 Discussion of our Approach to the LRD

This chapter discusses why our rather complex benchmarking approach for the LRD is necessary. Furthermore, we compare our application of the LRD to that of Rameau and Yang et al. in Refs. <sup>127,131</sup>.

In our benchmarking approach, we applied the LRD to the ARPES spectrum measured with short pulse XUV light, extracted the self-energy, and then compared the  $\text{Re}\Sigma$  and  $\text{Im}\Sigma$  to those extracted from the ARPES measured with narrow-bandwidth XUV light. The MDC fit evaluation contained in this approach makes this approach computationally slow. In a more obvious and faster benchmarking approach, we could apply the LRD to the short pulse XUV ARPES spectrum and calculate the sum of absolute differences in intensity to the narrow-bandwidth XUV ARPES spectrum. This absolute sum could be minimized in a fit algorithm, where the parameters of the LRD (PSF parameters and iterations) are varied until convergence.

The inset in Fig. 4.5 (c) shows the difference map between the narrow-bandwidth XUV ARPES spectrum and the short pulse XUV ARPES spectrum. There are clear differences in intensity between both spectra. In the fast approach, this would mean that LRD parameters were not appropriately chosen. Nonetheless, as we showed in this chapter, our approach of comparing the  $\text{Re}\Sigma$  and  $\text{Im}\Sigma$  shows that the used LRD parameters lead to physically meaningful results. This apparent contradiction can be resolved as follows. These features in

the difference map (see appendix A.3) are caused by slight shifts in parallel momentum and distortions between both spectra, caused by small differences in spot position on the sample, i.e., slightly changing measurement geometry. Due to these features in the difference map, the fitting process in the faster approach cannot converge to physically correct results. Therefore a correction of these shifts has to be done.

In our approach, the self-consistent calculation of the  $\text{Re}\Sigma$  and  $\text{Im}\Sigma$  (see inset Fig. 4.5 (c)) corrected these shifts in the difference map. Thus, the  $\text{Re}\Sigma$  and  $\text{Im}\Sigma$  are naturally suited as a benchmark for the LRD (see appendix A.3). Furthermore, the  $\text{Re}\Sigma$  and  $\text{Im}\Sigma$  are relevant quantities for discussing quasiparticle dynamics.

Now we compare our work to that of Rameau and Yang et al. in Refs. <sup>127,131</sup>. They do apply the LRD to high-resolution ARPES data. However, the broadening is much smaller than the intrinsic linewidth of the states. In our data, they are comparable, which is not ideal as the results of the LRD become less unique and thus possibly non-physical<sup>127,131,139</sup>. Thus we only deconvoluted to the level of our known 70 meV energy-resolution data to assure physically correct results. The benchmarking with higher-resolution data was only possible due to the ready availability of the narrow-bandwidth-XUV and the short pulse XUV line in the same setup with nearly identical measurement geometry\*.

Another difference is that Rameau, Yang, et al.<sup>127,131</sup> treat broadening, which is mainly caused by the detector setup. Thus, the broadening only acts on photoemitted electrons. This means that assuming a 2D gaussian PSF requires no further deliberations. Here, we explicitly expand the method to broadening due to photon bandwidth, which acts during the photoemission process itself. Therefore, we considered the influence of the initial and final states on the broadening in detail (see chapter 4.1).

In conclusion, we have shown that the LRD method removes the resolution artifact caused by the short pulse XUV bandwidth from the trARPES spectra and allows to achieve physical

---

\*Spectra were also taken with a gas discharge lamp. These spectra exhibit an ultimate resolution due to the negligible photon bandwidth  $< 1$  meV<sup>104,103</sup>. However, they were not suitable as a benchmark spectrum due to strong shifts and distortion caused by the widely different measurement geometry.

meaningful results. Thus, we can now discuss the quasiparticle dynamics under far-from-equilibrium conditions.

## **Far-from-Equilibrium Electron-Phonon Interactions in Optically-Excited Graphene**

---

This section discusses the main results of this thesis, which are far-from-equilibrium quasiparticle dynamics in doped graphene after IR femtosecond pulse excitation. Here, we measure the many-body response of graphene and find distinct features that we can explain with electron-phonon coupling in accordance with theory. Moreover, evaluating the NEQ many-body response with spectrally broad XUV pulses is only enabled via the usage of the deconvolution scheme on the ARPES spectra.

Large parts of this chapter are reproduced from our Publication<sup>1</sup> "Far-from-equilibrium electron-phonon interactions in optically-excited graphene." I performed the vast majority of the data evaluation and analysis. I carried out the measurements together with Marco Merboldt with further contributions from Jan Philipp Bange, Hannah Strauch, and Michael Stellbrink.

## 5.1 Introduction

In condensed matter physics, strong many-body-interactions can create exotic quantum phases such as Mott insulating states<sup>4,5</sup>, CDW phases<sup>6</sup> and superconductivity<sup>7</sup>. A common ansatz to understand these many-body effects is to separate the material system into subsystems, for example, the charge, the lattice, the orbital, and the spin, and then to study the interactions between these subsystems. In 2D systems, confinement of the charge carriers further facilitates strong interactions between the subsystems<sup>8</sup>. The quasiparticle picture is a common way to describe the interactions of the charge carrier subsystem with the other subsystems. Here, the self-energy describes the corrections to the single-particle electron-band-structure<sup>9</sup>. From ARPES spectra, we can extract these corrections and thereby the self-energy. Thereby, ARPES is a powerful tool to investigate many-body effects<sup>10,11</sup>. An advanced goal in modern solid-state physics is to control, e.g., many-body interactions. One control strategy is to use strong femtosecond laser pulses to excite the subsystems to non-equilibrium (NEQ)<sup>12-14</sup> conditions to create and to subsequently investigate such new "hidden"<sup>15-17</sup> and/or dynamically evolving<sup>18,24-31,19-23</sup> states in experiments.

Our goal is to increase the understanding of matter under far-from-equilibrium conditions by extracting the self-energy from time- and angle-resolved photoemission spectroscopy (trARPES) data. Although the extraction and interpretation of the quasiparticle dynamics in static ARPES data is a rather developed field<sup>10,9</sup>, in trARPES, this is a challenging task<sup>140,51,61,69</sup>. In trARPES, there is an inherent competition between the time and energy-resolution of the experiment, caused by the time-bandwidth product of the ultrashort XUV laser pulse. Femtosecond laser pulses are necessary to access the system during far-from-equilibrium conditions. However, such pulses have bandwidths of hundreds of meV. On the other side, the quasiparticle corrections to the single-particle electronic band structure are on the order of 10 – 100 meV. In addition, the spectrally broad XUV pulses cause resolution artifacts (RA) near the Fermi energy<sup>124</sup> (see section 4.1). However, the energy region near the Fermi energy is of particular interest due to the low energy quasiparticle dynamics<sup>39,141,142,9,143-145</sup>. Unfortunately, the RAs prevent any reliable discussion of the quasiparticle dynamics near the Fermi energy. Therefore, we deconvolve the resolution broadening

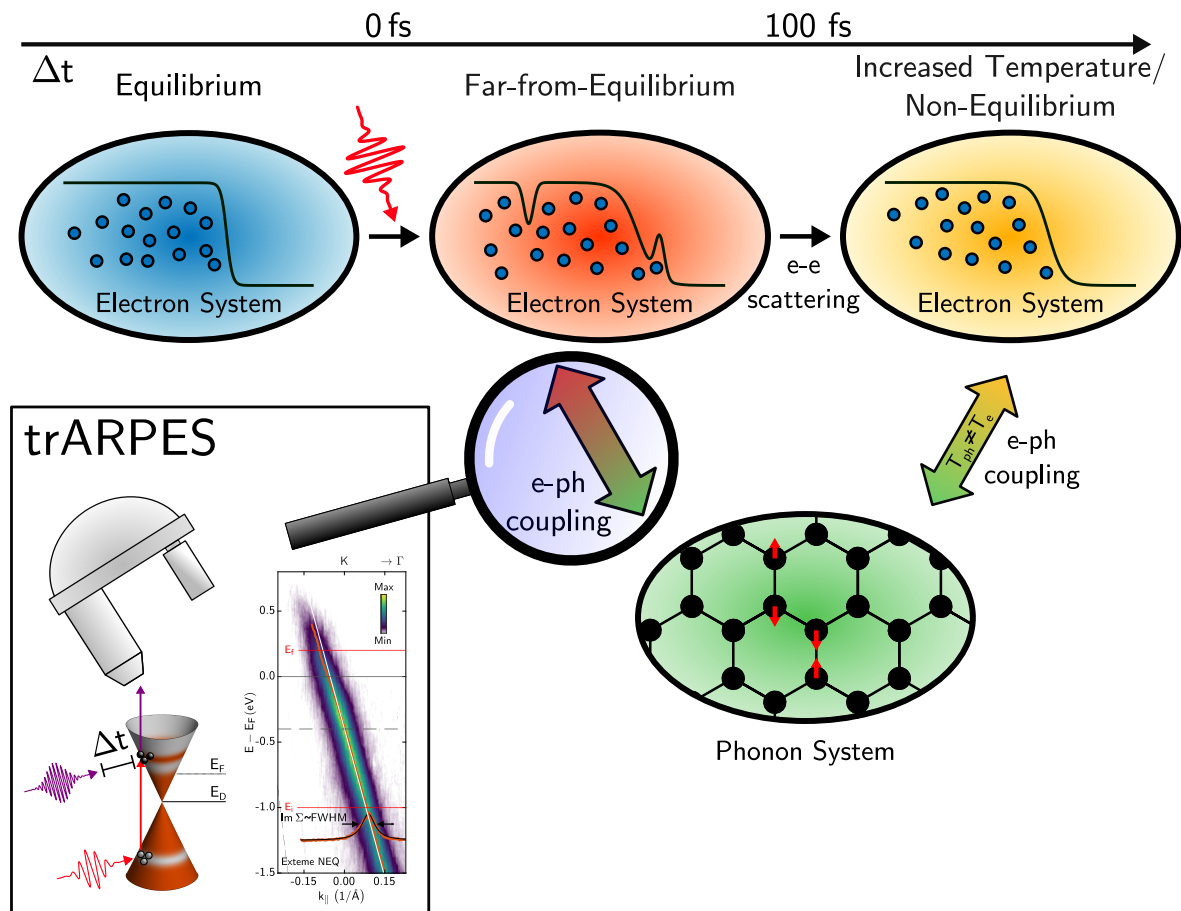


FIGURE 5.1. Interaction between subsystems in graphene after femtosecond IR interband excitation. The equilibrium Fermi-Dirac charge carrier distribution (blue ellipse) is excited into an far-from-equilibrium distribution (red ellipse). Coupling with the phonon system (green ellipse) and e-e scattering processes develop the far-from-equilibrium charge carrier distribution into a Fermi-Dirac distribution with increased temperature (yellow ellipse). Then the phonon and electron system equilibrate their temperatures through e-ph coupling. The far-from-equilibrium e-ph scattering is investigated with trARPES in a pump-probe scheme. In trARPES, optical IR femtosecond pulses pump the charge carriers in graphene to far-from-equilibrium distributions. With XUV probe pulses, we analyze the many-body response via MDC linewidth evaluation from ARPES spectra.

from the 2D ARPES spectra with the Lucy-Richardson-deconvolution (LRD)<sup>125,126,63,127</sup>. As shown in chapter 4, the LRD allows us to circumvent the RAs. In addition, the theoretical framework developed for many-body interactions in static experiments can fail<sup>146,147</sup> under NEQ conditions, which may require a more complex time-resolved NEQ formalism<sup>148</sup>.

This work aims to shed light on the many-body-response in the sub 100 fs regime with trARPES. Therefore, we investigate the many-body response through the self-energy extracted from trARPES. To achieve far-from-equilibrium conditions, we excite the charge carrier system in the prototypical 2D Dirac system graphene<sup>85</sup> with a femtosecond IR pulse. After such an excitation, the charge carrier distribution will be in far-from-equilibrium conditions (see Fig. 5.1 red ellipse) and then transition towards NEQ (see Fig. 5.1 yellow ellipse). We distinguish between far-from-equilibrium and NEQ conditions in the system.

- Under **NEQ** conditions, the distributions of charge carriers and phonons are described by Fermi-Dirac distributions and Bose-Einstein distributions, respectively. However, the temperatures for these distributions differ, i.e., the subsystems are in NEQ (see Fig. 5.1 yellow ellipse).
- Under **far-from-equilibrium** conditions, the phonon and charge carrier system are also NEQ to each other. In addition, however, the charge carrier system is not distributed according to a Fermi-Dirac distribution (see Fig. 5.1 red ellipse). Furthermore, the phonon system might also not be in a Bose-Einstein distribution. Such far-from-equilibrium carrier distributions have been observed in a number of experiments in various systems<sup>53,149,150,59,151–154</sup>.

In our experiment, in the far-from-equilibrium state, we find a strong modification of the quasiparticle self-energy. Therefore, we emphasize that our work shows such a modification of the self-energy under far-from-equilibrium conditions with MDC linewidth analysis in trARPES in graphene. We divide this strong response into an overall broadening and a series of spectrally localized features. We can attribute the localized features to a coupling between electrons and optical phonons on timescales well below 100 fs. Furthermore, we assign the general broadening to a general opening of phase space for e-e many-body effects under far-from-equilibrium conditions.

The following chapters will be structured as follows. First, I discuss the literature on quasiparticle dynamics in n-doped graphene and present the different contributions to the self-energy. Then, I discuss the literature on trARPES in graphene, where I will focus on the thermalization processes after femtosecond pulse excitation. Thereafter, I present our static

ARPES data and trARPES on graphene. First, I will compare the 70 meV energy-resolution static data to the existing literature. There, I will shortly motivate why I need to apply the deconvolution algorithm to our XUV trARPES data during that comparison. Then, I will show the many-body response of the self-energy measured with trARPES in far-from-equilibrium conditions. The deconvolution process itself and its benchmarking are discussed in a separate methods chapter (see chapter 4).

## 5.2 Review on Quasiparticle Dynamics in Doped Graphene/SiC with Static ARPES

Many-body interactions in doped graphene renormalize the spectral function. This has been studied in detail experimentally<sup>39,141,142,155</sup> and theoretically<sup>156–162</sup>. Bostwick et. al.<sup>39,141,142</sup> investigate the quasiparticle dynamics with ARPES (Fig. 5.2 and 5.3). They use increasing potassium doping to manipulate the electron density, i.e. to shift Dirac energy  $E_D$  away from Fermi Energy  $E_F$ . Such a shift manipulates the quasiparticle dynamics. Moreover, these changes in the quasiparticle dynamics give more insights into their origins. (Fig. 5.2 and 5.3 will be not explained in all detail at this point. Instead, we will use these figures to clarify several points in the ensuing chapters.)

The bands in the ARPES spectra in Fig. 5.2 clearly deviate from the expected linear quasi-relativistic Dirac-dispersion (chapter 2.2) around the Dirac point. The band's Fermi velocity increases close to the Dirac point. This increase leads to a kink-like structure (see Fig. 5.2 (e-h) light blue arrow at  $E_D$ ) in the band dispersion. This kink becomes more pronounced with higher doping concentrations and is fixed to the shifting  $E_D$ . This kink is related to electron plasmon (e-pl) many-body interactions<sup>39,142</sup>. In later publications, Bostwick et al.<sup>164,165</sup> are even able to resolve a finer satellite structure in freestanding graphene, which they attribute to a plasmaron quasiparticle. However, the attribution as plasmaron satellites is still under debate<sup>166</sup>.

Secondly and much less noticeable, Bostwick et al. identified a phonon kink that spans to about 200 meV below the Fermi energy. The kink's position and extend with respect to the Fermi energy is independent of the doping concentration (yellow arrow Fig. 5.2 (e-h) with  $\hbar\omega_p$ ).

To investigate the quasiparticle dynamics more thoroughly, Bostwick et al. extracted the MDC FWHM (which is proportional to the imaginary part of the self-energy). They plotted the FWHM vs. energy for several doping concentrations (see 5.3, increasing doping bottom to to

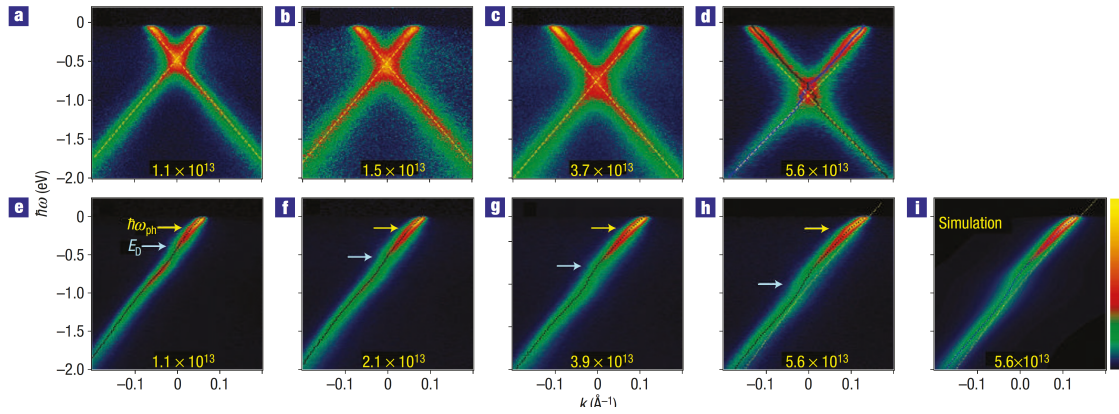


FIGURE 5.2. Experimental ARPES spectra of graphene for increasing potassium doping. (a-d) 2D ARPES spectra of the Dirac state along the  $\Gamma$ -K direction with increasing doping left to the right (yellow number, given in  $\text{cm}^{-2}$ ). Dashed lines mark a linear continuation of the bands from below  $E_D$ ; these lines do not describe the upper bands hinting at band renormalizations due to many-body interactions. (e-h) 2D ARPES spectra of the Dirac state perpendicular to the  $\Gamma$ -K direction. One Dirac arm is not visible due to the dark-corridor effect<sup>163</sup>. The band dispersion has been extracted with an MDC Lorentz fit evaluation (black dotted lines). The extracted dispersions deviate from a linear band. These deviations are the band renormalization introduced by the  $\text{Re}\Sigma$ . There are two kinks in the dispersions. One is at 200 meV (yellow arrow) for all dopings, and the other is fixed to the downwards shifting  $E_D$  (light blue arrow). The first is related to e-ph scattering, and the second is related to e-pl scattering. There are also variations in the FWHM, which are proportional to  $\text{Im}\Sigma$ . (i) The ARPES spectrum has been simulated in a self-consistent way from the bare band structure (yellow dotted line h and i), and the  $\text{Im}\Sigma$  extracted from (h). The close resemblance of the ARPES spectra (h) and (i) shows that many-body interactions can explain the observed kinks in the self-consistent quasiparticle picture. Figure adapted and reprinted from Ref. <sup>142</sup>. © Elsevier 2022.

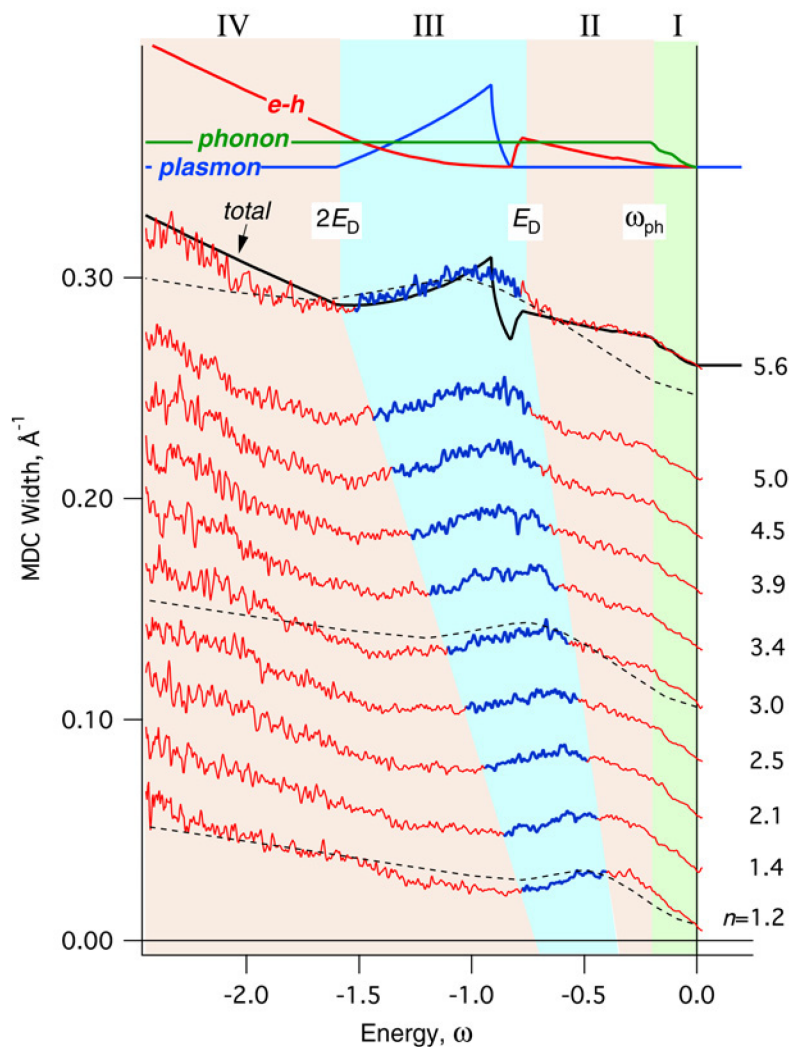


FIGURE 5.3. FWHM widths ( $\propto \text{Im}\Sigma$ ), extracted from MDC ARPES profiles in graphene for different potassium doping. The FWHM has been extracted from a Lorentz fit evaluation from ARPES spectra for increasing (bottom to top) doping concentration [ $1/\text{cm}^2$ ]. Each profile is offset by  $0.025 \text{ \AA}^{-1}$  from the previous. For  $n = 5.6 \text{ cm}^{-2}$ , Bostwick et al. plotted the total  $\text{Im}\Sigma$  from their scattering model (black line). At the top, their model is divided into the contributions due to e-ph scattering (green line), e-pl scattering (blue line), and e-h scattering (red line). (I - IV) mark regions where one of the interactions dominates the behavior of the total  $\text{Im}\Sigma$ . The dashed black lines ( $n = [1.2 \text{ } 3 \text{ } 5.6] \text{ cm}^{-2}$ ) represent the results of  $4 \times \text{Im}\Sigma$  from  $G_0W$  calculations from Ref. <sup>162</sup>. The multiplication accounts for different substrates between these calculations and the results presented by Bostwick et al.. Figure adapted and reprinted from Ref. <sup>142</sup>. © Elsevier 2022.

top). Bostwick et al. also introduced models to distinguish the different sources of many-body interactions. They introduce three main interactions (see figure 5.4) that contribute to the quasiparticle lifetime. These three channels represent other quasiparticles, with which the photoholes (yellow spheres in Fig. 5.4) can scatter with the many-body system.

- (a) Scattering via absorption or emission of optical phonons (e-ph interactions).
- (b) Scattering through the spontaneous generation of an electron-hole pair. (e-h interactions).
- (c) Scattering via absorption or emission of low energy plasmons (e-pl interactions).

The contribution of defect scattering is negligible and below the resolution of the used detector.

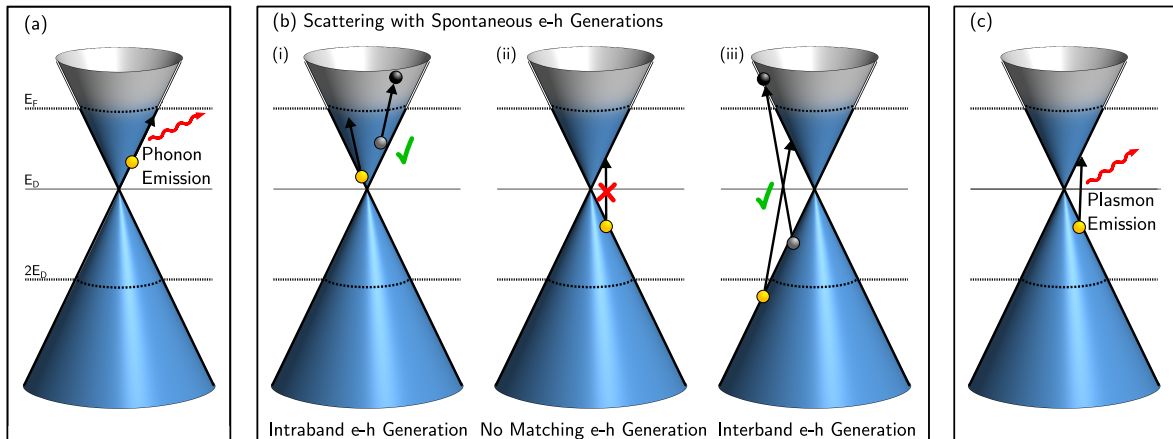


FIGURE 5.4. Scattering channels for photoholes (yellow spheres) in the Dirac cone for doped graphene. (a) Scattering of the photohole towards  $E_F$  due to phonon emission. (b) Scattering of the photohole due to the spontaneous generation of an electron-hole pair (black and grey spheres). (i) A photohole between  $E_F$  and  $E_D$  can scatter towards the Fermi energy by intraband e-h excitation. (ii) A photohole below  $E_F$  and above  $2E_D$  has to scatter with an energy-momentum vector with a small momentum component, i.e., a rather vertical energy-momentum vector in this Fig. Close to  $E_F$  there are no e-h pair generations with a matching vertical energy-momentum vector available. Thus the photohole is unlikely to scatter via an e-h pair generation below  $E_F$  and above  $2E_D$ . (iii) A photohole below the  $2E_D$  can generate interband e-h excitation. (c) Scattering of the photohole towards  $E_F$  due to plasmon emission.

In the following chapters, I first discuss the e-ph contributions to the quasiparticle dynamics. After that, I review the e-h and e-pl contributions to the quasiparticle dynamics together, and in the end, I discuss the plasmaron shortly.

### 5.2.1 Electron-Phonon Coupling

Now we discuss the quasiparticle dynamics caused by e-ph interaction. A photohole left in the photoemission process can lose its energy and decay towards the Fermi edge through the emission of a phonon. The process is depicted in Fig. 5.4 (a).

There is extensive literature on e-ph quasiparticle dynamics in ARPES in Refs. <sup>39,141,142,155–161</sup> for doped graphene. Bostwick et al. <sup>39,141</sup> discuss a model (see Fig. 5.3 topmost green line) where  $\text{Im}\Sigma$  is constant for all energies except in a window below the Fermi energy. The abrupt changes of the self-energy around the Fermi energy are a common feature in band renormalizations caused by the absence of electron-phonon scattering due to phase space constraints in many materials<sup>9</sup>. In Fig. 5.5 (a), the band renormalization of the linear bare band is sketched exaggeratedly. Such features in ARPES are commonly referred to as phonon kinks<sup>9</sup>.

First, we determine the phonon modes that can interact with electrons. Only optical phonon modes can couple effectively to electrons<sup>157</sup>. In Fig. 5.5 (b), we see an arbitrary momentum map for graphene and in (d) we see the phonon band structure. For phonon emission/absorption to take place, energy and momentum have to be conserved. For that reason only specific phonon modes are permitted in e-ph coupling. The  $E_{2g}$  phonon mode facilitates intravalley scattering of photoholes and the  $A_1$  phonon mode intervalley scattering<sup>155,160</sup> (see red arrows in Fig. 5.5 (b)). To quantify the interaction further, the Eliashberg coupling function  $\alpha^2 F(\omega)$  can be calculated (see Fig. 5.5 (c)). This function is a measure of how strong phonons can interact with the photohole depending on the phonon energy<sup>9</sup>. In Fig. 5.5 (d) the coupling strength  $\lambda_{q\nu}$  has also been color coded unto the phonon band structure.  $\lambda_{q\nu}$  is a measure of how strong each phonon mode contributes to Eliashberg function. Only

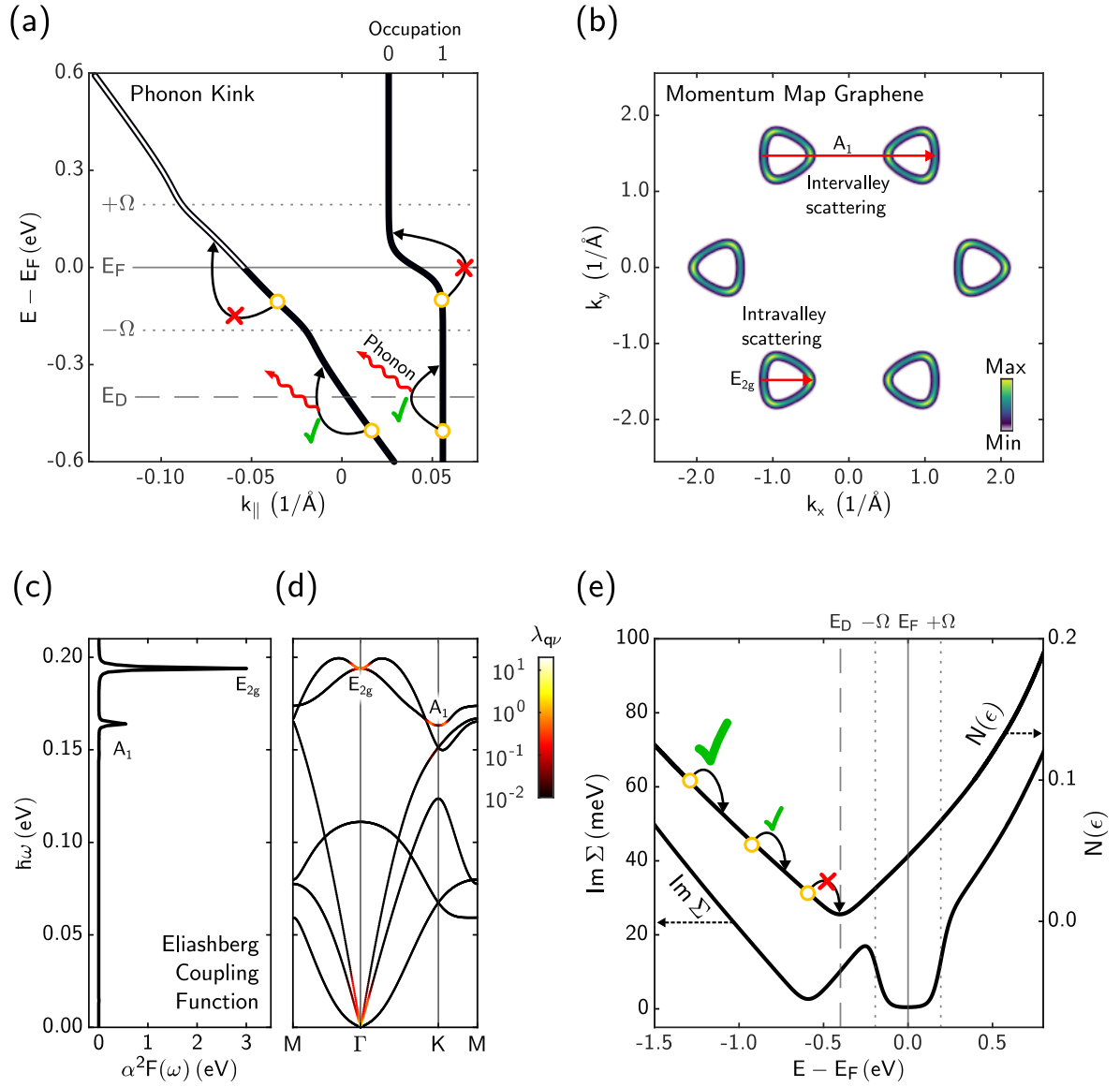


FIGURE 5.5. Electron-phonon contributions to the self-energy. (a) Exaggerated phonon kink (left curve) and Fermi-Dirac distribution (right curve). Empty yellow circles with arrows signify the allowed (green checkmark) and forbidden (red cross) e-ph scattering processes. (b) Momentum map of graphene. The red arrows indicate which phonon modes contribute to e-ph intra- and intervalley scattering processes. (c) Eliashberg coupling function for doped graphene with  $E_D = -400$  meV. (d) Phonon band structure. The e-ph coupling strength  $\lambda_{qv}$  is color-coded unto phonon band structure (e)  $\text{Im}\Sigma$  according to equation 5.2 with the density of states. The greater size of the green checkmarks signifies a greater likelihood of the process at that energy. Dr. Dino Novko calculated the Eliashberg coupling function and the DOS shown here.

the dominant  $E_{2g}$  phonon mode with a energy  $\Omega = \hbar\omega = 196$  meV and the  $A_1$  mode at  $\hbar\omega = 164$  meV interact effectively with the photohole.

With this base, we can understand the phonon kink (see Fig. 5.5 (a)). A photohole (empty yellow circle) has to lose(gain) either the  $E_{2g}$  or the  $A_1$  phonon energy when it emits(absorbs) a phonon. Furthermore, there has to be an electron exactly at this phonon energy above the photohole to fill the photohole, i.e., there has to be available phase space. So if the energetic distance to the Fermi energy of the photohole is:

- $E - E_F > \Omega$  the second condition is always fulfilled, and the photohole can scatter with a phonon.
- $E - E_F < \Omega$  there is no phase space available. Thus, the photohole is forbidden from scattering with a phonon. Thus the  $\text{Im}\Sigma$  decreases, and the quasiparticle lifetime increases.

For a photocarrier above the Fermi energy, similar arguments can be applied. Thus we see the phonon kink in a window of one phonon energy  $\Omega$  around the Fermi energy (see Refs. [39,141,157,9](#) for example).

Besides the phonon kink, there is more structure in  $\text{Im}\Sigma$  from e-ph coupling. Bostwick et al. [39,141,142](#) use a model based on the equation

$$\text{Im}\Sigma(\epsilon) = \pi \int_0^\infty d\omega \alpha^2 F(\omega) \times [1 - f(\epsilon - \omega) + f(\epsilon + \omega) + 2n(\omega)] \quad (5.1)$$

from Refs. [167,168](#). Here,  $f$  is the Fermi-Dirac-distribution for the charge carrier system,  $n$  is the Bose-Einstein distribution for the phonon system,  $\omega$  is the phonon energy, and  $\epsilon$  is the photohole energy. This equation counts all the possible phonon absorptions and emissions for a photohole with the energy  $\epsilon$ . Bostwick et al. [39,142,141](#) approximated the Eliashberg function with the phonon-density-of-states at the energies of the  $E_{2g}$  and  $A_1$  phonon. With this approximation, they predicted the phonon kink correctly. However, this equation doesn't consider electron-density of states (ELDOS)  $N$ . As we saw above the scattering rate of a photohole, i.e., the inverse of the  $\text{Im}\Sigma$ , with the optical phonon depends on the available phase, i.e., whether there are occupied electron states one phonon energy above the photohole's

energy. Furthermore, the available number of these states is described by  $N$ , so the form of  $N$  should also influence the  $\text{Im}\Sigma$ . To include  $N$ , we use the following equation from Refs. <sup>167,169</sup>

$$\text{Im}\Sigma(\epsilon) = \pi \int_0^\infty d\omega \alpha^2 F(\omega) \left( \frac{\bar{N}(\epsilon - \omega)}{N(0)} [n(\omega) + 1 - f(\epsilon - \omega)] \dots \right. \\ \left. + \frac{\bar{N}(\epsilon + \omega)}{N(0)} [n(\omega) + f(\epsilon + \omega)] \right). \quad (5.2)$$

In a collaboration with us, Dr. Dino Novko calculated the Eliashberg coupling function  $\alpha^2 F(\omega)$  and the ELDOS  $N$  (see Fig. 5.5). With that we can calculate the  $\text{Im}(\Sigma)$  (see Fig. 5.5 (e)). Here we notice additional features. The  $\text{Im}(\Sigma)$  has a minimum one  $\Omega$  below the ELDOS, or else the ELDOS is imprinted onto the  $\text{Im}(\Sigma)$  but shifted down by  $\Omega$ . This structure can be also understood in terms of available phase space. For example, a photohole  $\Omega$  below the Dirac point is unlikely to emit a phonon since the ELDOS at the Dirac point goes to zero (see Fig. 5.5 (e) red cross). However, away from  $E_D$ , the ELDOS increases linearly; thus, the phase space increases thus  $\text{Im}\Sigma$  increases (see Fig. 5.5 (e) green check marks).

A detailed derivation of the equation 5.2 can be found in the supplement in our publication [1]. It is based on the Fan-Migdal approximation<sup>170,171</sup>, where the renormalization is assumed to be small and the Eliashberg coupling function is averaged over the Fermi surface<sup>170</sup>. Despite these assumptions the pure Fan-Migdal approximation and equation 5.2 produce the same results (see supplement of our publication [1] Fig. S5.2 (c) green vs. blue line). Furthermore in the standard density functional perturbation theory the Coulomb screening of the electron-phonon matrix elements is static (adiabatic), i.e the electron-phonon coupling matrix element is always screened by the dielectric function  $\epsilon(\mathbf{q}, \omega = 0)$ <sup>172,171</sup>. In graphene, this assumption is not adequate to describe photoemission data<sup>155</sup>. The relevant phonon energies are greater than 150 meV where  $\epsilon(\mathbf{q}, \omega = 0) \neq \epsilon(\mathbf{q}, \omega = \omega_{\text{ph}})$ . So these non adiabatic dynamical screening effects and in addition the substrate screening have to be accounted for. With these effect the resulting Eliashberg Coupling function changes, namely the coupling to the  $E_{2g}$  mode is enhanced<sup>173,174</sup> (see supplement of our publication<sup>1</sup> Fig. S5.2 (b) or Fig. 5.5 (c)).

## 5.2.2 Electron-Hole and Electron-Plasmon Coupling

In Fig. 5.4 (b), the possible decay mechanisms for the photohole through spontaneous e-h generation are shown. In this process, the photohole can scatter towards the Fermi energy by creating a new e-h pair. For this process to occur, energy and momentum conservation must be full-filled, and there must be available phase space for the e-h excitation.

With this in mind, we can divide the energy range into three areas<sup>39</sup> (Fig. 5.4 (b)). In the first area between the Fermi energy and the Dirac point (compare region II in Fig. 5.3), the photohole can mainly decay by scattering with intraband e-h generations. In this region, the data can be described by  $\text{Im}\Sigma = \omega^\alpha \ln(\omega)$  (see Region II in Fig. 5.3). This region becomes larger for higher doping concentrations. Thus, the  $\omega^\alpha \ln(\omega)$  behavior becomes more discernible for higher doping concentrations. Hodges et al.<sup>175</sup> derived the  $\omega^\alpha \ln(\omega)$  dependence for 2D metals where  $\alpha = 2$ . They integrated over the phase space for all allowed e-h scattering processes. Bostwick et al. expanded this to a conical band structure and showed  $\alpha \approx 1.5$  for graphene in this region.

In the next region  $E_D < \omega < 2E_D$  (region III in Fig. 5.3)  $\text{Im}\Sigma$  drops abruptly and only starts to rise again close to  $2E_D$ . Photohole decay in this region requires an energy-momentum vector with a small momentum component, i.e., a vertical energy-momentum vector. However, there are no e-h excitations around the Fermi energy with matching vertical energy-momentum vectors. Thus a photohole can not scatter with e-h excitations in the region  $E_D < \omega < 2E_D$ .

In the third region where  $\omega > 2E_D$  (region IV in Fig. 5.3), more interband e-h processes become viable producing the increase in  $\text{Im}\Sigma$  once again according to the  $\omega^\alpha \ln(\omega)$  dependence from Ref. <sup>175</sup>.

In the region close to the Dirac point, plasmon emission dominates the photohole decay. To describe the plasmon contribution to the  $\text{Im}\Sigma$ , Bostwick et al.<sup>39</sup> introduced a scattering model. The ordinary plasmon dispersion in 2D is<sup>95</sup>

$$\omega_{pl}(q) = \sqrt{4\pi m e^2 q / n(1 + \epsilon)}. \quad (5.3)$$

In the equation the rest-mass  $m$  will be replaced by the relativistic mass  $m_r = E_D/v_F$  and further adjusted according to the experimental carrier masses<sup>82,176</sup>. The dielectric constant is set  $\epsilon = 10$ <sup>39</sup>. Fig. 5.6 shows the plasmon dispersion together with the spectrum of allowed spontaneous e-h excitations. Plasmons exist in principle from  $0 < q < \infty$  but above a critical  $q_c$  when the plasmon dispersion overlaps with the e-h excitation spectrum, plasmons will decay into electron-hole pairs (Landau damping). So the plasmon scattering can only contribute to  $\text{Im}\Sigma$  outside the spectrum of allowed e-h excitations in Fig. 5.6.

The remaining plasmon modes have predominantly vertical energy-momentum vectors. Furthermore, the e-pl scattering process must conserve energy and momentum. Thus, e-pl scattering processes are only possible for photoholes near the Dirac point. Visually this is shown in Fig. 5.6, where the red arrow is an exemplary plasmon. Now with these assumptions,

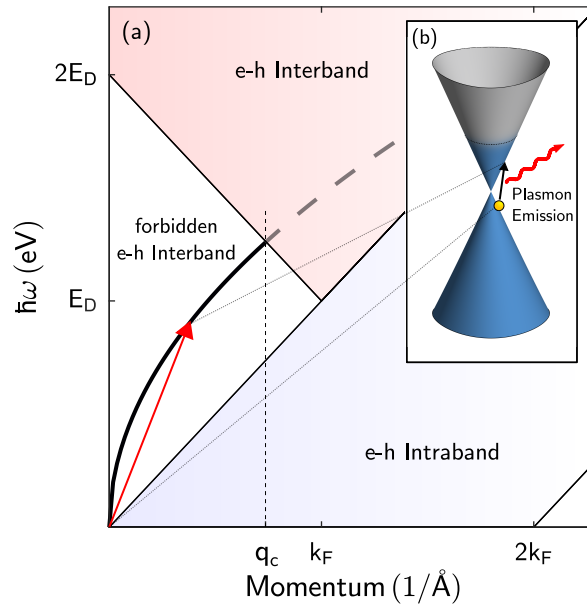


FIGURE 5.6. Plasmon scattering of photoholes. (a) Plasmon dispersion overlaid onto the spectrum of allowed spontaneous e-h excitations. The dielectric constant is  $\epsilon = 10$  as in Ref. <sup>39</sup>. (b) An exemplary photohole near the Dirac point (empty blue circle) scatters with a plasmon. The red arrow in (a) shows the plasmon that can be involved in this process.

Bostwick et al. sum up the plasmon decays for each energy and plot the plasmon contribution to  $\text{Im}\Sigma$  in Region III in Fig. 5.3 (blue line). Again, the plasmon interactions contribute only close to the Dirac energy. Therefore e-plasmon interactions lead to a distinct increase in the  $\text{Im}\Sigma$  around the Dirac point (see Fig. 5.3 Region III). Furthermore, this increase is bound to the Dirac point and shifts doping concentration since the Dirac point shifts (see Fig. 5.3 Region III).

Usually, the low-energy e-pl coupling is forbidden in 2D and 3D electron gases. \* In such metals, plasmons only play a role at energies  $\approx 20 \text{ eV}$ <sup>181</sup>. However, in graphene, low-energy plasmons are possible due to the quasi-relativistic band structure of graphene. Low-energy plasmons are thus a special property of Dirac materials.

These considerations discussed above were published by Bostwick et al. in Ref. <sup>39</sup>. After this initial publication, Hwang. et al.<sup>162</sup> performed more sophisticated  $G_0W$  calculations, where e-pl and e-h contribution are treated together for doped graphene on SiO. These calculations

\*In 2D materials, non-trivial kinematic constraint prevents electrons with low excess energy from coupling to plasmons<sup>177-180</sup>. In 3D materials, only electrons above the critical plasma energy can transfer their energy to the plasmons since the plasmon spectrum is nondispersive<sup>36,179,180</sup>.

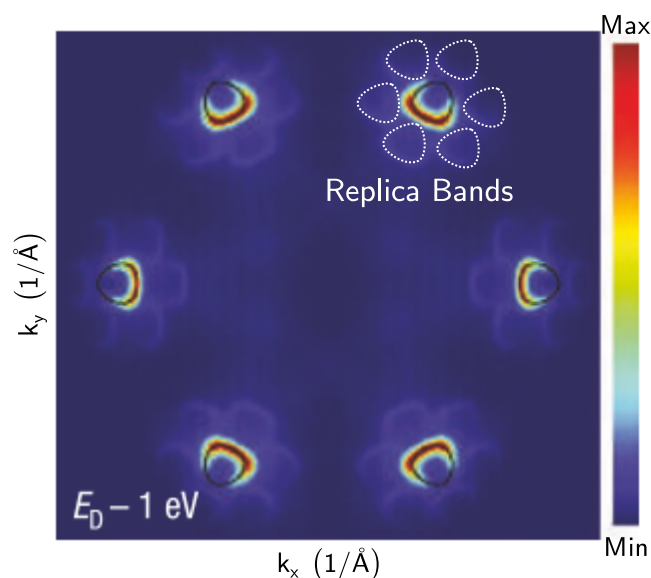


FIGURE 5.7. ARPES momentum map of doped graphene. The dashed white lines indicate the replica bands. The black lines indicate the main bands. Figure adapted and reprinted from Ref. <sup>39</sup>. © 2022 Springer Nature.

are qualitatively in agreement with the results from Bostwick et al.<sup>39</sup>, and they also support the existence of the low-energy e-pl scattering peak. In a later publication Bostwick et al. compared their data with these calculations<sup>142</sup> (see Fig. 5.3 three dashed lines).

A different explanation for the plasmon features around  $E_D$  (see Fig. 5.2 (e-h) light blue arrow at  $E_D$ ) was introduced by the groups of Lanzara and Rollings<sup>182,183</sup>. They argue that the feature is an energy-gap from symmetry breaking induced by a  $6\sqrt{3} \times 6\sqrt{3}$  superlattice potential created by the first substrate graphene layer. They ascribe the replica bands observed in ARPES (Fig. 5.7) to this effect. However, in Ref. <sup>141</sup>, Bostwick et al. lay out a convincing list of arguments against this case. The most striking argument is that if the superlattice potential induces the replica bands, there should be band gaps where the replica bands and the main bands cross. These band gaps are not observed in the ARPES data. Instead, Bostwick et al. assign the replica to interference effects between outgoing photoelectrons. Some of the outgoing photoelectrons can scatter with the first substrate layer, and thus replica bands have the  $6\sqrt{3} \times 6\sqrt{3}$  geometry.

### 5.2.3 Plasmaron

In later publications, Bostwick et al.<sup>164,165</sup> were able to resolve a fine structure of satellite bands around the Dirac point (see Fig. 5.8) in free-standing graphene samples. Such satellite bands are beyond the quasiparticle picture. Instead, these satellites arise in a more complete description of the spectral function, namely the incoherent parts of the spectral function<sup>10</sup>. In this case, the Dirac cone splits into four bands and takes a diamond-like shape close to the Dirac point ((see Fig. 5.8) (b) and (h)). The lower bands are assigned to the formation of a composite quasiparticle between a plasmon and a hole, the so-called plasmaron. The strength of these sidebands depends on the screening of the substrate. In their work, Bostwick et al. used a novel preparation method detailed in Ref. <sup>184</sup> to produce quasi freestanding graphene with low screening. Furthermore, the separation of the sidebands rises with the doping level of the sample. They note that in the samples in their previous works<sup>39,142</sup> these sidebands can only occur as weak shoulders in the MDC cuts due to the higher screening. Despite these works, the assignment of these satellites to plasmarons is still under debate<sup>166</sup>.

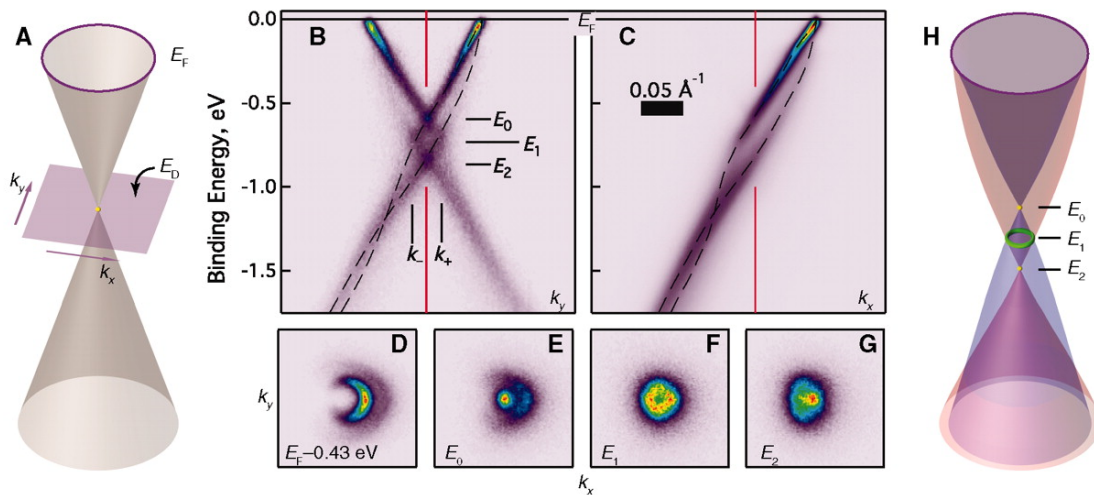


FIGURE 5.8. A) Schematic Dirac cone in the non-interacting single-particle picture. B) ARPES spectrum along the  $\Gamma - K$  direction. C) ARPES spectrum perpendicular to the  $\Gamma - K$  direction. The red lines mark the K-Point. The dashed lines indicate the hole and the plasmaron band dispersions. D-G) ARPES momentum maps at different binding energies. H) Schematic Dirac-spectrum with plasmaron satellite bands. Figure adapted and reprinted from Ref. <sup>164</sup>. Reprinted with permission from AAAS.

### 5.3 Review on Ultrafast Population Dynamics in Graphene

This chapter will review the literature on the population dynamics after optical pump excitation. Graphene, other Dirac materials and stacked 2D materials provide an excellent platform for conducting trARPES experiments. The appearance of Dirac cones associated with Dirac physics provides many exciting phenomena. For example, in graphene/Ir(111), a super periodic moiré potential creates Dirac cone replicas with mini gaps at the band crossings<sup>185</sup>. Furthermore, twisted bilayer graphene can have flat bands<sup>186</sup>. The previous chapter discussed

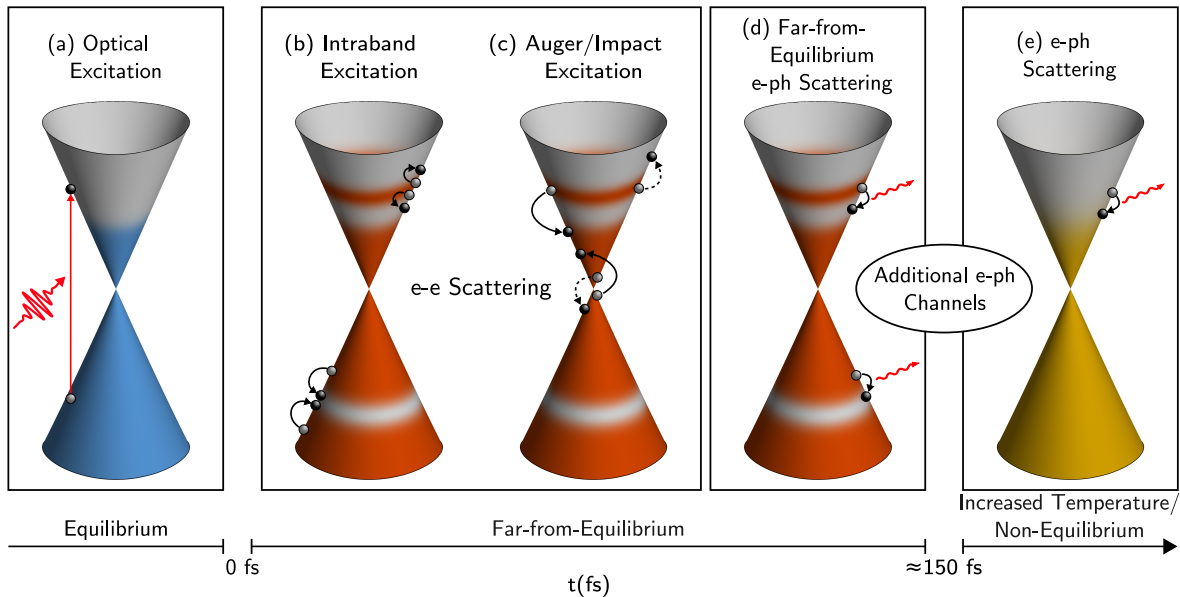


FIGURE 5.9. Thermalization processes in n-Doped graphene after ultrafast IR Excitation in the electron system (Dirac cones). (a) The system in equilibrium is excited with a femtosecond IR pulse. The distribution of charge carriers is imprinted in blue on the Dirac cone. Optical interband transitions create a far-from-equilibrium carrier distribution (red in (b-d)). The far-from-equilibrium carrier distribution will thermalize within  $\approx 150$  fs to a Fermi-Dirac distribution with increased temperature (yellow) in (e). The thermalization is mediated by e-e scattering processes (b-c) and far-from-equilibrium e-ph emission processes (d). An excited electron/hole thermalizes by e-e intraband scattering processes (b) or interband excitation processes (c). The dashed arrows show Auger interband scattering processes and the full arrows interband impact scattering processes. After the electron system has thermalized, it will equilibrate with the phonon system through e-ph emissions. The time until the electron system reaches a Fermi-Dirac distribution with increased temperature of  $\approx 150$  fs is estimated from our experiment for our sample and our excitation conditions (see chapter 5.5.2).

how doping could sensitively manipulate the many-body interactions in graphene<sup>39</sup>, and how low-energy plasmons can create plasmaron quasiparticles<sup>164</sup>. In many trARPES experiments, pump pulses optically excite graphene into dynamically evolving states, and then the XUV probe pulse monitors the subsequent changes in the electronic structure. Population dynamics extracted from trARPES spectra provide information about these changes. There are a number of experiments following this approach in Refs. <sup>18,24-31,19-23</sup>.

For this thesis, we now discuss the creation of far-from-equilibrium charge carrier distributions (see Fig. 5.1 red ellipse) and their subsequent thermalization in graphene and other Dirac materials. Such carrier distributions have been created and investigated in a number of works<sup>53,54,59,149-154,187,188</sup>, where ultrafast pump pulses ( $h\nu > 2E_D$ ) induced optical interband excitations. For our n-doped graphene sample, the thermalization process is sketched in Fig. 5.9 and has been divided into three timescales.

- (a) In equilibrium, the charge carriers are distributed according to a Fermi-Dirac distribution at RT. A high-intensity femtosecond IR pulse induces optical interband transitions to create a far-from-equilibrium distribution.
- (b-d) The far-from-equilibrium charge carrier distribution thermalizes within  $\approx 150$  fs back to a Fermi-Dirac distribution with increased temperature. This thermalization process is governed electron-electron scattering (b-c) and by electron-phonon scattering (d)
- (e) The electron system is distributed according to a Fermi-Dirac distribution with increased temperature. This temperature is higher than the phonon system's temperature, i.e., both systems are in NEQ with respect to each other. Thus the electron and phonon system equilibrate due to electron-phonon scattering processes.

In the following, we will focus on the thermalization of the far-from-equilibrium charge carrier distribution to a Fermi-Dirac distribution with increased temperature, i.e., (b-d). First, we will review the e-e and e-ph scattering processes that mediate this thermalization. Then we discuss how the interplay of these scattering processes governs the population dynamics.

### **Far-from-Equilibrium Electron-Electron Scattering.**

Electron-electron scattering processes partially mediate the thermalization of the far-from-

equilibrium charge carrier distribution. An interplay between intraband-, Auger- and impact scattering events lead to a momentum and energy redistribution in the electronic system<sup>53,59,147,149,151,153,187,191,192,190</sup>. These processes are mediated by the Coulomb force, which is screened to a short-range force in most materials by mobile charge carriers. However, graphene's two-dimensionality and vanishing density of states near the Dirac point reduce this screening. These two-electron processes can be divided depending on how they change the charge carrier distributions. First, for intraband scattering (see Fig. 5.10 (b)), the electrons stay within the same band. Furthermore, pseudospin conservation suppresses back-scattering

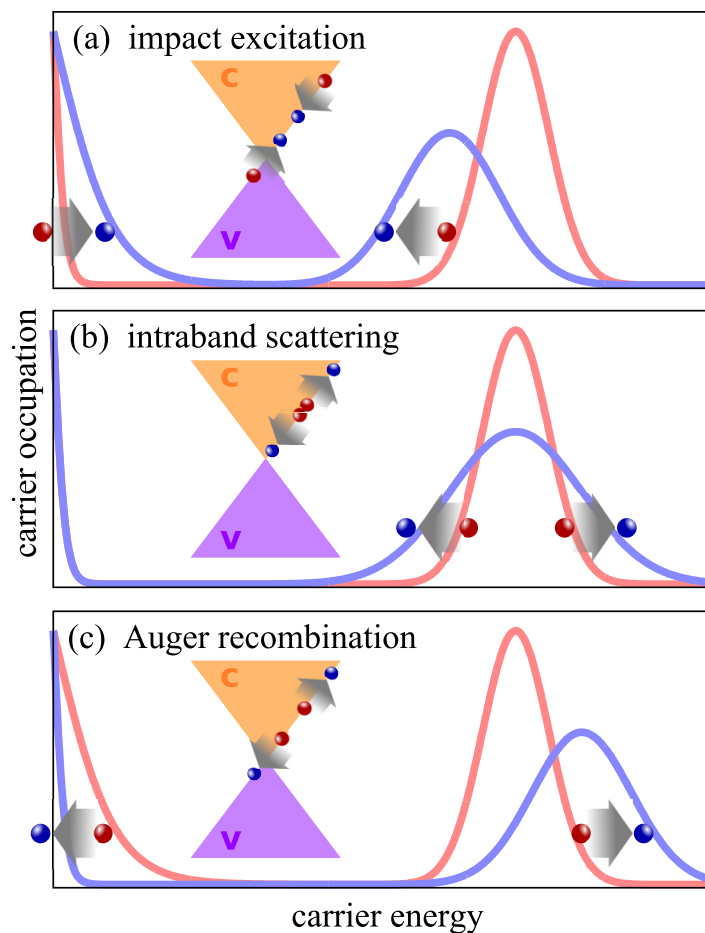


FIGURE 5.10. Change in a given charge carrier distribution in impact excitation (a), intraband scattering (b), and Auger recombination (c) scattering processes in a Dirac-Cone. The red line and spheres mark the charge carrier and distribution before the scattering event, whereas blue mark them after the event. Figure adapted and reprinted from Ref. <sup>189</sup>. © 2022 American Physical Society.

processes. These processes will smear sharp features in a given distribution. Second, in inter-band scattering processes, electrons can scatter into different bands. In Auger recombination (see Fig. 5.10 (c)), the number of charge carriers in the valence decreases, and the average kinetic energy increases. For impact ionization (see Fig. 5.10 (a)), the number of charge carriers increases, and the average kinetic energy decreases. A more detailed description of these processes can be found in the thesis of Marius Keunecke in Ref. <sup>105</sup> and in the work of Malic et al. in Ref. <sup>193</sup>.

### Far-from-Equilibrium Electron-Phonon Scattering.

The electron system can only lose energy through the emission of phonons. Such processes take place on timescales with far-from-equilibrium charge carrier distributions and on timescales with Fermi-Dirac distributions with increased temperature. In Ref. <sup>195</sup>, it is predicted that e-ph processes can transfer up to 90 percent of the energy, injected by the laser pulse into the electron system, into the phonon system even before the electron system equilibrates in simple metals. On far-from-equilibrium timescales in graphene, this process is mediated by

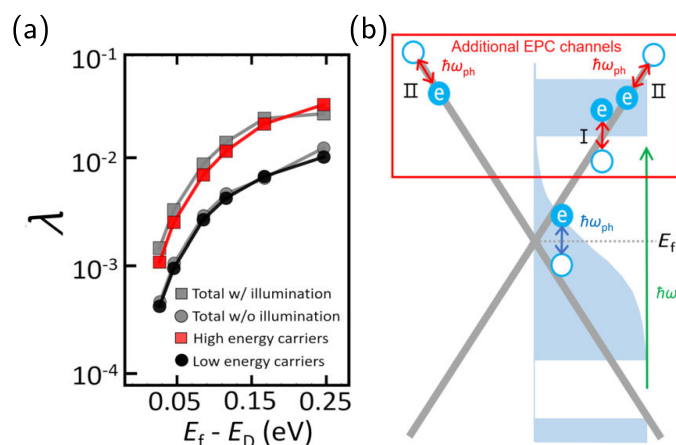


FIGURE 5.11. (a) Contributions to the e-ph coupling strength ( $\lambda$ ) by low and high energy carriers as a function of doping with and without laser illumination. (b) Sketch of e-ph Coupling Channels under far-from-equilibrium Charge Carrier Distributions. Deep blue arrows mark the charge carrier decay processes mediated by e-ph coupling in equilibrium. The green arrow indicates the photoexcitation, and the far-from-equilibrium distribution is shaded light blue. The red rectangle signifies the area where the far-from-equilibrium distribution facilitates additional e-ph processes (red arrows). Figure adapted and reprinted from Ref. <sup>194</sup>. Used under Creative Commons CC BY license.

the same optical  $E_{2g}$  and  $A_1$  phonon modes that we discussed in section 5.2.1 in the context of the equilibrium e-ph quasiparticle dynamics. However, the vastly different charge carrier distribution can influence and even enhance the strength of e-ph coupling under NEQ conditions. For example, Hu et al.<sup>194</sup> theoretically show that the e-ph coupling can be enhanced with the far-from-equilibrium charge carrier distribution and with the Fermi-Dirac distribution with increased temperature. This enhancement is caused by the additional e-ph channels that open up due to photo excited charge carriers and thermally excited charge carriers (see Fig. 5.11). Pomarico et al.<sup>140</sup> even demonstrated such an enhancement experimentally in bilayer graphene in the regime where the electron system has a Fermi-Dirac charge carrier distribution with increased temperature and the phonon system temperature is in NEQ with the electron system temperature. Furthermore, in that work, they demonstrated this effect independently with trARPES and ultrafast terahertz time-domain spectroscopy.

### **Interplay between Electron-Electron and Electron-Phonon Processes.**

The interplay between e-e and e-ph scattering processes governs the population dynamics. This interplay is influenced by the properties of the graphene or Dirac material samples and the excitation conditions. Therefore the timescales of the thermalization process can vary a lot.<sup>53,59,149,151,153,196</sup> Johannsen et al.<sup>196</sup> investigated the tunability of the population dynamics of graphene with p- and n-doped samples (see Fig. 5.12). They showed that the doping concentrations manipulate the phase space for different e-e and e-ph processes. Therefore the population dynamics have vastly different time scales depending on the doping concentration. Other studies investigated these effects in even more detail. For example, in Ref. <sup>153</sup>, the use of hole-doped-graphene leads to a bottleneck effect at the Dirac point of the unoccupied Dirac cone. The e-ph coupling is suppressed due to bottleneck effect until e-e processes have thermalized the charge carrier distribution. After this step, the charge carrier distribution will have a temperature of several thousand degrees Celsius. Only on larger timescales e-ph coupling reduces the temperature and thus the total energy of the charge carrier system. On the other hand, in HOPG, G. Rohde et al.<sup>154</sup> measured the ultrafast thermalization of an far-from-equilibrium charge carrier distribution into a Fermi-Dirac distribution with increased

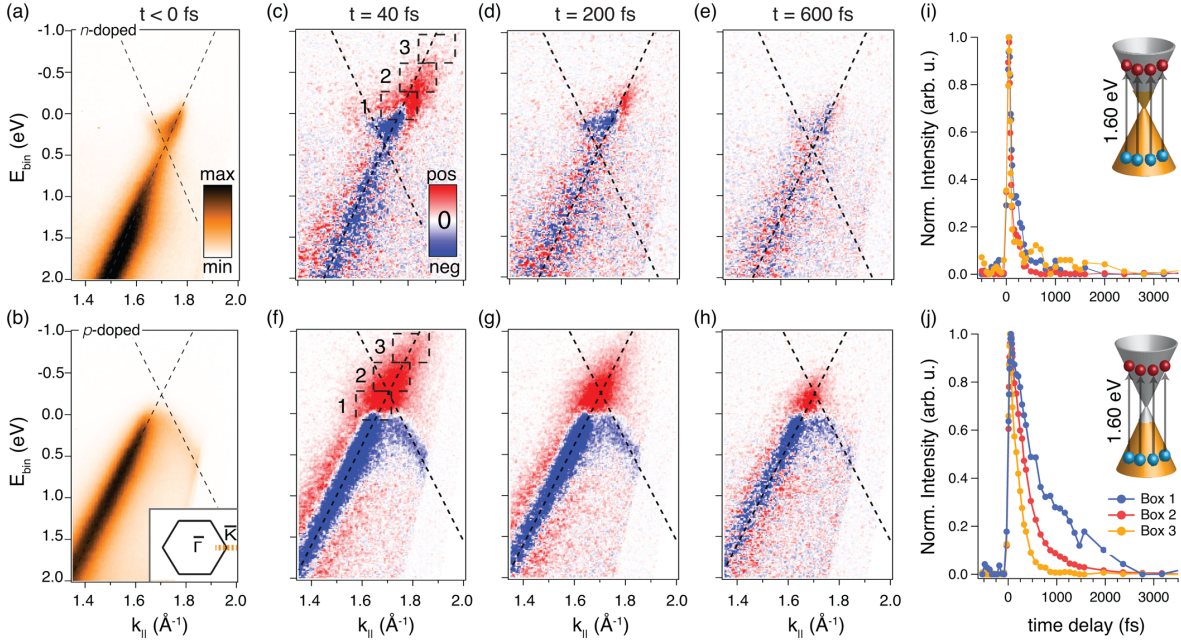


FIGURE 5.12. Comparison of the relaxation dynamics in n- and p-doped graphene after optical laser excitation monitored with trARPES. (a-b) ARPES spectra of p- and n- doped graphene before the arrival of the pump pulse. (c-h) trARPES difference map at different pump-probe delays for both samples. (i-j) Integrated ARPES intensity from three boxes in (c,f) vs. pump-probe delay. The excitation processes for both samples are sketched in the insets in (i-j). The n- and p- doped samples show population dynamics on widely different timescales. Figure adapted and reprinted from Ref. <sup>196</sup>. Used under terms of Creative Commons Attribution 4.0 International license

temperature on a time scale of  $\approx 50$  fs. The authors showed that e-ph coupling reduces the total energy in electron even on these timescales.

## 5.4 Quasiparticle Dynamics under Far-from-Equilibrium Conditions

This thesis aims to measure the many-body response in a regime where a Fermi-Dirac and Bose-Einstein distribution cannot describe electron and phonon distribution. In chapter 5.2 we saw how the self-energy could be extracted from equilibrium ARPES spectra with MDC line width analysis, and how the self-energy gives deep insights into the many-body interactions in graphene. In chapter 5.2, we saw how the  $\text{Im}\Sigma$  could be understood as the scattering rate for

a photohole created in the PES process. Thus, the inverse of  $\text{Im}\Sigma$  is the quasiparticle lifetime (see for example Ref. [10,39,141,142](#)). On the other hand, in trARPES experiments, in section 5.3, for trARPES, we discussed the population lifetime derived from population dynamics after femtosecond laser pulse excitation into NEQ or far-from-equilibrium conditions. Importantly, the population lifetime derived from trARPES and the quasiparticle lifetime derived from static ARPES are generally not the same quantity<sup>[55,147](#)</sup>. Nevertheless, in particular systems and/or under weak pump fluence conditions, these lifetimes might agree with each other<sup>[150](#)</sup>. In Ref. [147,190,197](#) Kemper et al., the role of the self-energy in the thermalization process after the pump is discussed. There, the authors illustrate that the self-energy, the charge carrier distribution, and the distributions of the other involved subsystems evolve dynamically

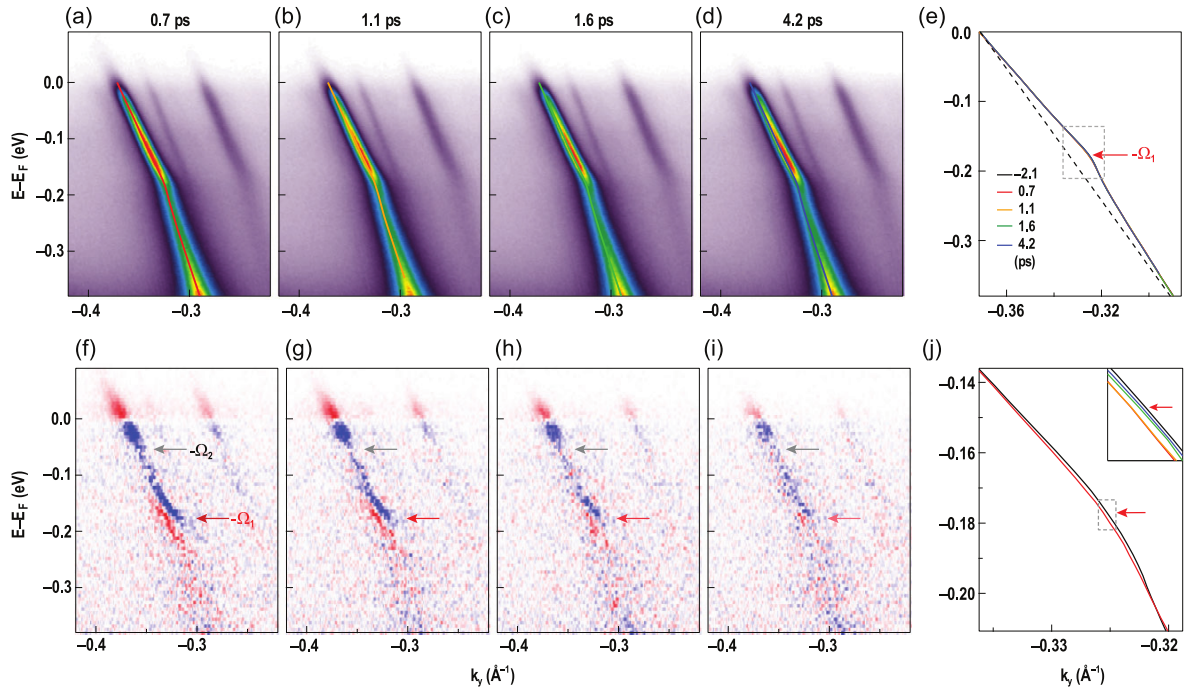


FIGURE 5.13. Self-energy dynamics in Kekulé -ordered graphene. (a-d) trARPES spectra of the phonon kink for several pump-probe delays. (f-i) Corresponding trARPES difference maps. (e) Band-dispersions extracted from the APRES spectra (a-d). The dashed line is the bare band structure. (j) shows the zoom into dispersion. The enlarged area is indicated with the dashed box in (e). In the insert, a further zoom-in is shown according to the enlarged dashed box in (j). Only then the small band renormalization is discernible. Figure adapted and reprinted from Ref. [68](#).

together. Hence, tracking the self-energy time-delay-dependent represents another valuable quantity for understanding the thermalization processes after femtosecond optical excitation.

At first, measuring the time-delay-dependent evolution of the self-energy in trARPES might seem straightforward. However, the self-energy from MDC linewidth analysis has rarely been extracted in trARPES despite many studies addressing the femto- to picosecond charge carrier dynamics<sup>53,54,51,150,154,187,188,198</sup>. Park et al. investigated the self-energy dynamics in Kekulé-ordered graphene (see Fig. 5.13). The phase for e-ph coupling is modified after femtosecond pump excitation. This modification of phase space changes the form of the phonon kink. Notably, the experiment has a time-resolution of 480 fs, and the observed dynamics are NEQ dynamics where the electron system distribution is a Fermi-Dirac distribution. Furthermore, the observed changes in the band dispersion are small. To investigate far-from-equilibrium self-energy dynamics, pulse lengths below 50 fs are required. Such pulses, however, introduce resolution broadening to ARPES spectra. Hence it is challenging to extract these small changes and thereby the self-energy. In the following chapters, we will present methods to overcome this challenge.

## 5.5 Experimental Results from ARPES and trARPES on Graphene

In the following chapters we present our static ARPES and trARPES data on graphene. First, we will compare the 70 meV energy-resolution static data to the existing literature. Then, we will discuss the far-from-equilibrium many-body quasiparticle dynamics measured with trARPES.

### 5.5.1 Quasiparticle Dynamics Analysed with Static ARPES

In this section, we measure the quasiparticle dynamics in thermal equilibrium in graphene at RT. First, we compare our 70 meV-resolution results with the literature. Then we motivate the need for the Lucy-Richardson deconvolution treatment on the trARPES data.

A graphene/SiC sample was provided by Dr. Klaus Pierz, Dr. Hans Werner Schumacher, and Dr. Davood Momeni<sup>199,200</sup>. This sample's quasiparticle dynamics are characterized by static ARPES measurements. In Fig. 5.14 we discuss the results in terms of ARPES spectra,  $\text{Re}\Sigma$  and  $\text{Im}\Sigma$ .

First, we compare our static 70 meV energy-resolution results taken with the narrow-bandwidth-XUV line to literature results from<sup>39,141,142</sup>, which were measured on similar samples (see Fig. 5.14 (a), (c-d) black and grey lines.). The ARPES spectrum shows only one arm of the Dirac cone. This suppression of photoemission intensity of the other arm is the so-called dark corridor effect<sup>163</sup>. The dark corridor is a final state interference effect of the photoemission process. The interference stems from the phase differences between photoelectrons from the two graphene sublattices. Next we inspect the dispersion of the Dirac band (Fig. 5.14 (a) black line). The dispersion shows clear deviations from the linear bare band structure (5.14 (a) white line). The most obvious band renormalization is around the Dirac point. This band renormalization feature is related to the plasmon interaction as discussed in chapter 5.2.2. To identify additional and less obvious features, we performed a MDC Lorentz\* fit evaluation<sup>†39,159,201</sup>. In Fig. 5.14 we discuss the bare band structure (white line in (a)), the  $\text{Re}\Sigma$  (c) and  $\text{Im}\Sigma$  (d) as function of energy. The self energy and bare band structure were calculated as described in Ref. 40. More details on the calculation are in appendix A.3.

In Fig. 5.14 (d, black vs. grey line), we compare  $\text{Im}\Sigma$  to the results from Bostwick et al.<sup>39,142,141</sup>. The behavior is qualitatively similar but with an offset. This offset of about 50(20) meV is mainly caused by an increased sample temperature in our measurements ( $\approx 300$  K vs.  $\approx 20$  K) and is also caused by a higher linewidth broadening due to our experimental setup. An increase in temperature leads to an increase  $\text{Im}\Sigma$  due to an increased

---

\*Strictly the experimental MDC curves are described by resolution broadened Lorentzian peaks. In our experiments, the resolution broadening is mainly described by a convolution with a  $\text{sech}^2$  peak that acts in the energy direction (see chapter 4.3). Nevertheless, in the MDC direction, the MDC peak form can be largely described by a Lorentzian peak convolved with a  $\text{sech}^2$  peak due to the linear Dirac state dispersion. Such a peak is still reasonably well described by a Lorentzian peak. Therefore the MDC fit evaluation with Lorentzian peak form is sufficient here.

†The dark corridor effect is helpful in the Lorentz fits evaluation. A Lorentz fit of one peak has fewer fit parameters than a fit of two (possibly overlapping) peaks. The reduction of fit parameters makes the fit results more reliable. Thus we even facilitated the dark corridor effect by tuning the XUV polarisation in our normal-incidence measurement geometry.

contribution of e-ph coupling and can be estimated to about  $70 \text{ meV}^{\ddagger}$ . Results for  $\text{Re}\Sigma$  (see Fig 5.14 (C)) have not been published elsewhere for our particular doping concentration. Nevertheless, since the  $\text{Re}\Sigma$  and  $\text{Im}\Sigma$  are self-consistent, a comparison of the  $\text{Im}\Sigma$  is sufficient. Furthermore, we can identify the energy regions where the quasiparticle lifetime is dominated

<sup>‡</sup>In a first approximation, the e-ph contribution to  $\text{Im}\Sigma$  has been estimated by  $\text{Im}\Sigma_{\text{ph}} = -\pi\lambda T^{\text{empty citation}}$  where  $\lambda = 0.08$  is the total electron-phonon coupling strength which Dino Novko calculated in our publication<sup>1</sup>.

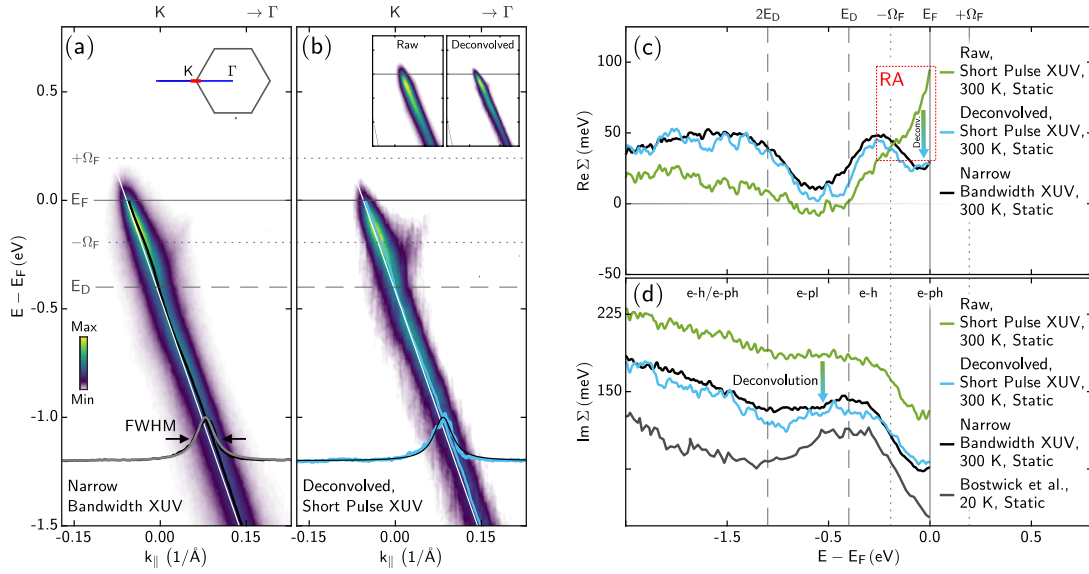


FIGURE 5.14. Quasiparticle dynamics in graphene/SiC from static ARPES. (a) Static narrow-bandwidth XUV ARPES spectrum of graphene/SiC. The top-right inset signifies the measured cut along  $\Gamma - K$  in the Brillouin-zone (blue line) and the momentum range visible in the spectrum (red line). (b) Static Deconvolved Short Pulse ARPES Spectrum. The insets demonstrate a sharpening effect from the deconvolution procedure. Exemplary MDC (horizontal profiles black) are plotted with the corresponding Lorentz fit (grey or black line) and the resulting dispersions. The linear bare band structure (white line) was calculated from the extracted dispersion and FWHM in a self-consistent way (see appendix A.3) together with the  $\text{Re}\Sigma$  and  $\text{Im}\Sigma$  in (c) and (d). Panel (c) compares the  $\text{Im}\Sigma$  with the results from Ref. <sup>142</sup> (Also shown as Fig. 5.3 in this thesis.) for a doping of  $n = 1.2 \cdot 10^{13} \text{ cm}^{-2}$  (grey line) and shows the effect of the deconvolution (blue vs. light blue line). The areas where  $\text{Im}\Sigma$  is dominated by e-ph, e-h, or e-pl contributions are marked. (d) The deconvolution procedure removes the resolution artifact (RA) from the short pulse XUV spectra (green vs. light blue line). The deconvolution procedure is physically correct since it reproduces the  $\text{Re}\Sigma$  and  $\text{Im}\Sigma$  in accordance with the  $70 \text{ meV}$  energy-resolution short pulse XUV results (compare black and light blue lines in (c-d)).

by electron-hole, electron-plasmon, and electron-phonon interactions as in done Refs.<sup>39,142</sup> (compare with Fig. 5.3 in chapter 5.2). Now we discuss the features in more detail.

First we discuss the e-ph region of  $\Omega$  around the Fermi energy in detail. We see the phonon kink in  $\text{Re}\Sigma$  (Fig. 5.14 (d) black line) and the corresponding reduction of the  $\text{Im}\Sigma$ , i.e., an increase in quasiparticle lifetime (Fig. 5.14 (d) black line). This increase is caused by reduced phase space for e-ph scattering in that region (as discussed in chapter 5.2.1).

Now we focus on the regions marked as e-h and e-pl between  $2E_D$  and  $-200$  meV in Fig. 5.14 (d, black vs. grey line). In Refs.<sup>39,142,141</sup>, samples with higher doping concentrations (see Fig. 5.3 regions II and III, topmost data  $n = 5.6$  cm<sup>-2</sup> in chapter 5.2) have also been investigated. In these samples these regions are clearly distinct in  $\text{Im}\Sigma$  (i.e. FWHM) with a  $\omega^\alpha \ln(\omega)$  behaviour in the e-h region (see Fig. 5.3 region II) and an asymmetric peak-like structure in the plasmon region (see Fig. 5.3 region III). With low doping concentration, as with our sample, these features overlap, and there is a single peak-like structure here, which is in agreement with comparable samples in literature (compare black and grey line Fig. 5.14).

In the region below  $2E_D$  in Fig. 5.14, Bostwick et al.<sup>39,142,141</sup> suggest that the steady increase in  $\text{Im}\Sigma$  (black and grey line) is only governed by e-h contributions. However, as discussed in chapter 5.2.1, the e-ph contribution will also lead to a steady increase. Thus in this work, the region is labeled as e-h/e-ph.

Next, we briefly revisit the changes in the ARPES spectra when we conduct the measurements with the spectrally broad short pulse XUV line (a more detailed discussion was already given in chapter 4). When we try to extract  $\text{Re}\Sigma$  with the same procedure as for the 70 meV energy-resolution data, the results are widely different (compare green and blue lines in Fig. 5.14 (c)). In the e-ph region,  $\text{Re}\Sigma$  rises, i.e., the dispersion bends towards higher energies. This feature is a resolution artifact (RA)<sup>124</sup> caused by the stronger energy broadening by the short pulse XUV. This RA makes meaningful discussion of the quasiparticle dynamics in the interesting region near the Fermi energy unreliable. Thus, we introduce a Lucy Richardson deconvolution procedure (LRD) on the ARPES data based on Refs.<sup>125–127,131</sup> to mitigate the RA's effects. The deconvolution procedure sharpens the low resolution image (see insets in

Fig. 5.14 (c)). With the procedure,  $\text{Im}\Sigma$  and  $\text{Re}\Sigma$  from these deconvolved spectra (Fig. 5.14 (c)) resemble results from the high resolution data (compare light blue and black line in Fig. 5.14 (c-d)).

To summarize, our quasiparticle dynamics results from n-doped graphene measured with static ARPES are consistent with the literature. Furthermore, the LRD procedure allows us to extract comparable quasiparticle dynamics results from ARPES spectra measured with a spectrally broad short-pulse XUV line. Hence we can now discuss the quasiparticle dynamics under far-from-equilibrium conditions.

### 5.5.2 Far-from-Equilibrium Quasiparticle Dynamics with trARPES

In this section, we investigate the quasiparticle dynamics of graphene on SiC in the far-from-equilibrium conditions during and shortly after an ultrafast infrared pump pulse excitation on a sub 100 fs time scale. We conducted trARPES measurements with an ultrafast pump pulse with a photon energy of  $h\nu = 1.2$  eV, a pulse length of FWHM 37(3) fs (see chapter

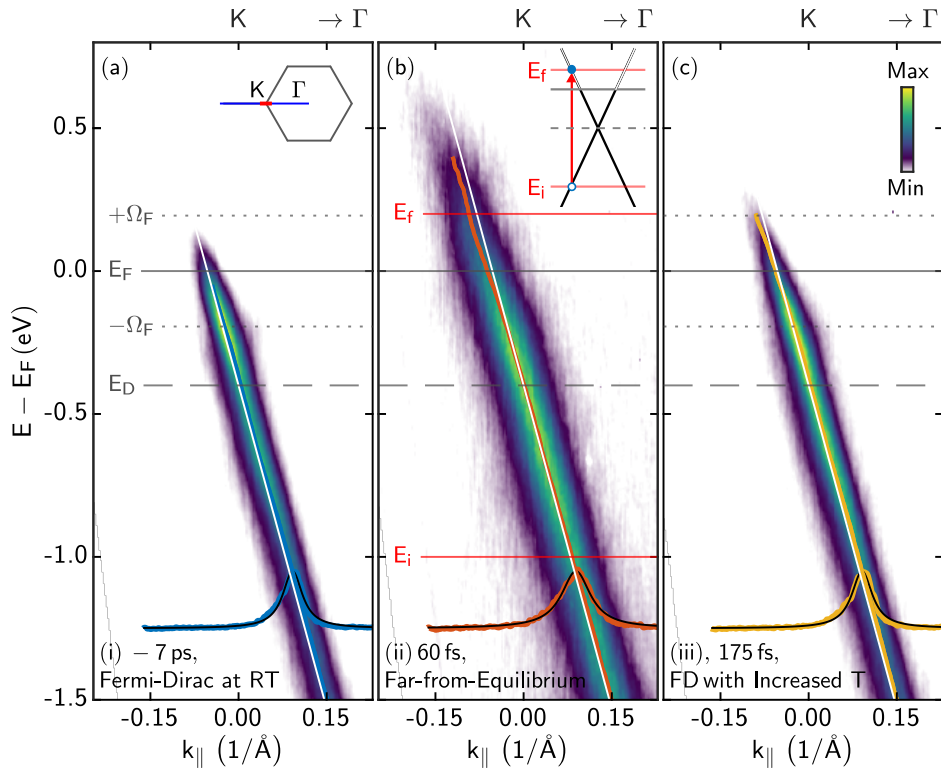


FIGURE 5.15. Deconvolved trARPES spectra at the three characteristic timescales measured with the short pulse XUV. (a) Spectrum before the pump pulse arrives, where graphene's electron and phonon subsystems are in equilibrium. The top-right inset signifies the measured cut along  $\Gamma - K$  in the Brillouin-zone (blue line) and the momentum range visible in the spectrum (red line). (b) Spectrum directly after the optical excitation (see inset). There is a clear deviation from the bare band structure (white line) at  $E_F$  (light red horizontal line). (c) Spectrum after the pump pulse where the electron subsystem is largely thermalized back to a Fermi-Dirac distribution with increased temperature.

A.2), and a fluence of  $1.3 \text{ mJ/cm}^2$  on the sample. The probe pulse is the short pulse XUV line as described in chapter 3.3.4 with a pulse length of  $17(8) \text{ fs}$  (see chapter A.2) and a photon energy of  $h\nu = 21.7 \text{ eV}$ .

Fig. 5.15, shows deconvolved ARPES spectra at three exemplary delay times. At first glance, we notice the overall broadening of the linewidth in Fig. 5.15 (b) compared with the

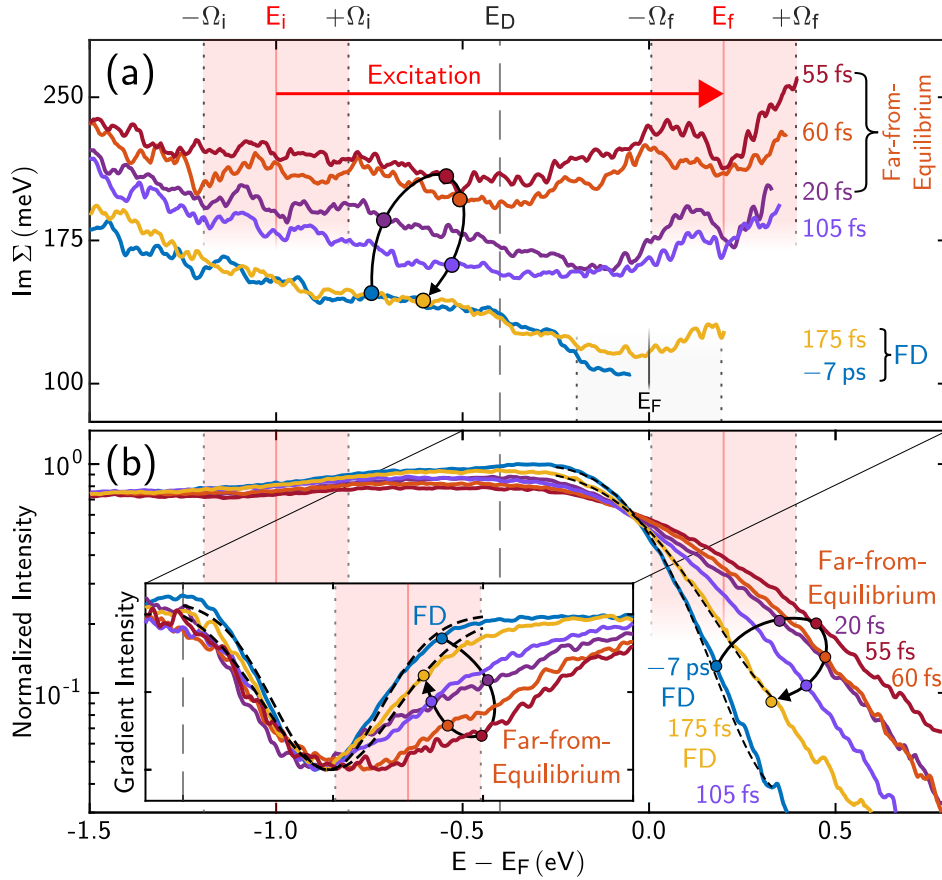


FIGURE 5.16. (a) Pump-probe delay-dependent evolution of  $\text{Im}\Sigma$  obtained from deconvolved data sets. The black curved arrow is a guide to the eye and subsequently connects the data from  $-7 \text{ ps}$  to  $175 \text{ fs}$  pump-probe delay. (b) Momentum-integrated EDCs (not deconvolved) show Fermi-Dirac distributions (fitted with black dashed lines) for delays of  $-7 \text{ ps}$  and  $175 \text{ fs}$  and significant far-from-equilibrium deviations from a pure Fermi-Dirac distribution for intermediate delay-steps, where additional charge carriers are detected in a broad energy window around  $E_f \pm \Omega_f$  (red area). The deviation from the pure Fermi-Dirac distribution is highlighted in the inset by plotting the gradient of the photoemission intensity along the energy axis. In this visualization, symmetric and asymmetric peaks indicate a pure FD distribution and additional far-from-equilibrium charge carriers, respectively.

unperturbed system (a). Furthermore in Fig. 5.15 (c), around  $E_f$ , the dispersion deviates strongly from the linear bare band. In the  $\text{Re}\Sigma$  this behaviour leads to a negative peak imprinted onto a decrease (see appendix Fig. A.4 red area between  $\pm\Omega_f$ ). In the  $\text{Im}\Sigma$ , we will see a feature at same position. These features are already visible in the undeconvolved data and thus, they are no artifacts introduced by the deconvolution procedure (see chapter 4.5 Fig. 4.9).

From here on, we will mainly discuss the  $\text{Im}\Sigma$ , since it is related to the intuitive concept of the quasiparticle lifetime (results for the  $\text{Re}\Sigma$  of the following measurements are collected in the appendix Fig. A.4).

In Fig. 5.16 (a)  $\text{Im}\Sigma$  is extracted from deconvolved data and then shown for time-delays between -7 ps and 175 fs. We find that the quasiparticle linewidth  $\text{Im}\Sigma$  shows a complex and transient far-from-equilibrium behavior. There are two major signatures in this behavior.

- (1)  $\text{Im}\Sigma$  shows a distinct sequence of local maxima and minima dominantly found in the  $E_i \pm \Omega_i$  and  $E_f \pm \Omega_f$  energy windows 5.16 (a) around the initial state and final state energies  $E_{i,f}$  of the pump excitation. These features are strong at 20 fs, 55 fs, and 60 fs (reddish lines).
- (2) We find an energy-independent overall increase of  $\text{Im}\Sigma$ , i.e., a decrease of the quasiparticle lifetime. This broadening is maximal at 55 fs and then decreases until it vanishes at 175 fs (see Fig. 5.16 (a)).

To analyze these far-from-equilibrium many-body interactions, we first take a closer look at the optically-induced electron dynamics in graphene. Fig. 5.16 (b) shows the pump-probe delay-dependent momentum-integrated energy-distribution-curves (EDC). Here, the time-resolved data can be grouped into three characteristic steps of the thermalization process.

- (i) **Fermi-Dirac Distribution at RT:** Before the pump pulse arrives at the sample ( $\Delta t = -7$  ps, blue lines in Fig. 5.16 and 5.15), the electron and phonon subsystems of graphene are in thermal equilibrium, and the EDC can be fitted with a 300 K Fermi-Dirac distribution, shown as a black dashed line in Fig. 5.16 (b). Also, the

inset of 5.16 (b) shows the derivative of the EDC, which is symmetric around  $E_F$  in the case of an ideal Fermi-Dirac distribution.

- (ii) **Far-from-Equilibrium:** During and directly after the optical excitation (20 fs to 60 fs measurements, reddish in Fig. 5.16 and 5.15), the electronic and phononic subsystems are in far-from-equilibrium conditions, and the respective quasiparticle occupations cannot be described by Fermi-Dirac and Bose-Einstein distributions. The far-from-equilibrium contribution is directly visible for the electronic subsystem by a large number of additional charge carriers above the Fermi level, and by the strong asymmetric shape of the intensity gradient in the inset of Fig. 5.16 (b).
- (iii) **Fermi-Dirac Distribution with Increased Temperature:** For delays larger than  $\approx 100$  fs, the electron subsystem is largely thermalized back to a Fermi-Dirac distribution with increased temperature. Thus Fermi-Dirac distribution with  $T \approx 800$  K fits the data (yellow data and corresponding black-dashed Fermi-Dirac fits). It is worth to note that, the charge carrier and phonon subsystems can still be in NEQ with respect to each other<sup>54,202</sup>.

### 5.5.2.1 Electron-Phonon Interaction under Far-from-Equilibrium Conditions

In the following section we discuss the series of peaks and dips in the energy regions  $\pm\Omega_{i,f}$  (see red regions Fig. 5.16 (a)) in the  $\text{Im}\Sigma$  under far-from-equilibrium conditions. We relate these features to the far-from-equilibrium e-ph coupling.

In order to get quantitative access to the far-from-equilibrium renormalization of the quasiparticle lifetime, Fig. 5.17 (a) and (b) show the experimentally determined  $\text{Im}\Sigma$  for the three characteristic timescales: Fermi-Dirac (FD) Distribution at RT (i) and at  $\approx 800$  K (iii) in Fig. 5.17 (a) as thick blue and thick yellow lines, respectively, and the far-from-equilibrium timescales (ii) in Fig. 5.17 (b) as a thick red line. At  $\Delta t = -7$  ps (Fig. 5.17 (a), thick blue) the charge carriers can be described by a Fermi-Dirac distribution at 300 K and the experimentally determined  $\text{Im}\Sigma$ , especially the distinct drop at  $E_F - \Omega_F$ , mirrors the result discussed in Fig. 5.16 (a) for the unpumped case. In the case of  $\Delta t = 175$  fs (Fig. 5.17 (a), thick yellow line), the Fermi-Dirac distribution with increased temperature is formed via photoexcitation of

electron-hole pairs and subsequent thermalization via electron-electron and electron-phonon scattering<sup>188</sup>. Here, the experiment shows that the dip in  $\text{Im}\Sigma$  at  $E_F \pm \Omega_F$  is extenuated. For all data on timescales in the far-from-equilibrium case (ii), a distinct additional structure is found at energies corresponding to the windows of one  $\Omega = \hbar\omega_{E_{2g}}$  around initial  $E_i = -1$  eV and final states  $E_f = 0.2$  eV of the optical excitation (red areas in Fig. 5.17 (b)).

For a detailed understanding of the far-from-equilibrium many-body response found in the experiment, we model how the electron-phonon interaction depends on the distribution of the quasiparticles, i.e., with a Fermi-Dirac charge carrier distribution vs. with a far-from-equilibrium charge carrier distribution. Therefore, we calculate the imaginary part of the self-energy with the ansatz from equation 5.2 (see chapter 5.2.1). In comparison to the experiment, it is insightful to first discuss the impact of Fermi-Dirac distributions at various electronic temperatures on the quasiparticle scattering rate, i.e.,  $\text{Im}\Sigma$ . At room temperature (Fig. 5.17 (a), 300 K, thin blue line), the sudden change of the Fermi-Dirac distribution at the

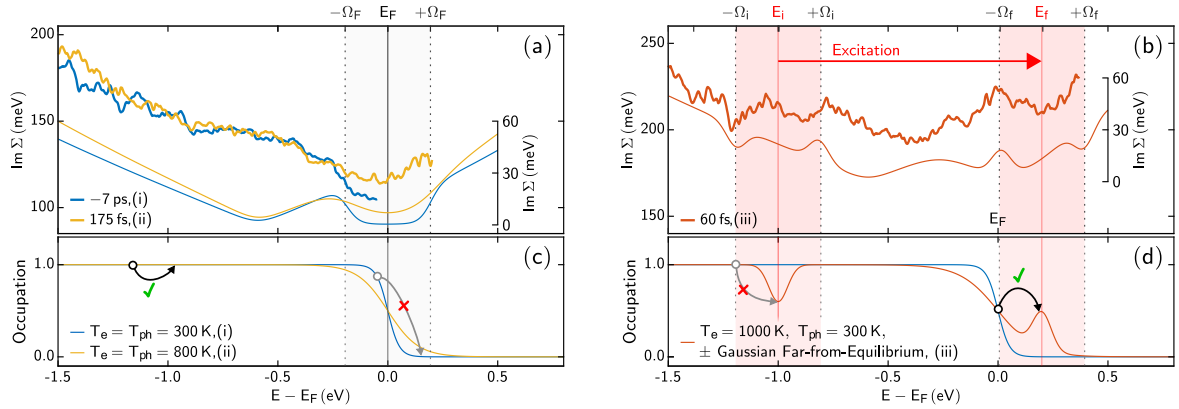


FIGURE 5.17. Comparison of far-from-equilibrium many-body interactions in experiment and theory. (a)  $\text{Im}\Sigma$  as a function of energy for thermalized electron distributions at -7 ps with electronic and phononic temperatures of  $T_e = T_{ph} = 300$  K (thick blue line: experiment, thin blue line: theory) and at 175 fs with elevated temperatures of  $\approx 800$  K (thick yellow line: experiment, thin yellow line: theory). (b)  $\text{Im}\Sigma$  as a function of energy for a delay of 60 fs, where the electronic system exhibits a strong far-from-equilibrium charge carrier distribution (thick red line: experiment, thin red line: theory). (c) and (d) Charge carrier distribution functions and schemes of possible electron-phonon scattering processes in the case of equilibrium Fermi-Dirac distributions, (c), and a strong far-from-equilibrium distribution, (d).

Fermi level leads to a change in the phase space available for the scattering of electrons with optical phonons, which is illustrated in the scheme in Fig. 5.17 (c). For energies smaller than  $E_F - \Omega_F$ , a photohole can always decay towards  $E_F$  via the emission of an optical phonon (black arrow). However, in the  $E_F \pm \Omega_F$  energy window, this scattering channel is largely closed because possible final states for the photohole above  $E_F$  are occupied (grey arrow). In consequence, the quasiparticle scattering time becomes large and, concomitant,  $\text{Im}\Sigma$  shows a corresponding dip within the phonon window (grey area around  $E_F$  in Fig. 5.17 (a), (c)). Suppose the electron and the phonon temperatures are increased (800 K, Fig. 5.17 (a), (c) thin yellow lines). In that case, the Fermi-Dirac distribution is broadened, and additional phase space for scattering a photohole with optical phonons becomes available. Consequently, the quasiparticle lifetime decreases, and the dip in  $\text{Im}\Sigma$  is less pronounced. All these signatures can be found in the analysis of  $\text{Im}\Sigma$  in the experimental data. In particular, the distinct and temperature-dependent drop in  $\text{Im}\Sigma$  at  $E_F - \Omega_F$  is confirmed in the experimental data. In the theoretical curves, the overall smaller  $\text{Im}\Sigma$  is expected since the model only considers electron-phonon scattering processes. Note that in the model, the vanishing  $\text{Im}\Sigma$  at  $E - E_F \approx -0.6$  eV is a result of the vanishing density of states at the Dirac point<sup>158,155</sup>, and, as we focus on the phonon window, we do not further discuss this signature. Nevertheless, the analysis of the quasiparticle lifetime in for Fermi-Dirac distributed charge carriers with equation 5.2 (see chapter 5.2.1) shows that the renormalization of the self-energy from electron-phonon coupling can be understood based on phase space arguments. This result is in agreement with earlier trARPES experiments that measured increased population lifetimes within the phonon window for thermally distributed charge carriers<sup>150,68</sup>. In the following, we will transfer this concept established for thermal Fermi-Dirac distributions to far-from-equilibrium charge carrier occupations.

The distinct energy-dependent sequence of local maxima and minima in  $\text{Im}\Sigma$  under far-from-equilibrium conditions, is consistently found for all pump-probe delay-dependent data, as long as the electronic system exhibits a strong non-Fermi-Dirac non-equilibrium distribution (20 fs to 60 fs measurements, reddish lines, Fig. 5.16 (b)). Notably, the signatures become less pronounced at intermediate pump-probe delays (105 fs), where the carrier distribution starts to establish a Fermi-Dirac distribution at elevated temperature. In order to explain this

distinct shape of  $\text{Im}\Sigma$ , we follow the same approach as discussed above for the equilibrium case. The far-from-equilibrium excitation is modelled phenomenologically by including the optical excitation via adding and subtracting Gaussian hole and electron distributions at  $E_i = -1.0$  eV and  $E_f = 0.2$  eV, respectively, to the Fermi-Dirac distribution (Fig. 5.17 (d))<sup>203,204</sup>. In order to simulate an optical excitation with 1.2 eV photons, these distributions are centered at  $E_i = -1.0$  eV and  $E_f = 0.2$  eV, and the total number of particles is conserved. Since the additional far-from-equilibrium charge carriers are a substantial perturbation to the Fermi-Dirac distribution in both experiment and our model, they will impact the phase space available for electron-phonon scattering. The resulting quasiparticle lifetime of the model is shown in Fig. 5.17 (b) as a thin red line. Clearly, the model reproduces the distinct maxima and minima in  $\text{Im}\Sigma$  at energies  $E_{i,f} \pm \Omega_{i,f}$ . These signatures can now be understood when, e.g., one considers the quasiparticle lifetime of a photohole at  $E_F \approx E_f - \Omega_f$  (Fig. 5.17 (d), black arrow). Here, the photohole lifetime is reduced as the far-from-equilibrium charge carriers at  $E_f$  open up additional phase space for scattering with optical phonons. Hence, we find an excellent qualitative agreement between the far-from-equilibrium model calculations and the experimental data. The maxima and minima in  $\text{Im}\Sigma$  are observed at  $E_{i,f} \pm \Omega_{i,f}$ , i.e., at the energies where the quasiparticle lifetime is expected to be strongly dominated by far-from-equilibrium electron-phonon scattering. Interestingly, in experiment, we find that the far-from-equilibrium signatures are more pronounced at  $E_f \pm \Omega_f$  than at  $E_i \pm \Omega_i$ . For this, one needs to consider that the far-from-equilibrium quasiparticle distribution for the holes at  $E_i$  must thermalize significantly faster than for the electrons at  $E_f$ . The reason is that the distance from the Fermi level is much larger for the photo-excited holes ( $|E_i - E_F| = 1$  eV) than for the electrons ( $|E_f - E_F| = 0.2$  eV), so that considerably more phase space is available for hole scattering processes<sup>205,52</sup>. In combination with the limited time- and energy-resolution of our experiment, the energy dependence of  $\text{Im}\Sigma$  is less well resolved at  $E_i \pm \Omega_i$  in comparison to  $E_f \pm \Omega_f$ .

From these observations, we can conclude that the linewidth analysis of the trARPES data provides a clear signature of how the optically-induced far-from-equilibrium quasiparticle distribution leads to a transient modification of many-body interactions on the sub-100 fs

timescale. Furthermore, we have shown that such a lifetime analysis is feasible, despite the experiment's residual energy broadening and finite time-resolution.

### 5.5.2.2 Overall Increase of $\text{Im}\Sigma$ under Far-from-Equilibrium Conditions

In this section, the second major signature of our experiment, i.e., the energy-independent overall increase of  $\text{Im}\Sigma$ , will be discussed (see Fig. 5.18 (a)). In particular, we found that  $\text{Im}\Sigma$  (see Fig. 5.18 (a)) increases with the creation of far-from-equilibrium charge carrier distributions at early times, and decreases as the charge carrier distribution develops towards a Fermi-Dirac distribution with increased temperature at later times. This behavior is most obvious when the gradient of the EDCs (see inset Fig. 5.18 (b)) and the overall increase of  $\text{Im}\Sigma$  (see Fig. 5.18 (a)) are compared. If the gradient of the EDC intensity is a symmetric peak around the Fermi energy, the distribution is a Fermi-Dirac distribution. In contrast an asymmetric peak indicates a far-from-equilibrium distribution. As can be seen in Fig. 5.18, the overall increase of  $\text{Im}\Sigma$  and asymmetry of the peak in the gradient of the EDC intensity seem related. Now, we inspect the linearly plotted momentum integrated EDC intensity below  $E_F$  (see Fig. 5.18 (a)). At  $-7$  ps (blue line), the EDC intensity can be described by the Fermi-Dirac fit (black line) with a predetermined temperature of 300 K. When the same fit is plotted with  $T = 3000$  K and compared to the far-from-equilibrium EDCs (reddish lines), we notice an additional intensity loss, i.e., holes between  $E_i$  and  $E_F$ . In the following, we will see that these holes and excited electrons cause the overall increase in  $\text{Im}\Sigma$ .

In Fig. 5.19, we quantify the relation between the changes in EDC intensity and the overall increase of  $\text{Im}\Sigma$ . We extracted the mean increase of  $\text{Im}\Sigma$  and the number of excess charge carriers. First, we extracted the mean increase of  $\text{Im}\Sigma$  as a function of delay as illustrated with the red shaded area in Fig. 5.19 (c). The mean increase describes the overall broadening of  $\text{Im}\Sigma$ . Second, the number of excess charge carriers is extracted by analyzing the area between the momentum integrated EDC at  $-7$  ps and the EDCs at the respective time delay (see 5.19 (b)). In Fig. 5.19 (a), both quantities rise during the pump pulse duration at early delays and then decay at later delays. However, the mean increase in  $\text{Im}\Sigma$  decays faster (see exponential fits in the insets in Fig 5.19 (a)). Nevertheless, the overall broadening is related

to the number of excess charge carriers as will be shown in this section. Now we discuss our observations. First, we create a modified conceptual far-from-equilibrium distribution function to reflect the observations from above (see Fig. 5.18 (b), red line) to explain the relevant physical processes more clearly. The intensity loss between  $E_i$  and  $E_F$  (see Fig. 5.18 (b) red line) is qualitatively modelled by a constant decrease in that region (see Fig. 5.18

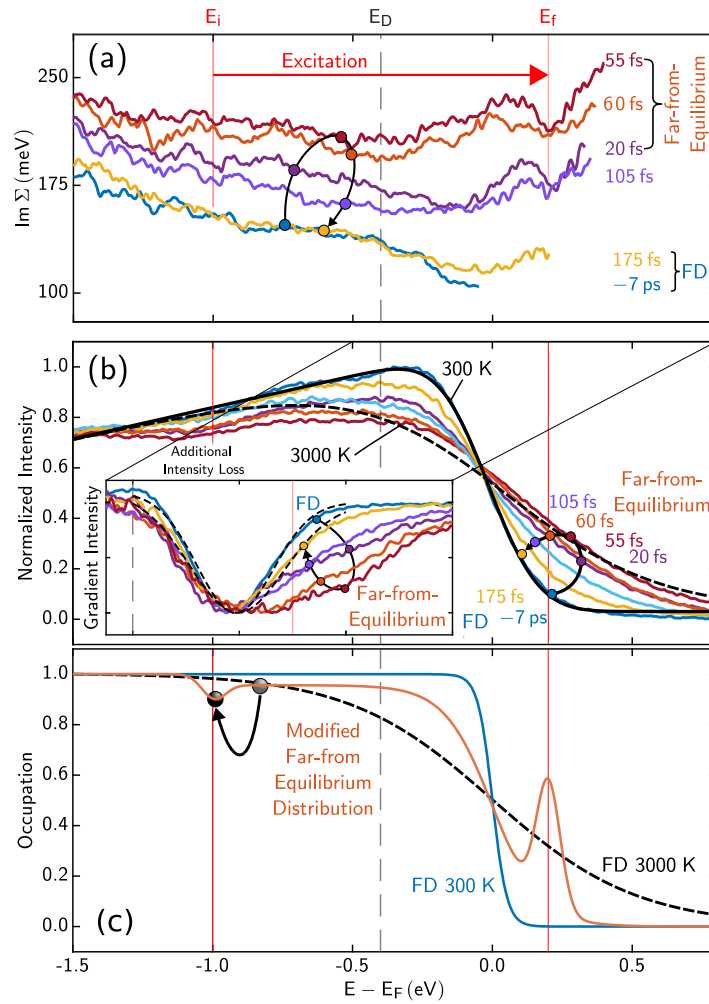


FIGURE 5.18. (a) Pump-probe delay-dependent momentum integrated EDC intensities (not deconvolved). A Fermi-Dirac Distribution (FD) with a fixed  $T = 300$  K has been fitted to the 7 ps data (black line). Another Fermi-Dirac Distribution with  $T = 3000$  K shows that the momentum integrated EDCs under far-from-equilibrium (reddish curves) conditions are not well described by this Fermi-Dirac distribution. (b) The far-from-equilibrium charge carrier distribution used to explain the e-ph quasiparticle dynamics in the previous chapter is modified to conceptually account for the loss in intensity between  $E_i$  and  $E_F$ .

(c) red line). The dynamic evolution of the distribution due to the scattering processes of holes from the  $E_i$  towards  $E_F$  creates such a distribution. These scattering processes can be e-h-, e-pl-, and e-ph-scattering processes, and they can even start during the pump pulse duration of 40 fs<sup>205,52,59,154</sup>. Furthermore, the e-h scattering processes will be faster at  $E_i$  than at  $E_f$  due to increased phase space created by the greater distance to the Fermi energy<sup>205</sup>.

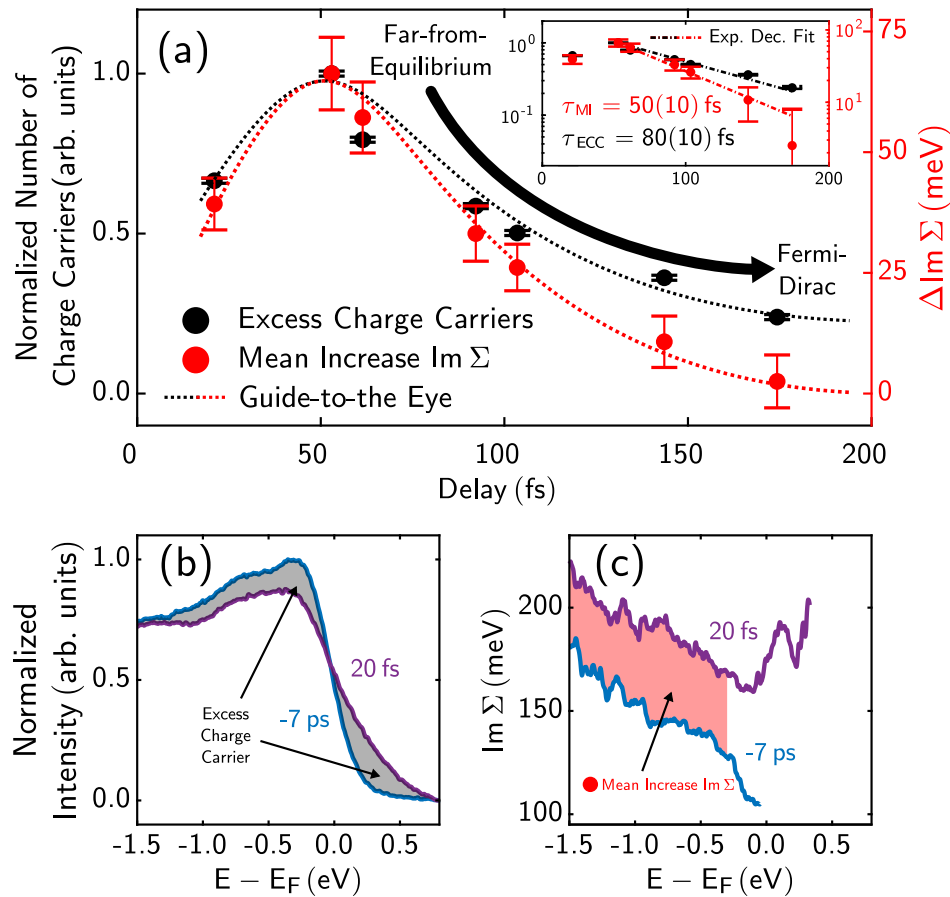


FIGURE 5.19. Population-dynamics vs. overall increase in  $\text{Im} \Sigma$ . (a) Mean increase in  $\text{Im} \Sigma$  and number of excess charge carriers vs. pump-probe delay. The dotted lines are guides-to-the-eye to clarify the temporal behavior. With increasing delay, the charge carrier distribution develops from a far-from-equilibrium distribution toward a Fermi-Dirac distribution. In the inset, the mean lifetime of the number of excess charge carriers  $\tau_{\text{ECC}}$  and the mean lifetime of the mean increase of  $\text{Im} \Sigma$   $\tau_{\text{MI}}$  were extracted with exponential decay fits. The intensities for this figure are extracted from raw spectra, whereas the  $\text{Im} \Sigma$  are from deconvolved spectra. (b) Exemplary extraction of the excess charge carriers for 20 fs pump-probe delay. (c) Exemplary extraction of the mean increase for 20 fs pump-probe delay.

Hence under far-from-equilibrium conditions, the intensity increase at  $E_f$  is stronger than the intensity loss at  $E_i$  (see Fig. 5.18 (b), reddish lines), which is captured qualitatively in the far-from-equilibrium distribution by tuning the Gaussian peaks  $E_i$  and  $E_f$  accordingly (see Fig. 5.18 (b))<sup>‡</sup>.

In general, this relation between the mean increase in  $\text{Im}\Sigma$  and excess charge carriers can be explained as follows. The excess electrons/holes open up phase space for quasiparticle scattering events. Therefore photoholes will scatter faster, and thus the  $\text{Im}\Sigma$  increases.

In the following, I will discuss which scattering channels can explain the overall increase in  $\text{Im}\Sigma$  and its relation to charge carrier distributions. First, I will discuss electron-electron scattering channels. There, I will show how spontaneous e-h generation qualitatively explains our observations using a model that considers the increase in phase space under far-from-equilibrium charge carrier distributions. Then I will explore the limits of that model by comparison to the literature. Thereafter I consider how electron-plasmon interactions might influence  $\text{Im}\Sigma$  under far-from-equilibrium charge carrier distributions. Afterward, I will show that an increase in phonon temperature cannot explain our observations. Then, at last, I will shortly consider if increased electron-boson interaction strengths under far-from-equilibrium conditions might play a role and if I can distinguish such effects.

### **Electron-Electron Scattering Channels.**

An overall energy-independent increase of  $\text{Im}\Sigma$  under a far-from-equilibrium charge carrier distribution is expected in graphene because the redistribution of charge carriers opens up phase space for spontaneous e-h generation processes (see Fig. 5.20). A photohole can only scatter by an e-h generation when momentum and energy conservation are satisfied. However, on the linear dispersion of a Dirac Cone, this condition is always satisfied independent of the photohole's energy. Therefore the additional phase space will lead to an energy independent increase of  $\text{Im}\Sigma$  caused by scattering processes of the photohole with e-h generations (see Fig. 5.20).

---

<sup>‡</sup>These modifications can influence features in the  $\text{Im}\Sigma$  caused by the electron-phonon interaction discussed in section 5.5.2.1. However, the form of the features remains qualitatively the same.

To model the  $\text{Im}\Sigma$  we use a perturbative approach, where we estimate the inverse lifetime  $1/\tau$ , i.e., scattering rate of photoholes, similar to Ref. <sup>205</sup> as follows

$$\frac{1}{\tau}(\omega) = \pi\hbar \int dE' f(\omega + E') \int dE f(E) \cdot (1 - f(E + E')) |M(E')|^2. \quad (5.4)$$

These integrals count the number of possible e-h generations with energy  $E'$ , i.e., available phase space for e-h generations, for a photohole at energy  $\omega$  for a given charge carrier distribution  $f$ . The matrix element of the screened electronic interaction  $M(E')$  connects the initial and final states. In the energy range of about 4 eV, we can assume that the matrix element is constant, as has been done in Ref. <sup>205</sup>, since photoemission experiments show that

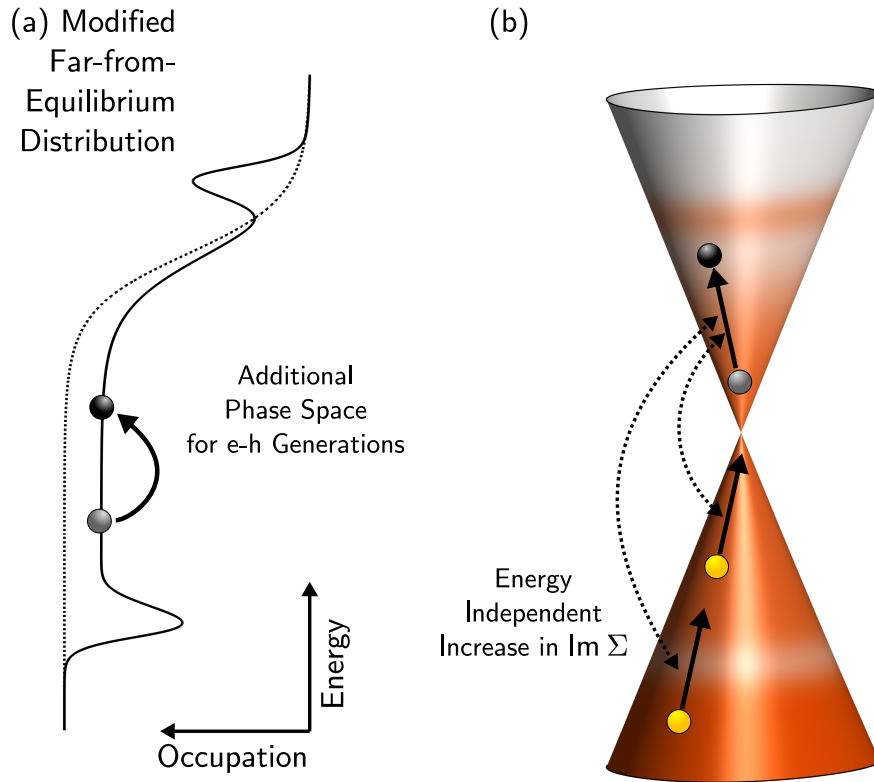


FIGURE 5.20. Scattering through spontaneous e-h generations in far-from-equilibrium charge carrier distributions. (a) In a conceptual charge carrier distribution, additional phase space for e-h excitations is opened up. (b) In the Dirac state, photoholes can now decay via new possible e-h excitations independent of their energy. Note that the far-from-equilibrium charge carrier distribution here is not physically correct since the number of charge carriers is not conserved but it is conceptually justified.

this assumption is valid<sup>206</sup>. Furthermore, an angular average has been made in this equation as in<sup>206,207</sup>. This inverse lifetime can be compared to  $\text{Im}\Sigma$  below  $E_F$  [ $E_f$ ] for Fermi-Dirac [far-from-equilibrium] charge carrier distributions. (Above  $E_F$  [ $E_f$ ]  $\text{Im}\Sigma$  would also reflect the lifetime of a single excited electron).

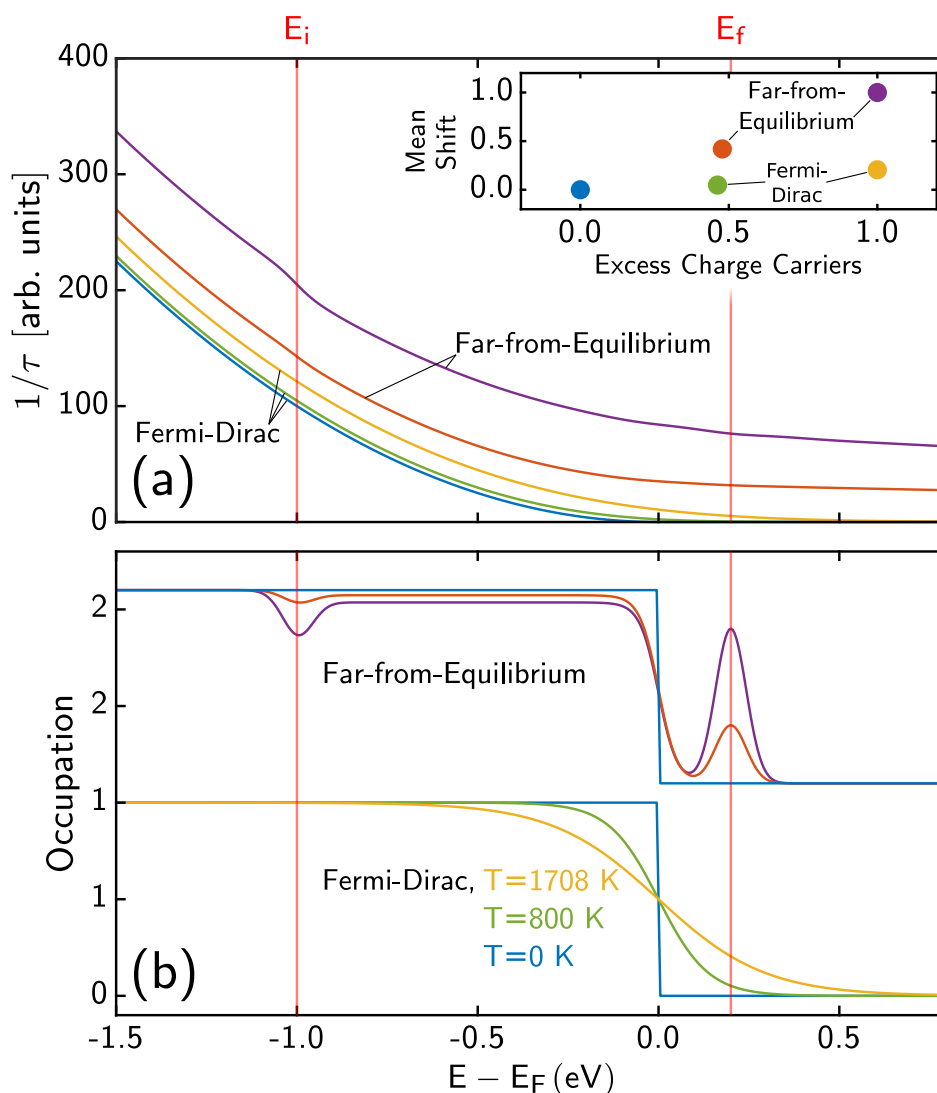


FIGURE 5.21. Theoretical inverse photohole lifetime with different charge carrier distributions. (a) The photohole lifetime has been calculated with equation 5.4 for the several exemplary charge carrier distributions shown in (b). In the inset, the mean increase in inverse lifetime is plotted vs. the excess charge carriers, where the 0 K Fermi-Dirac distribution is used for reference. All charge carrier distributions conserve the number of electrons.

In Fig. 5.21, the inverse lifetime has been plotted for several exemplary charge carrier distributions. For a Fermi-Dirac distribution at 0 K, the inverse lifetime increases as  $\omega^2$ . (see 5.21 (a-b) blue lines). Furthermore, the inverse lifetime increases energy-independent with temperature (see 5.21 (a-b) blue, green and yellow lines). When exemplary far-from-equilibrium distributions are used (see 5.21 (a-b) red and magenta lines) the inverse lifetime also increases largely energy-independent with small deviations around  $E_i$  and  $E_f$ . Thus spontaneous e-h generations can explain the energy-independent increase in the  $\text{Im}\Sigma$ .

In analogy to the analyses of the experimental data, we extract the mean increase of the inverse photohole lifetime and number of excess charge carriers from these simulations (see inset 5.21). We note that a Fermi-Dirac distribution and a far-from-equilibrium distribution with the same number of excess charge carriers lead to different results in the mean increase of the inverse lifetime. In particular, in a far-from-equilibrium distribution, the resulting mean increase of the inverse lifetime is greater than for a Fermi-Dirac distribution. This difference can be understood as follows: An excess charge carrier opens up more phase space with a greater distance from the Fermi energy, and in a far-from-equilibrium distribution, this distance is greater on average. With this modelling, we can understand the temporal behavior of the mean increase of  $\text{Im}\Sigma$  and the number of excess charge carriers (see Fig. 5.19 (a)). At early delays, the charge carrier distribution can be described as a far-from-equilibrium distribution, and at later delays, the charge carrier distribution develops towards a Fermi-Dirac distribution with increased temperature. Therefore the excess charge carriers influence the mean increase of  $\text{Im}\Sigma$  less at later delays. Hence, the mean increase of  $\text{Im}\Sigma$  recovers faster than the number of excess charge carriers.

**Comparison of the Electron-Hole Generation Model to Literature.** Now we compare our model, which was based on equation 5.4, to the literature in Ref. <sup>39,141,142</sup>. Our model describes the increase in  $\text{Im}\Sigma$  only qualitatively, and the  $\omega^2$  energy dependence is not in agreement with the literature, where the increase  $\text{Im}\Sigma$  with energy follows a  $\omega^\alpha \ln(\omega)$  dependence<sup>39,141,142</sup> (as discussed in section 5.2.2). This difference is caused by the form of the Fermi surface, where a spherical Fermi surface causes a  $\omega^2$  dependence, and a cylindrical Fermi surface causes the  $\omega^\alpha \ln(\omega)$  dependence with  $\alpha = 2$ <sup>175</sup>. Bostwick et al. extracted  $\alpha$  as 1.5<sup>39,141,142</sup> as a

consequence of the conical bandstructure and the 2D character of graphene. Nevertheless, here we are interested in the increase of  $\text{Im}\Sigma$ , which we could qualitatively describe by just considering the increase in phase space under far-from-equilibrium and Fermi-Dirac distributions with equation 5.4.

Furthermore, in contrast to the work in Ref. <sup>205</sup>, the electronic density of states (ELDOS) has not been considered. When we consider the e-ph interaction in equation 5.2, the inclusion of the ELDOS was critical because the photohole could only interact with specific phonon modes with given energy so that the ELDOS was imprinted onto the  $\text{Im}\Sigma$  (see section 5.2.1). However, in the e-h interaction, a photohole can decay with a range of energies, i.e., can interact with a range of spontaneous e-h generations with different energies so that the ELDOS will not be imprinted onto the  $\text{Im}\Sigma$ . In addition, in Ref. <sup>205</sup>, the DOS was explicitly included to capture a strong increase in the ELDOS at the onset of *d*-electrons which is not the case in graphene.

**Electron-Plasmon and Electron-Hole Interaction around the Dirac Point.** In section 5.2.2 we also discussed the complex form of the electron-electron contribution to the  $\text{Im}\Sigma$  that was measured and explained by Bostwick et al. <sup>39,141,142</sup>. There the e-h contribution to  $\text{Im}\Sigma$  rises as  $\omega^\alpha \ln(\omega)$  away from the Fermi energy, then decreases around the Fermi energy and rises again as  $\omega^\alpha \ln(\omega)$  (see red line in Fig. 5.3 in section 5.2.2). The decrease around  $E_D$  stems from the missing vertical e-h excitations around the Fermi energy under Fermi-Dirac equilibrium distributions. However, under far-from-equilibrium distributions, photoholes near  $E_D$  will now find spontaneous electron-hole generations near  $E_D$ , which were not available before with a Fermi-Dirac distribution. This effect might lead to a distinct feature, where the increase in  $\text{Im}\Sigma$  is stronger around  $E_D$ . Nevertheless, the increase in phase space might still create an energy-independent increase in  $\text{Im}\Sigma$  when e-pl interactions are included. To explain this point, we consider the equilibrium model for e-pl scattering from Bostwick et al. <sup>142,39</sup> discussed in chapter 5.2.2. Only plasmon modes in the window of forbidden e-h excitations in the e-h excitation continuum (see Fig. 5.6) do not decay into e-h pairs due to Landau damping. Therefore photoholes can only interact with these plasmon modes leading to a localization of the plasmon contribution to  $\text{Im}\Sigma$  around  $E_D$ . A far-from-equilibrium distribution, as in

Fig. 5.20, might weaken the window of forbidden e-h excitation (see Fig. 5.6), which could, in turn, weaken the e-pl contribution to  $\text{Im}\Sigma$  because Landau damping could now suppress more low-energy plasmon modes. These two competing contributions to  $\text{Im}\Sigma$  from e-h and e-pl interactions might, in sum, lead to an energy-independent increase in  $\text{Im}\Sigma$ . However, the sudden decrease of the e-h contribution to  $\text{Im}\Sigma$  around  $E_D$  is also only small (few meV) since  $E_D$  is only  $-0.4$  eV in our sample so that it might not even be visible in our data.

**Conclusion on Electron-Electron Scattering.** Spontaneous e-h generations as the scattering process can qualitatively describe the overall increase in the  $\text{Im}\Sigma$  under far-from-equilibrium distributions. Furthermore, we can also describe the temporal behavior of the overall increase in the  $\text{Im}\Sigma$  and its relation to the number of excess charge carriers with e-h generations as the scattering process. However, a quantitative calculation of the contributions to  $\text{Im}\Sigma$  from inelastic e-h and e-pl scattering events under far-from-equilibrium distribution is not trivial. In the future, more quantitative  $G_0W$  calculations like in Ref. <sup>162</sup> but for far-from-equilibrium charge carrier distributions would be needed. Some literature<sup>208,209</sup> addresses plasmons in graphene in far-from-equilibrium conditions. However, this literature deals with photo inverted charge carrier distributions in hole-doped graphene. Therefore we cannot apply this literature to our experiment. Furthermore, measurements under different doping concentrations might help to disentangle e-h and e-pl contributions as the features become more discernible at higher doping concentrations (see Fig. 5.3).

### Electron-Phonon Scattering.

So far, the model introduced for the e-ph contribution to  $\text{Im}\Sigma$  (see section 5.5.2.1) has been used to explain a series of dips and peaks around  $E_i$  and  $E_f$ . Beyond these features an increase in the phonon temperature in the model (Equation 5.2 in chapter 5.2.1) may generate an overall increase in  $\text{Im}\Sigma$  (see Fig. 5.22). To explain the magnitude of the overall broadening by a phonon temperature increase, we need to assume temperatures of  $\approx 4000$  K. In Ref. <sup>53</sup>, it was shown that the electronic temperature in IR pump pulse excited graphene might reach up to several thousand Kelvin for some ps after the far-from-equilibrium regime. Thus, one might expect a sufficient increase in phonon temperature in the thousands of Kelvins. However,

these studies used a hole-doped graphene sample where the Dirac point acts as a bottleneck, increasing population lifetime drastically. In our experiment, the population lifetime is shorter. The electronic temperature is at roughly 800 K at a delay of 175 fs. This time is insufficient to heat the phonon system to thousands of degrees K. Furthermore, the overall  $\text{Im}\Sigma$ -increase in the experiment is energy-independent. In the model, however, it diverges away from the Dirac point (see Fig. 5.22). For these reasons, an increase in phonon temperature cannot explain the overall increase in  $\text{Im}\Sigma$ .

### Interaction Strengths.

Furthermore, aside from phase space arguments, the many-body electron-boson interaction strength might also transiently change under far-from-equilibrium conditions<sup>140,64,195,194,210</sup>. However, so far, we cannot disentangle the contributions to the  $\text{Im}\Sigma$  and thus cannot make a reliable statement.

### Conclusion on the Overall Increase in the $\text{Im}\Sigma$ .

We note that an overall spectral broadening of trARPES data around time-zero is a typical

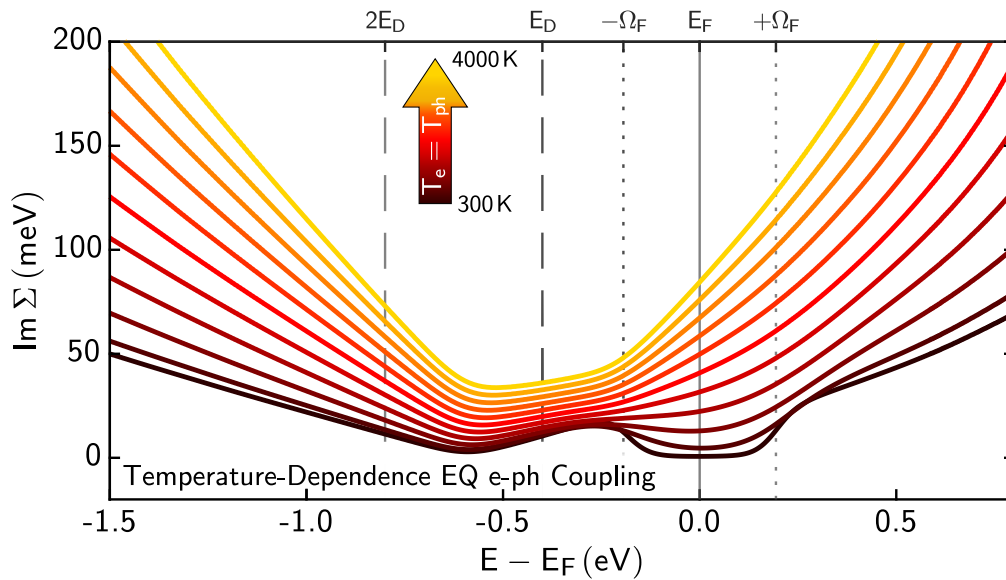


FIGURE 5.22. Theoretical phonon temperature dependence of  $\text{Im}\Sigma$  from equation 5.2. An increase in phonon temperature cannot explain the overall broadening in the extreme NEQ, neither in magnitude nor form.

observation and is mostly disregarded as space-charge effects in time-resolved photoemission data. However, our analysis indicates that, at least partially, such broadening must be expected and is caused by the transiently increased phase space available for various quasiparticle scattering processes and possible also by increased many-body interaction strengths<sup>140,64,195,194,210</sup>. In particular, we show that spontaneous e-h generations are most likely the dominant scattering channel causing this overall spectral broadening.

## 5.6 Outlook

Here I give an outlook on future studies based on the results of this work. First, I will discuss whether the quasiparticle dynamics under far-from-equilibrium distributions are governed entirely by phase space arguments or whether part of the signal can also be attributed to an enhancement of interaction strengths. Then I will discuss how one could obtain more quantitative results by varying various parameters during the measurement. Then we will show a possible phonon absorption feature in the deconvolved EDC data. Finally, I will give a few examples of systems where the LRD approach could be used in the future.

### 5.6.1 Interaction Strength Enhancement

This section discusses whether we can assign parts of the NEQ many-body response to increased interaction strengths. Although we can assign the series of distinct peaks qualitatively to e-ph coupling, a complete quantitative agreement is not reached. Future studies could disentangle the contribution from phase space contributions and the contribution from possibly increased many-body interaction strengths. For example, the strength of dips and peaks assigned to e-ph coupling depends on the exact form of the far-from-equilibrium distribution. However, the exact distribution cannot be deduced from momentum integrated EDC intensity due to the remaining experimental broadening, which persists even after the deconvolution procedure. In addition, increased e-ph interaction strengths would also increase the size of the dips and peaks. Therefore, we cannot disentangle these contributions so far. Nevertheless, the extreme theoretical NEQ charge carrier distribution that we assumed in Fig. 5.17 seems

to have stronger and more pronounced gauss peaks at  $E_i$  and  $E_f$  than might be expected from momentum integrated EDCs in the far-from-equilibrium distribution (see Fig. 5.18). This possible inconsistency would be a first hint toward increased interaction strengths during far-from-equilibrium conditions in our experiment. Such increased interaction strengths are predicted in Refs. <sup>195,194,210</sup> and even experimentally shown in Refs. <sup>140,64</sup>.

### **Additional Studies in Graphene/SiC.**

Future studies could engage this challenge experimentally by performing our measurements under systematically varied parameters such as fluence, sample temperature, pump photon energy, and doping concentration of the sample. On the theoretical side, first, one could aim at models which account for all relevant quasiparticle scattering channels. In these models, parameters could be systematically varied to disentangle contributions from phase space and enhanced interaction strengths. Beyond that, the dynamical evolution between population dynamics and self-energy might be modeled as outlined in <sup>146,147,190,211</sup>.

## **5.6.2 Phonon Absorption Signatures**

Another interesting feature from our experiment is shown in Fig. 5.23 in the momentum integrated EDC from the deconvolved spectra (see Fig. 5.23). This feature was not discussed so far. There is a second peak at  $+\Omega_f$  in the gradient of the momentum integrated EDCs (see inset in Fig. 5.23). This intensity might stem from electrons that absorbed one  $E_{2g}$  phonon, which was earlier emitted by another electron. A similar signal in trARPES population dynamics in graphene has recently been observed in Ref. <sup>212</sup>. In contrast, in that work, the electrons were observed one phonon energy below the  $E_f$  and, thus, emitted one phonon. However, e-e Auger scattering processes might also create additional populations above  $E_f$  (and have been studied in our group <sup>187,105</sup>). Further investigations might include the population dynamics with more delay steps. The peak at  $+\Omega_f$  should appear on slightly later timescales <sup>187</sup> than the peak at  $E_i$ , and the exact timescales might provide further information. If this signal is caused by phonon absorption, this might also hint that the phonon system has an far-from-equilibrium distribution with a strong occupation at the  $E_{2g}$  phonon mode.

Polaron satellite bands<sup>213–215</sup> might also cause our observed signature. Such a polaron satellite would be similar to a plasmaron satellite band from chapter 5.2.3. But there are no satellite signatures in the ARPES spectra (see Fig. 5.15).

However, the discussed features at  $+\Omega_f$  are only barely discernible in the raw data and are overall small (see Fig. 5.16 (b)). Therefore further effort has to be taken to ensure that these features are not artifacts introduced by the LRD deconvolution procedure.

### 5.6.3 LRD in other Sample Systems

Beyond our specific system, the LRD deconvolution methods can be applied to different material systems. We showed that the investigation of quasiparticle dynamics in trARPES by application of the LRD deconvolution methods delivered reasonable results, so it should be applicable to other systems. However, it must be noted that our LRD approach is only reasonable for ARPES spectra of surface states (see chapters 4.3).

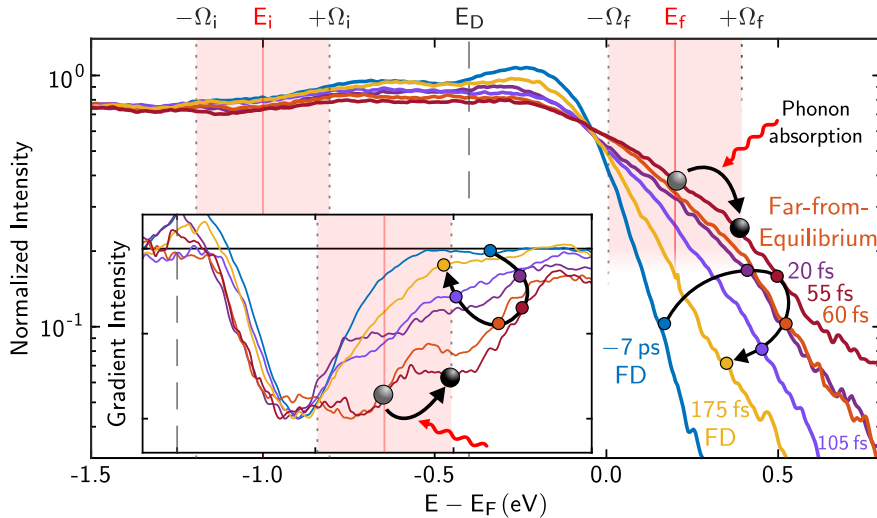


FIGURE 5.23. Momentum-integrated deconvolved EDCs show a second slight increase in intensity at  $\Omega_f$  when in far-from-equilibrium conditions. This second increase is exactly one phonon energy above  $E_i$ . This feature might be explained through the absorption of phonons by the excited charge carriers at  $E_i$ . In the inset, this is more clearly visible in the intensity gradient.

### 5.6.3.1 Gated Samples and Plasmons in Photoinverted Graphene

Doping through alkali deposition is a common way to control the electron density in 2D systems (for example see Refs. <sup>216,39,9,165</sup>). However, a more flexible way to control the electron density might be the electrical gating of layered 2D samples<sup>217</sup>. Although the preparation of such samples is more complicated and requires specialized sample holders, this control strategy is very flexible during the experiment. For example, in graphene, flexible control of many-body interactions has already been demonstrated in static ARPES experiments<sup>218</sup>. In detail, the plasmon feature is more pronounced and isolated at higher doping concentrations<sup>39,142</sup> (see Fig. 5.2 Region III). Therefore, one could flexibly investigate how plasmon emission affects the many-body response in far-from-equilibrium conditions and whether there is an increase in e-pl coupling strength.

Interestingly, theoretical work on hole-doped graphene on NEQ plasmon emission in photoinverted distributions has already been done<sup>208</sup>. Here, our procedure might be useful since the signature of the plasmon emission in  $\text{Im}\Sigma$  is expected near the equilibrium Fermi edge and at the similar sharp upper edge of the photoinverted population (see Fig. 5.24). At both edges, resolution artifacts are expected to influence the FWHM and dispersion of the trARPES spectrum measured with a spectrally broad short pulse XUV source. These RAs could be mitigated with our LRD procedure (see chapter 4).

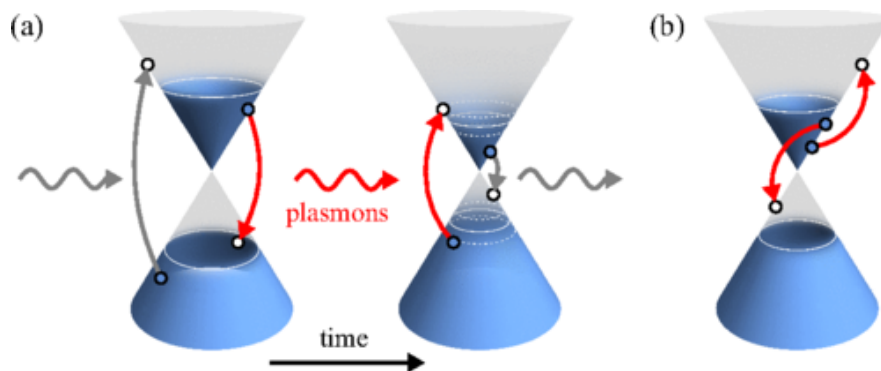


FIGURE 5.24. Schematic carrier thermalization in photo-inverted graphene. (a) far-from-equilibrium Plasmon Emission in Photo-Inverted Graphene. (b) Auger Recombination. Both processes turn e-h pairs into electrons described by a Fermi-Dirac distribution with increased temperature. Figure adapted and reprinted from Ref. <sup>208</sup>. © 2022 American Physical Society.

### 5.6.3.2 Plasmarons in Freestanding Graphene

In the graphene sample used in our experiments, plasmaron bands are only expected as weak shoulders. However, in quasi freestanding graphene plasmaron satellites, bands are stronger<sup>164,165</sup>. However, with broad bandwidth pulses used in trARPES the fine plasmaron are difficult to resolve. Hence, our LRD approach might also resolve these plasmaron bands under far-from-equilibrium conditions.

## 5.7 Conclusion

In conclusion, we were able to experimentally quantify far-from-equilibrium many-body interactions during and shortly after the optical excitation via an analysis of the quasiparticle spectral function. This is surprising at first because femtosecond ARPES requires broad-bandwidth optical pulses, which are known to lead to resolution artifacts around the Fermi level, and usually prevent an analysis of band renormalization in the meV range. We largely remove these resolution artifacts by the application of the LRD to our data. Furthermore, in accordance with theoretical simulations, we find that the far-from-equilibrium redistribution of electrons and holes due to the optical excitation opens up new channels for quasiparticle scatterings resulting in delay-dependent transient quasiparticle lifetime broadening. This observation partly explains the often-observed overall broadening of spectral features, i.e., increase in  $\text{Im}\Sigma$ , in time-resolved photoemission. This overall broadening can be qualitatively explained by the increased phase space for spontaneous electron-hole generations. In addition, in  $\text{Im}\Sigma$  in extreme non-equilibrium, spectrally distinct features are observable, which can be understood as additional phonon windows at energies where the optical excitation creates additional holes below and electrons above the Fermi level. Our results are important for understanding many-body physics in non-equilibrium and, in particular, for the optical creation of new and hidden states of matter. The same methodology could be applied in order to resolve the role of electron-phonon coupling in far-from-equilibrium in other graphene-based or layered systems hosting strongly coupled phonons.

## Bibliography

1. Düvel, M. *et al.* Far-from-Equilibrium Electron–Phonon Interactions in Optically Excited Graphene. *Nano Letters*. ISSN: 1530-6984. <https://pubs.acs.org/doi/full/10.1021/acs.nanolett.2c01325> (June 2022).
2. Maniraj, M. *et al.* A case study for the formation of stanene on a metal surface. *Communications Physics* **2**, 12. ISSN: 2399-3650. <https://www.nature.com/articles/s42005-019-0111-2> (Dec. 2019).
3. Jansen, G. S. M. *et al.* Efficient orbital imaging based on ultrafast momentum microscopy and sparsity-driven phase retrieval. *New Journal of Physics* **22**, 063012. ISSN: 1367-2630. arXiv: 2001.10918. <https://doi.org/10.1088/1367-2630/ab8aae> (June 2020).
4. Chen, G. *et al.* Evidence of a gate-tunable Mott insulator in a trilayer graphene moiré superlattice. *Nature Physics* **15**, 237. ISSN: 1745-2481. <https://doi.org/10.1038/s41567-018-0387-2> (Mar. 2019).
5. Lagoin, C., Suffit, S., Baldwin, K., Pfeiffer, L. & Dubin, F. Mott insulator of strongly interacting two-dimensional semiconductor excitons. *Nature Physics* **18**, 149. ISSN: 1745-2481. <https://doi.org/10.1038/s41567-021-01440-8> (Feb. 2022).
6. Chen, C.-W., Choe, J. & Morosan, E. Charge density waves in strongly correlated electron systems. *Reports on Progress in Physics* **79**, 084505. ISSN: 0034-4885. <https://iopscience.iop.org/article/10.1088/0034-4885/79/8/084505> (Aug. 2016).
7. Cao, Y. *et al.* Unconventional superconductivity in magic-angle graphene superlattices. *Nature* **556**, 43–50. ISSN: 1476-4687. <https://doi.org/10.1038/nature26160> (2018).
8. Keimer, B. & Moore, J. E. The physics of quantum materials. *Nature Physics* **13**, 1045–1055. ISSN: 1745-2481. <https://doi.org/10.1038/nphys4302> (2017).
9. Damascelli, A., Hussain, Z. & Shen, Z.-X. Angle-resolved photoemission studies of the cuprate superconductors. *Reviews of Modern Physics* **75**, 473–541. <https://link.aps.org/doi/10.1103/RevModPhys.75.473> (2003).
10. Hüfner, S. Photoelectron Spectroscopy. *Advanced Texts in Physics* <http://link.springer.com/10.1007/978-3-662-09280-4> (2003).
11. Sobota, J. A., He, Y. & Shen, Z.-X. Angle-resolved photoemission studies of quantum materials. *Reviews of Modern Physics* **93**, 025006. <https://link.aps.org/doi/10.1103/RevModPhys.93.025006> (2021).
12. Basov, D. N., Averitt, R. D. & Hsieh, D. Towards properties on demand in quantum materials. *Nature Materials* **16**, 1077–1088. ISSN: 1476-4660. <https://doi.org/10.1038/nmat5017> (2017).
13. De la Torre, A. *et al.* Colloquium: Nonthermal pathways to ultrafast control in quantum materials. *Reviews of Modern Physics* **93**, 041002. <https://link.aps.org/doi/10.1103/RevModPhys.93.041002> (2021).
14. Kennes, D. M. *et al.* Moiré heterostructures as a condensed-matter quantum simulator.

- Nature Physics* **17**, 155–163. ISSN: 1745-2481. <https://doi.org/10.1038/s41567-020-01154-3> (2021).
15. Stojchevska, L. *et al.* Ultrafast Switching to a Stable Hidden Quantum State in an Electronic Crystal. *Science* **344**, 177–180. ISSN: 0036-8075. eprint: [1401.6786](https://arxiv.org/abs/1401.6786) (2014).
  16. Vaskivskiy, I. *et al.* Controlling the metal-to-insulator relaxation of the metastable hidden quantum state in  $1T$ -TaS<sub>2</sub>. *Science Advances* **1**, e1500168. <https://www.science.org/doi/abs/10.1126/sciadv.1500168> (2015).
  17. Duan, S. *et al.* Optical manipulation of electronic dimensionality in a quantum material. *Nature* **595**, 239–244. <https://doi.org/10.1038/s41586-021-03643-8> (July 2021).
  18. Budden, M. *et al.* Evidence for metastable photo-induced superconductivity in K3C60. *Nature Physics* **17**, 611–618. ISSN: 1745-2481. <https://doi.org/10.1038/s41567-020-01148-1> (2021).
  19. Perfetti, L. *et al.* Time Evolution of the Electronic Structure of  $1T$ -TaS<sub>2</sub> through the Insulator-Metal Transition. *Phys. Rev. Lett.* **97**, 067402. <https://link.aps.org/doi/10.1103/PhysRevLett.97.067402> (6 Aug. 2006).
  20. Schmitt, F. *et al.* Transient Electronic Structure and Melting of a Charge Density Wave in TbTe<sub>3</sub>. English. *Science* **321**, 1649–1652. ISSN: 0036-8075. <https://www.science.org/doi/10.1126/science.1160778> (Sept. 2008).
  21. Frigge, T. *et al.* Optically excited structural transition in atomic wires on surfaces at the quantum limit. *Nature* **544**, 207–211. ISSN: 0028-0836. <https://www.nature.com/articles/nature21432> (Apr. 2017).
  22. Horstmann, J. G. *et al.* Coherent control of a surface structural phase transition. *Nature* **583**, 232–236. ISSN: 0028-0836. eprint: [1906.11155](https://arxiv.org/abs/1906.11155) (2020).
  23. Danz, T., Domröse, T. & Ropers, C. Ultrafast nanoimaging of the order parameter in a structural phase transition. *Science (New York, N.Y.)* **371**, 371–374. ISSN: 0036-8075. <https://www.science.org/doi/10.1126/science.abd2774> (Jan. 2021).
  24. Giannetti, C. *et al.* Ultrafast optical spectroscopy of strongly correlated materials and high-temperature superconductors: a non-equilibrium approach. *Advances in Physics* **65**, 58. <https://doi.org/10.1080/00018732.2016.1194044> (2016).
  25. Fausti, D. *et al.* Light-Induced Superconductivity in a Stripe-Ordered Cuprate. *Science* **331**, 189–191. <https://www.science.org/doi/abs/10.1126/science.1197294> (2011).
  26. Rohwer, T. *et al.* Collapse of long-range charge order tracked by time-resolved photoemission at high momenta. *Nature* **471**, 490–493. ISSN: 0028-0836. <https://www.nature.com/articles/nature09829> (2011).
  27. Nicholson, C. W. *et al.* Beyond the molecular movie: Dynamics of bands and bonds during a photoinduced phase transition. *Science* **362**, 821–825. <https://www.science.org/doi/10.1126/science.aar4183> (2018).
  28. Mathias, S. *et al.* Self-amplified photo-induced gap quenching in a correlated electron material. *Nature Communications* **7**, 12902. ISSN: 2041-1723. <https://doi.org/10.1038/ncomms12902> (2016).
  29. Porer, M. *et al.* Non-thermal separation of electronic and structural orders in a persisting charge density wave. *Nature Materials* **13**, 857–861. ISSN: 1476-1122. eprint: [1604.05627](https://arxiv.org/abs/1604.05627) (July 2014).
  30. Haupt, K. *et al.* Ultrafast Metamorphosis of a Complex Charge-Density Wave. English.

- Physical Review Letters* **116**, 016402. ISSN: 0031-9007. <https://journals.aps.org/prl/abstract/10.1103/PhysRevLett.116.016402> (Jan. 2016).
31. Hellmann, S. *et al.* Time-domain classification of charge-density-wave insulators. *Nature Communications* **3**, 1069. ISSN: 2041-1723. <https://www.nature.com/articles/ncomms2078> (2012).
  32. Hertz, H. Ueber einen Einfluss des ultravioletten Lichtes auf die elektrische Entladung. *Annalen der Physik* **267**, 983–1000. ISSN: 1521-3889. <https://onlinelibrary.wiley.com/doi/full/10.1002/andp.18872670827> (Jan. 1887).
  33. Einstein, A., Einstein & A. Über einen die Erzeugung und Verwandlung des Lichtes betreffenden heuristischen Gesichtspunkt. *AnP* **322**, 132–148. ISSN: 0003-3804. <https://ui.adsabs.harvard.edu/abs/1905AnP...322..132E/abstract> (1905).
  34. Pöhls, J. F. *Build-up of a preparation-chamber for ARPES of thin film perovskites* Thesis (Georg-August-Universität Göttingen, 2020).
  35. Steil, S. *Ultrafast Spin-Dependent Electron Dynamics at the Cobalt/Alq<sub>3</sub> Interface* Thesis (Technische Universität Kaiserslautern, 2014).
  36. Seah, M. P. & Dench, W. A. Quantitative electron spectroscopy of surfaces: A standard data base for electron inelastic mean free paths in solids. *Surface and Interface Analysis* **1**, 2–11. ISSN: 10969918. <https://onlinelibrary.wiley.com/doi/10.1002/sia.740010103> (1979).
  37. Williams, R. H. Electron spectroscopy of surfaces. *Contemporary Physics* **19**, 389–413. ISSN: 13665812. <https://www.tandfonline.com/doi/abs/10.1080/00107517808210892> (1978).
  38. Golze, D., Dvorak, M. & Rinke, P. The GW Compendium: A Practical Guide to Theoretical Photoemission Spectroscopy. *Frontiers in Chemistry* **7**. ISSN: 2296-2646. arXiv: 1912.04893. <http://arxiv.org/abs/1912.04893%20http://dx.doi.org/10.3389/fchem.2019.00377> (July 2019).
  39. Bostwick, A., Ohta, T., Seyller, T., Horn, K. & Rotenberg, E. Quasiparticle dynamics in graphene. *Nature Physics* **3**, 36–40. ISSN: 1745-2481. <http://www.nature.com/articles/nphys477> (2007).
  40. Kordyuk, A. A. *et al.* Bare electron dispersion from experiment: Self-consistent self-energy analysis of photoemission data. *Physical Review B* **71**, 214513. <https://link.aps.org/doi/10.1103/PhysRevB.71.214513> (2005).
  41. Time-resolved two-photon photoemission from metal surfaces. *Journal of Physics: Condensed Matter* **14**, R1099–R1141. ISSN: 0953-8984. <https://iopscience.iop.org/article/10.1088/0953-8984/14/43/202> (Nov. 2002).
  42. Bauer, M., Marienfeld, A. & Aeschlimann, M. Hot electron lifetimes in metals probed by time-resolved two-photon photoemission. *Progress in Surface Science* **90**, 319–376. ISSN: 00796816. <https://linkinghub.elsevier.com/retrieve/pii/S0079681615000192> (Aug. 2015).
  43. Femtosecond time-resolved two-photon photoemission studies of electron dynamics in metals. *Progress in Surface Science* **56**, 239–310. ISSN: 00796816. <https://linkinghub.elsevier.com/retrieve/pii/S0079681698000021> (Dec. 1997).
  44. Reutzel, M., Li, A., Gumhalter, B. & Petek, H. Nonlinear Plasmonic Photoelectron Response of Ag(111). *Physical Review Letters* **123**, 017404. <https://journals.aps.org>

- [org / prl / abstract / 10 . 1103 / PhysRevLett.123.017404](https://doi.org/10.1103/PhysRevLett.123.017404) (2019).
45. Reutzler, M., Li, A. & Petek, H. Coherent Two-Dimensional Multiphoton Photoelectron Spectroscopy of Metal Surfaces. *Physical Review X* **9**, 011044. <https://link.aps.org/doi/10.1103/PhysRevX.9.011044> (2019).
  46. Reutzler, M., Li, A., Wang, Z. & Petek, H. Coherent multidimensional photoelectron spectroscopy of ultrafast quasiparticle dressing by light. *Nature Communications* **11**, 2230. ISSN: 2041-1723. <https://doi.org/10.1038/s41467-020-16064-4> (2020).
  47. Reutzler, M., Li, A. & Petek, H. Above-threshold multiphoton photoemission from noble metal surfaces. *Physical Review B* **101**, 075409. <https://link.aps.org/doi/10.1103/PhysRevB.101.075409> (2020).
  48. Band structure dependence of hot-electron lifetimes in a Pb/Cu(111) quantum-well system. *Physical Review B* **81**, 155429. ISSN: 1098-0121. <https://link.aps.org/doi/10.1103/PhysRevB.81.155429> (Apr. 2010).
  49. Fauster, T., Weinelt, M. & Hofer, U. Quasi-elastic scattering of electrons in image-potential states. *Prog. Surf. Sci.* **82**, 224–243. <https://www.sciencedirect.com/science/article/pii/S0079681607000159> (2007).
  50. Madéo, J. *et al.* Directly visualizing the momentum-forbidden dark excitons and their dynamics in atomically thin semiconductors. *Science* **370**, 1199–1204. <https://science.sciencemag.org/content/sci/370/6521/1199.full.pdf> (2020).
  51. Na, M. X. *et al.* Direct determination of mode-projected electron-phonon coupling in the time domain. *Science* **366**, 1231–1236. <https://science.sciencemag.org/content/sci/366/6470/1231.full.pdf> (2019).
  52. Bauer, M., Marienfeld, A. & Aeschlimann, M. Hot Electron Lifetimes in Metals Probed by Time-Resolved Two-Photon Photoemission. *Prog. Surf. Sci.* **90**, 319–376. ISSN: 0079-6816. <http://www.sciencedirect.com/science/article/pii/S0079681615000192> (2015).
  53. Gierz, I. *et al.* Snapshots of non-equilibrium Dirac carrier distributions in graphene. *Nature Materials* **12**, 1119–1124. ISSN: 1476-1122. <http://dx.doi.org/10.1038/nmat3757> (2013).
  54. Johannsen, J. C. *et al.* Direct View of Hot Carrier Dynamics in Graphene. *Phys. Rev. Lett.* **111**, 027403. ISSN: 0031-9007. <https://link.aps.org/doi/10.1103/PhysRevLett.111.027403> (2013).
  55. Yang, S.-L. *et al.* Inequivalence of Single-Particle and Population Lifetimes in a Cuprate Superconductor. *Phys. Rev. Lett.* **114**, 247001. <https://link.aps.org/doi/10.1103/PhysRevLett.114.247001> (24 June 2015).
  56. Schmitt, D. *et al.* Formation of moiré interlayer excitons in space and time. *arXiv e-prints*, arXiv:2112.05011. arXiv: [2112.05011](https://arxiv.org/abs/2112.05011) [[cond-mat.mes-hall](https://arxiv.org/abs/2112.05011)] (Dec. 2021).
  57. Wallauer, R. *et al.* Momentum-Resolved Observation of Exciton Formation Dynamics in Monolayer WS<sub>2</sub>. *Nano Letters* **21**. PMID: 34165994, 5867–5873. eprint: <https://doi.org/10.1021/acs.nanolett.1c01839>. <https://doi.org/10.1021/acs.nanolett.1c01839> (2021).
  58. Dong, S. *et al.* Direct measurement of key exciton properties: Energy, dynamics, and spatial distribution of the wave function. *Natural Sciences* **1**, e10010. ISSN: 2698-6248. <https://doi.org/10.1038/nat10010> (2019).

- [//onlinelibrary.wiley.com/doi/abs/10.1002/ntls.10010](https://onlinelibrary.wiley.com/doi/abs/10.1002/ntls.10010) (2021).
59. Gierz, I. *et al.* Tracking Primary Thermalization Events in Graphene with Photoemission at Extreme Time Scales. *Phys. Rev. Lett.* **115**, 086803. <http://link.aps.org/doi/10.1103/PhysRevLett.115.086803> (2015).
  60. Perfetti, L. *et al.* Ultrafast Electron Relaxation in Superconducting  $\text{Bi}_2\text{Sr}_2\text{CaCu}_2\text{O}_{8+\delta}$ . *Physical Review Letters* **99**, 197001. ISSN: 0031-9007. <https://link.aps.org/doi/10.1103/PhysRevLett.99.197001> (Nov. 2007).
  61. Gatti, G. *et al.* Light-Induced Renormalization of the Dirac Quasiparticles in the Nodal-Line Semimetal  $\text{ZrSiSe}$ . *Physical Review Letters* **125**, 076401. <https://link.aps.org/doi/10.1103/PhysRevLett.125.076401> (2020).
  62. Lee, W. *et al.* Time-resolved ARPES Determination of a Quasi-Particle Band Gap and Hot Electron Dynamics in Monolayer  $\text{MoS}_2$ . *Nano Letters* **21**, 7363–7370. ISSN: 1530-6984. <https://doi.org/10.1021/acs.nanolett.1c02674> (2021).
  63. Rameau, J. D. *et al.* Photoinduced changes in the cuprate electronic structure revealed by femtosecond time- and angle-resolved photoemission. *Physical Review B* **89**, 115115. <https://link.aps.org/doi/10.1103/PhysRevB.89.115115> (2014).
  64. Zhang, W. *et al.* Ultrafast quenching of electron–boson interaction and superconducting gap in a cuprate superconductor. *Nature Communications* **5**. <https://doi.org/10.1038/ncomms5959> (Sept. 2014).
  65. Rameau, J. D. *et al.* Energy dissipation from a correlated system driven out of equilibrium. *Nature Communications* **7**, 13761. ISSN: 2041-1723. <https://doi.org/10.1038/ncomms13761> (2016).
  66. Mor, S. *et al.* Ultrafast Electronic Band Gap Control in an Excitonic Insulator. *Physical Review Letters* **119**, 086401. <https://link.aps.org/doi/10.1103/PhysRevLett.119.086401> (2017).
  67. Liu, F., Ziffer, M. E., Hansen, K. R., Wang, J. & Zhu, X. Direct Determination of Band-Gap Renormalization in the Photoexcited Monolayer  $\text{MoS}_2$ . *Physical Review Letters* **122**, 246803. <https://journals.aps.org/prl/abstract/10.1103/PhysRevLett.122.246803> (2019).
  68. Zhang, H. *et al.* Self-energy dynamics and mode-specific phonon threshold effect in a Kekulé-ordered graphene. *National Science Review*, nwab175. ISSN: 2095-5138. <https://doi.org/10.1093/nsr/nwab175> (2021).
  69. Nilforoushan, N. *et al.* Photoinduced renormalization and electronic screening of quasi-two-dimensional Dirac states in  $\text{BaNiS}_2$ . *Physical Review Research* **2**, 043397. <https://link.aps.org/doi/10.1103/PhysRevResearch.2.043397> (2020).
  70. Maklar, J. *et al.* A quantitative comparison of time-of-flight momentum microscopes and hemispherical analyzers for time- and angle-resolved photoemission spectroscopy experiments. *Review of Scientific Instruments* **91**, 123112. ISSN: 0034-6748. arXiv: 2008.05829. <https://doi.org/10.1063/5.0024493> (Dec. 2020).
  71. Choudhary, K., Kalish, I., Beams, R. & Tavazza, F. High-throughput Identification and Characterization of Two-dimensional Materials using Density functional theory. *Scientific Reports 2017 7:1* **7**, 1–16. ISSN: 2045-2322. <https://www.nature.com/articles/s41598-017-05402-0> (July 2017).
  72. JVASP 667, Jarvis DFT repository (accessed Juli 08, 2022). <https://www.ctcms.jhu.edu/jvasp>

- [nist.gov/~knc6/static/JARVIS-DFT/JVASP-667.xml](http://nist.gov/~knc6/static/JARVIS-DFT/JVASP-667.xml).
73. Novoselov, K. S. *et al.* Electric Field Effect in Atomically Thin Carbon Films. *Science* **306**, 666–669. ISSN: 0036-8075. <https://www.science.org/doi/10.1126/science.1102896> (Oct. 2004).
  74. Wallace, P. R. The Band Theory of Graphite. *Physical Review* **71**, 622–634. ISSN: 0031-899X. <https://link.aps.org/doi/10.1103/PhysRev.71.622> (May 1947).
  75. McClure, J. W. Diamagnetism of Graphite. *Physical Review* **104**, 666. ISSN: 0031899X. <https://journals.aps.org/pr/abstract/10.1103/PhysRev.104.666> (Nov. 1956).
  76. McClure, J. W. Band Structure of Graphite and de Haas-van Alphen Effect. *Physical Review* **108**, 612–618. ISSN: 0031-899X. <https://journals.aps.org/pr/abstract/10.1103/PhysRev.108.612> (Nov. 1957).
  77. McClure, J. W. Analysis of Multicarrier Galvanomagnetic Data for Graphite. *Physical Review* **112**, 715. ISSN: 0031899X. <https://journals.aps.org/pr/abstract/10.1103/PhysRev.112.715> (Nov. 1958).
  78. McClure, J. W. Theory of Diamagnetism of Graphite. *Physical Review* **119**, 606–613. ISSN: 0031-899X. <https://journals.aps.org/pr/abstract/10.1103/PhysRev.119.606> (July 1960).
  79. Slonczewski, J. C. & Weiss, P. R. Band Structure of Graphite. *Physical Review* **109**, 272–279. ISSN: 0031-899X. <https://journals.aps.org/pr/abstract/10.1103/PhysRev.109.272> (Jan. 1958).
  80. Landau, L. D. On the theory of phase transitions. I. *Zh. Eksp. Teor. Fiz.* **11**, 19 (1937).
  81. Peierls, R. *Quelques propriétés typiques des corps solides* in *Annales de l'institut Henri Poincaré* **5** (1935), 177–222.
  82. Novoselov, K. S. *et al.* Two-dimensional gas of massless Dirac fermions in graphene. *Nature* **438**, 197–200. ISSN: 0028-0836. <http://www.nature.com/articles/nature04233> (Nov. 2005).
  83. Novoselov, K. S. *et al.* Two-dimensional gas of massless Dirac fermions in graphene. *Nature* **2005 438:7065 438**, 197–200. ISSN: 1476-4687. <https://www.nature.com/articles/nature04233> (Nov. 2005).
  84. Geim, A. K. & Novoselov, K. S. The rise of graphene. *Nature Materials* **6**, 183–191. ISSN: 1476-1122. <https://www.nature.com/articles/nmat1849> (Mar. 2007).
  85. Wehling, T., Black-Schaffer, A. & Balatsky, A. Dirac materials. *Advances in Physics* **63**, 1–76. ISSN: 0001-8732. arXiv: 1405.5774. <https://doi.org/10.1080/00018732.2014.927109> (Jan. 2014).
  86. Balatsky, A. V., Vekhter, I. & Zhu, J.-X. Impurity-induced states in conventional and unconventional superconductors. *Reviews of Modern Physics* **78**, 373–433. ISSN: 0034-6861. arXiv: 0411318 [cond-mat]. <https://link.aps.org/doi/10.1103/RevModPhys.78.373> (May 2006).
  87. Zahid Hasan, M., Xu, S.-Y., Hsieh, D., Andrew Wray, L. & Xia, Y. in *Contemporary Concepts of Condensed Matter Science* 143–174 (Elsevier, Jan. 2013). ISBN: 9780444633149. <https://linkinghub.elsevier.com/retrieve/pii/B9780444633149000068>.
  88. Qi, X.-L. & Zhang, S.-C. Topological insulators and superconductors. *Reviews of Modern Physics* **83**, 1057–1110. ISSN: 0034-6861. arXiv: 1008.2026. <https://journals.aps.org/rmp/abstract/10.1103/RevModPhys.83.1057>

- [aps.org/rmp/abstract/10.1103/RevModPhys.83.1057](https://aps.org/rmp/abstract/10.1103/RevModPhys.83.1057) (Oct. 2011).
89. Vollhardt, D. & Wolfe, P. *The superfluid phases of helium 3* <https://doi.org/10.1201/b12808> (Courier Corporation, 2013).
  90. Volovik, G. E. *Exotic Properties of Superfluid Helium 3* ISBN: 978-981-02-0705-2. <https://www.worldscientific.com/worldscibooks/10.1142/1439> (WORLD SCIENTIFIC, Mar. 1992).
  91. Lv, B. Q. *et al.* Experimental Discovery of Weyl Semimetal TaAs. *Physical Review X* **5**, 031013. ISSN: 2160-3308. <https://link.aps.org/doi/10.1103/PhysRevX.5.031013> (July 2015).
  92. Beyond Graphene: Chemistry of Group 14 Graphene Analogues: Silicene, Germanene, and Stanene. *ACS nano* **13**, 8566–8576. ISSN: 1936-086X. <https://pubs.acs.org/doi/full/10.1021/acsnano.9b04466> (Aug. 2019).
  93. Castro Neto, A. H., Guinea, F., Peres, N. M. R., Novoselov, K. S. & Geim, A. K. The electronic properties of graphene. *Reviews of Modern Physics* **81**, 109–162. ISSN: 0034-6861. arXiv: 0709.1163. <https://link.aps.org/doi/10.1103/RevModPhys.81.109> (Jan. 2009).
  94. Mittendorff, M. *et al.* Anisotropy of excitation and relaxation of photogenerated charge carriers in graphene. *Nano letters* **14**, 1504–1507. <https://pubs.acs.org/doi/abs/10.1021/nl404730y> (2014).
  95. Stern, F. Polarizability of a Two-Dimensional Electron Gas. *Physical Review Letters* **18**, 546–548. ISSN: 0031-9007. <https://link.aps.org/doi/10.1103/PhysRevLett.18.546> (Apr. 1967).
  96. Reinert, F., Nicolay, G., Schmidt, S., Ehm, D. & Hüfner, S. Direct measurements of the L - gap surface states on the (111) face of noble metals by photoelectron spectroscopy. *Physical Review B* **63**, 115415. ISSN: 0163-1829. <https://journals.aps.org/prb/abstract/10.1103/PhysRevB.63.115415> (Mar. 2001).
  97. Baer, D. & Shutthanandan, V. in *Comprehensive Biomaterials II* 86–107 (Elsevier, Jan. 2017). ISBN: 9780081006924. <https://linkinghub.elsevier.com/retrieve/pii/B9780128035818092857>.
  98. Woodruff, D. Low Energy Electron Diffraction. *Reference Module in Materials Science and Materials Engineering*. <https://linkinghub.elsevier.com/retrieve/pii/B9780128035818034007> (Jan. 2016).
  99. Düvel, M. *Setup of an angle- and time resolved photoemission spectroscopy system and first investigations on the SnPc/Ag(111) hybrid system* Master Thesis (Georg-August-Universität Göttingen, 2017).
  100. Specs Group. *2D CCD Detector User Manual 2.0* 2014.
  101. Chiang, C. T. *et al.* Boosting laboratory photoelectron spectroscopy by megahertz high-order harmonics. *New Journal of Physics* **17**, 013035. ISSN: 1367-2630. <https://iopscience.iop.org/article/10.1088/1367-2630/17/1/013035> (Jan. 2015).
  102. Corder, C. *et al.* Ultrafast extreme ultraviolet photoemission without space charge. *Structural Dynamics* **5**, 054301. ISSN: 23297778. arXiv: 1801.08124. <https://ascitation.org/doi/abs/10.1063/1.5045578> (Sept. 2018).
  103. Iwasawa, H. High-resolution angle-resolved photoemission spectroscopy and microscopy. *Electronic Structure* **2**, 043001. ISSN: 2516-1075. <https://doi.org/10.1088/2516-1075/abb379> (Dec. 2020).

104. Group, S. *ARPES* <https://www.specs-group.com/nc/specsgroup/knowledge/methods/detail/arpes/>. Accessed on 2012-04-29.
105. Keunecke, M. *Ultrafast electron dynamics measured with a novel time-resolved high-repetition rate momentum microscopy setup* Thesis (Georg-August-Universität Göttingen, 2021).
106. Keunecke, M. *et al.* Time-resolved momentum microscopy with a 1 MHz high-harmonic extreme ultraviolet beamline. *Review of Scientific Instruments* **91**, 063905. <https://aip.scitation.org/doi/abs/10.1063/5.0006531> (2020).
107. Chen, C., Fan, Y. X., Eckardt, R. C. & Byer, R. L. Recent Developments In Barium Borate. <https://doi.org/10.1117/12.939612> **0681**, 12–19. ISSN: 1996756X. <https://www.spiedigitallibrary.org/conference-proceedings-of-spie/0681/0000/Recent-Developments-In-Barium-Borate/10.1117/12.939612.full> (Mar. 1987).
108. Arend, G. *Femtosecond Ultraviolet Light Sources for Time-Resolved Photoelectron Spectroscopy* Master Thesis (Georg-August-Universität Göttingen, 2020).
109. Gordon, J. P., Martinez, O. E. & Fork, R. L. Negative group-velocity dispersion using refraction. *JOSA A, Vol. 1, Issue 10, pp. 1003-1006* **1**, 1003–1006. ISSN: 1520-8532. <https://opg.optica.org/viewmedia.cfm?uri=josaa-1-10-1003&seq=0&html=true> (Oct. 1984).
110. Marx, D. F. W. *Hot-electron dynamics in stanene on Au(111)* Bachelor Thesis (Georg-August-Universität Göttingen, 2019).
111. Vogt, S. *Timeresolved Two-Photon-Photoemission on Ag (111) and Cs/Ag (111)* Bachelor Thesis (Georg-August-Universität Göttingen, 2019).
112. Multiple-harmonic conversion of 1064 nm radiation in rare gases. *Journal of Physics B: Atomic, Molecular and Optical Physics* **21**, L31–L35. ISSN: 0953-4075. <https://iopscience.iop.org/article/10.1088/0953-4075/21/3/001> (Feb. 1988).
113. McPherson, A. *et al.* Studies of multiphoton production of vacuum-ultraviolet radiation in the rare gases. *Journal of the Optical Society of America B* **4**, 595. ISSN: 0740-3224. <https://opg.optica.org/viewmedia.cfm?uri=josab-4-4-595&seq=0&html=true> (Apr. 1987).
114. Kulander, K. C., Schafer, K. J. & Krause, J. L. in, 95–110 (Springer, Boston, MA, 1993). [https://link.springer.com/chapter/10.1007/978-1-4615-7963-2\\_10](https://link.springer.com/chapter/10.1007/978-1-4615-7963-2_10).
115. Corkum, P. B. Plasma perspective on strong field multiphoton ionization. *Physical Review Letters* **71**, 1994–1997. ISSN: 0031-9007. <https://journals.aps.org/prl/abstract/10.1103/PhysRevLett.71.1994> (Sept. 1993).
116. Heyl, C. *Scaling and Gating Attosecond Pulse Generation* Thesis (Lund University, 2014).
117. Lewenstein, M., Balcou, P., Ivanov, M. Y., L’Huillier, A. & Corkum, P. B. Theory of high-harmonic generation by low-frequency laser fields. *Physical Review A* **49**, 2117–2132. ISSN: 1050-2947. <https://journals.aps.org/prl/abstract/10.1103/PhysRevA.49.2117> (Mar. 1994).
118. Twisted high-harmonic generation. *Nature Photonics* **2015** *9:11* **9**, 710–712. ISSN: 1749-4893. <https://www.nature.com/articles/nphoton.2015.204> (Oct. 2015).
119. Disentangling Long Trajectory Contributions in Two-Colour High Harmonic Generation. *Applied Sciences* **2018**, *Vol. 8, Page 341* **8**, 341.

- ISSN: 2076-3417. <https://www.mdpi.com/2076-3417/8/3/341/htm%20https://www.mdpi.com/2076-3417/8/3/341> (Feb. 2018).
120. L., K. in *Advances in Solid State Lasers Development and Applications* (InTech, Feb. 2010). ISBN: 978-953-7619-80-0. <http://www.intechopen.com/books/advances-in-solid-state-lasers-development-and-applications/high-harmonic-generation>.
  121. Winterfeldt, C., Spielmann, C. & Gerber, G. Colloquium: Optimal control of high-harmonic generation. *Reviews of Modern Physics* **80**, 117–140. ISSN: 00346861 (2008).
  122. Heyl, C. M., Arnold, C. L., Couairon, A. & L’Huillier, A. Introduction to macroscopic power scaling principles for high-order harmonic generation. *Journal of Physics B: Atomic, Molecular and Optical Physics* **50**, 013001. ISSN: 0953-4075. <https://iopscience.iop.org/article/10.1088/1361-6455/50/1/013001> (Jan. 2017).
  123. Bange, J. P. *Time-resolved ARPES using femto-second extreme ultraviolet light pulses* Thesis (Georg-August-Universität Göttingen, 2020).
  124. Kaminski, A. & Fretwell, H. M. On the extraction of the self-energy from angle-resolved photoemission spectroscopy. *New Journal of Physics* **7**, 98–98. ISSN: 1367-2630. <http://dx.doi.org/10.1088/1367-2630/7/1/098> (2005).
  125. Lucy, L. B. An iterative technique for the rectification of observed distributions. *The Astronomical Journal* **79**, 745. ISSN: 00046256. [http://adsabs.harvard.edu/cgi-bin/bib\\_query?1974AJ.....79..745L](http://adsabs.harvard.edu/cgi-bin/bib_query?1974AJ.....79..745L) (June 1974).
  126. Richardson, W. H. Bayesian-Based Iterative Method of Image Restoration\*. *Journal of the Optical Society of America* **62**, 55. ISSN: 0030-3941. <https://opg.optica.org/viewmedia.cfm?uri=josa-62-1-55&seq=0&html=true> (Jan. 1972).
  127. Yang, H.-B. *et al.* Emergence of preformed Cooper pairs from the doped Mott insulating state in Bi<sub>2</sub>Sr<sub>2</sub>CaCu<sub>2</sub>O<sub>8</sub>+ $\delta$ . *Nature* **456**, 77–80. ISSN: 0028-0836. <http://www.nature.com/articles/nature07400> (Nov. 2008).
  128. Fister, T. T. *et al.* Deconvolving instrumental and intrinsic broadening in core-shell x-ray spectroscopies. *Physical Review B* **75**, 174106. ISSN: 1098-0121. <https://link.aps.org/doi/10.1103/PhysRevB.75.174106> (May 2007).
  129. Hanisch, R. Methods and problems in optical astronomy data management and analysis. *Data Analysis in Astronomy*, 31–41 (1997).
  130. Cannell, M. B., McMorland, A. & Soeller, C. in *Handbook Of Biological Confocal Microscopy* (ed Pawley, J. B.) 488–500 (Springer US, Boston, MA, 2006). ISBN: 978-0-387-45524-2. [https://doi.org/10.1007/978-0-387-45524-2\\_25](https://doi.org/10.1007/978-0-387-45524-2_25).
  131. Rameau, J., Yang, H.-B. & Johnson, P. Application of the Lucy–Richardson deconvolution procedure to high resolution photoemission spectra. *Journal of Electron Spectroscopy and Related Phenomena* **181**, 35–43. ISSN: 03682048. <https://linkinghub.elsevier.com/retrieve/pii/S036820481000126X> (July 2010).
  132. Kevan, S. D. & Gaylord, R. H. High-resolution photoemission study of the electronic structure of the noble-metal (111) surfaces. *Physical Review B* **36**, 5809–5818. ISSN: 0163-1829. <https://link.aps.org/doi/10.1103/PhysRevB.36.5809> (Oct. 1987).
  133. Shockley, W. On the Surface States Associated with a Periodic Potential. *Physical Review* **56**, 317–323. ISSN: 0031-899X. <https://doi.org/10.1103/PhysRev.56.317> (Oct. 1944).

- [// link . aps . org / doi / 10 . 1103 / PhysRev . 56 . 317](https://link.aps.org/doi/10.1103/PhysRev.56.317) (Aug. 1939).
134. Ortega, J. E. *et al.* One-dimensional versus two-dimensional surface states on stepped Au(111). *Physical Review B* **65**, 165413. ISSN: 0163-1829. <https://journals.aps.org/prb/abstract/10.1103/PhysRevB.65.165413> (Apr. 2002).
  135. Hoesch, M. *et al.* Spin structure of the Shockley surface state on Au(111). *Physical Review B - Condensed Matter and Materials Physics* **69**, 241401. ISSN: 01631829. <https://journals.aps.org/prb/abstract/10.1103/PhysRevB.69.241401> (June 2004).
  136. Tusche, C., Krasnyuk, A. & Kirschner, J. Spin resolved bandstructure imaging with a high resolution momentum microscope. *Ultramicroscopy* **159**, 520–529. ISSN: 03043991. <https://linkinghub.elsevier.com/retrieve/pii/S03043991155000698> (Dec. 2015).
  137. Bright high-repetition-rate source of narrow-band extreme-ultraviolet harmonics beyond 22 eV. *Nature Communications* 2015 6:1 **6**, 1–7. ISSN: 2041-1723. <https://www.nature.com/articles/ncomms8459> (June 2015).
  138. Guo, Q. *et al.* A narrow bandwidth extreme ultra-violet light source for time- and angle-resolved photoemission spectroscopy. *Structural Dynamics* **9**, 024304. ISSN: 2329-7778. <https://aca.scitation.org/doi/abs/10.1063/4.0000149> (Apr. 2022).
  139. Da Costa, O. P. *et al.* *A Practical Guide of Deconvolution Application* (accessed August 30 2022). 2021. [https://asset-downloads.zeiss.com/catalogs/download/mic/86baa56d-3854-4eda-a342-693258d9c35a/EN\\_wp\\_LSM-Plus\\_Practical-Guide-of-Deconvolution.pdf](https://asset-downloads.zeiss.com/catalogs/download/mic/86baa56d-3854-4eda-a342-693258d9c35a/EN_wp_LSM-Plus_Practical-Guide-of-Deconvolution.pdf).
  140. Pomarico, E. *et al.* Enhanced electron-phonon coupling in graphene with periodically distorted lattice. *Physical Review B* **95**, 024304. ISSN: 2469-9950. <https://link.aps.org/doi/10.1103/PhysRevB.95.024304> (Jan. 2017).
  141. Bostwick, A. *et al.* Symmetry breaking in few layer graphene films. *New Journal of Physics* **9**, 385–385. ISSN: 1367-2630. <http://dx.doi.org/10.1088/1367-2630/9/10/385> (2007).
  142. Bostwick, A. *et al.* Renormalization of graphene bands by many-body interactions. *Solid State Communications* **143**, 63–71. ISSN: 00381098. <https://linkinghub.elsevier.com/retrieve/pii/S0038109807003171> (July 2007).
  143. Rotenberg, E. & Kevan, S. Electron-phonon coupling in W(110)-(1×1)H. *Journal of Electron Spectroscopy and Related Phenomena* **126**, 125–132. ISSN: 03682048. <https://linkinghub.elsevier.com/retrieve/pii/S0368204802001470> (Oct. 2002).
  144. Valla, T., Fedorov, A. V., Johnson, P. D. & Hulbert, S. L. Many-Body Effects in Angle-Resolved Photoemission: Quasiparticle Energy and Lifetime of a Mo(110) Surface State. *Physical Review Letters* **83**, 2085–2088. ISSN: 0031-9007. <https://link.aps.org/doi/10.1103/PhysRevLett.83.2085> (Sept. 1999).
  145. Balasubramanian, T., Jensen, E., Wu, X. L. & Hulbert, S. L. Large value of the electron-phonon coupling parameter ( $\lambda = 1.15$ ) and the possibility of surface superconductivity at the Be(0001) surface. *Physical Review B* **57**, R6866–R6869. ISSN: 0163-1829. <https://link.aps.org/doi/10.1103/PhysRevB.57.R6866> (Mar. 1998).

146. Kemper, A. F., Sentef, M. A., Moritz, B., Freericks, J. K. & Devereaux, T. P. Effect of dynamical spectral weight redistribution on effective interactions in time-resolved spectroscopy. *Physical Review B* **90**, 075126. <https://link.aps.org/doi/10.1103/PhysRevB.90.075126> (2014).
147. Kemper, A. F., Abdurazakov, O. & Freericks, J. K. General Principles for the Nonequilibrium Relaxation of Populations in Quantum Materials. *Phys. Rev. X* **8**, 041009. <https://link.aps.org/doi/10.1103/PhysRevX.8.041009> (4 Oct. 2018).
148. Perfetto, E., Pavlyukh, Y. & Stefanucci, G. Real-Time *GW*: Toward an Ab Initio Description of the Ultrafast Carrier and Exciton Dynamics in Two-Dimensional Materials. *Phys. Rev. Lett.* **128**, 016801. <https://link.aps.org/doi/10.1103/PhysRevLett.128.016801> (1 Jan. 2022).
149. Gierz, I. Probing carrier dynamics in photo-excited graphene with time-resolved ARPES. *Journal of Electron Spectroscopy and Related Phenomena* **219**. SI: The electronic structure of 2D and layered materials, 53–56. ISSN: 0368-2048. <http://www.sciencedirect.com/science/article/pii/S0368204816301657> (2017).
150. Gierz, I., Link, S., Starke, U. & Cavalleri, A. Non-equilibrium Dirac Carrier Dynamics in Graphene Investigated with Time- and Angle-Resolved Photoemission Spectroscopy. *Faraday Discuss.* **171**, 311–321. ISSN: 1359-6640. <http://dx.doi.org/10.1039/C4FD00020J> (2014).
151. Gierz, I. *et al.* Population inversion in monolayer and bilayer graphene. *Journal of Physics: Condensed Matter* **27**, 164204. ISSN: 0953-8984. arXiv: 1409.0211. <https://iopscience.iop.org/article/10.1088/0953-8984/27/16/164204> (Apr. 2015).
152. Mathias, S. *et al.* Self-amplified photo-induced gap quenching in a correlated electron material. *Nature Communications* **7**, 1–8. ISSN: 20411723. <http://dx.doi.org/10.1038/ncomms12902> (2016).
153. Ulstrup, S. *et al.* Ultrafast Electron Dynamics in Epitaxial Graphene Investigated with Time- and Angle-Resolved Photoemission Spectroscopy. *Journal of Physics: Condensed Matter* **27**, 164206. ISSN: 0953-8984. eprint: 1601.00745. <https://iopscience.iop.org/article/10.1088/0953-8984/27/16/164206> (Jan. 2016).
154. Rohde, G. *et al.* Ultrafast Formation of a Fermi-Dirac Distributed Electron Gas. *Physical Review Letters* **121**, 256401. ISSN: 0031-9007. <https://link.aps.org/doi/10.1103/PhysRevLett.121.256401> (Dec. 2018).
155. Calandra, M. & Mauri, F. Electron-phonon coupling and electron self-energy in electron-doped graphene: Calculation of angular-resolved photoemission spectra. *Phys. Rev. B* **76**, 205411. <https://link.aps.org/doi/10.1103/PhysRevB.76.205411> (20 Nov. 2007).
156. Park, C.-H., Giustino, F., Spataru, C. D., Cohen, M. L. & Louie, S. G. First-Principles Study of Electron Linewidths in Graphene. *Phys. Rev. Lett.* **102**, 076803. <https://link.aps.org/doi/10.1103/PhysRevLett.102.076803> (7 Feb. 2009).
157. Park, C.-H., Giustino, F., Cohen, M. L. & Louie, S. G. Velocity Renormalization and Carrier Lifetime in Graphene from the Electron-Phonon Interaction. *Physical Review Letters* **99**, 086804. <https://link.aps.org/doi/10.1103/PhysRevLett.99.086804> (2007).
158. Tse, W.-K. & Das Sarma, S. Phonon-Induced Many-Body Renormalization of the Electronic Properties of Graphene. *Phys. Rev. Lett.* **99**, 236802. <https://link.aps.org/doi/>

- 10.1103/PhysRevLett.99.236802 (23 Dec. 2007).
159. Siegel, D. A. *et al.* Many-body interactions in quasi-freestanding graphene. *Proceedings of the National Academy of Sciences* **108**, 11365–11369. <https://www.pnas.org/content/pnas/108/28/11365.full.pdf> (2011).
160. Zhou, S. Y., Siegel, D. A., Fedorov, A. V. & Lanzara, A. Kohn anomaly and interplay of electron-electron and electron-phonon interactions in epitaxial graphene. *Physical Review B* **78**, 193404. ISSN: 1098-0121. arXiv: 0810.4159. <https://link.aps.org/doi/10.1103/PhysRevB.78.193404> (Nov. 2008).
161. Nicol, E. J. & Carbotte, J. P. Phonon spectroscopy through the electronic density of states in graphene. *Physical Review B* **80**, 081415. ISSN: 1098-0121. <https://link.aps.org/doi/10.1103/PhysRevB.80.081415> (Aug. 2009).
162. Hwang, E. H., Hu, B. Y.-K. & Das Sarma, S. Inelastic carrier lifetime in graphene. *Physical Review B* **76**, 115434. ISSN: 1098-0121. <https://link.aps.org/doi/10.1103/PhysRevB.76.115434> (Sept. 2007).
163. Gierz, I., Henk, J., Höchst, H., Ast, C. R. & Kern, K. Illuminating the dark corridor in graphene: Polarization dependence of angle-resolved photoemission spectroscopy on graphene. *Physical Review B* **83**, 121408. <https://link.aps.org/doi/10.1103/PhysRevB.83.121408> (2011).
164. Bostwick, A. *et al.* Observation of Plasmarons in Quasi-Freestanding Doped Graphene. *Science* **328**, 999–1002. ISSN: 0036-8075. <https://science.sciencemag.org/content/328/5981/999> %20<https://www.science.org/doi/10.1126/science.1186489>%20<http://www.ncbi.nlm.nih.gov/pubmed/20489018> (May 2010).
165. Walter, A. L. *et al.* Effective screening and the plasmaron bands in graphene. *Physical Review B* **84**, 085410. ISSN: 1098-0121. <https://link.aps.org/doi/10.1103/PhysRevB.84.085410> (Aug. 2011).
166. Lischner, J., Vigil-Fowler, D. & Louie, S. G. Physical Origin of Satellites in Photoemission of Doped Graphene: An Ab Initio G W Plus Cumulant Study. *Physical Review Letters* **110**, 146801. ISSN: 0031-9007. <https://link.aps.org/doi/10.1103/PhysRevLett.110.146801> (Apr. 2013).
167. Grimvall, G. The Electron-Phonon Interaction in Normal Metals. *Physica Scripta* **14**, 63–78. ISSN: 0031-8949. <https://iopscience.iop.org/article/10.1088/0031-8949/14/1-2/013> (July 1976).
168. Grimvall, G. *The electron-phonon interaction in metals* 304. ISBN: 9780444861054 (North-Holland Pub. Co. ;Sole distributors for the U.S.A. and Canada Elsevier North-Holland, Amsterdam ;;New York, 1981).
169. Sharapov, S. G. & Carbotte, J. P. Effects of energy dependence in the quasiparticle density of states on far-infrared absorption in the pseudogap state. *Physical Review B* **72**, 134506. <https://link.aps.org/doi/10.1103/PhysRevB.72.134506> (2005).
170. Allen, P. B. & Mitrović, B. in (eds Ehrenreich, H., Seitz, F. & Turnbull, D.) 1–92 (Academic Press, 1983). <https://www.sciencedirect.com/science/article/pii/S0081194708606657>.
171. Giustino, F. Electron-phonon interactions from first principles. *Rev. Mod. Phys.* **89**, 015003. <https://link.aps.org/doi/10.1103/RevModPhys.89.015003> (1 Feb. 2017).
172. Baroni, S., de Gironcoli, S., Dal Corso, A. & Giannozzi, P. Phonons and related crystal properties from density-functional perturbation theory. *Rev. Mod. Phys.* **73**, 515. <https://link.aps.org/doi/10.1103/RevModPhys.73.515>.

- [// link.aps.org/doi/10.1103/RevModPhys.73.515](https://link.aps.org/doi/10.1103/RevModPhys.73.515) (2 July 2001).
173. Sohler, T., Calandra, M. & Mauri, F. Density-functional calculation of static screening in two-dimensional materials: The long-wavelength dielectric function of graphene. *Phys. Rev. B* **91**, 165428. <https://link.aps.org/doi/10.1103/PhysRevB.91.165428> (16 Apr. 2015).
174. Novko, D., Despoja, V. & Šunjić, M. Changing character of electronic transitions in graphene: From single-particle excitations to plasmons. *Phys. Rev. B* **91**, 195407. <https://link.aps.org/doi/10.1103/PhysRevB.91.195407> (19 May 2015).
175. Hodges, C., Smith, H. & Wilkins, J. W. Effect of Fermi Surface Geometry on Electron-Electron Scattering. *Physical Review B* **4**, 302–311. ISSN: 0556-2805. <https://journals.aps.org/prb/abstract/10.1103/PhysRevB.4.302> (July 1971).
176. Zhang, Y., Tan, Y.-W., Stormer, H. L. & Kim, P. Experimental observation of the quantum Hall effect and Berry's phase in graphene. *Nature* **438**, 201–204. ISSN: 0028-0836. <https://www.nature.com/articles/nature04235> % 20http://www.nature.com/articles/nature04235 (Nov. 2005).
177. Xu, S. *et al.* Energy Dependence of Electron Lifetime in Graphite Observed with Femto-second Photoemission Spectroscopy. *Physical Review Letters* **76**, 483. ISSN: 10797114. <https://journals.aps.org/prl/abstract/10.1103/PhysRevLett.76.483> (Jan. 1996).
178. Giuliani, G. F. & Quinn, J. J. Lifetime of a quasiparticle in a two-dimensional electron gas. *Physical Review B* **26**, 4421. ISSN: 01631829. <https://journals.aps.org/prb/abstract/10.1103/PhysRevB.26.4421> (Oct. 1982).
179. Hawrylak, P. Effective mass and lifetime of electrons in a layered electron gas. *Physical Review Letters* **59**, 485. ISSN: 00319007. <https://journals.aps.org/prl/abstract/10.1103/PhysRevLett.59.485> (July 1987).
180. Many-body effects in a layered electron gas. *Physical Review B* **37**, 10187. ISSN: 01631829. <https://journals.aps.org/prb/abstract/10.1103/PhysRevB.37.10187> (June 1988).
181. Jensen, E., Bartynski, R. A., Gustafsson, T. & Plummer, E. W. Distortion of an Unoccupied Band in Be by the Electron-Plasmon Interaction. *Physical Review Letters* **52**, 2172. ISSN: 00319007. <https://journals.aps.org/prl/abstract/10.1103/PhysRevLett.52.2172> (June 1984).
182. Zhou, S. Y. *et al.* First direct observation of Dirac fermions in graphite. *Nature Physics* **2**, 595–599. ISSN: 1745-2473. arXiv: 0608069 [cond-mat]. <https://www.nature.com/articles/nphys393> (Sept. 2006).
183. Zhou, S. *et al.* ARPES study of the electronic dynamics from graphene to graphite in APS March Meeting Abstracts (Mar. 2007), L28.008. <https://ui.adsabs.harvard.edu/abs/2007APS..MARL28008Z>.
184. Riedl, C., Coletti, C., Iwasaki, T., Zakharov, A. A. & Starke, U. Quasi-Free-Standing Epitaxial Graphene on SiC Obtained by Hydrogen Intercalation. *Physical Review Letters* **103**, 246804. ISSN: 0031-9007. <https://link.aps.org/doi/10.1103/PhysRevLett.103.246804> (Dec. 2009).
185. Pletikosić, I. *et al.* Dirac Cones and Minigaps for Graphene on Ir(111). *Physical Review Letters* **102**, 056808. ISSN: 0031-9007. <https://link.aps.org/doi/10.1103/PhysRevLett.102.056808> (Feb. 2009).
186. Lisi, S. *et al.* Observation of flat bands in twisted bilayer graphene. *Nature Physics* **17**, 189–

193. ISSN: 1745-2473. <http://dx.doi.org/10.1038/s41567-020-01041-x> (Feb. 2021).
187. Keunecke, M. *et al.* Direct Access to Auger recombination in Graphene. *arXiv e-prints*, arXiv:2012.01256. arXiv: 2012 . 01256 (2020).
188. Malic, E. *et al.* Carrier Dynamics in Graphene: Ultrafast Many-Particle Phenomena. *Annalen der Physik* **529**, 1700038. ISSN: 0003-3804. <https://onlinelibrary.wiley.com/doi/abs/10.1002/andp.201700038> (2017).
189. Winzer, T., Jago, R. & Malic, E. Experimentally accessible signatures of Auger scattering in graphene. *Physical Review B* **94**, 235430. ISSN: 24699969. <https://journals.aps.org/prb/abstract/10.1103/PhysRevB.94.235430> (Dec. 2016).
190. Freericks, J. & Kemper, A. F. What do the two times in two-time correlation functions mean for interpreting tr-ARPES? *Journal of Electron Spectroscopy and Related Phenomena* **251**, 147104. ISSN: 03682048. arXiv: 2109 . 13444. <https://doi.org/10.1016/j.elspec.2021.147104> (Aug. 2021).
191. Brida, D. *et al.* Ultrafast collinear scattering and carrier multiplication in graphene. *Nature Communications* **4**, 1987. ISSN: 2041-1723. arXiv: 1209 . 5729. <https://www.nature.com/articles/ncomms2987><http://arxiv.org/abs/1209.5729> (Oct. 2013).
192. Yamashita, M. & Otani, C. Intrinsic and extrinsic effects on intraband optical conductivity of hot carriers in photoexcited graphene. *Physical Review Research* **3**, 013150. ISSN: 2643-1564. <https://link.aps.org/doi/10.1103/PhysRevResearch.3.013150> (Feb. 2021).
193. Malic, E., Winzer, T., Bobkin, E. & Knorr, A. Microscopic theory of absorption and ultrafast many-particle kinetics in graphene. *Phys. Rev. B* **84**, 205406. <http://link.aps.org/doi/10.1103/PhysRevB.84.205406> (2011).
194. Hu, S.-Q. *et al.* Tracking photocarrier-enhanced electron-phonon coupling in nonequilibrium. *npj Quantum Materials* **7**. <https://doi.org/10.1038/s41535-021-00421-7> (Jan. 2022).
195. Baranov, V. V. & Kabanov, V. V. Theory of electronic relaxation in a metal excited by an ultrashort optical pump. *Phys. Rev. B* **89**, 125102. <https://link.aps.org/doi/10.1103/PhysRevB.89.125102> (12 Mar. 2014).
196. Johannsen, J. C. *et al.* Tunable Carrier Multiplication and Cooling in Graphene. *Nano Letters* **15**, 326–331. ISSN: 1530-6984. <http://dx.doi.org/10.1021/nl503614v> (2015).
197. Kemper, A. F. & Freericks, J. K. Relationship between Population Dynamics and the Self-Energy in Driven Non-Equilibrium Systems. *Entropy 2016, Vol. 18, Page 180* **18**, 180. ISSN: 1099-4300. arXiv: 1604 . 02101. <https://www.mdpi.com/1099-4300/18/5/180> (May 2016).
198. Tan, S., Argondizzo, A., Wang, C., Cui, X. & Petek, H. Ultrafast Multiphoton Thermionic Photoemission from Graphite. *Phys. Rev. X* **7**, 011004. <http://link.aps.org/doi/10.1103/PhysRevX.7.011004> (2017).
199. Comeback of epitaxial graphene for electronics: large-area growth of bilayer-free graphene on SiC. *2D Materials* **3**, 041002. ISSN: 2053-1583. <https://iopscience.iop.org/article/10.1088/2053-1583/3/4/041002> (Sept. 2016).
200. Momeni Pakdehi, D. *et al.* Minimum Resistance Anisotropy of Epitaxial Graphene on SiC. *ACS Applied Materials and Interfaces* **10**, 6039–6045. ISSN: 19448252. <https://>

- [pubs.acs.org/doi/full/10.1021/acsami.7b18641](https://pubs.acs.org/doi/full/10.1021/acsami.7b18641) (Feb. 2018).
201. Pletikosić, I., Kralj, M., Milun, M. & Pervan, P. Finding the bare band: Electron coupling to two phonon modes in potassium-doped graphene on Ir(111). *Physical Review B* **85**, 155447. <https://link.aps.org/doi/10.1103/PhysRevB.85.155447> (2012).
202. Caruso, F., Novko, D. & Draxl, C. Photoemission signatures of nonequilibrium carrier dynamics from first principles. *Phys. Rev. B* **101**, 035128. <https://link.aps.org/doi/10.1103/PhysRevB.101.035128> (3 Jan. 2020).
203. Malic, E., Winzer, T., Bobkin, E. & Knorr, A. Microscopic theory of absorption and ultrafast many-particle kinetics in graphene. *Phys. Rev. B* **84**, 205406. <https://link.aps.org/doi/10.1103/PhysRevB.84.205406> (20 Nov. 2011).
204. Tomadin, A., Brida, D., Cerullo, G., Ferrari, A. C. & Polini, M. Nonequilibrium dynamics of photoexcited electrons in graphene: Collinear scattering, Auger processes, and the impact of screening. *Phys. Rev. B* **88**, 035430. <https://link.aps.org/doi/10.1103/PhysRevB.88.035430> (3 July 2013).
205. Zarate, E., Apell, P. & Echenique, P. M. Calculation of low-energy-electron lifetimes. *Physical Review B* **60**, 2326–2332. <https://link.aps.org/doi/10.1103/PhysRevB.60.2326> (1999).
206. Berglund, C. N. & Spicer, W. E. Photoemission Studies of Copper and Silver: Theory. *Physical Review* **136**, A1030. ISSN: 0031899X. <https://journals.aps.org/pr/abstract/10.1103/PhysRev.136.A1030> (Nov. 1964).
207. Kane, E. O. Electron Scattering by Pair Production in Silicon. *Physical Review* **159**, 624. ISSN: 0031899X. <https://journals.aps.org/pr/abstract/10.1103/PhysRev.159.624> (July 1967).
208. Hamm, J. M., Page, A. F., Bravo-Abad, J., Garcia-Vidal, F. J. & Hess, O. Nonequilibrium plasmon emission drives ultrafast carrier relaxation dynamics in photoexcited graphene. *Physical Review B* **93**, 041408. ISSN: 2469-9950. <https://link.aps.org/doi/10.1103/PhysRevB.93.041408> (Jan. 2016).
209. Page, A. F., Ballout, F., Hess, O. & Hamm, J. M. Nonequilibrium plasmons with gain in graphene. *Physical Review B* **91**, 075404. ISSN: 1098-0121. <https://link.aps.org/doi/10.1103/PhysRevB.91.075404> (Feb. 2015).
210. Sentef, M. *et al.* Examining Electron-Boson Coupling Using Time-Resolved Spectroscopy. *Physical Review X* **3**, 041033. <https://link.aps.org/doi/10.1103/PhysRevX.3.041033> (2013).
211. Abdurazakov, O. *et al.* Nonequilibrium electron dynamics in pump-probe spectroscopy: Role of excited phonon populations. *Physical Review B* **98**, 245110. ISSN: 2469-9950. arXiv: 1807.01323. <https://link.aps.org/doi/10.1103/PhysRevB.98.245110> (Dec. 2018).
212. Na, M. X. *et al.* Direct determination of mode-projected electron-phonon coupling in the time domain. *Science* **366**, 1231–1236. eprint: <https://www.science.org/doi/pdf/10.1126/science.aaw1662>. <https://www.science.org/doi/abs/10.1126/science.aaw1662> (2019).
213. Caruso, F., Verdi, C., Poncé, S. & Giustino, F. Electron-plasmon and electron-phonon satellites in the angle-resolved photoelectron spectra of *n*-doped anatase  $\text{TiO}_2$ . *Physical Review B* **97**, 165113. ISSN: 2469-9950. <https://link.aps.org/doi/10.1103/PhysRevB.97.165113> (Apr. 2018).

214. Franchini, C., Reticcioli, M., Setvin, M. & Diebold, U. Polarons in materials. *Nature Reviews Materials* **6**, 560–586. ISSN: 2058-8437. <https://www.nature.com/articles/s41578-021-00289-w> (July 2021).
215. Moser, S. *et al.* Tunable Polaronic Conduction in Anatase  $\text{TiO}_2$ . *Physical Review Letters* **110**, 196403. ISSN: 00319007. arXiv: 1303.5640. <https://journals.aps.org/prl/abstract/10.1103/PhysRevLett.110.196403> (May 2013).
216. Ehlen, N. *et al.* Direct observation of a surface resonance state and surface band inversion control in black phosphorus. *Physical Review B* **97**, 045143. ISSN: 2469-9950. <https://link.aps.org/doi/10.1103/PhysRevB.97.045143> (Jan. 2018).
217. Hofmann, P. Accessing the spectral function of in operando devices by angle-resolved photoemission spectroscopy. *AVS Quantum Science* **3**, 21101. ISSN: 26390213. arXiv: 2011.11490. <https://doi.org/10.1116/5.0038637> (June 2021).
218. Muzzio, R. *et al.* Momentum-resolved view of highly tunable many-body effects in a graphene/hBN field-effect device. *Physical Review B* **101**, 201409. ISSN: 2469-9950. arXiv: 2001.03355. <https://link.aps.org/doi/10.1103/PhysRevB.101.201409> (May 2020).

## List of Figures

- 1.1 Far-from-equilibrium electron-phonon interactions in optically-excited graphene. Femtosecond infrared pulses (red arrow) optically excite charge carriers above the Fermi energy (middle panel) in n-doped graphene. These charge carriers form an far-from-equilibrium non-equilibrium charge carrier distribution (left panel). These charge carriers can interact with strongly coupled phonon modes (green arrow middle panel). Femtosecond extreme ultraviolet pulses are used to measure angle-resolved photoemission spectroscopy spectra (right panel) and to track the electron-phonon interaction with the quasiparticle dynamics. Figure created by Lukas Kroll. 2
- 1.2 Schematic of the time-resolved angle-resolved photoemission spectroscopy setup of this thesis. The schematic of the setup has been reduced to the most important parts. A femtosecond fiber laser system provides IR and green pulses with a pulse length of  $\approx 40$  fs. The green laser beam is focused into a noble gas jet, where the non-linear HHG process creates XUV pulses. The spectrum of these pulses consists of multiple odd harmonics HHG lines. For angle-resolved photoemission spectroscopy, we require a single HHG line with a photon energy of  $\approx 20$  eV. Therefore an array of grazing-incidence plate rejector, multilayer mirrors, and metal filters select the ninth harmonic. The femtosecond XUV pulses serve as probe pulses for our ARPES setup. On the other beam path, the IR pump pulses can be delayed with a delay stage. APRES spectra are then measured pump-probe delay-dependent with a hemispherical 2D-CCD ARPES detector. An exemplary series of trARPES spectra of the Dirac-cone of graphene after strong excitation is shown in the bottom right. 3
- 1.3 Application of the Lucy-Richardson deconvolution algorithm (LRD) to trARPES data. (a) An APRES spectrum measured with the narrow-bandwidth XUV line (70 meV energy-resolution) has no notable resolution artifact. (b) An APRES spectrum measured with the spectrally broad short pulse XUV (200 – 300 meV energy-resolution) line has a resolution artifact, i.e., the dispersion bends towards the Fermi energy. (c) The LRD has been applied to the ARPES spectrum from (b). The resolution artifact has been removed in the resulting ARPES spectrum. 4
- 2.1 ARPES with hemispherical 2D CDD detectors. (a) In ARPES, XUV photons photo emit electrons (green sphere) from a sample. These electrons carry information in their kinetic energy, their emission angle  $\theta$ , and the azimuth angle  $\phi$ , which are measured by the analyzer. First, the photoelectrons pass through an electrostatic lens system, where the emission angle is mapped onto the radial distance. Then, a slit selects electrons from only one azimuth. Third, the hemispherical analyzer maps the kinetic energy into the direction perpendicular to the emission angle mapping direction. In the 2D CCD detector, the electrons are amplified in a multichannel plate (MCP) and then detected with a phosphor screen and CCD camera. (b) The picture collected with the CCD camera is the ARPES spectrum. In the ARPES spectrum, the photoemission intensity is color-coded against  $k_{\parallel}$  and energy. The picture in (a) is adapted Ref. <sup>34</sup>. 9

- 2.2 (a) Three-step-model of photoemission. (b) Momentum conservation at the surface. The photoelectron's  $k_{\parallel}$  is conserved in the transmission process. Figures are reprinted from Ref. <sup>35</sup>. 10
- 2.3 The universal curve for different materials. The mean free path of electrons in different materials is plotted vs. electron's kinetic energy. The magenta area marks the energy range for UPS ARPES. The graph is adapted from Ref. <sup>36</sup>. © 2022 John Wiley & Son, Inc.. 11
- 2.4 One-step-model versus three-step-model of photoemission. Figure adapted and reprinted from Ref. <sup>10</sup>. © 2022 Springer Nature. 12
- 2.5 Possible initial (d-e) and final states (a-c) in the one-step-model of PES. Figure adapted and reprinted from Ref. <sup>10</sup>. © 2022 Springer Nature. 13
- 2.6 Estimation of the self-energy from ARPES spectra. The many-body interactions induce band renormalizations on the electronic structure, which are measured by ARPES. The bare band structure (dashed black line) is renormalized by the  $\text{Re}\Sigma$  (white double arrow) to the measured dispersion (black line). An MDC profile (black MDC profile) is a Lorentzian profile where the  $\text{FWHM} \propto \text{Im}\Sigma$  and  $k_m$  can be extracted with a Lorentzian fit (red line). In this spectrum, the experimental resolution broadens this profile. However, the broadening effect is small, and thus a Lorentzian fit suffices. Still, this broadening introduces an offset to  $\text{Im}\Sigma$ . See section 5.5.1 for a more detailed discussion of the resolution effects. 16
- 2.7 Two-photon-photoemission. (a) An electron (yellow sphere) is excited in the unoccupied band structure and then photoemitted with a second photon after a time-delay  $\Delta_t$ . The electron carries information about the unoccupied band structure. (b) In tr2PPE, several ARPES spectra are collected  $\Delta_t$ -dependent. In a time trace, the 2PPE yield is plotted vs. delay for an area of the ARPES spectrum (yellow arrow). The FWHM of the time trace is proportional to the lifetime  $\tau$  of the unoccupied state. (c) Lifetime Map. The lifetime can then be calculated from time traces for every point of the underlying ARPES spectrum and then plotted in a lifetime map for the energy and momentum range of the underlying ARPES spectrum. Figure adapted and reprinted from Ref. <sup>48</sup>. © 2022 American Physical Society. 19
- 2.8 Tracking primary thermalization events in graphene with photoemission at extreme time scales. (a) trARPES spectra of photo excited graphene at different pump-probe delays. (b) Energy-distribution-curve (EDC) (black line) from the Spectra in (a). A Fermi-Dirac (FD) fit (red line) has been performed to extract the non-thermal charge carriers (NTC) contribution (blue area) to EDC. (c) Sketch of impact ionization (green) and Auger heating (yellow) processes on a Dirac NTC. Occupied states are marked in red and Unoccupied states are marked in white on the Dirac cone. In the population dynamics, the two processes show different signatures when the number of electrons inside the conduction band ( $N_{\text{CB}}$ ) and their average kinetic energy ( $E_{\text{CB}}/N_{\text{CB}}$ ) are plotted vs. the pump-probe delay. (d) Experimental ( $N_{\text{CB}}$ ) and ( $E_{\text{CB}}/N_{\text{CB}}$ ) vs. time-delay. The signature shows directly that impact ionization governs the ultrafast thermalization of the charge carriers. These experiments have been conducted with sub 10 fs pump and probe pulses. Figure adapted and reprinted from<sup>59</sup>. © 2022 American Physical Society. 21
- 2.9 Ultrafast electron relaxation in superconducting  $\text{Bi}_2\text{Sr}_2\text{CaCu}_2\text{O}_{8+\delta}$  by time-resolved photoemission spectroscopy. (a) Schematic of the excitation scheme. 50 fs pulses were used. (b) ARPES spectrum at 30 K of along the nodal momentum cut indicated in the momentum map band structure in (d). (c) trARPES intensity for 0 fs (blue line) and  $-200$  fs (black line). The dashed pink line indicates a fully thermalized Fermi-Dirac Distribution.

- Hence at 0 fs, there are NEQ contributions in the ARPES intensity (compare blue and pink dashed line). (e) trARPES intensity for several pump-probe delays. At 100 fs (green line), the NEQ contributions have vanished. Thus the photo-excited population has thermalized. (f) Temperatures have been extracted from the ARPES intensity distributions and plotted logarithmically vs. time-delay. The temperature decay on three different timescales. First the charge carrier distribution thermalizes in Fermi-Dirac distribution with increased temperature (red points). Second energy is transferred from the electron system into hot phonons (white points). Third, the energy is transferred into the entire phonon system (blue points). Figure adapted and reprinted from Ref. <sup>60</sup>. © 2022 American Physical Society. 23
- 2.10 Light-induced renormalization of the Dirac quasiparticles in the nodal-line semimetal ZrSiSe. (a) Simulated ARPES spectrum from ab-initio DFT+U+V broadened by experimental resolution. (b) Experimental trARPES spectrum at  $t_0$ . (c) MDC curve (red bars) and Lorentzian fits (red lines). The energies of the MDC have been indicated in (b) with dashed lines. (d) Energy vs. peak positions from the Lorentzian fits in (c) for different time-delays. (e) Energy vs. peak positions from the DFT+U+V (red) and DFT (yellow). (f) Change in band position  $\Delta k$  with respect to DFT+U+V calculations. The black line is the change in band position between the DFT and DFT+U+V calculations. The DFT+U+V calculations include electron correlations, whereas the DFT calculations do not include them. Thus electron correlations are suppressed by the excited high-energy electron-hole pairs since, in temporal overlap, the data resemble the DFT calculations. Figure adapted and reprinted from <sup>61</sup>. © 2022 American Physical Society. 24
- 2.11 The extent of the photoemission horizon is plotted in the band structure of graphene for photon energies of 6 eV (Fifth-harmonic with BBOs, blue) and 21.7 eV (Ninth-harmonic of the HHG, purple). A work function of 4.3 eV was assumed for this plot. The band structure is from DFT calculations from the Jarvis DFT repository<sup>71,72</sup>. 25
- 2.12 Spatial and electronic structure of graphene. (a) Crystal structure of graphene made from two sublattices A (red) and B (blue). The vectors  $\delta_i$  connect each atom to its nearest-neighbors. The lattice vectors  $a_1$  and  $a_2$  span the unit cell (blue shaded area). (b) Tight-binding band structure of graphene  $\pi$ -bands. (c) Brillouin zone of graphene.  $b_1$  and  $b_2$  are the reciprocal lattice vectors. (d) Dirac cone in graphene. Around the K point, graphene has a linear quasi-relativistic Dirac dispersion. The chirality (helicity)  $\Lambda = \sigma \cdot k/|k| = \pm 1$  is the quantum number of the Pseudospin (black spheres). The chirality conservation suppresses backscattering on impurities in graphene (dashed arrow). 27
- 2.13 Electron-hole continuum (blue and red shaded areas) in: (a) Two-dimensional-free-electron-gas, (b) Intrinsic graphene and (c) Doped graphene. The insets show exemplary e-h excitations for the e-h continua, i.e., areas of allowed e-h excitations, in the respective materials. The collective plasmon dispersions are marked as grey lines. Dashed grey lines mark Landau damped parts of the plasmon dispersion, whereas solid lines mark persistent parts. 31
- 3.1 Schematic configuration of the main UHV chamber for ARPES experiments. The main chamber is under UHV ( $p \approx 10^{-11}$  mbar). Samples can be inserted from a separate Load chamber. The manipulator allows for sample movement and rotation. An LN2 cooler and resistive PBN heater element are integrated into the manipulator. For sample preparation, a sputter gun is attached to the main chamber, and an organic and a metal evaporator in the evaporation chamber. Sample surfaces can be investigated with the LEED/Auger device. The *Specs Phoibos*

- 150 2D CCD detector is the ARPES detector. The 2PPE beamlines are coupled into the chamber with a UV transparent window. In contrast, part of the trARPES beamline and the entire VUV lamp are connected with the main chamber's vacuum during measurements. A helium cryostat can be used for ARPES measurements down to 20 K. For clarity, some components are sketched at different angles. The actual angle indicates where those components are actually mounted. 36
- 3.2 FHG and THG beamlines for 2PPE. Both beamlines start with the laser pulses ( $\lambda = 1030$  nm,  $h\nu = 1.2$  eV,  $\tau = 40$  fs) from the HFC laser output (red line). Attenuators regulate the input power  $P_{in} = 0 - 5$  W. A tiltable mirror can switch the beam path between the THG or FHG line. Series of nonlinear crystals triple or quadruple the photon energy in the THG (green rectangle) or FHG (magenta rectangle) lines. Both beams are temporally compressed with a prism compressor (yellow rectangles). The time-delays for tr2PPE are introduced with interferometers (grey rectangle). Both beams are focused down on the sample through a UV transparent window. The beams' polarisations are controlled with  $\lambda/2$ -plates. The picture is adapted from<sup>108</sup>. 40
- 3.3 Three-step model of high-harmonic generation. (1) The Coulomb potential of the atom is bent by a high-intensity laser pulse leading to tunnel ionization processes. (2) The free electron propagates in the electric field and collects excess kinetic energy. (3) The electron recombines with the atom and emits its excess energy as a high-energy photon. Reprinted and adapted from<sup>118</sup>. © 2022 Springer Nature. 41
- 3.4 Electron trajectories in the HHG Process. The electron trajectories for different transmission times during the fundamental laser period. The excess energy of electron recombining with the core is color-coded onto the trajectories.  $U_p$  is the pondermotive force. Reprinted and adapted from<sup>119</sup> under Creative Commons Attribution License 4.0. 42
- 3.5 A typical HHG spectrum. The HHG spectrum consists of a comb of harmonics. In the perturbative regime, low-order harmonic processes contribute but decrease with harmonic order. HHG peaks dominate the spectrum with constant intensity in the plateau region. Near the cut-off, the HHG intensity drops off rapidly. The picture is reprinted and adapted from<sup>121</sup>. © 2022 American Physical Society. 43
- 3.6 Schematic of the trARPES beamline. The femtosecond XUV probe pulse is created in the HHG chamber from the SHG of the HFC or uncompressed amplifier output. At first both laser outputs were frequency-doubled with BBOs and the 1.2 eV components were removed with separator mirrors (S). In the mirror chamber, the ninth harmonic line is filtered from the HHG spectrum with rejectors (Rej), multilayer mirrors (ML), and thin Al/Sn foil filters. The XUV beam is focused onto the sample with a curved multilayer mirror (cML). A window (W) can separate the mirror chamber's and the main chamber's vacuum. The pump beam is temporally delayed with the delay stage. Then it is focused onto the sample and coupled into the main chambers vacuum through a CaF<sub>2</sub> window. 46
- 4.1 Application of the Lucy-Richardson deconvolution algorithm (LRD) to trARPES data. (a) A high-resolution APRES spectrum measured with the narrow-bandwidth XUV line has no notable resolution artifact. (b) An APRES spectrum measured with the spectrally broad short pulse XUV line has a resolution artifact, i.e., the dispersion bends towards the Fermi energy. 49
- 4.2 Energy and momentum broadening due to spectrally broad XUV pulses in different photoemission processes. (a) Since the final state is an inverse LEED state inside and outside the materials, the ARPES signal is only broadened in kinetic energy  $\Delta_E$ . (b)

- In bulk photoemission, the ARPES signal can be broadened in  $\Delta_{k_{\parallel}}$  and energy, where the extent of the broadening also depends on the underlying band structure. The photoemission processes are sketched for different spectral components of the XUV pulse, lower energy (red), center energy (black), and higher energy (blue). 51
- 4.3 Simulation of the resolution artifact. (a) Simulated ARPES spectrum of a linear Dirac-arm. (b) The experimental resolution was introduced by a convolution with a two-dimensional Gaussian PSF (see inset), and the dispersion was extracted with an MDC Gauss-fit evaluation (red line). The RA (red box) is the deviation from the underlying linear dispersion (black line). (c) Dependence of the RA at 300 K of the resolution FWHM used in the PSF. (d) Temperature dependence of the RA for  $\Delta_E = 120$  meV. The insets in the (c) and (d) show how the RA influences the extracted  $\text{Re}\Sigma$  and  $\text{Im}\Sigma$ . The  $\text{Im}\Sigma$  in the inset in (c) has been normalized for a better clarity. Note that the trend of an increasing RA amplitude in  $\text{Im}\Sigma$  is also visible in the unnormalized data in absolute values. 53
- 4.4 (a) ARPES spectrum of the SS with the HeI line. (b) ARPES spectrum of the SS with the short pulse XUV line. The EDCs (black and red profiles) were extracted in normal emission. The EDCs were symmetrized in (c), then the symmetric HeI EDC was deconvolved from the symmetric XUV EDC, leading to the PSF, e.g., the spectrum of the XUV line (d) (blue). Several simple peak forms with an FWHM of 250 meV were plotted for comparison. 56
- 4.5 Benchmarking of the LRD. A short pulse XUV ARPES spectrum (b) was deconvolved with a 2D  $\text{sech}^2$  PSF (see inset), producing a deconvolved ARPES spectrum (c). A high-resolution ARPES spectrum (a), taken with the narrow-bandwidth XUV line, is shown for benchmarking. (d-e) show that the LRD successfully removed the RA from the  $\text{Re}\Sigma$  and  $\text{Im}\Sigma$ . The inset (c) is the difference map between (a) and (c). The dashed lines in (c) indicate some exemplary LRD artifacts. 58
- 4.6  $\Delta_E$  dependence of the LRD. The extracted  $\text{Re}\Sigma$  (a) and  $\text{Im}\Sigma$  (b) depend on the variation of  $\Delta_E$  in the PSF for the LRD. The  $\text{Re}\Sigma$  converges onto the  $\text{Re}\Sigma$  from the narrow-bandwidth ARPES spectrum (black line). In contrast the  $\text{Im}\Sigma$  decreases with increasing  $\Delta_E$ .  $\text{Re}\Sigma$  and  $\text{Im}\Sigma$  from the narrow-bandwidth ARPES spectrum have been plotted as black lines. The number of iterations is  $N = 12$ . 59
- 4.7 Iteration ( $N$ ) dependence of the LRD. The  $\text{Re}\Sigma$  (a) and  $\text{Im}\Sigma$  (b) converge with  $N$  unto the  $\text{Re}\Sigma$  and  $\text{Im}\Sigma$  from the narrow-bandwidth measurement (black lines).  $\Delta|\text{Im}\Sigma|$  and  $\Delta|\text{Re}\Sigma|$  are a measure for the convergence of the LRD (see insets) and show that 12 iterations suffice while avoiding artifacts.  $\Delta_E$  is 200 meV. 60
- 4.8 Comparison of raw and deconvolved trARPES spectra. In (a-f), we compare the ARPES spectra before and after the deconvolution. White lines mark the bare band structure. Colored lines mark the dispersion extracted from the Lorentz fit evaluation. One exemplary MDC profile (colored profile) together with the fitted Lorentzian peak (black curve) is shown for each ARPES spectrum. The bare band structure has been plotted in white. 63
- 4.9 Influence of the LRD on the extracted self energies in trARPES. (a-c) compares the extracted  $\text{Re}\Sigma$  and  $\text{Im}\Sigma$  before (semi-transparent lines) and after (opaque lines) application of the LRD to a ARPES spectrum with a Fermi-Dirac distribution at RT ( $-7$  ps, blue lines), to a ARPES spectrum with a far-from-equilibrium distribution (60 fs, red lines) and to a ARPES spectrum with a Fermi-Dirac distribution at increased temperature (175 fs, yellow lines). 64
- 5.1 Interaction between subsystems in graphene after femtosecond IR interband excitation. The equilibrium Fermi-Dirac

charge carrier distribution (blue ellipse) is excited into an far-from-equilibrium distribution (red ellipse). Coupling with the phonon system (green ellipse) and e-e scattering processes develop the far-from-equilibrium charge carrier distribution into a Fermi-Dirac distribution with increased temperature (yellow ellipse). Then the phonon and electron system equilibrate their temperatures through e-ph coupling. The far-from-equilibrium e-ph scattering is investigated with trARPES in a pump-probe scheme. In trARPES, optical IR femtosecond pulses pump the charge carriers in graphene to far-from-equilibrium distributions. With XUV probe pulses, we analyze the many-body response via MDC linewidth evaluation from ARPES spectra. 70

5.2 Experimental ARPES spectra of graphene for increasing potassium doping. (a-d) 2D ARPES spectra of the Dirac state along the  $\Gamma$ -K direction with increasing doping left to the right (yellow number, given in  $\text{cm}^{-2}$ ). Dashed lines mark a linear continuation of the bands from below  $E_D$ ; these lines do not describe the upper bands hinting at band renormalizations due to many-body interactions. (e-h) 2D ARPES spectra of the Dirac state perpendicular to the  $\Gamma$ -K direction. One Dirac arm is not visible due to the dark-corridor effect<sup>163</sup>. The band dispersion has been extracted with an MDC Lorentz fit evaluation (black dotted lines). The extracted dispersions deviate from a linear band. These deviations are the band renormalization introduced by the  $\text{Re}\Sigma$ . There are two kinks in the dispersions. One is at 200 meV (yellow arrow) for all dopings, and the other is fixed to the downwards shifting  $E_D$  (light blue arrow). The first is related to e-ph scattering, and the second is related to e-pl scattering. There are also variations in the FWHM, which are proportional to  $\text{Im}\Sigma$ . (i) The ARPES spectrum has been simulated in a self-consistent way from the bare band structure (yellow dotted

line h and i), and the  $\text{Im}\Sigma$  extracted from (h). The close resemblance of the ARPES spectra (h) and (i) shows that many-body interactions can explain the observed kinks in the self-consistent quasiparticle picture. Figure adapted and reprinted from Ref. <sup>142</sup>. © Elsevier 2022. 73

5.3 FWHM widths ( $\propto \text{Im}\Sigma$ ), extracted from MDC ARPES profiles in graphene for different potassium doping. The FWHM has been extracted from a Lorentz fit evaluation from ARPES spectra for increasing (bottom to top) doping concentration [ $1/\text{cm}^2$ ]. Each profile is offset by  $0.025 \text{ \AA}$  from the previous. For  $n = 5.6 \text{ cm}^{-2}$ , Bostwick et al. plotted the total  $\text{Im}\Sigma$  from their scattering model (black line). At the top, their model is divided into the contributions due to e-ph scattering (green line), e-pl scattering (blue line), and e-h scattering (red line). (I - IV) mark regions where one of the interactions dominates the behavior of the total  $\text{Im}\Sigma$ . The dashed black lines ( $n = [1.2 \ 3 \ 5.6] \text{ cm}^{-2}$ ) represent the results of  $4 \times \text{Im}\Sigma$  from  $G_0W$  calculations from Ref. <sup>162</sup>. The multiplication accounts for different substrates between these calculations and the results presented by Bostwick et al.. Figure adapted and reprinted from Ref. <sup>142</sup>. © Elsevier 2022. 74

5.4 Scattering channels for photoholes (yellow spheres) in the Dirac cone for doped graphene. (a) Scattering of the photohole towards  $E_F$  due to phonon emission. (b) Scattering of the photohole due to the spontaneous generation of an electron-hole pair (black and grey spheres). (i) A photohole between  $E_F$  and  $E_D$  can scatter towards the Fermi energy by intraband e-h excitation. (ii) A photohole below  $E_F$  and above  $2E_D$  has to scatter with an energy-momentum vector with a small momentum component, i.e., a rather vertical energy-momentum vector in this Fig. Close to  $E_F$  there are no e-h pair generations with a matching vertical energy-momentum vector available. Thus the photohole is

- unlikely to scatter via an e-h pair generation below  $E_F$  and above  $2E_D$ . (iii) A photohole below the  $2E_D$  can generate interband e-h excitation. (c) Scattering of the photohole towards  $E_F$  due to plasmon emission. 75
- 5.5 Electron-phonon contributions to the self-energy. (a) Exaggerated phonon kink (left curve) and Fermi-Dirac distribution (right curve). Empty yellow circles with arrows signify the allowed (green checkmark) and forbidden (red cross) e-ph scattering processes. (b) Momentum map of graphene. The red arrows indicate which phonon modes contribute to e-ph intra- and intervalley scattering processes. (c) Eliashberg coupling function for doped graphene with  $E_D = -400$  meV. (d) Phonon band structure. The e-ph coupling strength  $\lambda_{qv}$  is color-coded onto phonon band structure (e)  $\text{Im}\Sigma$  according to equation 5.2 with the density of states. The greater size of the green checkmarks signifies a greater likelihood of the process at that energy. Dr. Dino Novko calculated the Eliashberg coupling function and the DOS shown here. 77
- 5.6 Plasmon scattering of photoholes. (a) Plasmon dispersion overlaid onto the spectrum of allowed spontaneous e-h excitations. The dielectric constant is  $\epsilon = 10$  as in Ref.<sup>39</sup>. (b) An exemplary photohole near the Dirac point (empty blue circle) scatters with a plasmon. The red arrow in (a) shows the plasmon that can be involved in this process. 81
- 5.7 ARPES momentum map of doped graphene. The dashed white lines indicate the replica bands. The black lines indicate the main bands. Figure adapted and reprinted from Ref.<sup>39</sup>. © 2022 Springer Nature. 82
- 5.8 A) Schematic Dirac cone in the non-interacting single-particle picture. B) ARPES spectrum along the  $\Gamma - K$  direction. C) ARPES spectrum perpendicular to the  $\Gamma - K$  direction. The red lines mark the K-Point. The dashed lines indicate the hole and the plasmaron band dispersions. 87
- D-G) ARPES momentum maps at different binding energies. H) Schematic Dirac-spectrum with plasmaron satellite bands. Figure adapted and reprinted from Ref.<sup>164</sup>. Reprinted with permission from AAAS. 84
- 5.9 Thermalization processes in n-Doped graphene after ultrafast IR Excitation in the electron system (Dirac cones). (a) The system in equilibrium is excited with a femtosecond IR pulse. The distribution of charge carriers is imprinted in blue on the Dirac cone. Optical interband transitions create an far-from-equilibrium carrier distribution (red in (b-d)). The far-from-equilibrium carrier distribution will thermalize within  $\approx 150$  fs to a Fermi-Dirac distribution with increased temperature (yellow) in (e). The thermalization is mediated by e-e scattering processes (b-c) and far-from-equilibrium e-ph emission processes (d). An excited electron/hole thermalizes by e-e intraband scattering processes (b) or interband excitation processes (c). The dashed arrows show Auger interband scattering processes and the full arrows interband impact scattering processes. After the electron system has thermalized, it will equilibrate with the phonon system through e-ph emissions. The time until the electron system reaches a Fermi-Dirac distribution with increased temperature of  $\approx 150$  fs is estimated from our experiment for our sample and our excitation conditions (see chapter 5.5.2). 85
- 5.10 Change in a given charge carrier distribution in impact excitation (a), intraband scattering (b), and Auger recombination (c) scattering processes in a Dirac-Cone. The red line and spheres mark the charge carrier and distribution before the scattering event, whereas blue mark them after the event. Figure adapted and reprinted from Ref.<sup>189</sup>. © 2022 American Physical Society. 87
- 5.11 (a) Contributions to the e-ph coupling strength ( $\lambda$ ) by low and high energy carriers as a function of doping with and without laser illumination. (b)

- Sketch of e-ph Coupling Channels under far-from-equilibrium Charge Carrier Distributions. Deep blue arrows mark the charge carrier decay processes mediated by e-ph coupling in equilibrium. The green arrow indicates the photoexcitation, and the far-from-equilibrium distribution is shaded light blue. The red rectangle signifies the area where the far-from-equilibrium distribution facilitates additional e-ph processes (red arrows). Figure adapted and reprinted from Ref. <sup>194</sup>. Used under Creative Commons CC BY license. 88
- 5.12 Comparison of the relaxation dynamics in n- and p-doped graphene after optical laser excitation monitored with trARPES. (a-b) ARPES spectra of p- and n- doped graphene before the arrival of the pump pulse. (c-h) trARPES difference map at different pump-probe delays for both samples. (i-j) Integrated ARPES intensity from three boxes in (c,f) vs. pump-probe delay. The excitation processes for both samples are sketched in the insets in (i-j). The n- and p- doped samples show population dynamics on widely different timescales. Figure adapted and reprinted from Ref. <sup>196</sup>. Used under terms of Creative Commons Attribution 4.0 International license 90
- 5.13 Self-energy dynamics in Kekulé -ordered graphene. (a-d) trARPES spectra of the phonon kink for several pump-probe delays. (f-i) Corresponding trARPES difference maps. (e) Band-dispersions extracted from the APRES spectra (a-d). The dashed line is the bare band structure. (j) shows the zoom into dispersion. The enlarged area is indicated with the dashed box in (e). In the insert, a further zoom-in is shown according to the enlarged dashed box in (j). Only then the small band renormalization is discernible. Figure adapted and reprinted from Ref. <sup>68</sup>. 91
- 5.14 Quasiparticle dynamics in graphene/SiC from static ARPES. (a) Static narrow-bandwidth XUV ARPES spectrum of graphene/SiC. The top-right inset signifies the measured cut along  $\Gamma - K$  in the Brillouin-zone (blue line) and the momentum range visible in the spectrum (red line). (b) Static Deconvolved Short Pulse ARPES Spectrum. The insets demonstrate a sharpening effect from the deconvolution procedure. Exemplary MDC (horizontal profiles black) are plotted with the corresponding Lorentz fit (grey or black line) and the resulting dispersions. The linear bare band structure (white line) was calculated from the extracted dispersion and FWHM in a self-consistent way (see appendix A.3) together with the  $\text{Re}\Sigma$  and  $\text{Im}\Sigma$  in (c) and (d). Panel (c) compares the  $\text{Im}\Sigma$  with the results from Ref. <sup>142</sup> (Also shown as Fig. 5.3 in this thesis.) for a doping of  $n = 1.2 \cdot 10^{13} \text{ cm}^{-2}$  (grey line) and shows the effect of the deconvolution (blue vs. light blue line). The areas where  $\text{Im}\Sigma$  is dominated by e-ph, e-h, or e-pl contributions are marked. (d) The deconvolution procedure removes the resolution artifact (RA) from the short pulse XUV spectra (green vs. light blue line). The deconvolution procedure is physically correct since it reproduces the  $\text{Re}\Sigma$  and  $\text{Im}\Sigma$  in accordance with the 70 meV energy-resolution short pulse XUV results (compare black and light blue lines in (c-d)). 94
- 5.15 Deconvolved trARPES spectra at the three characteristic timescales measured with the short pulse XUV. (a) Spectrum before the pump pulse arrives, where graphene's electron and phonon subsystems are in equilibrium. The top-right inset signifies the measured cut along  $\Gamma - K$  in the Brillouin-zone (blue line) and the momentum range visible in the spectrum (red line). (b) Spectrum directly after the optical excitation (see inset). There is a clear deviation from the bare band structure (white line) at  $E_F$  (light red horizontal line). (c) Spectrum after the pump pulse where the electron subsystem is largely thermalized

- back to a Fermi-Dirac distribution with increased temperature. 97
- 5.16 (a) Pump-probe delay-dependent evolution of  $\text{Im}\Sigma$  obtained from deconvolved data sets. The black curved arrow is a guide to the eye and subsequently connects the data from  $-7$  ps to 175 fs pump-probe delay. (b) Momentum-integrated EDCs (not deconvolved) show Fermi-Dirac distributions (fitted with black dashed lines) for delays of  $-7$  ps and 175 fs and significant far-from-equilibrium deviations from a pure Fermi-Dirac distribution for intermediate delay-steps, where additional charge carriers are detected in a broad energy window around  $E_f \pm \Omega_f$  (red area). The deviation from the pure Fermi-Dirac distribution is highlighted in the inset by plotting the gradient of the photoemission intensity along the energy axis. In this visualization, symmetric and asymmetric peaks indicate a pure FD distribution and additional far-from-equilibrium charge carriers, respectively. 98
- 5.17 Comparison of far-from-equilibrium many-body interactions in experiment and theory. (a)  $\text{Im}\Sigma$  as a function of energy for thermalized electron distributions at  $-7$  ps with electronic and phononic temperatures of  $T_e = T_{\text{ph}} = 300$  K (thick blue line: experiment, thin blue line: theory) and at 175 fs with elevated temperatures of  $\approx 800$  K (thick yellow line: experiment, thin yellow line: theory). (b)  $\text{Im}\Sigma$  as a function of energy for a delay of 60 fs, where the electronic system exhibits a strong far-from-equilibrium charge carrier distribution (thick red line: experiment, thin red line: theory). (c) and (d) Charge carrier distribution functions and schemes of possible electron-phonon scattering processes in the case of equilibrium Fermi-Dirac distributions, (c), and a strong far-from-equilibrium distribution, (d). 101
- 5.18 (a) Pump-probe delay-dependent momentum integrated EDC intensities (not deconvolved). A Fermi-Dirac Distribution (FD) with a fixed  $T = 300$  K has been fitted to the 7 ps data (black line). Another Fermi-Dirac Distribution with  $T = 3000$  K shows that the momentum integrated EDCs under far-from-equilibrium (reddish curves) conditions are not well described by this Fermi-Dirac distribution. (b) The far-from-equilibrium charge carrier distribution used to explain the e-ph quasiparticle dynamics in the previous chapter is modified to conceptually account for the loss in intensity between  $E_i$  and  $E_F$ . 105
- 5.19 Population-dynamics vs. overall increase in  $\text{Im}\Sigma$ . (a) Mean increase in  $\text{Im}\Sigma$  and number of excess charge carriers vs. pump-probe delay. The dotted lines are guides-to-the-eye to clarify the temporal behavior. With increasing delay, the charge carrier distribution develops from a far-from-equilibrium distribution toward a Fermi-Dirac distribution. In the inset, the mean lifetime of the number of excess charge carriers  $\tau_{\text{EEC}}$  and the mean lifetime of the mean increase of  $\text{Im}\Sigma$   $\tau_{\text{MI}}$  were extracted with exponential decay fits. The intensities for this figure are extracted from raw spectra, whereas the  $\text{Im}\Sigma$  are from deconvolved spectra. (b) Exemplary extraction of the excess charge carriers for 20 fs pump-probe delay. (c) Exemplary extraction of the mean increase for 20 fs pump-probe delay. 106
- 5.20 Scattering through spontaneous e-h generations in far-from-equilibrium charge carrier distributions. (a) In a conceptual charge carrier distribution, additional phase space for e-h excitations is opened up. (b) In the Dirac state, photoholes can now decay via new possible e-h excitations independent of their energy. Note that the far-from-equilibrium charge carrier distribution here is not physically correct since the number of charge carriers is not conserved but it is conceptually justified. 108
- 5.21 Theoretical inverse photohole lifetime with different charge carrier distributions. (a) The photohole lifetime has been calculated

- with equation 5.4 for the several exemplary charge carrier distributions shown in (b). In the inset, the mean increase in inverse lifetime is plotted vs. the excess charge carriers, where the 0 K Fermi-Dirac distribution is used for reference. All charge carrier distributions conserve the number of electrons. 109
- 5.22 Theoretical phonon temperature dependence of  $\text{Im}\Sigma$  from equation 5.2. An increase in phonon temperature cannot explain the overall broadening in the extreme NEQ, neither in magnitude nor form. 113
- 5.23 Momentum-integrated deconvolved EDCs show a second slight increase in intensity at  $\Omega_f$  when in far-from-equilibrium conditions. This second increase is exactly one phonon energy above  $E_i$ . This feature might be explained through the absorption of phonons by the excited charge carriers at  $E_i$ . In the inset, this is more clearly visible in the intensity gradient. 116
- 5.24 Schematic carrier thermalization in photo-inverted graphene. (a) far-from-equilibrium Plasmon Emission in Photo-Inverted Graphene. (b) Auger Recombination. Both processes turn e-h pairs into electrons described by a Fermi-Dirac distribution with increased temperature. Figure adapted and reprinted from Ref. <sup>208</sup>. © 2022 American Physical Society. 117
- A.1 Energy resolution of the XUV ARPES experiments. The overall experimental resolution has been extracted from static ARPES spectra of n-doped graphene. First, amplitude profiles are extracted from the MDC Lorentz fit evaluations. To these profiles, a convolution of a Fermi-Dirac distribution with a  $\text{sech}^2$  peak was fitted (red lines). The FWHM of the  $\text{sech}^2$  peak is overall experiment resolution with the respective line. In (a), the underlying ARPES spectrum was taken with the short pulse XUV beamline. In (b), the underlying ARPES spectrum was taken with the narrow bandwidth XUV beamline. 147
- A.2 Estimation of the temporal resolution of the trARPES experiment with the short pulse XUV beamline. The number of excited charge carrier was extracted as a function of pump-probe delay by integrating the photoemission signal above the Fermi level (0-650) meV as a function of pump-probe delay (black circles). The data is fitted with an error function (red line) in a delay region where the number of excited charge carriers rises (red filled black circles). The blue peak shows the extracted cross correlation between the IR pump pulse and the short pulse XUV pulse. 148
- A.3 The self-energies are calculated with the bare bandstructure resulting from the self-consistency algorithm. (a)  $\text{Im}\Sigma$  calculated from the FWHM (b). Comparison between  $\text{Re}_{\text{KK}}\Sigma$  calculated through KK relation and from the  $\text{Re}_D\Sigma$  Dispersion. 150
- A.4  $\text{Re}\Sigma$  vs. Pump-Probe Delay Corresponding to Fig. 5.16 152
- A.5 Exemplary Resolution Artifact with far-from-equilibrium distribution. (a) The resolution artifact around the Fermi energy has a more complex form (red box, red line) if an far-from-equilibrium charge carrier distribution (red distribution) is the basis for the RA simulation. The gained/lost population at  $E_i$  and  $E_f$  introduce new RAs compared to an equilibrium distribution. The true dispersion is plotted in black. (b) The  $\text{Im}\Sigma$  has been extracted from the simulated spectrum in (a). The LRD was applied to the simulated spectrum from (a), and the  $\text{Im}\Sigma$  was extracted (red dotted line). The deconvolved ARPES spectrum is not shown here. After the LRD, the effects of the far-from-equilibrium RA on the  $\text{Im}\Sigma$  are weaker (see Fig. A.5 red boxes). 154
- A.6  $\Delta_{k_{\parallel}}$  Dependence of the LRD. The extracted  $\text{Re}\Sigma$  depend on the variation of  $\Delta_{k_{\parallel}}$  in the PSF for the LRD. A deconvolution artifact (red box) appears with increasing  $\Delta_{k_{\parallel}}$ . The inset shows the PSF with  $\Delta_{k_{\parallel}}$  indicated. The energy resolution FWHM

- was  $\Delta_E = 200\text{meV}$  and the number of iterations was  $N = 12$ . 155
- A.7 Pump-fluence-dependent analysis of (a) quasiparticle lifetimes ( $\text{Im}\Sigma$ ; after data deconvolution) and (b) momentum-integrated EDCs (raw data) at a pump-probe delay of 40 fs with far-from-equilibrium charge carrier distributions. 156

## **A.1 Energy Resolution in ARPES with the XUV Beamlines**

The overall experimental energy resolution has been estimated for the different XUV beamlines (see Fig. A.1). First we extracted intensity amplitude profiles (see Fig. A.1 black lines) from static ARPES measurements of graphene. These amplitudes are the peak amplitudes from the MDC Lorentz fit evaluations (see chapter 5.5.1). These profiles were fitted with a convolution of a Fermi-Dirac distribution with a  $\text{sech}^2$  peak (see Fig. A.1 red lines). The linewidth of XUV is the main contribution to the resolution broadening. The  $\text{sech}^2$  peak form fits best to the spectrum of the XUV light (see chapter 4.3), and thus it was chosen for the fit as the peak form for the experimental broadening.

The resolution of the short pulse XUV from the evaluation above is (FWHM= 210meV). However, we estimate the general resolution of the short pulse XUV trARPES setup to be between 200 – 300 meV for the following reason. In chapter 4.3 the linewidth of the short pulse XUV estimated from the Shockley-surface state in Au(111) by deconvolution is greater FWHM= 250meV than the resolution estimated from the Fermi-Dirac distribution fit in this section. These different results can stem from the different methods. Furthermore, the measurements were performed on different days, so that HHG generation conditions might differ. The general resolution of the short pulse XUV trARPES setup takes these differences into account.

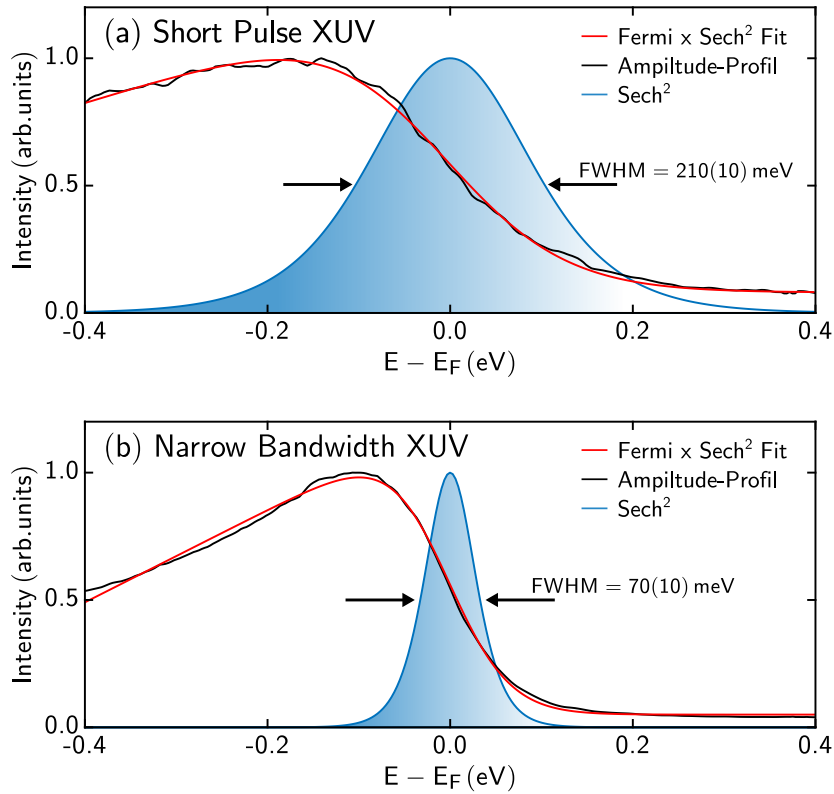


FIGURE A.1. Energy resolution of the XUV ARPES experiments. The overall experimental resolution has been extracted from static ARPES spectra of n-doped graphene. First, amplitude profiles are extracted from the MDC Lorentz fit evaluations. To these profiles, a convolution of a Fermi-Dirac distribution with a  $\text{sech}^2$  peak was fitted (red lines). The FWHM of the  $\text{sech}^2$  peak is overall experiment resolution with the respective line. In (a), the underlying ARPES spectrum was taken with the short pulse XUV beamline. In (b), the the underlying ARPES spectrum was taken with the narrow bandwidth XUV beamline.

## A.2 Time Resolution of the trARPES Experiment

The time resolution of the trARPES experiment is estimated from the rise-time of the number of photo excited charge carriers in graphene (see Fig. A.2 black circles). Marco Merboldt has carried out the evaluation. The numbers of photo excited charge carriers are obtained by integrating the photoemission signal from the Fermi energy to 650 meV above the Fermi energy as a function of pump-probe delay. An exemplary evaluation is shown in Fig. A.2. Then, an error function has been fitted (see Fig. A.2 red line) to the number of excited charge carriers in delay region where the number of excited charge carriers rises (see Fig. A.2 red filled black circles). From the fit, we extract a cross correlation with an FWHM of 45(4) fs of the compressed fundamental output and the XUV light (This result is the mean from multiple data sets). Furthermore, from the measurement of the auto correlation of the HHG driver 515 nm pulses, we determine their pulse duration to  $42 \pm 3$  fs. Likewise, we determine the pulse duration of the compressed 1030 nm fundamental output of the fiber laser to 37(3) fs. Consequently, we extract an XUV pulse duration of 17(8) fs.

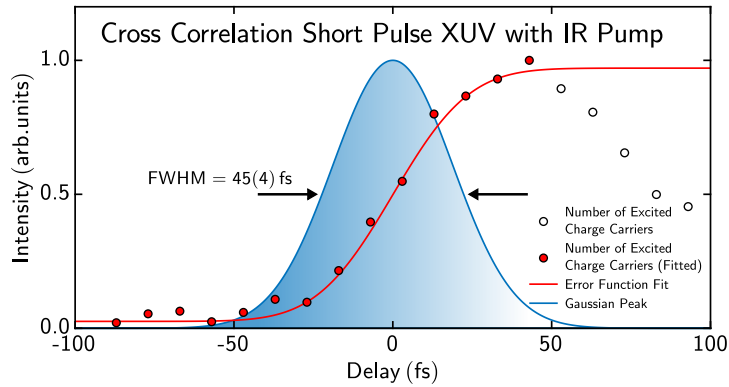


FIGURE A.2. Estimation of the temporal resolution of the trARPES experiment with the short pulse XUV beamline. The number of excited charge carrier was extracted as a function of pump-probe delay by integrating the photoemission signal above the Fermi level (0-650) meV as a function of pump-probe delay (black circles). The data is fitted with an error function (red line) in a delay region where the number of excited charge carriers rises (red filled black circles). The blue peak shows the extracted cross correlation between the IR pump pulse and the short pulse XUV pulse.

### A.3 Self-Consistent Calculation of the Self-Energy

This chapter presents a method from Ref.<sup>40</sup> to calculate the bare band structure together  $\text{Re}\Sigma$  and  $\text{Im}\Sigma$  self-consistently from the ARPES spectra.

The spectral function depends on the self-energy and the bare bandstructure<sup>9,38</sup> (see chapter 2.1.2). We can extract the FWHM and dispersion (i.e., peak positions) with the usual MDC Lorentz fit evaluation. The  $\text{Im}\Sigma$  is proportional to the FWHM, so the quasiparticle dynamics are often discussed with the FWHM. However, the bare band structure is unknown; therefore, the  $\text{Re}\Sigma$  is unknown. Therefore, one cannot say if the observed features in the  $\text{Im}\Sigma$  can be attributed to many-body interactions in the self-consistent quasiparticle picture<sup>39,141,142,40</sup>.

In Ref.<sup>40</sup>, a method that extracts the self-energy and the bare band structures directly from an ARPES spectrum is introduced. We applied this method to calculate the bare bandstructure for our data (see Fig. A.3). First, we note the  $\text{Im}\Sigma$  and  $\text{Re}\Sigma$  in the quasiparticle picture are related to each other by the Hilbert transformation due to the Kramers-Kronig relations (KK) due to the causality of the Green's function<sup>9,38</sup> (see chapter 2.1.2). The ansatz to calculate the bare bandstructure is to assume a trial bare band structure based on a few parameters and calculate the  $\text{Im}_D\Sigma$  and  $\text{Re}_D\Sigma$  from the dispersion and FWHM (see equations 2.7 and 2.6). Then the KK relations are used to transform the  $\text{Im}_D\Sigma$  into the  $\text{Re}_{\text{KK}}\Sigma$ .  $\text{Re}_{\text{KK}}\Sigma$  is then compared with  $\text{Re}_D\Sigma$ . Now the trial bare band structure is fitted until  $\text{Re}_{\text{KK}}\Sigma$  and  $\text{Re}_D\Sigma$  converge onto each other. Thus, the bare band structure is varied with this algorithm until the resulting self-energy is self-consistent. If the algorithm converges, this is a strong indication that the quasiparticle picture applies to the given systems. Thus the observed features in the  $\text{Im}\Sigma$  and  $\text{Re}\Sigma$  can be attributed to many-body interactions in the quasiparticle picture.

In Fig. A.3 we discuss the results of the method for the 70 meV energy-resolution ARPES spectrum taken with the narrow-bandwidth XUV beamline. We assumed a linear dispersion as the trial bare band structure and varied the  $v_F$  and the position of the  $K$ -point.  $\text{Re}_{\text{KK}}\Sigma$  and  $\text{Re}_D\Sigma$  (see Fig. A.3 (b) red and black line) largely agree with each other. This agreement shows that the features in  $\text{Im}\Sigma$  and  $\text{Re}\Sigma$  are self-consistent under the quasiparticle picture. However, around  $E_D$ ,  $\text{Re}_{\text{KK}}\Sigma$  and  $\text{Re}_D\Sigma$  deviate slightly. The second Dirac arm causes

this deviation since it is not entirely suppressed in the underlying ARPES spectra. Thus the second Dirac arm leads to an overestimation of the FWHM there (see chapter 5.5.1 Fig. 5.14). However, these small deviations do not prevent the discussion of the quasiparticle dynamics. Moreover, in the interesting trARPES spectra, the second Dirac is even more suppressed (see Fig. 4.8). These calculations have been performed for all the different static ARPES spectra shown in this thesis. In the case of the trARPES data, we have performed the procedure only for the deconvolved data at  $-7$  ps delay and used these bare band structure parameters for all data at the other pump-probe delays. The aforementioned approach was

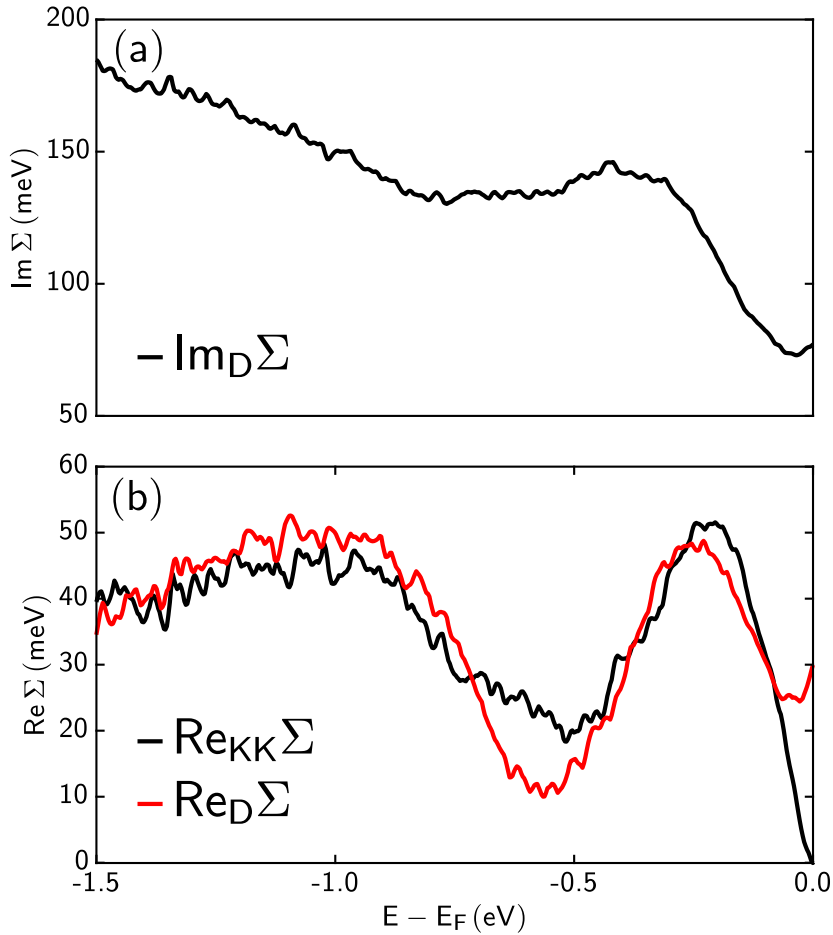


FIGURE A.3. The self-energies are calculated with the bare bandstructure resulting from the self-consistency algorithm. (a)  $\text{Im}\Sigma$  calculated from the FWHM (b). Comparison between  $\text{Re}_{\text{KK}}\Sigma$  calculated through KK relation and from the  $\text{Re}_D\Sigma$  Dispersion.

only enabled by making one assumption. We mirrored  $\text{Im}_D\Sigma$  around  $E_F$  before the Hilbert transformation. With this assumption, we implicitly assumed electron-hole symmetry, which

set  $\text{Re}_D\Sigma(E = E_F) = 0$ . This assumption is necessary since the dispersion and FWHM in an ARPES spectrum can only be extracted in a limited range. Therefore, the highest possible upper end is given by the highest occupied state, which is the Fermi energy in static measurements. However, the KK relations contain integrals from plus to minus infinity. So if we use the numeric Hilbert transformation, the results will diverge towards the edges of the range. This divergence is especially severe since the interesting phonon-kink features are near the Fermi energy. However, particle-hole symmetry is not present in doped graphene. Nevertheless, in Ref.<sup>40</sup>, it was shown that the error would be contained to a small offset in the  $\text{Re}\Sigma$ . At the lower end of the energy range,  $\text{Re}_{\text{KK}}\Sigma$  will diverge, but this edge is below the range we are showing and discussing in this thesis, so this can be neglected.

The bare band structure could also be calculated from the single-particle band structure calculations such as density-functional-theory<sup>38</sup>. However, this introduces uncertainties to the self-energies extracted with such assumptions. To understand the sources of these uncertainties, we compile the values of  $v_F$ , extracted in this section, from the different datasets and the value calculated by density-functional-theory by Dr. Dino Novko into a list. The maximum variations in this list were  $< 2\%$ . These variations are most likely a consequence of small differences in spot position and, thus, measurement geometry that leads to small distortions and shifts in the energy or momentum scale due to lens errors in the electrostatic lens system of the ARPES detector. We have already corrected most of these shifts and distortions in the ARPES spectra but small effects remain. Unfortunately, these small effects can still significantly distort the extracted  $\text{Re}\Sigma$  since it is usually in the meV range. However, the algorithm from Ref.<sup>40</sup> automatically changes the bare bandstructure parameters so that the remaining small shifts and distortions are taken into account in the bare band structure.

## A.4 Additional data from the trARPES measurements from Graphene

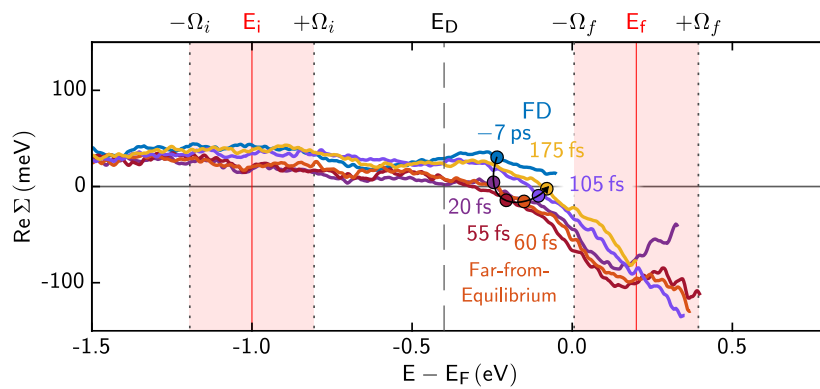


FIGURE A.4.  $\text{Re}\Sigma$  vs. Pump-Probe Delay Corresponding to Fig. 5.16

## A.5 Far-from-Equilibrium Resolution Artifact

In Fig A.5 we have simulated a resolution artifact (RA) caused by an exemplary far-from-equilibrium charge carrier distribution in same way as in chapter 4.1. The Gaussian peak of excited carriers in the far-from-equilibrium distribution is reflected in RA as there are multiple sharp edges in an occupation that introduce RAs. The exact form and magnitude of the far-from-equilibrium RA depend sensitively on the form of the underlying charge carrier distribution. However, the exact form of the pristine distribution is not accessible, so the actual far-from-equilibrium RA cannot be precisely predicted. However, when we apply the LRD (see chapter 4) to the simulated spectrum with the far-from-equilibrium RA (Fig. A.5 red dashed line), the influence of the far-from-equilibrium RA on the extracted  $\text{Im}\Sigma$  decreases. This trend holds with different charge carrier distributions and different LRD parameters. Therefore, if an far-from-equilibrium resolution artifact causes features in the  $\text{Im}\Sigma$ , these features should decrease in amplitude after applying the LRD. In chapter 4.5 the interesting features around  $E_i$  and  $E_f$  in far-from-equilibrium, which were attributed to e-ph coupling as one of the main results of the thesis, do not decrease after application of the LRD; thus, these features are unlikely to be caused by a resolution artifacts.

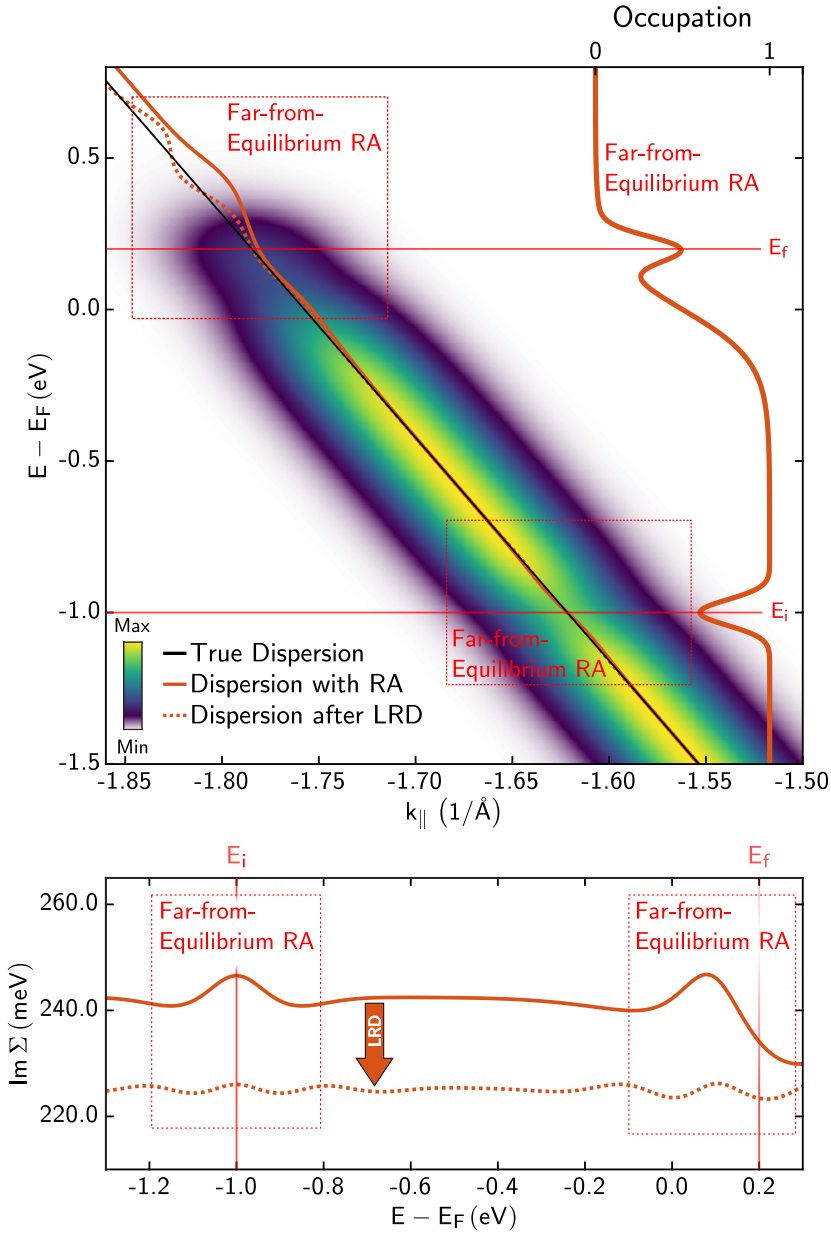


FIGURE A.5. Exemplary Resolution Artifact with far-from-equilibrium distribution. (a) The resolution artifact around the Fermi energy has a more complex form (red box, red line) if an far-from-equilibrium charge carrier distribution (red distribution) is the basis for the RA simulation. The gained/lost population at  $E_i$  and  $E_f$  introduce new RAs compared to an equilibrium distribution. The true dispersion is plotted in black. (b) The  $\text{Im}\Sigma$  has been extracted from the simulated spectrum in (a). The LRD was applied to the simulated spectrum from (a), and the  $\text{Im}\Sigma$  was extracted (red dotted line). The deconvolved ARPES spectrum is not shown here. After the LRD, the effects of the far-from-equilibrium RA on the  $\text{Im}\Sigma$  are weaker (see Fig. A.5 red boxes).

## A.6 Momentum Broadening Dependence of the LRD

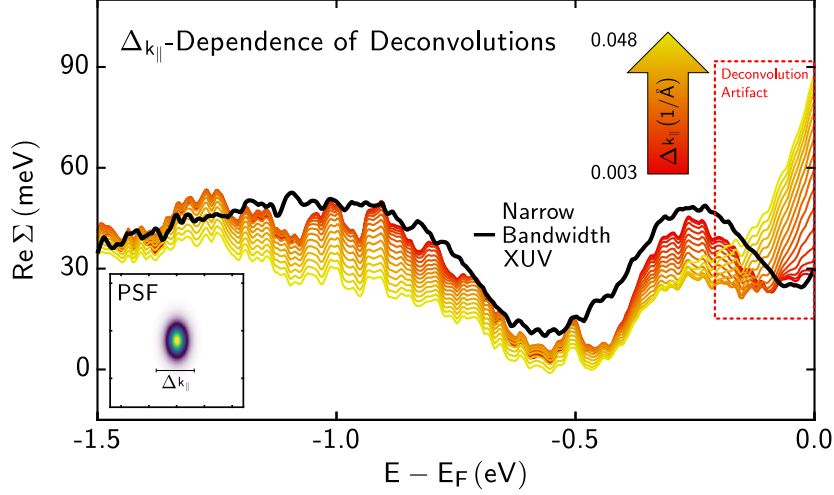


FIGURE A.6.  $\Delta k_{\parallel}$  Dependence of the LRD. The extracted  $\text{Re}\Sigma$  depend on the variation of  $\Delta k_{\parallel}$  in the PSF for the LRD. A deconvolution artifact (red box) appears with increasing  $\Delta k_{\parallel}$ . The inset shows the PSF with  $\Delta k_{\parallel}$  indicated. The energy resolution FWHM was  $\Delta E = 200\text{meV}$  and the number of iterations was  $N = 12$ .

## A.7 Pump-Fluence-Dependent Analysis of the Self-Energy

In Fig. A.7, we show a pump-fluence-dependent analysis of  $\text{Im}\Sigma$  and momentum-integrated EDCs at a pump-probe delay of 40 fs. With increasing incident fluence from  $0.5\text{ mJ/cm}^2$  up to  $1.5\text{ mJ/cm}^2$ , more and more charge carriers are redistributed over the full energy range due to the optical excitation and the subsequent scattering processes<sup>188</sup>, as is directly evident in the decreasing and increasing photoemission signal below and above  $E_F$ , respectively (Fig. A.7(b)). Concomitantly, independent of energy, the MDC linewidth increases with increasing pump-fluence as more and more phase space for far-from-equilibrium electron-hole scattering becomes available (Fig. A.7(a)). In addition, we observe the distinct signatures for far-from-equilibrium electron-phonon scattering at  $E_{i,f} \pm \Omega_{i,f}$  (red areas), as detailed in the main text.

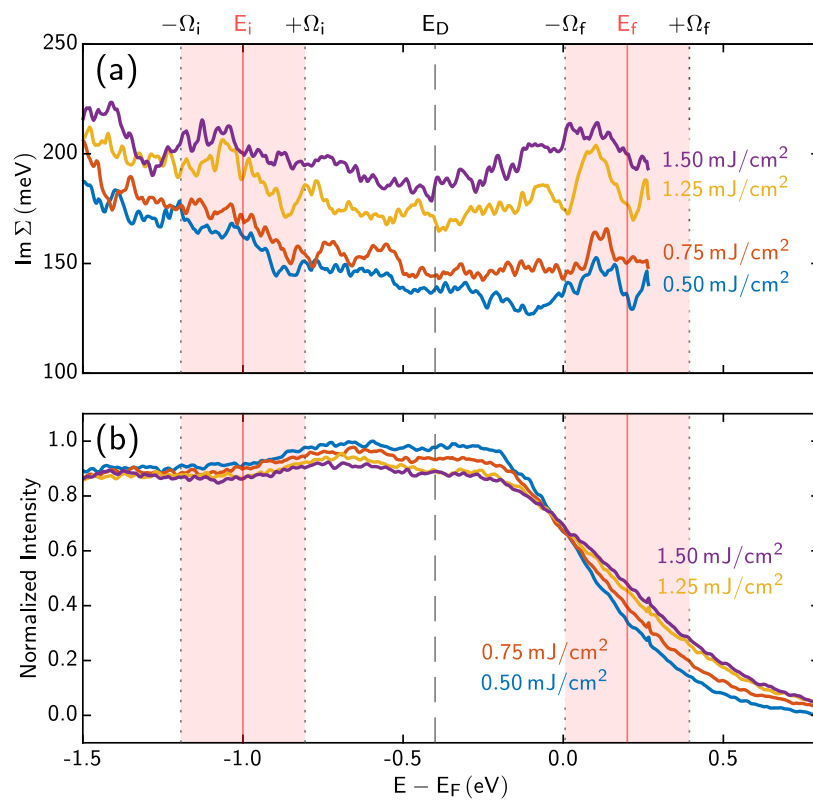


FIGURE A.7. Pump-fluence-dependent analysis of (a) quasiparticle lifetimes ( $\text{Im}\Sigma$ ; after data deconvolution) and (b) momentum-integrated EDCs (raw data) at a pump-probe delay of 40 fs with far-from-equilibrium charge carrier distributions.